

Displacement laser interferometry with sub-nanometer uncertainty

CIP-DATA LIBRARY TECHNISCHE UNIVERSITEIT EINDHOVEN

Cosijns, Suzanne J.A.G.

Displacement laser interferometry with sub-nanometer uncertainty /
by Suzanne J.A.G. Cosijns. - Eindhoven : Technische Universiteit Eindhoven,
2004.

Proefschrift. - ISBN 90-386-2656-8

NUR 978

Subject headings: optical interferometry ; light-interferometers / heterodyne
laser interferometry / periodic deviations / refractometry / displacement mea-
surement ; measurement uncertainty / dimensional metrology / nanotechno-
logy

This thesis was prepared with the \LaTeX 2 ϵ documentation system.

Printed by Grafisch bedrijf Ponsen & Looijen, Wageningen, The Netherlands.

Copyright ©2004 by S.J.A.G. Cosijns

All rights reserved. No part of this thesis may be reproduced, stored in a
retrieval system, or transmitted, in any form or by any means, electronic,
mechanical, photocopying, recording, or otherwise, without the prior written
permission from the copyright owner.

Displacement laser interferometry with sub-nanometer uncertainty

PROEFSCHRIFT

ter verkrijging van de graad van doctor
aan de Technische Universiteit Eindhoven
op gezag van de Rector Magnificus, prof.dr. R.A. van Santen,
voor een commissie aangewezen door het College voor Promoties
in het openbaar te verdedigen op
maandag 11 oktober 2004 om 16.00 uur

door

Suzanne Johanna Antonetta Geertruda Cosijns

geboren te Eindhoven

Dit proefschrift is goedgekeurd door de promotoren:

prof.dr.ir. P.H.J. Schellekens
en
prof.dr.ir. G.M.W. Kroesen

Copromotor:
dr. H. Haitjema

Samenvatting

In de huidige industrie heerst een tendens naar hogere resolutie en nauwkeurigheid in mechanische metrologie. Samen met de miniaturisering wordt hierdoor de vraag naar subnanometer onzekerheden in de dimensionele metrologie steeds groter. Verplaatsingsinterferometers worden wereldwijd gebruikt als precisie verplaatsingsmeetsystemen. Deze dissertatie beschrijft de afwijkingenbronnen welke in ogenschouw moeten worden genomen als men met deze systemen met (sub-)nanometer onzekerheid wil meten, samen met mogelijke methoden om deze afwijkingen te voorkomen of te compenseren.

In interferometrische verplaatsingsmetingen met nanometer onzekerheid over kleine afstanden (beneden 1 mm) worden de metingen beïnvloedt door periodieke afwijkingen afkomstig van polarisatiemenging. In metingen met nanometer onzekerheid over grotere afstanden worden deze afwijkingen overschaduwd door afwijkingen geïntroduceerd door brekingsindexvariaties van het medium waarin gemeten wordt.

Om de effecten van periodieke afwijkingen te onderzoeken zijn modellen ontwikkeld en getest. Een model gebaseerd op Jones-matrices maakt het mogelijk om periodieke afwijkingen te voorspellen welke afkomstig zijn van afwijkingen in de optische uitlijning en van polarisatie afwijkingen in de componenten van de interferometer. Om de polarisatie afwijkingen van optische componenten mee te nemen in de modelvorming zijn verscheidene meetmethoden ontwikkeld en gebruikt. Ten einde de polarisatie afwijkingen van een heterodyne laserhead te meten wordt een tweetal nieuwe meetopstellingen geïntroduceerd. Verder is een meetmethode, gebaseerd op ellipsometrie, ontwikkeld om de optische componenten te karakteriseren.

Met behulp van metingen welke met deze opstellingen worden uitgevoerd in combinatie met het ontwikkelde model kan worden geconcludeerd dat periodieke afwijkingen, afkomstig van verschillende afwijkingenbronnen, niet kunnen worden opgeteld. Het superpositiebeginsel kan niet zomaar worden gebruikt daar er een wisselwerking bestaat tussen de verschillende bronnen van afwijkingen welke een inherente compensatie kan veroorzaken.

Om de voorspelde periodieke afwijkingen te controleren op juistheid is een compleet interferometer systeem geplaatst op een kalibratie opstelling welke gebaseerd is op een Fabry-Pérot interferometer. Met dit systeem kan een herleidbare kalibratie worden uitgevoerd met een totale slag van 300 μm en een onzekerheid van 0,94 nm. Voorafgaand aan deze meting zijn de po-

larisatie eigenschappen van de afzonderlijke componenten van de interferometer doorgemeten om een goede voorspelling van de periodieke afwijkingen mogelijk te maken. The metingen werden vergeleken met het model en de standaardafwijking hiervan was 0,14 nm voor periodieke afwijkingen met een kleine amplitude en 0,30 nm voor periodieke afwijkingen met een amplitude van enkele nanometers.

Uit de kalibraties en metingen kan geconcludeerd worden dat het Jones model, in combinatie met de genoemde meetmethoden ter karakterisatie van de interferometer componenten, een goed en praktisch gereedschap vormt voor ontwerpers van interferometer systemen of componenten hiervan. Dit gereedschap maakt het de ontwerper mogelijk de juiste componenten en uitlijntoleranties te kiezen voor een praktische opstelling met (sub-)nanometer onzekerheid specificaties.

Een tweede herleidbare kalibratie opstelling, gebaseerd op een Fabry-Pérot interferometer, is ontworpen en gebouwd. Ten opzichte van de bestaande opstelling heeft dit systeem een verbeterde gevoeligheid, een kleinere slag en verbeterde onzekerheid van 0,24 nm over een slag van 1 μm , en 0,40 nm over een slag van 6 μm .

Om de onzekerheid van bestaande laser interferometer systemen te verbeteren is een nieuwe compensatiemethode bedacht voor heterodyne laser interferometer systemen. Deze methode is gebaseerd op een fase kwadratuur meting in combinatie met een compensatie algoritme, gebaseerd op Heydemann's compensatiemethode welke veel gebruikt wordt in homodyne interferometrie. Deze methode maakt het mogelijk om periodieke afwijkingen met een amplitude van 8 nm te reduceren tot een meting met een onzekerheid van 0,2 nm. Uit de metingen uitgevoerd met deze methode lijkt voort te komen dat periodieke afwijkingen afkomstig van ghost-reflecties in het optische systeem niet kunnen worden gecompenseerd.

Aangaande de brekingsindex van lucht zijn drie meetmethoden vergeleken. De drie empirische vergelijkingen welke in de literatuur kunnen worden gevonden zijn vergeleken met een absolute refractometer gebaseerd op een commerciële interferometer en met een tracker systeem gebaseerd op een Fabry-Pérot cavity. De tracker is getest om de bruikbaarheid van deze methode in een absolute brekingsindexmeting met verbeterde onzekerheid te onderzoeken. De ontwikkelde tracker heeft een relatieve onzekerheid van $8 \cdot 10^{-10}$. Uit de vergelijking van de drie meetmethoden kwam naar voren dat er temperatuur effecten waren, die de onzekerheid van de tracker beïnvloeden, welke nog niet verklaard kunnen worden. Desondanks kan uit de vergelijkingsmetingen geconcludeerd worden dat een absolute refractometer, gebaseerd op een Fabry-Pérot trillholte, de brekingsindex van een gas kan meten met een onzekerheid welke kleiner zal zijn dan die van de huidige methoden.

Abstract

Development in industry is asking for improved resolution and higher accuracy in mechanical measurement. Together with miniaturization the demand for sub nanometer uncertainty on dimensional metrology is increasing rapidly. Displacement laser interferometers are used widely as precision displacement measuring systems. This thesis describes the error sources which should be considered when measuring with these systems with (sub-)nanometer uncertainty, along with possible methods to overcome these errors.

When considering interferometric displacement measurements with nanometer uncertainty over small distances (below 1 mm) the measurements are influenced by periodic deviations originating from polarization mixing. In measurements with nanometer uncertainty over larger distances this error may become negligible compared to errors introduced by the refractive index changes of the medium in which the measurement takes place.

In order to investigate the effect of periodic deviations, models were developed and tested. A model based on Jones matrices enables the prediction of periodic deviations originating from errors in optical alignment and polarization errors of the components of the interferometer. In order to enable the incorporation of polarization properties of components used in interferometers, different measurement setups are discussed. Novel measurement setups are introduced to measure the polarization properties of a heterodyne laser head used in the interferometer system. Based on ellipsometry a setup is realized to measure the polarization properties of the optical components of the laser interferometer.

With use of measurements carried out with these setups and the model it can be concluded that periodic deviations originating from different error sources can not be superimposed, as interaction exists which may cause partial compensation.

To examine the correctness of the predicted periodic deviations an entire interferometer system was placed on a traceable calibration setup based on a Fabry-Pérot interferometer. This system enables a calibration with an uncertainty of 0,94 nm over a range of 300 μm . Prior to this measurement the polarization properties of the separate components were measured to enable a good prediction of periodic deviations with the model. The measurements compared to the model revealed a standard deviation of 0,14 nm for small periodic deviations and a standard deviation of 0,3 nm for periodic deviations

with amplitudes of several nanometers.

As a result the Jones model combined with the setups for measurement of the polarization properties form a practical tool for designers of interferometer systems and optical components. This tool enables the designer to choose the right components and alignment tolerances for a practical setup with (sub-)nanometer uncertainty specifications.

A second traceable calibration setup based on a Fabry-Pérot cavity was developed and built. Compared to the existing setup it has a higher sensitivity, smaller range and improved uncertainty of 0,24 nm over a range of 1 μm , and 0,40 nm over a range of 6 μm .

To improve the uncertainty of existing laser interferometer systems a new compensation method for heterodyne laser interferometers was proposed. It is based on phase quadrature measurement in combination with a compensation algorithm based on Heydemann's compensation which is used frequently in homodyne interferometry. The system enables a compensation of periodic deviations with an amplitude of 8 nm down to an uncertainty of 0,2 nm. From measurements it appears that ghost reflections occurring in the optical system of the interferometer cannot be compensated by this method.

Regarding the refractive index of air three measurement methods were compared. The three empirical equations which can be found in literature, an absolute refractometer based on a commercial interferometer and a newly developed tracker system based on a Fabry-Pérot cavity. The tracker was tested to investigate the feasibility of the method for absolute refractometry with improved uncertainty. The developed tracker had a relative uncertainty of $8 \cdot 10^{-10}$. The comparison revealed some temperature effects which cannot be explained yet. However the results of the comparison indicate that an absolute refractometer based on a Fabry-Pérot cavity will improve the uncertainty of refractive index measurement compared to existing methods.

Contents

Samenvatting	v
Abstract	vii
1 Introduction	1
1.1 Laser interferometry, the principles	2
1.1.1 Homodyne interferometers	4
1.1.2 Heterodyne interferometers	5
1.2 Error sources	7
1.2.1 Periodic deviations in laser interferometers	9
1.2.2 Refractometry	11
1.3 Project description and goals of this project	13
1.4 Thesis outline	14
2 Periodic deviations in laser interferometers	15
2.1 The origin of periodic deviations	15
2.2 Modeling of periodic deviations	17
2.3 Analytical modeling	17
2.3.1 Integral equation for an interferometer with linear optics	19
2.4 Verification of the model using a Babinet-Soleil compensator . .	21
2.5 Modular modeling of periodic deviations	24
2.5.1 The Jones matrices of the components	25
2.5.2 Modeling example	27
2.6 Interaction of periodic deviations	28
2.6.1 The influence of laser head radiation ellipticity	28
2.6.2 The influence of laser head radiation non-orthogonality	30
2.6.3 Combined error sources: Superposition principle	30
2.6.4 Interaction between polarizing beam splitter and polarizer	33
2.7 Conclusions	34
3 Polarization properties of interferometer components	35
3.1 Laser system	35
3.1.1 Carrier frequency method	37
3.1.2 Beat measurement method	41
3.1.3 Measurement results of commercial laser systems	44

3.2	Optical components: Ellipsometry	46
3.2.1	Ellipsometry	46
3.2.2	Repeatability measurement	48
3.2.3	Measurement results of optical components	48
3.3	Resulting periodic deviations	50
3.4	Conclusions	51
4	The integral calibration setup	53
4.1	Traceability	53
4.2	Fabry-Pérot interferometer	54
4.2.1	Uncertainty of the traceable calibration setup	57
4.3	Short range calibration of an entire laser interferometer	59
4.3.1	Linear optics	59
4.3.2	Plane mirror optics	62
4.4	Calibration of a homodyne interferometer	63
4.5	New designed Fabry-Pérot interferometer	65
4.5.1	Cavity length	65
4.5.2	Refractive index change	66
4.5.3	Mechanical construction	66
4.5.4	Uncertainty	68
4.5.5	Stability measurement	68
4.6	Conclusion	71
5	Compensation of periodic deviations	73
5.1	Compensation with two measurement receivers	73
5.2	Quadrature detection with a lock-in amplifier	76
5.3	Practical application	78
5.4	Measurement results	79
5.4.1	Common path verification	79
5.4.2	Verification of basic interferometer setups	81
5.4.3	Comparison probe and plane mirror optics	83
5.4.4	Traceable verification	87
5.5	Conclusions	90
6	The refractive index of air	93
6.1	Empirical equations	94
6.1.1	Parameter measurement	95
6.1.2	Uncertainty analysis of empirical equations	98
6.2	The absolute refractometer	99
6.2.1	Uncertainty analysis of the absolute refractometer	101
6.3	Tracker with improved uncertainty	102
6.3.1	Uncertainty analysis of the tracker	103
6.3.2	Frequency measurement	104
6.4	Comparison of refractometers	105
6.5	Measurement results	106
6.5.1	Absolute refractometer versus Empirical equations	106

6.5.2	Refractive index measurements	108
6.5.3	Discussion	113
6.6	Conclusions	115
7	Conclusions and recommendations	117
7.1	Periodic deviations	117
7.2	Refractive index of air	119
7.3	Recommendations	120
	Bibliography	122
A	List of symbols	131
B	Babinet-Soleil compensator	137
B.1	Calibration of the Babinet Soleil compensator	138
C	Verification of the Jones model	141
C.1	Effect of an elliptical polarized beam	141
C.2	Effect of a rotated beam splitter	145
D	Calculation of laser head polarization state measurements	153
D.1	Carrier frequency measurement	153
D.2	Beat frequency measurement	156
E	Uncertainty analysis of the Fabry-Pérot cavities	159
E.1	Existing Fabry-Pérot cavity	159
E.1.1	Axial mode effect	159
E.1.2	Transversal mode effect	160
E.1.3	Linear thermal expansion	161
E.1.4	Thermal gradients	161
E.1.5	Mirror tilt	163
E.1.6	Background slope	163
E.1.7	Cosine error	163
E.1.8	Total uncertainty of the Fabry-Pérot cavity	163
E.2	New designed cavity	164
E.2.1	Axial mode effect	164
E.2.2	Transversal mode effect	165
E.2.3	Mirror tilt	165
E.2.4	background slope	165
E.2.5	cosine error	165
E.2.6	Linear thermal expansion	165
E.2.7	Thermal gradients	167
E.2.8	Total uncertainty	167
F	Lock-in amplifier signals	169

G Refractive index equations	173
G.1 Birch and Down's equation	173
G.2 Bönsch and Potulski	173
G.3 Ciddor	174
Acknowledgments	175
Curriculum Vitae	177
Index	175

Chapter 1

Introduction

Development in industry is asking for improved resolution and higher accuracy in mechanical metrology. Together with miniaturization the demand for sub nanometer accuracy in dimensional metrology is increasing rapidly. In dimensional metrology the laser interferometer is a common used metrology system for the micrometer region, where in the nanometer region the use is spreading. Producers of CD-masters and DVD-masters as well as integrated circuit manufacturers are using laser interferometers in the nanometer region. In national metrology institutes laser interferometers are popular in use as calibration aids to calibrate other sensors, or to develop new traceable measurement devices, such as Atomic Force Microscopes [1, 2]. In such institutes laser interferometers are also used as high precision scales in coordinate measuring machines (CMM's) [3].

Integrated circuits are manufactured by means of lithography. Lithography is the process in which patterns, specific for a particular chip design, are projected onto resist on silicon wafers. This is done in a waferstepper or -scanner. A semiconductor device is built up from several layers, which need to be positioned onto each other. After each layer the wafer is extracted from the wafer scanner and etched. For the next illumination the wafer has to be repositioned and in order to form a connection of the lines in two different layers a certain overlay has to be guaranteed. The position information for this is gathered with use of laser interferometer systems. By miniaturization of integrated circuits the energy consumption can be reduced and the speed of chips can be increased. At this moment line widths of 80 nm are in use for volume production of 256MB DRAMs and other advanced memory devices such as Flash and very fast SRAMs. The overlay error should typically be 30% of the linewidth. Since the laser interferometer is only one component in the entire system the uncertainty of this system has to decrease below the nanometer region. Current demands on the laser interferometer system are already in the nanometer region.

The requirements for future lithography technology are presented by the ITRS-roadmap (International technology roadmap for semiconductors) [4]. In

table 1.1 the requirements for future line widths are presented according to ITRS, as well as the required metrology uncertainty with 3σ interval. As one of the difficult challenges the metrology and defect inspection of line widths ≥ 45 nm is mentioned through 2009. Beyond 2009 the challenge becomes even bigger for measuring critical dimensions down to 7,2 nm in 2018. This seems relatively far away, however the years mentioned are the years of first product shipment of integrated circuits from a manufacturing site with volume exceeding 10 000 units. Development capability must be available 2-3 years earlier [4].

Year	DRAM line width	overlay	metrology uncertainty
2003	100 nm	35 nm	3,5 nm
2005	80 nm	28 nm	2,8 nm
2007	65 nm	23 nm	2,3 nm
2010	45 nm	18 nm	1,8 nm
2013	32 nm	12,8 nm	1,3 nm
2016	22 nm	8,8 nm	0,9 nm
2018	18 nm	7,2 nm	0,7 nm

Table 1.1: Lithography technology requirements

To improve the accuracy of displacement laser interferometer systems toward the sub-nanometer level research has to be conducted in order to investigate the error sources at the nanometer level. This thesis describes the error sources which should be considered when measuring with nanometer uncertainty along with possible methods to overcome these errors. Note that this thesis deals with displacement interferometry, therefore wherever interferometry is mentioned displacement interferometry is meant.

1.1 Laser interferometry, the principles

The length interferometer, first introduced by Albert Michelson in 1881, has been developed into a measurement instrument with high accuracy. Since interferometry is based on the interference of light it is a non-contact measurement method of which the accuracy is influenced by the wavelength of the source and the medium in which the measurement takes place. Michelson's interferometer is schematically shown in figure 1.1.

Monochromatic light is directed at a semi-transparent mirror that acts as an amplitude dividing beam splitter. Part of the light is transmitted toward a movable mirror and reflected by this mirror. The other part of the light is reflected at 90° towards a fixed mirror, reflected and recombined at the beam splitter where their interference is observed. The electromagnetic waves propagating in reference and measurement arm can be represented as:

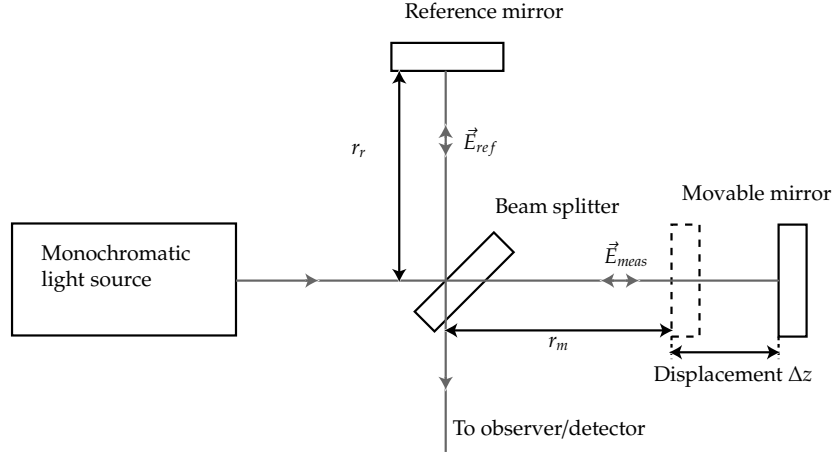


Figure 1.1: Schematic representation of Michelson's interferometer.

$$\vec{E}_{ref} = E_r e^{i(\omega t + \vec{k} \vec{r}_r - \phi_r)} \vec{e}_1 \quad (1.1)$$

$$\vec{E}_{meas} = E_m e^{i(\omega t + \vec{k} \vec{r}_m - \phi_m)} \vec{e}_2 \quad (1.2)$$

with E_r and E_m the amplitude of the respective E-fields, ω the angular frequency, t the time, \vec{k} the propagation vector, \vec{r} the position vector, ϕ_r and ϕ_m the phase in reference and measurement arm. After recombination in the beam splitter the electromagnetic field is the linear superposition of these waves. Assuming the propagation of the field in only one dimension, the irradiance at the detector becomes:

$$I = \epsilon_0 c \langle \vec{E}^2 \rangle \quad (1.3)$$

$$= \epsilon_0 c (E_r^2 + E_m^2 + 2E_r E_m \cos(k(r_m - r_r) - (\phi_m - \phi_r))) \quad (1.4)$$

where ϵ_0 is the vacuum permittivity, c the speed of light, k is the propagation constant ($k = \frac{2\pi}{\lambda}$) and r_m is the traveled optical distance in the measurement arm and r_r is the traveled optical distance in the reference arm. The constant $\epsilon_0 c$ is omitted in further calculations for convenience. If the waves were initially in phase ($\phi_r = \phi_m$) the cosine term depends on the difference in optical path length between reference and measurement arm. This is the case for a monochromatic light source. If further the two beams are of equal amplitude the irradiance is:

$$I = 2I_0 \left(1 + \cos\left(\frac{2\pi}{\lambda}(r_m - r_r)\right) \right) \quad (1.5)$$

When now the measurement mirror is displaced over a distance Δz while the reference mirror remains fixed, the optical path length changes $2n\Delta z$, with n the refractive index of the medium through which the light travels. The factor 2 is due to the fact that this distance is traveled twice by the light. If a detector is used the measurement signal will change as follows:

$$I = 2I_0 \left(1 + \cos \left(\frac{2\pi}{\lambda} (2n\Delta z) \right) \right) \quad (1.6)$$

If the wavelength of the light source is known the displacement can be calculated from the change in intensity on the detector. From this it can also be seen that it is a relative measurement, only displacement can be measured, not distance.

From Michelson's original length interferometer numerous different versions were derived, all working on the principle of measuring displacement with use of interference. Modern displacement interferometers use a HeNe-laser as a light source, due to the long coherence length and relatively short visible wavelength resulting in comfortable alignment and a smaller resolution. Laser interferometers can be divided in two kinds of interferometers: heterodyne and homodyne interferometers.

1.1.1 Homodyne interferometers

Most commercial homodyne laser interferometers consist of a stabilized single frequency laser source, polarization optics, photo detector(s) and measurement electronics. A homodyne laser source is typically a HeNe-laser with a single frequency beam as output consisting of either a single polarization under 45° or a circularly polarized beam. The beam is split into the reference arm and measurement arm of the interferometer by a beam splitter. Following a reflection off their respective targets, the beams recombine in the beam splitter. In order to observe interference the two beams must have equal polarizations. This is accomplished using a linear polarizer oriented at 45° to the beam splitter. The photo detector signal is run through electronics which count the fringes of the interference signal. A fringe is a full cycle of light intensity variation, going from light to dark to light. Every fringe corresponds to a path difference of half a wavelength corresponding to equation 1.6. Since there is no intrinsic time-dependency in the measurement signal this is also called a DC interferometer. Depending on the detector configuration, direction sensing and insensitivity to power changes can be derived as well as a compensation for periodic deviations such as developed by Heydemann [5]. In figure 1.2 the principle of such a homodyne interferometer is shown. Signal I_0 is used to normalize the intensity. Signals I_{S_0} and $I_{S_{90}}$ are used for phase quadrature measurement. Signal I_{S_0} is the normal signal of a homodyne interferometer (1.6) with signal $2I_0$ subtracted:

$$I_{S_0} = 2I_0 \cos \left(\frac{4\pi n \Delta z}{\lambda} \right) \quad (1.7)$$

Part of the measurement signal is split off and receives a phase shift of 90° , this measurement signal is called $I_{S_{90}}$:

$$I_{S_{90}} = 2I_0 \sin\left(\frac{4\pi n \Delta z}{\lambda}\right) \quad (1.8)$$

From these equations the displacement is calculated as follows:

$$\Delta z = \frac{\lambda}{4\pi n} \arctan\left(\frac{I_{S_{90}}}{I_{S_0}}\right) \quad (1.9)$$

When both signals are plotted against each other ideally a circle is described. If polarization mixing occurs periodic deviations are present in the measurement signals which results in an ellipse. Also different gains in both detector signals will result in an ellipse. Heydemann [5] presented a method to transform this ellipse into a circle and hence compensate for periodic deviations. Manufacturers of homodyne interferometers are Renishaw, Heidenhain, Sios and recently Interferomet.

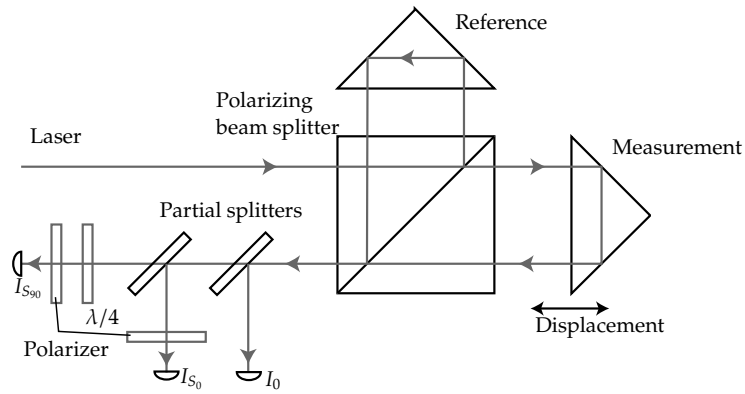


Figure 1.2: Schematic representation of the principle of a homodyne laser interferometer with power compensation and direction sensing. I_0 is used to eliminate effects of power changes, I_{S_0} and $I_{S_{90}}$ are used for phase quadrature measurement, enabling compensation of periodic deviations.

1.1.2 Heterodyne interferometers

The basic setup of a heterodyne interferometer is shown in figure 1.3. The light source of a heterodyne laser interferometer is a stabilized HeNe laser whose output beam contains two frequency components (f_1 and f_2), each with a unique linear polarization. Their electromagnetic field is represented by:

$$\vec{E}_1 = E_{01} e^{i(2\pi f_1 t + \phi_{01})} \vec{e}_1 \quad (1.10a)$$

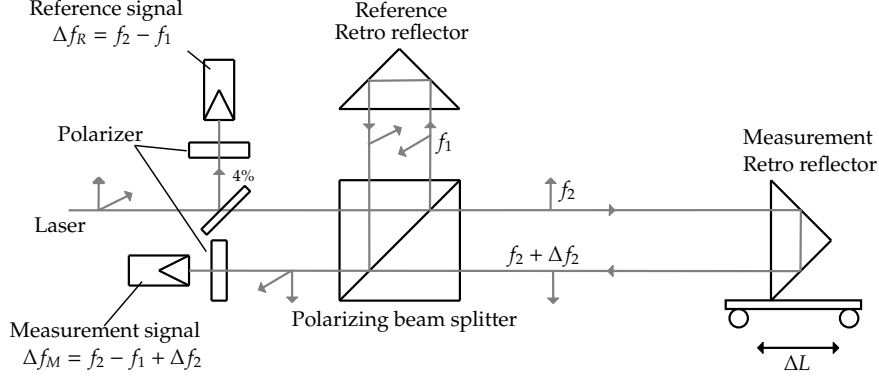


Figure 1.3: Schematic representation of the principle of a heterodyne laser interferometer. The reference retro reflector is in a steady position, while the measurement retro reflector is attached to the object of which the displacement should be measured.

$$\vec{E}_2 = E_{02} e^{i(2\pi f_2 t + \phi_{02})} \vec{e}_2 \quad (1.10b)$$

where E_{01} and E_{02} represent the amplitude and ϕ_{01} and ϕ_{02} represent the initial phase of the electromagnetic field. The frequency shift can be generated by a Zeeman laser. The Zeeman technique produces two frequencies by applying an axial magnetic field to the laser tube. Another way to generate a frequency shift is by an acousto optic modulator, for example a Bragg cell driven by a quartz oscillator. With the Zeeman technique the frequency split is limited to a maximum of ± 4 MHz. The acousto optic modulator enables a frequency split of 20 MHz or more. In a heterodyne interferometer the two polarizations are orthogonal to each other.

Part of the light emitted by the laser source is split off, passes a combining polarizer and falls onto a detector with a band-pass filter. The resulting signal is an alternating signal with a beat frequency equal to the split frequency in the laser head. This signal forms the reference measurement I_r , given by:

$$I_r = 2E_{01}E_{02} \cos(2\pi(f_2 - f_1)t + (\phi_{02} - \phi_{01})) \quad (1.11)$$

As can be seen from this equation the heterodyne interferometer works with a carrier frequency $(f_2 - f_1)$, therefore it is called an AC interferometer. The rest of the light emerges from the laser head and enters the interferometer optics, in figure 1.3 consisting of a polarizing beam splitter and two retro reflectors. In the polarizing beam splitter the two frequencies are split by means of polarization splitting. Frequency f_1 is reflected by the polarizing beam splitter and enters the reference arm, is reflected by the fixed retro reflector and is again reflected by the polarizing beam splitter. Frequency f_2 is transmitted by the polarizing beam splitter and enters the measurement arm, is reflected by the moving retro reflector and is again transmitted by the beam splitter. Ideally, both frequencies

emerge from the polarizing beam splitter in their own unique polarization orthogonal to each other. To enable interference the beams are transmitted through a polarizer under 45° with their polarization axes. After the polarizer the light falls onto a second detector with band-pass filter resulting in the measurement signal:

$$I_m = 2E_{01}E_{02} \cos(2\pi(f_2 - f_1)t + (\phi_{02} - \phi_{01}) + (\phi_{meas} - \phi_{ref})) \quad (1.12)$$

where $\phi_{meas} - \phi_{ref}$ is the difference in phase between the signal in the measurement arm and the reference arm. It consists of a constant term in the reference arm ϕ_{0r} and a phase in the measurement arm consisting of a constant term ϕ_{0m} combined with a changing term as a result of the moving retro reflector:

$$\phi_{meas} - \phi_{ref} = \Delta\phi + \phi_{0m} - \phi_{0r} \quad (1.13)$$

In a practical application the measurement retro reflector is attached to the object of which the displacement should be measured. As the retro reflector moves in the measurement arm with velocity v , a Doppler shift is generated for frequency f_2 :

$$\Delta f = \frac{2vf_2}{v_l} = \frac{2vnf_2}{c} \quad (1.14)$$

with v_l the velocity of light, n the refractive index of air and c the speed of light in vacuum. From this equation it follows that the maximum traveling speed of the retro reflector is limited due to the finite frequency shift between the two frequencies in the laser source. The phase change in the interference pattern resulting from the Doppler shift equals:

$$\Delta\phi = \int_{t_1}^{t_2} 2\pi\Delta f dt = \int_{t_1}^{t_2} 2\pi \frac{2vnf_2}{c} dt = 4\pi \frac{nf_2}{c} \int_{t_1}^{t_2} v dt = 4\pi n \frac{f_2}{c} \Delta l \quad (1.15)$$

where n is the refractive index of the medium through which the light travels (usually air) and Δl is the displacement of the retro reflector. So by measuring the phase change between the measurement (1.11) and the reference signal (1.12) the displacement of the retro reflector can be determined by using the inverse of equation (1.15) with vacuum wavelength λ_2 :

$$\Delta l = \frac{\Delta\phi\lambda_2}{4\pi n} \quad (1.16)$$

1.2 Error sources

In section 1.1 ideal interferometers were described and it was shown that for a heterodyne interferometer the displacement of a retro reflector could be determined by measuring the phase change between measurement and reference signal and by using equation (1.16). From this formula it can be seen that the

accuracy of the calculated displacement depends on the accuracy of the determination of the phase change $\Delta\phi$, the wavelength of light used λ_2 and the refractive index of the medium n . Apart from these inherent error sources there are numerous other error sources depending on the setup used. The errors in the laser interferometer can be divided into three categories: Setup dependent, instrument dependent and environment dependent.

In the category "Setup dependent" errors are found depending on the measurement setup. Typically these can be minimized or even eliminated by using a correct setup and alignment procedures. Examples of these errors are Abbe-error [6], cosine error, mechanical stability and deadpath error. The deadpath is the difference in distance in air between the reference and measurement paths of an interferometer configuration ($l_m - l_r$ in figure 1.4). Further the target uniformity (right side of figure 1.4) can influence the accuracy of the interferometer. Optics used in basic interferometers usually have a surface figure of $\lambda/10$, contributing to an error of up to 63 nm. Therefore, to achieve accuracies below the nanometer region high end optics have to be used.

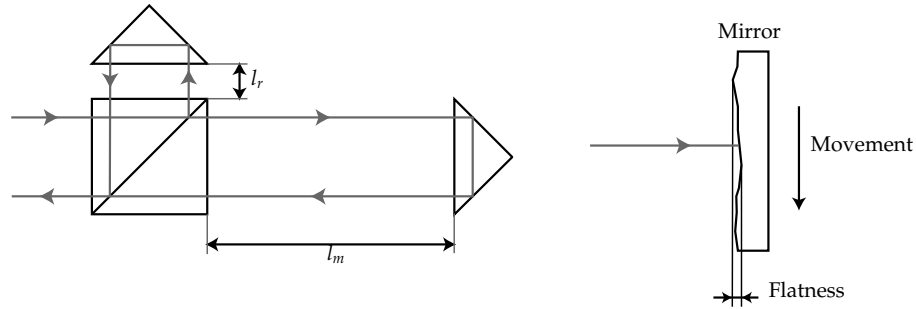


Figure 1.4: Schematic representation of the deadpath error $l_m - l_r$ and target uniformity.

In the category "Instrument dependent" the frequency of the laser source is found (relative stability between $2 \cdot 10^{-9}$ and $5 \cdot 10^{-8}$). Further the effect of electronics like counting errors and electronics nonlinearities (usually around 0,5 nm). The error resulting from the delay from interferometer optics to the measurement sample, also known as data aging was investigated by Demarest [7] and the limitations in phase measurement were investigated by Oldham [8]. Both data age uncertainty and phase measurement errors depend on the electronic system used. Ghost reflections, originating from plane surfaces of the optics, were modeled by Wu [9, 10] and can be minimized by using good anti-reflection coatings; since mica and calcite are poor substrates for surface coatings these should be avoided [9]. Periodic deviations are a result of polarization mixing and can result from all sources introducing non-ideal polarizations. They will be investigated in detail in this thesis and previous research in this field will be discussed in section 1.2.1.

In the category "Environment dependent" the thermal influence on the

interferometer is found, like linear expansion of the optics setup, or the thermal effects of optics itself. Also the refractive index of the medium through which the light travels (mostly air) belongs to this category. Usually this effect is compensated for, using Edlén's [11, 12] updated equation and measuring temperature, pressure, humidity and carbon dioxide component. The relative uncertainty is usually limited to $2 \cdot 10^{-8}$, resulting in an error of 20 nm per meter, or 1 nm in 50 mm. Further the influence of (air) turbulence as described by Bobroff [13] must be considered since this is a movement of thermal gradients in the air through the beam path. They can be minimized by enclosing the beam paths in protective tubes.

In conclusion the influences on accuracy of a laser interferometer are:

- Setup dependent
 - Cosine error
 - Abbe error
 - Deadpath error
 - Mirror uniformity
 - Mechanical stability
- Instrument dependent
 - Frequency stability laser source
 - Electronics
 - Periodic deviations
 - Ghost reflections
 - Data age uncertainty
- Environment dependent
 - Refractive index
 - Thermal influence
 - Turbulence

From the error sources mentioned above the principal limitations of the interferometer lie in the photonic noise (frequency stability) and periodic deviations inherent in the interferometer. For measurements over large displacements in air this error is overshadowed by the effect of the refractive index of air. These are the subjects of investigation in this thesis.

1.2.1 Periodic deviations in laser interferometers

When the measured displacement with a real interferometer is plotted against the actual displacement of the moving retro reflector an oscillation around the ideal straight line may be observed, as can be seen from figure 1.5. This effect is

known as a periodic deviation of the laser interferometer. As already mentioned in the previous section the periodic deviations are a result of polarization leakage in the interferometer. Periodic deviations manifest themselves as periodic deviations in the measurement. In 1983 Quenelle first mentioned the existence of periodic deviations as a result of alignment errors between laser and optics [14]. In 1987 Bobroff [13] showed the existence of periodic deviations as a result of the alignment of the polarizing beam splitter along with the quality of the coating. This periodic deviation had a frequency of one cycle per one wavelength optical path change. In the same year Sutton [15] proved the existence of periodic deviations with a frequency of two cycles per one wavelength optical path change. He did this by pressure scanning of the interferometer. From this time results the definition of first and second order periodic deviations: First order periodic deviations have a frequency of one cycle per one wavelength optical path change, and second order periodic deviations have a frequency of two cycles per one wavelength optical path change. In literature periodic deviations in laser interferometers are often called non-linearities.

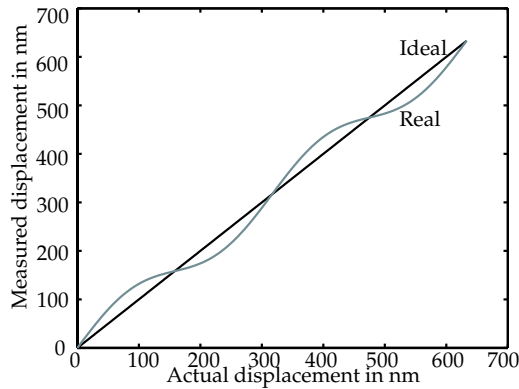


Figure 1.5: Schematic representation of measurement results with a periodic deviation. The magnitude of the periodic deviation is exaggerated for clarity.

In 1990 Rosenbluth and Bobroff modeled the individual influences of misalignment and ellipticity of the laser axes, differential transmission between the two arms of the interferometer, rotation of polarization by retro reflectors, leakage through the beam splitter and wave plate errors [16]. They concluded that frequency mixing is not a major cause of periodic deviations unless the mixing is asymmetric between the two arms of the interferometer. Regrettably this conclusion was not stated with numbers. In 1992 Hou and Wilkening presented an analytical model describing the individual influence of non-orthogonality and ellipticity of the laser beams as well as the limited extinction capability of the beam splitter [17]. De Freitas and Player showed that in contrast with earlier modeling a second order harmonic could result from rotational beam

alignment [18]. In 1995 they published a fairly complete model based on coherency matrix calculation [19]. The drift of periodic deviations in a heterodyne interferometer was investigated by Hou and Zhao in 1994 [20]. De Freitas [21] addressed the problem of how laser source birefringence and dichroism affect the linearity in heterodyne interferometry.

Along with the modeling several ways of observing periodic deviations are discussed in literature. Stone and Howard provided a simple technique to observe periodic deviations as a result of a rotated beam splitter by rotating the beam splitter around the yaw axis [22, 23]. However with the presented model they were not able to explain the measured amplitude of the existing third harmonic. Further measurements were made of interferometers against other sensors with nanometer resolution such as capacitive sensors by Haitjema [24, 25]. Wetzels [26] presented traceable measurements by measuring against a Fabry-Perot cavity, later this was also done by Howard [27]. Badami and Patterson [28] presented a frequency domain method for the measurement of periodic deviations in heterodyne interferometry which can also be used for in situ optimization of the interferometer. Patterson and Beckwith proposed a method for direct measurement of periodic deviations using a constant-speed moving system and a spectrum analyzer [29]. They experimentally demonstrated the compensation of periodic deviations by electrically subtracting the first-order periodic deviation signal from the measurement beat signal.

To prevent periodic deviations in laser interferometers a new interferometer design was presented by Tanaka et al. [30] and later another by Wu et al. [31]. Dubovitsky eliminated the effect of leakage by phase modulating the laser light [32]. All these designs require a special setup of the interferometer. Recently Eom and Choi [33] provided a simple method of compensating the periodic deviations by means of phase quadrature measurements in a heterodyne interferometer with a split frequency of 160 kHz. This method is widely used for homodyne interferometers and was originally developed by Heydemann [5].

From the summary above it can be concluded that a lot of research has been done already in order to model periodic deviations as well as to prevent or eliminate periodic deviations. The modeling often concentrates on single error sources or a small combination of influences. Further some conclusions contradict each other. In order to get some clarity a model has to be presented including all mentioned possible causes of periodic deviations and possibly more. Also the model should become a tool for designers of interferometers to make design choices in order to limit periodic deviations. Further this model should be verified unambiguously using traceable measurement techniques. Industry demands the elimination of periodic deviations in commercial heterodyne interferometers.

1.2.2 Refractometry

As already mentioned for measurements over large displacements in air the periodic deviations in a laser interferometer becomes overshadowed by the effect of the refractive index of air. In 1966 Edlén empirically derived an equation to

determine the refractive index of air from dispersion and measurements of the temperature, pressure, humidity and carbon dioxide content [11]. As starting point he defined standard air, meaning dry air with a temperature of 15 °C, a total pressure of 760 Torr (101,325 kPa) and 300 ppm carbon dioxide content. The relative uncertainty of this equation was determined at $\frac{u(n)}{n} = 5 \cdot 10^{-8}$ [34].

Since then the ITS-90 temperature scale was accepted [35] and new data were available for the density of air and the refractivity of water vapour. Birch and Downs [36, 12] took into account SI-units, updated the equation with use of these data and increased the carbon dioxide content of normal laboratory air to 450 ppm and included it as a constant. The 3σ uncertainty associated with these equations is $\frac{u(n)}{n} = 3 \cdot 10^{-8}$. Later Ciddor [37] derived a formula intended for a broader range of wavelengths and extreme environmental conditions (−40°C to 100°C, 80 to 120 kPa and 0 to 100% relative humidity). For this entire range he derived an overall uncertainty of $\frac{u(n)}{n} = 2$ to $5 \cdot 10^{-8}$. Bönsch and Potulski [38] revised Edlén's formula again, however no improvement of the accuracy was gained compared to Birch and Downs [12] and the results showed an agreement between the values calculated by both formula's within the stated uncertainties. However Bönsch and Potulski reintroduced a correction factor for the carbon dioxide content (standard 400 ppm), which Birch and Downs omitted. For all derived equations the total uncertainty associated with the calculated refractive index of air could easily be increased up to $\frac{u(n)}{n} = 1 \cdot 10^{-7}$ due to the additional individual accuracy of each atmospheric sensor used.

Up until today the effect of the refractive index of air is mostly determined with the use of Edlén's equation or one of the revised versions. To achieve nanometer uncertainty this is not enough. To improve the uncertainty of measurements, or to monitor the changes in refractive index directly, a refractometer can be used. Refractometers are based on measuring optical path differences while keeping an equal mechanical distance. Due to this principle also the refractive indices of other gases can be determined.

In the group Precision Engineering at the Eindhoven University of Technology a long tradition in refractometry exists. Already in 1986 the group was involved in the comparison between interference refractometers built in different countries [39]. Most of these refractometers were based on measuring a certain mechanical stable path in vacuum with a commercial interferometer, next the measurement path is filled with air while the reference path remains in vacuum. As a result the interferometer will measure an optical path change as a result of a changing refractive index. When the mechanical path length is known the change in refractive index can be determined. Limiting factor in this measurement is measuring the mechanical path length with a small uncertainty and keeping the mechanical path stable during measurement. At that time the relative uncertainty of the refractometers varied between $\frac{u(n)}{n} = 1 \cdot 10^{-8}$ and $\frac{u(n)}{n} = 6 \cdot 10^{-8}$ (2σ). Hou and Thalmann [40] also experimented with an equal setup, also with an uncertainty of $\frac{u(n)}{n} = 5 \cdot 10^{-8}$ (3σ). In the group Precision Engineering a second refractometer was built based on a permanent vacuum chamber [41] of which the length was varied within the measurement arm. The

uncertainty of this system was $\frac{u(n)}{n} = 1 \cdot 10^{-7}$. In 1997 Eickhoff and Hall [42] took a new approach by using a Fabry-Perot cavity and frequency measurement enabling a resolution much higher than commercial interferometers. The agreement with the revised Edlén equation was $5 \cdot 10^{-8}$ over several hours, the relative uncertainty however was not stated.

1.3 Project description and goals of this project

Most interferometer systems use polarizing optics. As a result of alignment errors of the optics and polarization errors in the optics polarization mixing will occur. The latter will result in contrast errors when homodyne interferometers are used, or frequency mixing when heterodyne interferometers are used. Both result in periodic deviations in the measurement. In industrial environments this can lead to production errors in the case of new generation wafer scanners or to position errors in systems which use interferometers in their control loop. In order to bring the accuracy of laser interferometer systems to the (sub-)nanometer level the origin of periodic deviations should be known. In order to achieve this in this project the periodic deviations will be analyzed and described. Since the periodic deviation errors in homodyne interferometers can be compensated for [5] the main focus in this thesis will be on heterodyne interferometers. The model should enable a designer of laser interferometer systems to make design choices, minimizing the periodic deviations. Since the polarization quality of the components used in the interferometer will also influence the periodic deviations they should be included in the model. Further to use the quality as input parameters of the model measurement methods should be developed to measure the polarization deviations in the optics used as well as the polarization deviations in the laser source. To test the model unambiguously verification measurements should be done using a traceable calibration setup with nanometer accuracy developed in an earlier PhD-program [26]. To improve the calibration uncertainty a new setup has to be designed based on this calibration setup with a maximum uncertainty of 0,5 nm.

Due to the high costs of vacuum equipment air is mostly preferred as the medium through which the light is transported. In order to improve the accuracy of laser interferometer systems working in air the absolute refractive index of air has to be measured with an uncertainty better than $2 \cdot 10^{-8}$. To test the feasibility of a new absolute refractometer based on a Fabry-Pérot cavity a tracker has to be built, which measures the change of refractive index with an uncertainty below $5 \cdot 10^{-9}$. To test the system a comparison should be made between the refractive index determined with the three versions of the modified Edlén's equation and an absolute refractometer based on a commercial interferometer.

1.4 Thesis outline

First in chapter 2 two models will be presented to calculate the periodic deviations. One is based on analytical modeling and the second is based on Jones [43] modeling. Also some modeling results will be shown for basic interferometers. Further a simple method will be presented to test part of the models. In chapter 3 the polarization measurements of interferometer components such as the laser head and optics will be presented. In chapter 4 the traceable calibration setup will be explained and the calibration of different complete interferometer setups is discussed. Further the design of a new traceable calibration setup is discussed and the stability is tested. Of both systems an uncertainty calculation is described. A possible method to compensate periodic deviations in heterodyne interferometers will be discussed in chapter 5. The influences of the refractive index of air will be explained in chapter 6 together with the design of the tracker system. A comparison between three versions of Edlén's equation, an absolute refractometer and a tracker with improved accuracy is also presented in chapter 6. Finally conclusions and recommendations are presented in chapter 7.

Chapter 2

Periodic deviations in laser interferometers

The field of interferometry tends toward more accurate measurements with increasing resolution. The principal limitations of laser interferometer systems are in the photonic noise and the residual periodic deviations which are inherent in periodic signals. Periodic deviations are present in the phase measurement system itself, but they can also result from the optics used: beam splitters, retardation plates used with plane mirrors and retro reflectors can influence the polarization state in interferometers using polarizing optics, or influence the contrast of interferometers with non-polarizing optics. The modeling of periodic deviations is important to understand the influence of different sources on the periodic deviations and in any future compensation for these errors. Until now research done on the influence of sources of periodic deviations [17, 18] was based on the calculation of different influences separately or a combination of influences from the beam splitter [22]. In this chapter the origin of periodic deviations will be discussed and a general model is presented to calculate the periodic deviations resulting from a combination of deviations in the polarization state of the light emitted by the laser and optics.

2.1 The origin of periodic deviations

The laser head shown in figure 2.1 consists of a laser source which emits two orthogonally polarized beams with a different frequency (f_1 and f_2). These two beams can be represented as:

$$\vec{E}_1 = E_0 \sin(2\pi f_1 t + \phi_{01}) \vec{e}_1 \quad (2.1)$$

$$\vec{E}_2 = E_0 \sin(2\pi f_2 t + \phi_{02}) \vec{e}_2 \quad (2.2)$$

A non-polarizing beam splitter divides the beam in two parts: one reference

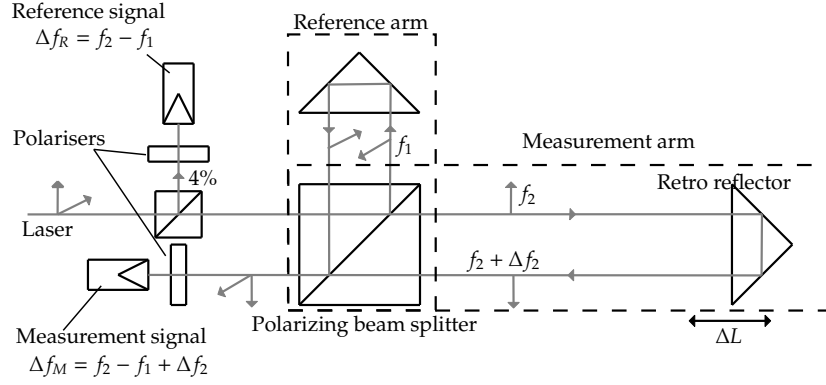


Figure 2.1: Schematic representation of the principle of a heterodyne laser interferometer.

part and one measurement part. The reference part passes a combining polarizer and falls on a detector resulting in an interference signal of which only the alternating current is measured due to the use of a band-pass filter, eliminating both the DC component and optical frequencies. This signal can be represented by:

$$I_{ref} = \frac{1}{2} E_0^2 \left[\cos \left(2\pi(f_2 - f_1)t + (\phi_{02} - \phi_{01}) \right) \right] \quad (2.3)$$

The measurement part is divided by a polarizing beam splitter in a reference arm and in a measurement arm. The signal in the measurement arm receives a Doppler shift as a result of the moving retro reflector, resulting in a phase shift of the measurement signal compared to the reference signal [44]:

$$\Delta\phi_2 = 2\pi\Delta f_2 t = \frac{4\pi n\Delta l}{\lambda_2} \quad (2.4)$$

with λ_2 representing the vacuum wavelength of the light reflected by the mirror and n the refractive index of air in the measurement path. With a polarizer the signal from the reference arm and the signal from the measurement arm are combined and result in an interference signal. From this interference signal the measurement signal is constructed containing the phase information and therefore containing the displacement of the retro reflector. In an ideal laser interferometer \vec{E}_1 enters the reference arm and \vec{E}_2 enters the measurement arm and the detected signal can be represented by:

$$I_{meas} = \frac{1}{2} E_0^2 \left[\cos \left(2\pi(f_2 - f_1)t + (\phi_{02} - \phi_{01}) + \Delta\phi_2 \right) \right] \quad (2.5)$$

where f_1 and f_2 are the frequency of measurement and reference arm, ϕ_{01} and ϕ_{02} are the initial phase of both frequencies and $\Delta\phi_2$ is the phase difference as a

result of the target movement. The measurement with a laser interferometer is based on measuring the phase difference between the measurement signal (2.5) and the reference signal (2.3). In a common laser interferometer the separation between both arms and therefore both polarization states is not ideal, part of the measurement frequency enters the reference arm and part of the reference frequency enters the measurement arm and gets a Doppler shift also. This results in an extra phase term in the measurement signal which now can be represented as:

$$I_{measnl} = \frac{1}{2} E_0^2 \left[\cos(2\pi(f_2 - f_1)t + (\phi_{02} - \phi_{01}) + \Delta\phi_2 + \Delta\phi_{pd}) \right] \quad (2.6)$$

The calculation in the interferometer however uses only one frequency resulting in periodic deviations in the measurement results. The extra phase term therefore represents the periodic deviations of the system.

2.2 Modeling of periodic deviations

Most commercial interferometers are based on polarization splitting, in these systems all deviations in polarization will cause periodic deviations. Earlier studies (see section 1.2.1) have proved that a number of different influences on periodic deviations in laser interferometers exist. These possible influences can be summarized as:

- Elliptically polarized laser beams
- Non-orthogonally polarized laser beams
- Rotational error in the alignment of laser and beam splitter
- Rotational error in the alignment of the mixing polarizer
- Different transmission coefficients in the beam splitter

All polarization errors in the optics also cause polarization mixing, which in heterodyne laser interferometry results in frequency mixing. Therefore apart from the influences mentioned above also the polarization errors in the optics should be considered in the model. The model should be able to calculate periodic deviations resulting from all these errors separately as well as from a combination. Unequal intensities of the two frequencies emitted by the laser head of a heterodyne interferometer results in a deteriorated contrast. In combination with ideal phase measuring this would not result in periodic deviations. The phase measuring electronics are not considered in this thesis.

2.3 Analytical modeling

The errors mentioned above can be represented schematically as in figure 2.2. The ellipticity of the laser beams is defined as $d\varepsilon_1$ and $d\varepsilon_2$, the non-orthogonality

and rotation of the laser referred to the beam splitter are both represented by α and β , i.e. for a rotational error of orthogonally polarized light $\beta = -\alpha$ and for non-orthogonality $\beta \neq -\alpha$. The transmission coefficients of the beam splitter are represented as χ and ξ . Finally the rotation angle of the polarizer compared to $\frac{\pi}{4}$ is referred to as θ .

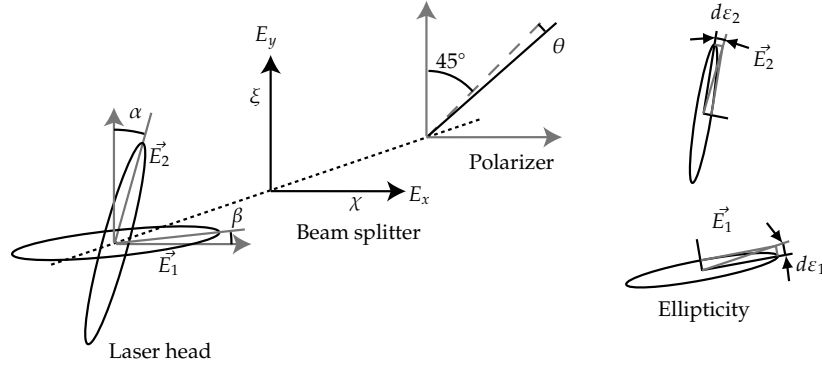


Figure 2.2: Schematic representation of the parameters influencing the periodic deviations in a laser interferometer.

Orthogonal elliptically polarized light with equal amplitudes emitted by the laser head can be represented as:

$$E_1 = E_0 [\cos(d\varepsilon_1) \sin(2\pi f_1 t + \phi_{01}) - \sin(d\varepsilon_2) \cos(2\pi f_2 t + \phi_{02})] \quad (2.7)$$

$$E_2 = E_0 [\sin(d\varepsilon_1) \cos(2\pi f_1 t + \phi_{01}) + \cos(d\varepsilon_2) \sin(2\pi f_2 t + \phi_{02})] \quad (2.8)$$

where $d\varepsilon_1$ and $d\varepsilon_2$ represent the ellipticity as shown in figure 2.2. For the simplicity of further formulas this can be represented as:

$$E_1(x_1, x_2) = E_0 [\cos(d\varepsilon_1) \sin(x_1) - \sin(d\varepsilon_2) \cos(x_2)] \quad (2.9)$$

$$E_2(x_1, x_2) = E_0 [\sin(d\varepsilon_1) \cos(x_1) + \cos(d\varepsilon_2) \sin(x_2)] \quad (2.10)$$

The transmission through the beam splitter can be described as a projection of the two beams on the polarization axes of the beam splitter. Each polarization axis of the beam splitter has its own attenuation and both arms receive a phase shift of which the difference contains a term representing the displacement. In mathematical form this can be represented as:

$$E_x = \xi [\cos \beta E_1(x_1 + \phi_1, x_2 + \phi_1) + \sin \alpha E_2(x_1 + \phi_1, x_2 + \phi_1)] \quad (2.11)$$

$$E_y = \chi [\sin \beta E_1(x_1 + \phi_2, x_2 + \phi_2) + \cos \alpha E_2(x_1 + \phi_2, x_2 + \phi_2)] \quad (2.12)$$

where ξ and χ are the transmission coefficients in respectively x and y direction of the beam splitter and α and β represent the non-orthogonality and rotational

alignment error. The phase retardance of the two beams emerging from the polarizing beam splitter are indicated as ϕ_1 and ϕ_2 respectively. In the interferometer one of these beams receives a phase shift ($\Delta\phi$) due to the moving retroreflector. In this representation this phase shift is $\Delta\phi = \phi_1 - \phi_2$. The intensity transmitted through a rotated polarizer can be represented as:

$$I = \left[E_x \cos\left(\frac{\pi}{4} - \theta\right) + E_y \sin\left(\frac{\pi}{4} - \theta\right) \right]^2 \quad (2.13)$$

where θ represents the angle of the polarizer compared to $\frac{\pi}{4}$ referred to the beam splitter axes.

After substitution of formulas (2.7-2.13) into each other and simplifying it using the knowledge of the use of a bandpass filter, eliminating DC components and optical frequencies, an equation follows of the form:

$$\begin{aligned} I_{meas} = & M \cos\left(2\pi(f_2 - f_1)t + (\phi_{02} - \phi_{01}) + \Delta\phi\right) \\ & + N \sin\left(2\pi(f_2 - f_1)t + (\phi_{02} - \phi_{01}) + \Delta\phi\right) \end{aligned} \quad (2.14)$$

This can be rewritten into one cosine term:

$$I_{meas} = \sqrt{M^2 + N^2} \cos\left(2\pi(f_2 - f_1)t + (\phi_{02} - \phi_{01}) + \Delta\phi - \arctan\left(\frac{N}{M}\right)\right) \quad (2.15)$$

This gives the formula for the intensity on the detector in the form of formula (2.6) but with a different amplitude. However as mentioned before the measurement of the interferometer is based on a phase measurement. The phase of the resulting formula therefore includes the periodic deviations. By calculation of N and M the periodic deviations are represented by $\arctan(N/M)$. The result is presented in the next paragraph.

2.3.1 Integral equation for an interferometer with linear optics

The periodic deviations of a linear interferometer resulting from a non-orthogonally, elliptically polarized laser light source passing a rotational misaligned beam splitter with different transmission coefficients and a rotated polarizer can be calculated with the use of equation (2.16):

$$\Delta\phi_{pd} = -\arctan \frac{(B + D) + (B - D) \sin(2\theta) + F \cos(2\theta)}{(A + C) + (A - C) \sin(2\theta) + E \cos(2\theta)} \quad (2.16)$$

With

$$\begin{aligned} A &= \chi^2 \begin{bmatrix} \cos \beta \sin \alpha \cos(d\varepsilon_1) \cos(d\varepsilon_2) \cos \Delta\phi \\ + \sin \beta \cos \alpha \sin(d\varepsilon_1) \sin(d\varepsilon_2) \cos \Delta\phi \\ - \cos \beta \cos \alpha \cos(d\varepsilon_1) \sin(d\varepsilon_2) \sin \Delta\phi \\ + \sin \beta \sin \alpha \sin(d\varepsilon_1) \cos(d\varepsilon_2) \sin \Delta\phi \end{bmatrix} \\ B &= \chi^2 \begin{bmatrix} \cos \beta \sin \alpha \cos(d\varepsilon_1) \cos(d\varepsilon_2) \sin \Delta\phi \\ + \sin \beta \cos \alpha \sin(d\varepsilon_1) \sin(d\varepsilon_2) \sin \Delta\phi \\ + \cos \beta \cos \alpha \cos(d\varepsilon_1) \sin(d\varepsilon_2) \cos \Delta\phi \\ - \sin \beta \sin \alpha \sin(d\varepsilon_1) \cos(d\varepsilon_2) \cos \Delta\phi \end{bmatrix} \\ C &= \xi^2 \begin{bmatrix} \sin \beta \cos \alpha \cos(d\varepsilon_1) \cos(d\varepsilon_2) \cos \Delta\phi \\ + \cos \beta \sin \alpha \sin(d\varepsilon_1) \sin(d\varepsilon_2) \cos \Delta\phi \\ - \cos \beta \cos \alpha \sin(d\varepsilon_1) \cos(d\varepsilon_2) \sin \Delta\phi \\ + \sin \beta \sin \alpha \cos(d\varepsilon_1) \sin(d\varepsilon_2) \sin \Delta\phi \end{bmatrix} \\ D &= \xi^2 \begin{bmatrix} \sin \beta \cos \alpha \cos(d\varepsilon_1) \cos(d\varepsilon_2) \sin \Delta\phi \\ + \cos \beta \sin \alpha \sin(d\varepsilon_1) \sin(d\varepsilon_2) \sin \Delta\phi \\ + \cos \beta \cos \alpha \sin(d\varepsilon_1) \cos(d\varepsilon_2) \cos \Delta\phi \\ - \sin \beta \sin \alpha \cos(d\varepsilon_1) \sin(d\varepsilon_2) \cos \Delta\phi \end{bmatrix} \\ E &= \chi\xi \begin{bmatrix} \cos \beta \cos \alpha \cos(d\varepsilon_1) \cos(d\varepsilon_2) \\ - \sin \beta \sin \alpha \sin(d\varepsilon_1) \sin(d\varepsilon_2) \\ + \sin \beta \sin \alpha \cos(d\varepsilon_1) \cos(d\varepsilon_2) \cos 2\Delta\phi \\ - \cos \beta \cos \alpha \sin(d\varepsilon_1) \sin(d\varepsilon_2) \cos 2\Delta\phi \\ - \cos \beta \sin \alpha \sin(d\varepsilon_1) \cos(d\varepsilon_2) \sin 2\Delta\phi \\ - \sin \beta \cos \alpha \cos(d\varepsilon_1) \sin(d\varepsilon_2) \sin 2\Delta\phi \end{bmatrix} \\ F &= \chi\xi \begin{bmatrix} - \cos \beta \sin \alpha \cos(d\varepsilon_1) \sin(d\varepsilon_2) \\ - \sin \beta \cos \alpha \sin(d\varepsilon_1) \cos(d\varepsilon_2) \\ + \sin \beta \sin \alpha \cos(d\varepsilon_1) \cos(d\varepsilon_2) \sin 2\Delta\phi \\ - \cos \beta \cos \alpha \sin(d\varepsilon_1) \sin(d\varepsilon_2) \sin 2\Delta\phi \\ + \cos \beta \sin \alpha \sin(d\varepsilon_1) \cos(d\varepsilon_2) \cos 2\Delta\phi \\ + \sin \beta \cos \alpha \cos(d\varepsilon_1) \sin(d\varepsilon_2) \cos 2\Delta\phi \end{bmatrix} \end{aligned}$$

Simplifying this formula with $\alpha = \beta = \theta = d\varepsilon_2 = 0$ and $\xi = \chi = 1$, which means an ideal interferometer except for one elliptically polarized laser beam, gives the following equation:

$$\Delta\phi_{pd} = -\arctan \left(\frac{-\sin(d\varepsilon_1) \cos(\Delta\phi)}{\sin(d\varepsilon_1) \sin(\Delta\phi) + \cos(d\varepsilon_1)} \right) \quad (2.17)$$

This is equal to equation 13 of Hou and Wilkening [17] where they use $\rho = d\varepsilon_1$. Another simplification follows from substituting $\beta = -\alpha$ and $d\varepsilon_1 = d\varepsilon_2 = \theta = 0$ and $\xi = \chi = 1$ which means a rotational misalignment of the beam splitter gives:

$$\Delta\phi_{pd} = -\arctan\left(\frac{-\sin^2\alpha \sin(2\Delta\phi)}{\cos^2\alpha - \sin^2\alpha \cos(2\Delta\phi)}\right) \quad (2.18)$$

Rewriting of this formula results in equation 11 found by Player and De Freitas [18]. So the mentioned different cases modeled by Hou and Wilkening [17] and Player and De Freitas [18] follow exactly from a simplification of the full formula 2.16.

2.4 Verification of the model using a Babinet-Soleil compensator

The model presented in section 2.2 combined different theories of causes of periodic deviations resulting from previous publications of various authors. To verify the theory in practice a Babinet-Soleil compensator was used, replacing the beam splitter-retro reflector optics of the modeled interferometer (see figure 2.3).

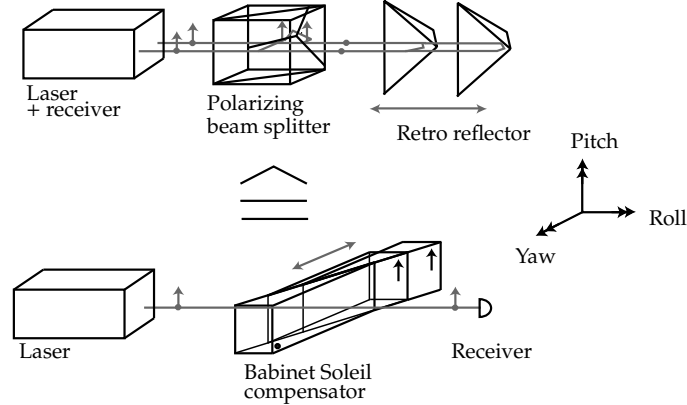


Figure 2.3: Schematical representation of the simulation of the interferometer optics with a Babinet-Soleil compensator.

The Babinet-Soleil compensator provides a common path for both polarization components, and therefore cancels out any influence of the refractive index of air. It also provides a convenient way to apply an optical path difference of a fraction of a wavelength. This optical path difference is produced due to a difference in refractive index for two orthogonal polarization states. The phase difference introduced between both polarization axes can be represented as [45]:

$$\Delta\phi_{BS} = 2\pi \left| \frac{n_{\perp}}{\lambda_{\perp 0}} - \frac{n_{\parallel}}{\lambda_{\parallel 0}} \right| \Delta d \quad (2.19)$$

where $\lambda_{\perp 0}$ and $\lambda_{\parallel 0}$ are the vacuum wavelengths of both polarization states, n_{\perp} and n_{\parallel} are the refractive indices for both polarization arms and Δd represents the thickness difference of the two materials in the Babinet-Soleil compensator (see also appendix B). By varying the thickness of the compensator (through movement of the wedges compared to each other, see figure 2.3) the optical path difference between both polarization states can be varied.

The test setup consists of a heterodyne laser source [83, 84] placed firmly on an optical bench, a Babinet-Soleil compensator which can be rotated around its roll-axis and a receiver [85] which can be rotated around its roll-axis also. The receiver was read out with a PC-card [86] with help of self written software which reads the card at maximum resolution and integrates over 10 measurements.

An important aspect for the verification of the model with use of a Babinet-Soleil compensator is the repeatability of the measurements. This repeatability was tested in three sessions done at different times during one day. The results are shown in figure 2.4. It shows a standard deviation of 0,1 nm which is sufficient for the tests to be done.

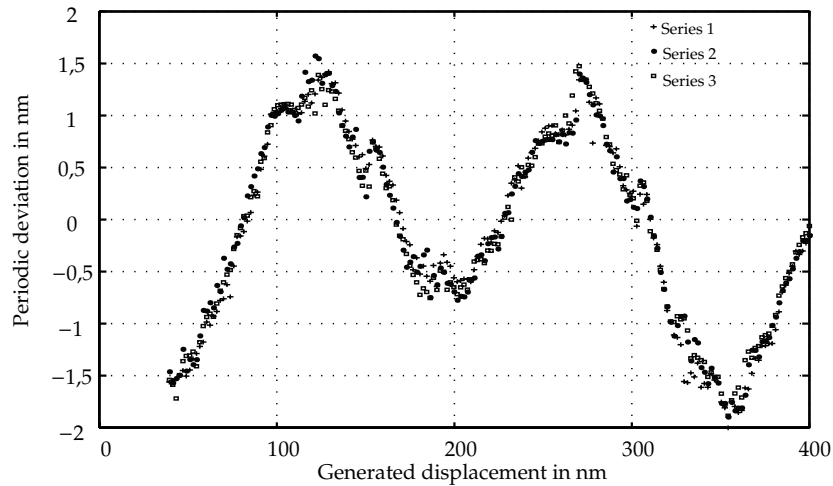


Figure 2.4: Result of the repeatability test for the Babinet-Soleil compensator.

To ensure a correct measurement of periodic deviations the scale of the Babinet-Soleil compensator was calibrated using a second Babinet-Soleil compensator as shown in figure 2.5. Initially for both Babinet-Soleil compensators the optical displacement was calibrated against the mechanical displacement at 0 , $\lambda/2$ and λ , see appendix B. Then four measurements of the periodic deviations of a laser-Babinet-Soleil-receiver configuration were done, like in figure 2.7, with the first Babinet-Soleil compensator at a phase shift representing 0 , $\lambda/4$, $\lambda/2$ and $3\lambda/4$. At these four initial phase shifts the second Babinet-Soleil compensator, used for further measurements, was displaced within the same

range as during the measurements ($0 - \lambda$). Averaging these four measurements results in the calibration as shown in figure 2.6 and was used to correct the measurements of periodic deviations.

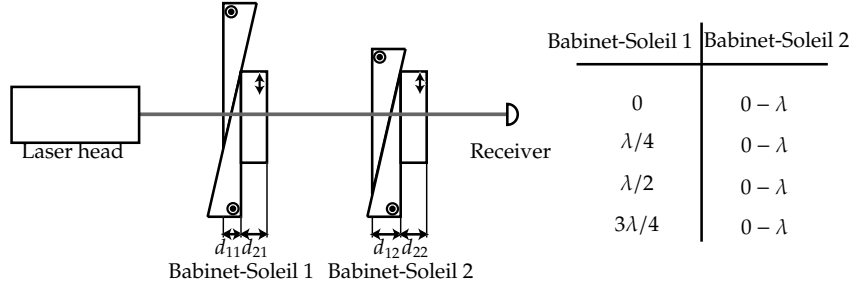


Figure 2.5: Schematic representation of the calibration of the Babinet-Soleil compensator.

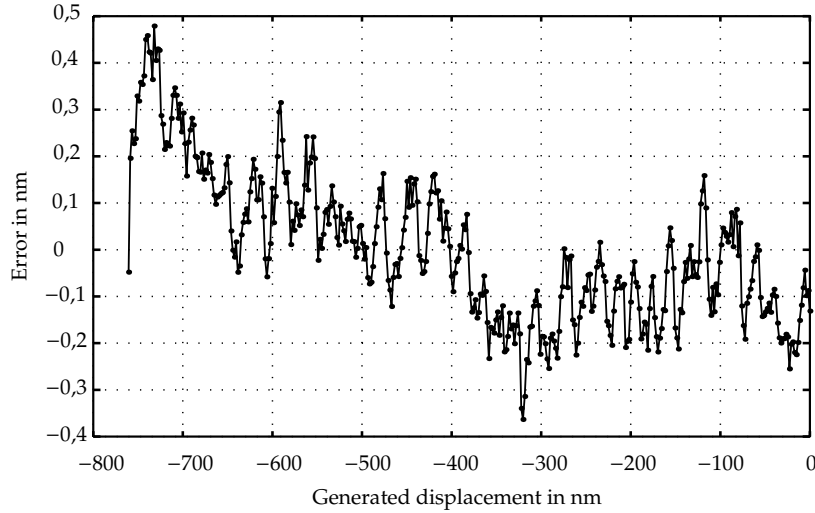


Figure 2.6: Calibration result for the Babinet-Soleil compensator.

In the measurement setup there are two controlled variables: the rotation angle of the Babinet-Soleil compensator (representing α and $-\beta$) and the rotation angle of the receiving polarizer (representing θ) which can both be set with a resolution of $0,01^\circ$. All other parameters are kept constant. To be able to model the interferometer correctly the non-orthogonality and ellipticity of the laser polarizations and the transmission coefficients of the Babinet-Soleil compensator were measured with use of a polarizer and a spectrum analyzer. The ellipticity for the laser polarizations appeared to be $0,38^\circ$ for E_1 and $-0,36^\circ$ for E_2 . The non-orthogonality was $0,2^\circ$. The transmission coefficients of the

Babinet-Soleil compensator were 0,72 for horizontal component and 0,71 for the vertical component. These values were used for further simulations comparing the model with the measurements with the Babinet-Soleil compensator.

In figure 2.7 two results are presented of the measurement with use of a Babinet-Soleil compensator together with the result of the analytical model.

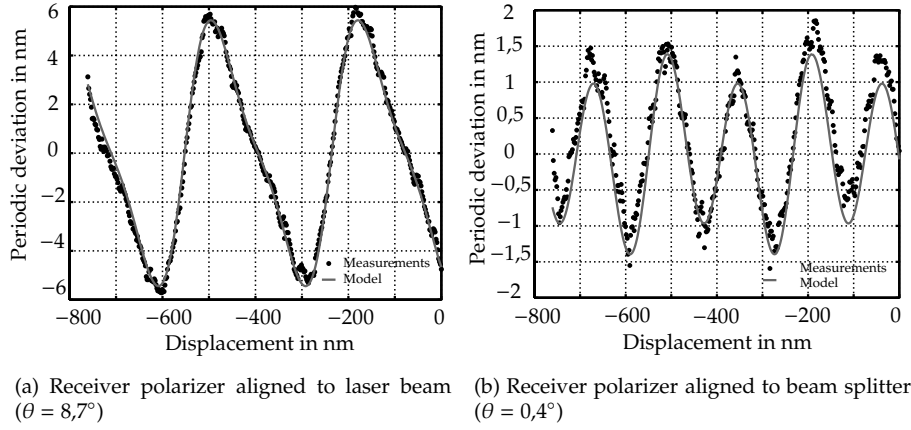


Figure 2.7: Theoretical and experimental results of the measurement of the periodic deviations in an interferometer with a rotated beam splitter ($\alpha = 8,6^\circ, \beta = -8,8^\circ$) and a rotated polarizer. Further variables used in the model were: the transmission coefficients $\xi = 0,72$ and $\chi = 0,71$, the ellipticity $d\varepsilon_1 = 0,38^\circ$ and $d\varepsilon_2 = -0,36^\circ$ as defined in figure 2.2.

Both figures show an excellent correspondence between the theory and the measurements resulting in a standard deviation of the model compared to the measurements of only 0,3 nm for the left figure and 0,2 nm for the right figure. Which will be partially caused by the reproducibility of the operators hand and the micrometer screw to set the Babinet Soleil.

2.5 Modular modeling of periodic deviations

To calculate the above mentioned analytical model of a linear interferometer is a time consuming task. In order to have a flexible model Jones matrix calculation can be used [23, 19]. Jones matrix calculation enables one to change the optical setup easily to calculate the effects of different optical setups on the periodic deviation. Further it enables the input of polarization properties of optical components. The axes definition used for the Jones matrix calculation is shown in figure 2.8. Here the angle of rotation of the beam splitter and the non-orthogonality angle are defined separately, in contrast to the definition for the analytical model (see figure 2.2). The angles are related to each other as follows:

$$\alpha + \beta = \eta_2 - \eta_1 \quad (2.20a)$$

$$\alpha = \alpha_{PBS} \quad (2.20b)$$

In the following subsection the Jones matrices of non-ideal interferometer components are described.

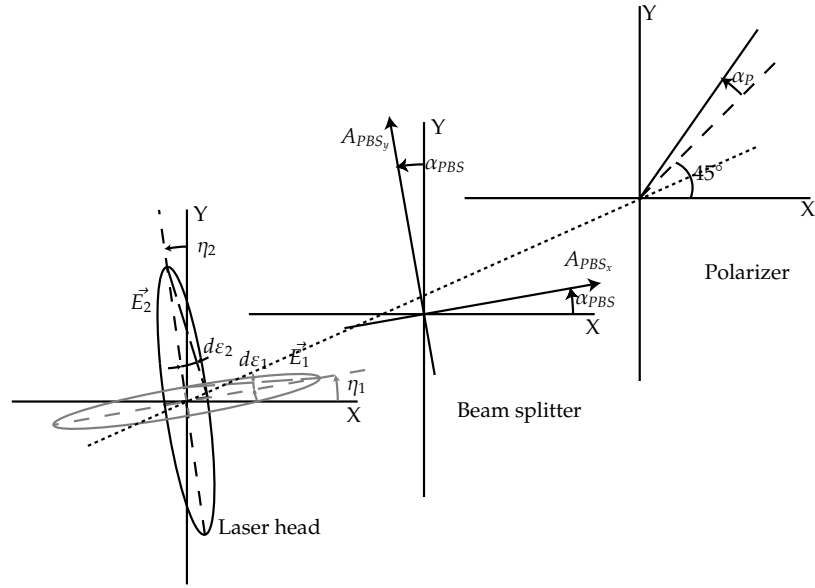


Figure 2.8: Schematic representation of the axes definition used in the Jones model of the heterodyne laser interferometer

2.5.1 The Jones matrices of the components

Elliptically, non-orthogonally polarized light emitted by a heterodyne laser head of one frequency can be represented with a Jones vector as follows:

$$\vec{E}_1 = R(\eta_1) * \begin{bmatrix} \cos(d\varepsilon_1) \\ -i * \sin(d\varepsilon_1) \end{bmatrix} * e^{i(2\pi f_1 t + \phi_{01})} \quad (2.21a)$$

for frequency f_1 and

$$\vec{E}_2 = R(\eta_2) * \begin{bmatrix} i * \sin(d\varepsilon_2) \\ \cos(d\varepsilon_2) \end{bmatrix} * e^{i(2\pi f_2 t + \phi_{02})} \quad (2.21b)$$

for frequency f_2 , where $d\varepsilon_1$ and $d\varepsilon_2$ represent the ellipticity of the light as shown in figure 2.8 and $\eta_1 - \eta_2$ represents the angle of non-orthogonality. In the ideal case ($d\varepsilon_1 = d\varepsilon_2 = 0, \eta_1 = \eta_2 = 0$) both plane waves become orthogonally linearly polarized. $R(\alpha)$ is the rotation matrix with angle α :

$$R(\alpha) = \begin{bmatrix} \cos(\alpha) & -\sin(\alpha) \\ \sin(\alpha) & \cos(\alpha) \end{bmatrix} \quad (2.22)$$

The beam splitter can be represented by two matrices, one for transmission and one for reflection.

$$PBS_t = R(\alpha_{PBS}) * \begin{bmatrix} A_{PBS_x} e^{i\delta_{PBS_x}} & 0 \\ 0 & 1 \end{bmatrix} * R(-\alpha_{PBS}) \quad (2.23a)$$

$$PBS_r = R(\alpha_{PBS}) * \begin{bmatrix} 1 & 0 \\ 0 & A_{PBS_y} e^{i\delta_{PBS_y}} \end{bmatrix} * R(-\alpha_{PBS}) \quad (2.23b)$$

Where α_{PBS} is defined as the angle of rotation around the roll axis. If ideally the P polarization is transmitted and S polarization is reflected then A_{PBS_x} is defined as the leakage coefficient of the S polarization direction into the P polarization direction of the transmitted light. δ_{PBS_x} is the phase change between the main axes of the transmitted light. A_{PBS_y} is defined as the leakage coefficient of the P polarization direction into the S polarization direction of the reflected light, δ_{PBS_y} is the phase change between the main axes of the reflected light.

In a plane mirror interferometer quarter wave plates are used. A non-ideal wave plate is described by:

$$WP = R\left(\frac{\pi}{4} + \alpha_{WP}\right) \begin{bmatrix} A_{WP_x} e^{-i(\frac{\phi_{WP} + d\phi_{WP}}{2})} & 0 \\ 0 & A_{WP_y} e^{i(\frac{\phi_{WP} + d\phi_{WP}}{2})} \end{bmatrix} R\left(-\frac{\pi}{4} - \alpha_{WP}\right) \quad (2.24)$$

here α_{WP} is the rotational misalignment of the wave plate compared to an angle of $\frac{\pi}{4}$, ϕ_{WP} represents the order of the wave plate ($\phi = \frac{\pi}{2}$ represents a quarter wave plate) and $d\phi_{WP}$ is the phase error of the wave plate. A_{WP_x} and A_{WP_y} represent the transmission coefficients of the main axes of the wave plate.

A polarizer can be described as follows:

$$P = T_p \begin{bmatrix} \cos^2(\frac{\pi}{4} + \alpha_p) & \sin(\frac{\pi}{4} + \alpha_p) \cos(\frac{\pi}{4} + \alpha_p) \\ \sin(\frac{\pi}{4} + \alpha_p) \cos(\frac{\pi}{4} + \alpha_p) & \sin^2(\frac{\pi}{4} + \alpha_p) \end{bmatrix} \quad (2.25)$$

Where T_p represents the transmission coefficient of the polarizer and α_p represents an extra phase shift introduced by the polarizer. According to Liu and Azzam [46] the retro reflectors always have two linear eigenstates. A moving retro reflector is then described as follows:

$$MRRF = \begin{bmatrix} A_{x_M} e^{i(\alpha_x + 3\pi + d\phi)} & 0 \\ 0 & A_{y_M} e^{i(\alpha_y + 3\pi + d\phi)} \end{bmatrix} \quad (2.26)$$

where A_{x_M} and A_{y_M} are the reflection coefficients of the retro reflector in x and y direction. α_x and α_y are the phase changes occurring in x and y direction due to the retro reflector. $d\phi$ is the phase change due to the movement of the retro reflector, for a steady retro reflector $d\phi = 0$. For a certain frequency f this phase change equals:

$$d\phi = \frac{4\pi n \Delta l f}{c} \quad (2.27)$$

where Δl represents the displacement of the retro reflector, and c is the velocity of light in vacuum. For a static (reference) retro reflector $d\phi$ would equal zero. For a single mirror the static phase shift would equal π instead of 3π .

2.5.2 Modeling example

In a heterodyne interferometer the phase change is measured by counting the zero-passings of the interference signal. To facilitate modeling the time dependency is replaced by a phase shift varying from 0 to 2π of one frequency compared to the other emerging from the laser head. This means for every position of the target, the phase shift of light emerging from the interferometer is calculated while frequency 1 is shifted up to 2π . From the output the phase of the first harmonic is calculated representing the periodic deviations.

Since Jones matrices only represent phase changes due to optical components both frequencies are modeled separately as well as the reference and measurement path. For the first frequency traveling through linear interferometer optics we would get:

$$\vec{E}_{rf_1} = PBS_r * RRF * PBS_r * \vec{E}_1 \quad (2.28)$$

$$\vec{E}_{mf_1} = PBS_t * MRRF * PBS_t * \vec{E}_1 \quad (2.29)$$

$$\vec{E}_{f_1} = \vec{E}_{rf_1} + \vec{E}_{mf_1} \quad (2.30)$$

For the second frequency this would hold the same formula, except \vec{E}_1 has to be replaced by \vec{E}_2 :

$$\vec{E}_{rf_2} = PBS_r * RRF * PBS_r * \vec{E}_2 \quad (2.31)$$

$$\vec{E}_{mf_2} = PBS_t * MRRF * PBS_t * \vec{E}_2 \quad (2.32)$$

$$\vec{E}_{f_2} = \vec{E}_{rf_2} + \vec{E}_{mf_2} \quad (2.33)$$

The returning E-field emerging from the beam splitter is the complex sum of both E-fields: $\vec{E}_{BS} = \vec{E}_{f_1} + \vec{E}_{f_2}$. From the beam splitter the beam passes a polarizer to create an interference signal: $\vec{E}_P = P * \vec{E}_{BS}$. The total intensity on the measurement detector is:

$$I_m = \vec{E}_P^\dagger \vec{E}_P = E_{P_x}^* E_{P_x} + E_{P_y}^* E_{P_y} \quad (2.34)$$

The electromagnetic field on the reference receiver can be described as:

$$\vec{E}_{P_r} = P * \vec{E}_r = P * (\vec{E}_1 + \vec{E}_2) \quad (2.35)$$

The total intensity on the reference detector is:

$$I_r = \vec{E}_r^\dagger \vec{E}_r = E_{P_r x}^* E_{P_r x} + E_{P_r y}^* E_{P_r y} \quad (2.36)$$

The phase difference between measurement signal and reference signal now contains the phase shift as the result of the displacement as well as an extra term representing the periodic deviations. The phase shift as the result of the displacement is the input of the model. The periodic deviation is the calculated phase change ($\Delta\phi_{meas}$) minus this phase change put in the system ($\Delta\phi$):

$$\Delta\phi_{pd} = \Delta\phi_{meas} - \Delta\phi \quad (2.37)$$

As an example and to verify the model mathematically the cases modeled by Hou and Wilkening (equation 2.17) and Player and De Freitas (equation 2.18) were also modeled using the Jones model (see appendix C). In this appendix it is shown that these cases are again a simplification of the total model.

2.6 Interaction of periodic deviations

With use of the Jones matrix model combinations of different sources of periodic deviations on an interferometer with linear optics as shown in figure 2.1 were modeled. In this section some results are shown. From the model also the Fourier spectrum of the periodic deviations are calculated. With use of the amplitude spectrum the dependence of first order and second order periodic deviations can be studied separately.

2.6.1 The influence of laser head radiation ellipticity

Since the principal limitations of the laser interferometer are in the polarization state of the laser head itself, the non-orthogonality and ellipticity are modeled first. If a Zeeman split laser source is used, the frequencies emerging from the laser source are circularly polarized. One left-handed and one right handed. With use of extra polarizing optics (e.g. a quarter wave plate) ideally two beams with orthogonal polarizations are created. However these optics will not be ideal and therefore the two frequencies emerging from the laser head will be slightly elliptically polarized, one left-handed and one right-handed. The periodic deviations resulting from an increasing elliptic polarization when using further ideal interferometer optics is shown in figure 2.9.

In the case where a laser emits two equal rotating elliptical polarizations the resulting periodic deviations are shown in figure 2.10. We now can compare figure 2.9 to figure 2.10 to see clearly the effect of contra-rotating or equal rotating ellipticity. The periodic deviations resulting from equal rotating elliptically polarized frequencies consists of a large first order periodic deviation (period $\lambda/2$ in linear interferometer), see figure 2.10 with a small second order periodic deviation. While the periodic deviations resulting from contra-rotating elliptical polarizations is a pure second order periodic deviation, see figure

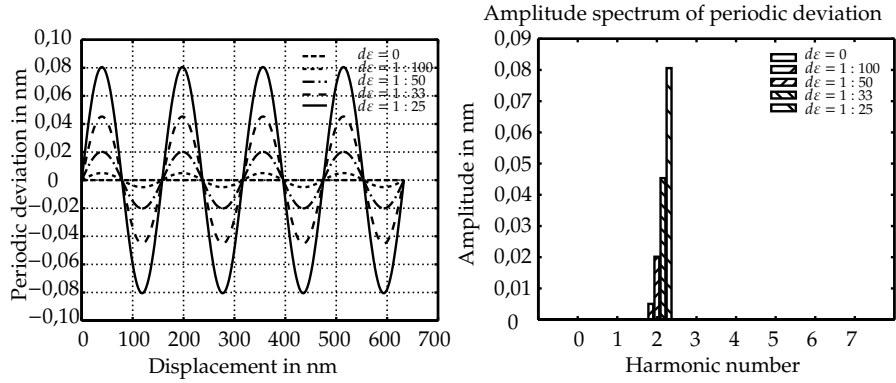


Figure 2.9: The periodic deviations as a result of increasing contra-rotating ellipticity ($d\epsilon_1 = -d\epsilon_2 = d\epsilon$) of the laser head.

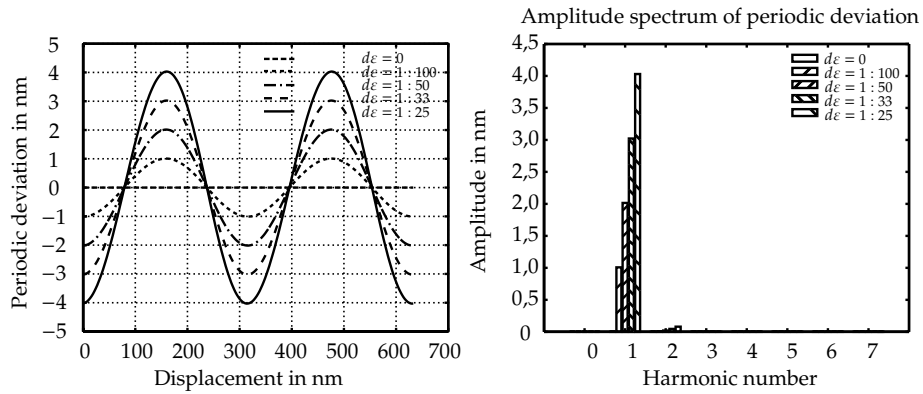


Figure 2.10: The periodic deviations as a result of increasing equal-rotating ellipticity ($d\epsilon_1 = d\epsilon_2 = d\epsilon$) of the light emitted by the laser head.

2.9. Further it can be shown that the amplitudes of the second order periodic deviation in both figures are equal. From this it can be concluded that an inherent compensation for the first order periodic deviation is gathered from contra-rotating ellipticity.

2.6.2 The influence of laser head radiation non-orthogonality

Another error source resulting from the laser head is the non-orthogonality between both emitted frequencies. The periodic deviations resulting from this is presented in figure 2.11. As can be seen from this figure the resulting periodic deviation is a nearly pure first order periodic deviation with a linear dependence on the angle of non-orthogonality.

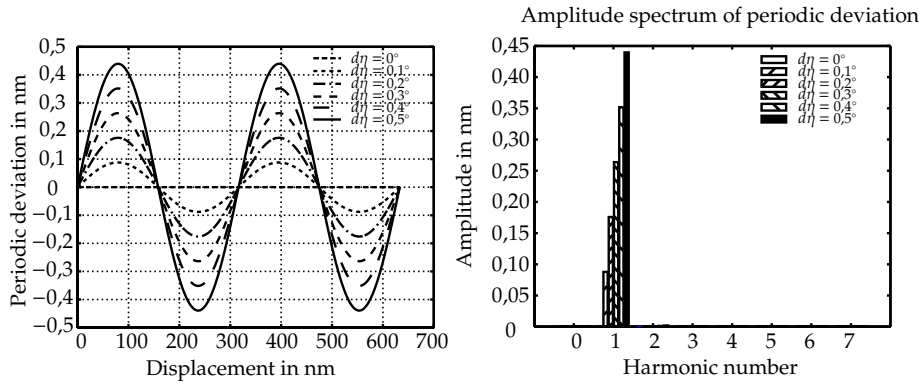


Figure 2.11: The periodic deviations as a result of increasing non-orthogonality ($d\eta$) of the light emitted by the laser head.

2.6.3 Combined error sources: Superposition principle

As shown in subsection 2.6.1 a contra-rotating ellipticity results in a pure second order periodic deviation. In subsection 2.6.2 it was shown that non-orthogonality of the frequencies resulted in a first order periodic deviation with a negligible second order. The question arises whether the periodic deviations resulting from elliptically non-orthogonally polarized beams equals the summation of periodic deviations resulting from both influences separately. In figure 2.12 the result is shown. From this figure it can be concluded that with a further ideal interferometer the effect of separate non-orthogonality and ellipticity can be added.

To investigate the possibility of superposition further a modeling example is given with a slightly rotated beam splitter ($\alpha_{PBS} = 0.5^\circ$). The influence of increasing (contra-rotating) ellipticity is presented in figure 2.13. Here it can be seen that the first-order periodic deviation introduced by the beam splitter rotation is increased by the increasing of the laser ellipticity as well as the second order. While with ideal optics only a second order periodic deviation

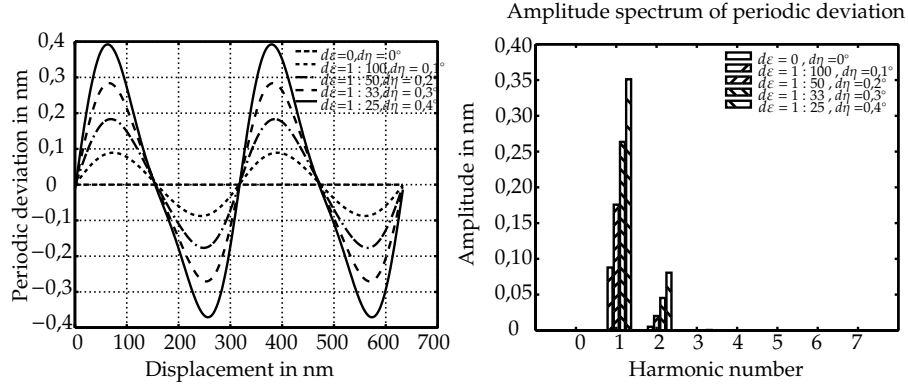


Figure 2.12: The periodic deviations as a result of increasing non-orthogonality ($d\eta$) and ellipticity ($d\varepsilon$) of the light emitted by the laser head.

existed (see figure 2.9). The influence of an increasing non-orthogonality is presented in figure 2.14. From this figure it can be seen that the second order periodic deviation introduced by the rotation of the beam splitter is decreased (minor influence) by the increasing of non-orthogonality while the first order remains increasing nearly equal to the case with ideal interferometer optics.

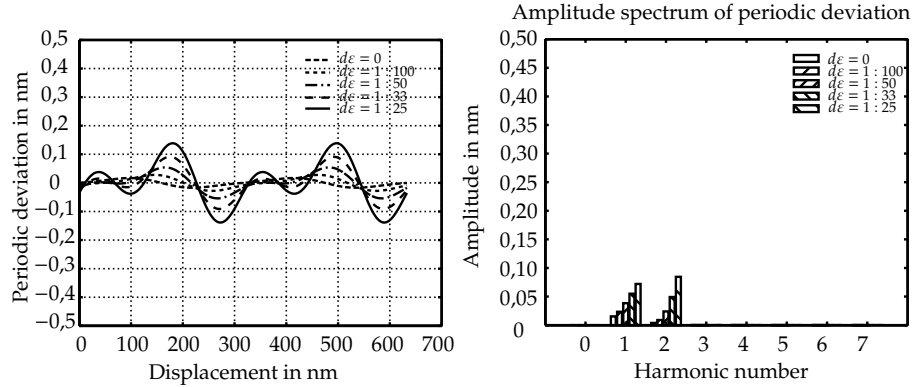


Figure 2.13: The periodic deviations as a result of a fixed rotated beam splitter ($\alpha_{PBS} = 0.5^\circ$) and increasing ellipticity ($d\varepsilon_1 = -d\varepsilon_2 = d\varepsilon$) of the light emitted by the laser head.

If the superposition principle would hold, the periodic deviations resulting from a rotated beam splitter with increasing laser ellipticity and non-orthogonality should be the sum of figures 2.13 and 2.14 minus one time the effect of rotating the beam splitter, since in both simulations this effect is present (0.02 nm in first order). The modeling output of the periodic deviations resulting from a rotated beam splitter in combination with an increasing laser ellipticity and non-orthogonality is shown in figure 2.15. Comparing figures 2.13, 2.14 and 2.15 it can be concluded that the superposition principle does not hold

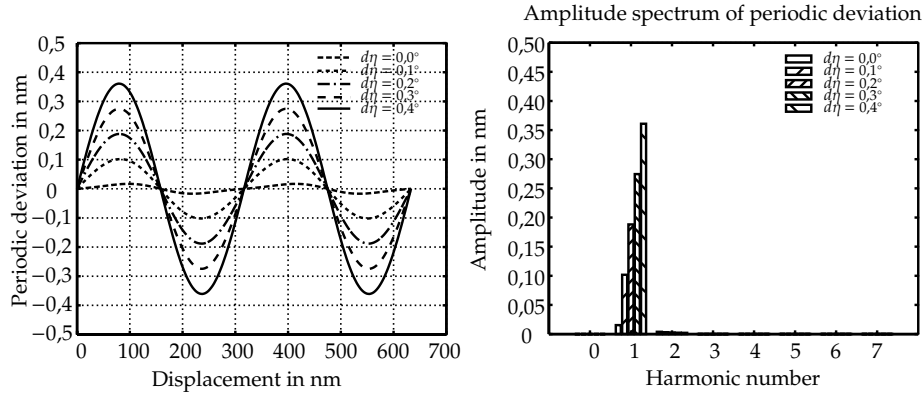


Figure 2.14: The periodic deviations as a result of a fixed rotated beam splitter ($\alpha_{PBS} = 0.5^\circ$) and increasing non-orthogonality ($d\eta$) of the light emitted by the laser head.

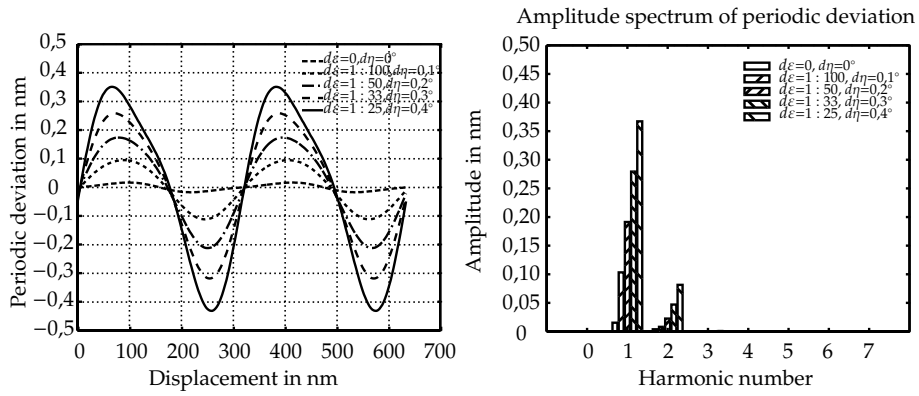


Figure 2.15: The periodic deviations as a result of a rotated beam splitter ($\alpha_{PBS} = 0.5^\circ$) and increasing non-orthogonality ($d\eta$) and ellipticity ($d\epsilon_1 = -d\epsilon_2 = d\epsilon$) of the light emitted by the laser head.

for non-ideal interferometer optics. This is best seen comparing all maximum amplitudes for the first harmonic: in figure 2.13 0,07 nm in figure 2.14 0,36 nm and in figure 2.15 0,37 nm, $0,36 \text{ nm} + 0,07 \text{ nm} - 0,02 \text{ nm} \neq 0,37 \text{ nm}$. It seems that a rotation of the beam splitter can partially compensate for the increasing non-orthogonality and ellipticity. The influence of each optical component has to be considered together with other error sources to enable a good prediction of periodic deviations in an interferometer.

2.6.4 Interaction between polarizing beam splitter and polarizer

To investigate rotational alignment effects of commonly used optics two cases are interesting to discuss. First the effect of a rotated beam splitter is simulated. Second the additional effect of a rotated polarizer was simulated. In figure 2.16 the periodic deviations are shown resulting from different angles of rotational misalignment of the beam splitter. In figure 2.17 the result is shown for different angles of the polarizer in front of the measurement detector, combined with a constant rotational angle of the beam splitter. All other parameters are assumed ideal.

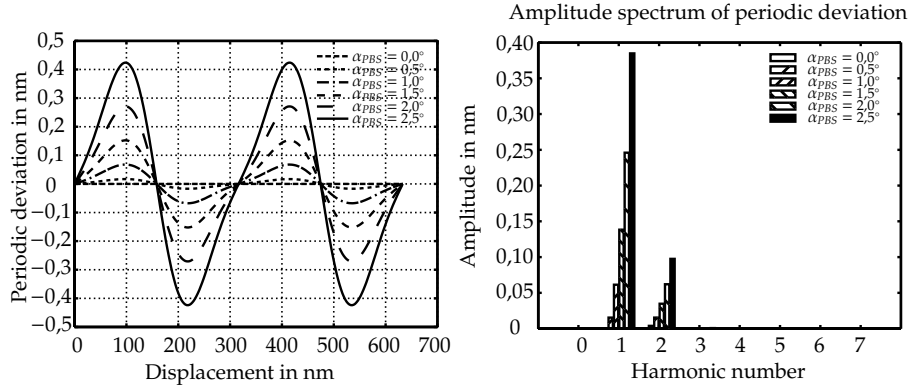


Figure 2.16: The periodic deviations as a result of increasing rotation of the polarizing beamsplitter angle (α_{PBS}) around the roll-axis as defined in figure 2.3.

From these figures it can be concluded that the rotation of the polarizer determines the period of the periodic deviations as mentioned by Stone [22]. A rotation of the polarizer equal to the angle of the rotated beam splitter results in a period of $\lambda/4$ and a polarizer aligned ideal to the orientation of the laser results in a period of $\lambda/2$. Both periods were observed earlier by Sutton [15]. This solves the discrepancy between authors which mention a period of $\lambda/4$ [18] and those who observed a period of $\lambda/2$ [16]. Further modeling showed that the effect was a result of bringing the projected amplitudes of the measurement arm on the polarizer into line with the projected amplitude of the reference arm on the polarizer. If in fact the transmission amplitudes are $A_x = 0,5$ for one

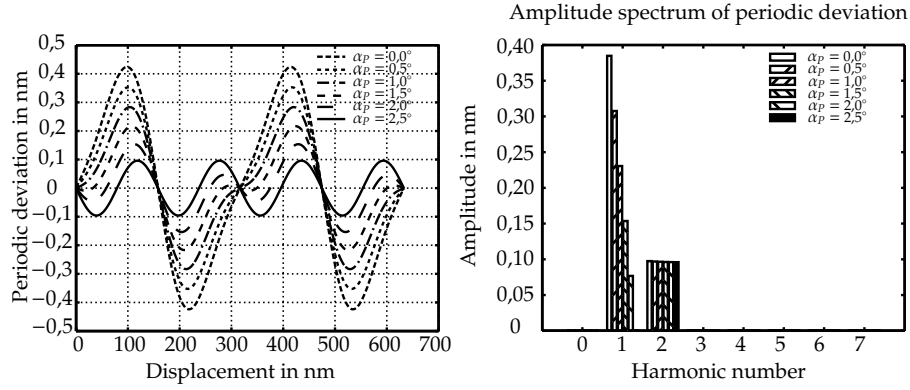


Figure 2.17: The periodic deviations as a result of increasing rotation of the receiver polarizer angle (α_P) when the beam splitter is rotated 2.5° around the roll-axis as defined in figure 2.3.

arm and $A_y = 1$ for the other arm, the measurement polarizer should have an angle of 18.4° with the 45° axis to reduce the effect of the first-order periodic deviation, which equals $(45^\circ - \arctan(0.5))$.

2.7 Conclusions

In this chapter two models were presented enabling the prediction of periodic deviations resulting from alignment errors and polarization errors of the light emitted by the laser head. The Jones model further enables the input of Jones matrices representing the optics present in an interferometer. Both models can be simplified to equations derived by other authors in literature for individual sources of periodic deviations in interferometers. It was shown that interaction of periodic deviations exists and therefore the superposition principle does not hold for periodic deviations: all possible causes of periodic deviations must be considered at once to enable an accurate prediction of the periodic deviations present in the interferometer. The influence of non-orthogonality of light emitted by the laser head was described quantitative and the difference in effect on periodic deviations of contra-rotating and equal rotating elliptically polarized light emitted by the laser head was shown.

Chapter 3

Polarization properties of interferometer components

In the previous chapter a model was presented to calculate the periodic deviations resulting from various errors in the interferometer. The principal uncertainty limitations are the polarization quality of the laser system and optics used in the interferometer. Therefore, in order to predict the total periodic deviations resulting from the interferometer, the polarization state of the laser system and optics must be measured. In this chapter two methods will be presented to measure the polarization state of the laser system and a comparison of the methods will be made, based on measurement results. Further, a method to measure the polarization state of interferometer optics will be discussed and some measurements are presented. Finally the effect of the components will be analyzed using the Jones model of the previous chapter.

3.1 Laser system

In a commercial laser interferometer the laser system is defined as a combination of the laser source and optics used for stabilization control and reference measurement, normally called the laser head. A schematic representation of a heterodyne laser head is shown in figure 3.1. The heterodyne laser head consists of a laser tube filled with Helium and Neon gas. Around the laser tube a magnetic field is applied with its main axis in the direction of the laser light. Due to the Zeeman effect, light with two frequencies is emitted by the laser source (Zeeman laser [47]). The electromagnetic field with one frequency is left handed circularly polarized and the other frequency right handed circularly polarized. In order to distinguish the two polarizations in the interferometer, a wave plate is used to create orthogonally linear polarized beams. Part of the beam is split off to stabilize the laser frequency. Further a part is split off to provide the reference measurement. Sometimes acousto optical modulators are used to enlarge the frequency split of the laser source (see bottom figure 3.1).

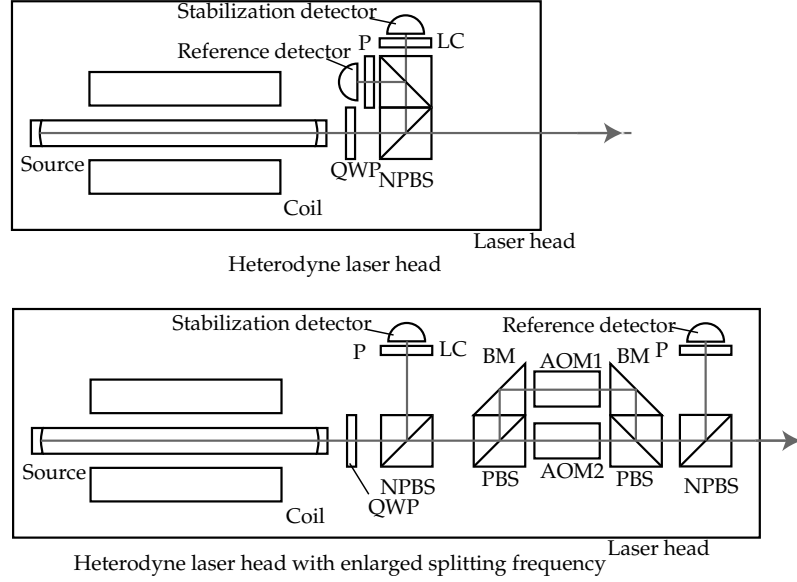


Figure 3.1: Schematic representation of two heterodyne laser heads. One with Zeeman split frequency and one with enlarged split frequency. NPBS: non polarizing beam splitter, PBS: polarizing beam splitter, P: polarizer, QWP: quarter wave plate, BM: bending mirror, AOM: acousto optic modulator, LC: Liquid crystal.

In that case both frequencies are split by means of polarization splitting; the first frequency enters an acousto optical modulator with frequency Δf_A and the second frequency enters an acousto optical modulator with frequency Δf_B . Both frequencies are then recombined and the splitting of the frequencies now equals $\Delta f_A - \Delta f_B + f_1 - f_2$, where f_1 and f_2 are the original laser frequencies. With an ideal laser source and ideal optics which are ideally aligned, the output of the laser head would be orthogonally linearly polarized. However in practical situations this is not the case and nonorthogonal elliptically polarized modes are emitted. The polarization errors of the laser system originate from inhomogeneities in the laser source, together with anisotropy of the cavity [48, 49, 50]. The optics used in the laser head to split off parts of the beam, which are used as stabilization and reference measurements, also contribute to the total polarization state of the E-field emerging from the laser head. In a homodyne interferometer the polarization state can be measured easily using a polarizer and a power meter. However, in a heterodyne laser source both frequencies are detected and therefore this method is not possible, so another method has to be found. An extra complication is the small ratio of ellipticity which has to be measured in addition to the low power emerging from a HeNe laser source which is approximately 300 μW . One way is to use a spectrum

analyzer as a power meter for different frequencies along with a circularly polarized homodyne laser source which functions as a carrier frequency to increase the measured power and enables the measurement of the frequencies on the spectrum analyzer. This method is called the "carrier frequency method". Another method is to measure a beat signal directly after the laser head with a frequency detector in combination with a lock-in amplifier. This is called the "beat measurement method". Both methods are explained in more detail in the next sections.

3.1.1 Carrier frequency method

In figure 3.2 the measurement setup for the carrier frequency method is presented schematically. The light emerging from the heterodyne interferometer is mixed with circularly polarized light emerging from a second laser source in a non-polarizing plate beam splitter. The light then passes through a polarizer onto an avalanche photodiode. A beam reductor is used along with a lens to focus the light on the detector. Further, to reduce the translation of the beam on the detector resulting from the rotation of the polarizer, the polarizer is placed close to the detector. With use of a spectrum analyzer the intensities of two different beat frequencies can be measured: $I(f_1, f_3)$ and $I(f_2, f_3)$; where f_1 and f_2 are the frequencies emerging from the heterodyne laser head and f_3 is the frequency emerging from the circular polarized laser source.

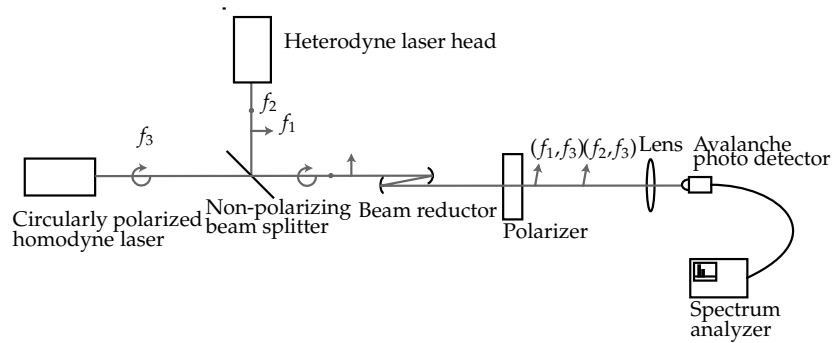


Figure 3.2: Schematic representation of the Carrier Frequency measurement setup.

The E-fields present in this carrier frequency measurement setup are depicted schematically in figure 3.3 along with the schematic representation of the measurements on the spectrum analyzer. The polarization states emerging from the heterodyne interferometer are represented as Jones vectors \vec{E}_1 and \vec{E}_2 with respective ellipticities $d\varepsilon_1$ and $d\varepsilon_2$ as also defined in section 2.5. The intensities of the two beat frequencies as function of the rotation angle of the polarizer are shown in the right hand side of figure 3.3. Here E_{M1} and E_{M2}

represent the amplitude of the major axes of E-fields \vec{E}_1 and \vec{E}_2 , E_{m1} and E_{m2} represent the amplitude of the minor axes of E-fields \vec{E}_1 and \vec{E}_2 . E_{p1} and E_{p2} are arbitrary amplitudes of the respective E-fields.

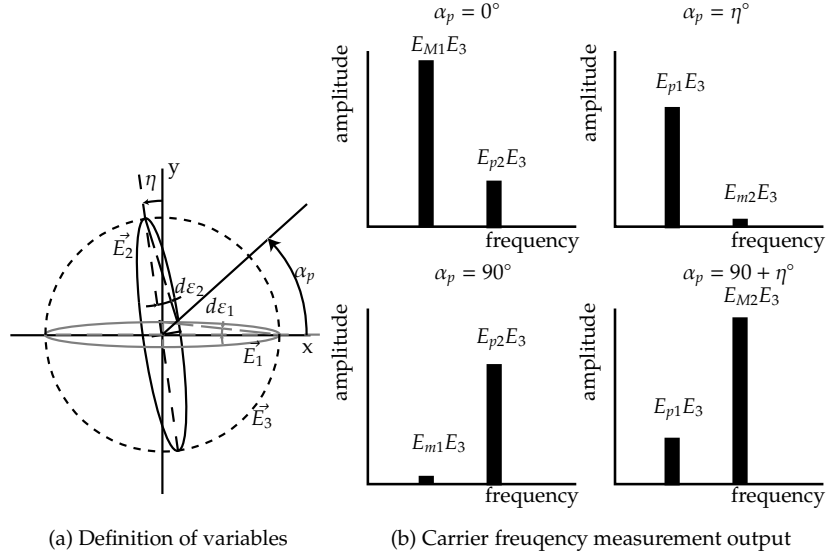


Figure 3.3: Schematic representation of the E-fields present in the carrier frequency method as well as the schematic representation of the output of this measurement setup. \vec{E}_1, \vec{E}_2 are the E-fields emerging from the heterodyne laser of which the ellipticity is $d\epsilon_1$ and $d\epsilon_2$ respectively, \vec{E}_3 emerges from the circular reference source and α_p represents the angle of the polarizer. E_{M1} and E_{M2} represent the amplitude of the major axes of E-fields \vec{E}_1 and \vec{E}_2 , E_{m1} and E_{m2} represent the amplitude of the minor axes of E-fields \vec{E}_1 and \vec{E}_2 . E_{p1} and E_{p2} are arbitrary amplitudes of the respective E-fields.

The intensities of the beat frequencies measured on the spectrum analyzer as a function of the polarizer angle α_p are derived in Appendix D:

$$I_a(f_1, f_3)^{\alpha_p} = 2E_{01}E_{03} \sqrt{\cos^2(\alpha_p) \cos^2(d\epsilon_1) + \sin^2(\alpha_p) \sin^2(d\epsilon_1)} \quad (3.1)$$

$$I_a(f_2, f_3)^{\alpha_p} = 2E_{02}E_{03} \sqrt{\cos^2(\alpha_p - \eta) \sin^2(d\epsilon_2) + \sin^2(\alpha_p - \eta) \cos^2(d\epsilon_2)} \quad (3.2)$$

From this equation it follows that the intensity of both beat frequency signals vary as a function of the polarizer angle α_p . The maximum and minimum intensities for the beat signal between f_1 and f_3 can be found at angles $\alpha_p = 0$

and $\alpha_p = \pi/2$:

$$I_a(f_1, f_3)^{\alpha_p=0} = 2E_{01}E_{03} \cos(d\varepsilon_1) \quad (3.3)$$

$$I_a(f_1, f_3)^{\alpha_p=\pi/2} = 2E_{01}E_{03} \sin(d\varepsilon_1) \quad (3.4)$$

The angles for the minimum and maximum intensity of the beat signal between f_2 and f_3 are $\alpha_p = \eta$ and $\alpha_p = \pi/2 + \eta$:

$$I_a(f_2, f_3)^{\alpha_p=\eta} = 2E_{02}E_{03} \sin(d\varepsilon_2) \quad (3.5)$$

$$I_a(f_2, f_3)^{\alpha_p=\pi/2+\eta} = 2E_{02}E_{03} \cos(d\varepsilon_2) \quad (3.6)$$

From these four measurements the non-orthogonality follows directly as the deviation in the angle between the minimum of E_1E_3 and the minimum of E_2E_3 and 90° . The ellipticity of the two output frequencies can be calculated from these measurements. As defined in figure 2.8 the ellipticity is defined as an angle $d\varepsilon$. For simplicity the inverse tangent of this angle is represented, indicating the ratio of amplitudes of the major and minor axes of the ellipse:

$$P1 = \frac{E_{M1}}{E_{m1}} = \frac{\cos(d\varepsilon_1)}{\sin(d\varepsilon_1)} = \frac{I_a(f_1, f_3)^{\alpha_p=0}}{I_a(f_1, f_3)^{\alpha_p=\pi/2}} \quad (3.7a)$$

$$P2 = \frac{E_{M2}}{E_{m2}} = \frac{\cos(d\varepsilon_2)}{\sin(d\varepsilon_2)} = \frac{I_a(f_2, f_3)^{\alpha_p=\pi/2+\eta}}{I_a(f_2, f_3)^{\alpha_p=\eta}} \quad (3.7b)$$

From the equations derived above it follows that the ellipticity and nonorthogonality of the laser head can be derived directly from the measurements without approximations. However to draw conclusions about the quality of the laser head the effects of the measurement system should be considered carefully. This is done in the next section.

Measurement considerations

In the setup a non-polarizing beam splitter is used to mix the beams of the heterodyne laser head with the beam of the homodyne laser head, further also a beam reductor is used. Since any kind of optics may influence the polarization of the laser beams the setup was calibrated. This was done removing the heterodyne laser source and replacing the AC detector with a DC power detector. The intensity of light of the circularly polarized reference source passing through the non-polarizing beam splitter, the beam reductor and through the polarizer is measured as a function of the polarizer angle. These results are used to correct the measurement data before calculating the ellipticity and non-orthogonality.

After calibration the heterodyne laser is aligned and the beat frequency intensity on the spectrum analyzer is maximized. For the measurement of the minimum several polarizer angles around the minimum are measured in order to find the correct minimum. The same angles are measured 90° shifted. This is done for both frequencies. In figure 3.4 the results are shown for the

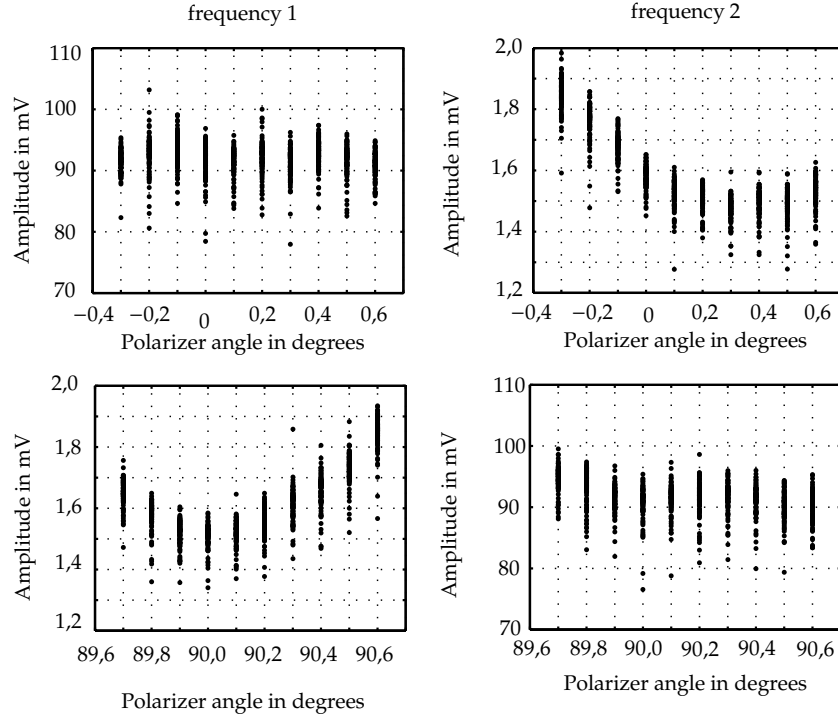


Figure 3.4: Results of the Carrier Frequency measurement on an Agilent 5519A laser head.

measurement on a commercial laser head [84]. In the figure the amplitude of the beat frequencies is plotted against the angle of the polarizer. On the left hand side the results are shown for frequency f_1 and on the right hand side the results are shown for frequency f_2 . In this figure it can be seen that the minimum of f_1 (bottom left) and the minimum of f_2 (upper right) are shifted 89.7° , which represents a non-orthogonality of 0.3° of the polarizations of this laser head. What can also be seen is that the distribution on the amplitude is relatively large. This is partly caused by the noise of the measuring system, but most of it is the result of the frequency modulation of both lasers used. In order to stabilize these laser heads a frequency modulation on the laser source. Since the laser under investigation is a Zeeman laser the gain curves of both frequencies lie on the slope of the atomic gain curve. Therefore a frequency modulation results in an amplitude modulation. In the carrier frequency method the intensities of beat frequencies are measured. The ellipticity of the E-field is defined as the maximum intensity divided by the minimum intensity, however the maximum and minimum can not be measured at the same time, and a modulating amplitude could influence the calculated values. To eliminate this effect the intensities were measured also as a function of the frequencies: amplitudes belonging to the same frequencies are divided to

calculate the ellipticity. This eliminates the amplitude modulation of the laser head under investigation from the ellipticity calculations. Here the assumption is made that the intensity modulation as a function of frequency modulation is constant. The homodyne laser used is an amplitude stabilized laser and as a result may drift in frequency resulting in a measurement error. This effect shows as a shift in the frequency distribution. In the measurements to be considered this shift was negligible. The necessity of dividing amplitudes per frequency makes this method very time consuming. Another disadvantage of this method is the possible non-linearity of the detector-spectrum analyzer system. A wide range of amplitudes is measured and the gain of the detector nor the gain of the spectrum analyzer (both commercial systems) is known and probably not constant over the entire working range. However some tests with reduced intensities did not indicate large effects. With this method it is also possible to test the polarization effect of optics on the two frequencies e.g. for a laser-polarizing beam splitter combination.

3.1.2 Beat measurement method

A second method to measure the ellipticity and non-orthogonality of the E-fields emerging from a heterodyne laser head is a beat frequency measurement. Here the beat frequency of the two emerging frequencies is directly measured with a dedicated AC-detector as a function of the polarizer angle. No carrier frequency is used. The amplitude of this beat frequency is measured with use of a lock-in amplifier [87]. This lock-in amplifier enables the measurement of intensity of a signal with equal (carrier) frequency as a reference signal. The setup for this measurement is represented schematically in figure 3.5.

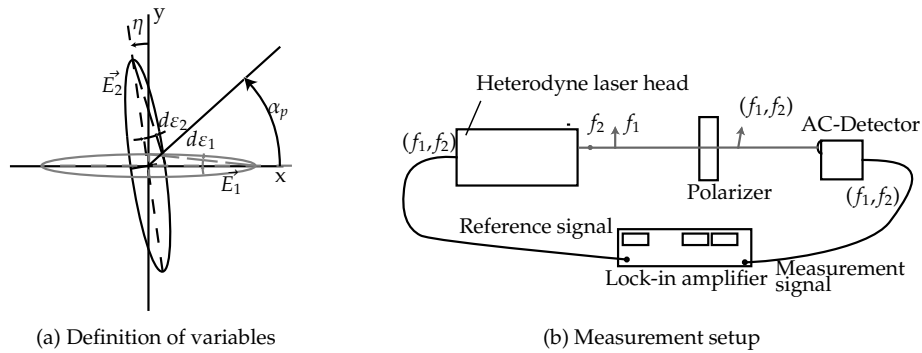


Figure 3.5: Schematic representation of the electromagnetic fields involved in the beat frequency measurement setup and the beat frequency measurement setup.

The reference frequency is taken directly from the laser head with use of dedicated hardware. The measurement signal is the beat signal after the polarizer at angle α_p . Both signals have the same frequency. With aid of the lock-in amplifier the intensity of the measurement signal at equal frequency as the

reference signal is measured. As a result electronic noise is filtered. The amplitude of the measurement signal as a function of angle α_p is recorded using a pc with GPIB interface. For each angle of the polarizer 50 measurements are taken and averaged. The intensity of the beat frequency measured with the lock-in amplifier is derived in Appendix D:

$$I_a(f_1, f_2)^{\alpha_p} = 2E_{01}E_{02} \sqrt{\left(\begin{array}{l} \cos^2(\alpha_p) \cos^2(d\varepsilon_1) + \sin^2(\alpha_p) \sin^2(d\varepsilon_1) \\ * (\cos^2(\alpha_p - \eta) \cos^2(d\varepsilon_2) + \sin^2(\alpha_p - \eta) \sin^2(d\varepsilon_2)) \end{array} \right)} \quad (3.8)$$

This intensity signal varies as a function of the polarizer angle. The minimum and maximum signals can be derived assuming $\eta \ll 1$ and $\sin(d\varepsilon_1), \sin(d\varepsilon_2) \ll \cos(d\varepsilon_1), \cos(d\varepsilon_2)$:

$$I_a(f_1, f_2)^{\alpha_p=0} \approx 2E_{01}E_{02} \cos(d\varepsilon_1) \sin(d\varepsilon_2) \quad (3.9)$$

$$I_a(f_1, f_2)^{\alpha_p=\pi/4+\eta/2} \approx E_{01}E_{02} \cos(d\varepsilon_1) \cos(d\varepsilon_2) \quad (3.10)$$

$$I_a(f_1, f_2)^{\alpha_p=\pi/2+\eta} \approx 2E_{01}E_{02} \sin(d\varepsilon_1) \cos(d\varepsilon_2) \quad (3.11)$$

From these three measurements the non-orthogonality follows directly from the location of the minima and maximum. Here again the inverse tangent of the ellipticity angle is represented, indicating the ratio of amplitudes of the major and minor axes of the ellipse:

$$P1 = \frac{E_{M1}}{E_{m1}} = \frac{\cos(d\varepsilon_1)}{\sin(d\varepsilon_1)} \approx \frac{2I_a(f_1, f_2)^{\alpha_p=\frac{\pi}{4}+\frac{\eta}{2}}}{I_a(f_1, f_2)^{\alpha_p=0}} \quad (3.12a)$$

$$P2 = \frac{E_{M2}}{E_{m2}} = \frac{\cos(d\varepsilon_2)}{\sin(d\varepsilon_2)} \approx \frac{2I_a(f_1, f_2)^{\alpha_p=\frac{\pi}{4}+\frac{\eta}{2}}}{I_a(f_1, f_2)^{\alpha_p=\frac{\pi}{2}+\eta}} \quad (3.12b)$$

With this method the effect of the measurement system should be considered also before drawing conclusions about the quality of the laser head. These considerations are presented in the next section.

Measurement considerations

Before measuring the signal of the beat frequency detector has to be tuned so that the minimum signal still is a nice sinusoid and the maximum signal does not result in an overload of the lock-in amplifier. The lock-in amplifier was calibrated for drift, linearity and phase angle between S0 and S90 signal. The calibration for linearity was conducted using an external wave generator with amplitude attenuation. The wave generator supplied a sine function with frequency equal to the reference frequency of the heterodyne laser. This function was used both as reference and measurement input. The lock-in amplifier matches the frequency of an internal oscillator with constant amplitude to the external reference signal, which is used internally in the lock-in amplifier (in

the mixing signal). Therefore attenuation of the reference signal will not influence the measured amplitude of the measurement signal. The amplitude of the lock-in amplifier was registered using the same averaging period as used in the measurements and showed a maximum deviation in linearity compared to the amplitude of the wave generator of 0,3%. The phasedifference between S_0 and S_{90} was tested using the internal oscillator as a reference and applying a phase difference varying from -180° to 180° on the reference signal and using this as an external measurement input. The output of the S_0 and S_{90} signal is registered using the same averaging and settings as during measurement. The inherent phase difference between S_0 and S_{90} was $0,6 \mu\text{rad}$. This deviation is a constant and will therefore not influence these measurements. The drift of the lock-in amplifier was measured for 2 hours. Only digital noise of $0,015 \text{ mV}$ could be registered. In a measurement this noise could influence the proportion result up to a noise of 1:4.

To conduct a measurement the angle of the polarizer was varied from -5° to 185° in steps of $2,5^\circ$. With use of a least square method, equation (3.8) was fitted to these measurements. In the fitting the ellipticity depends largely on the non-orthogonality derived. Therefore near the minima steps of $0,1^\circ$ were made and the non-orthogonality was determined by hand. This in turn was used as an input in the fitting procedure. An example is shown in figure 3.6.

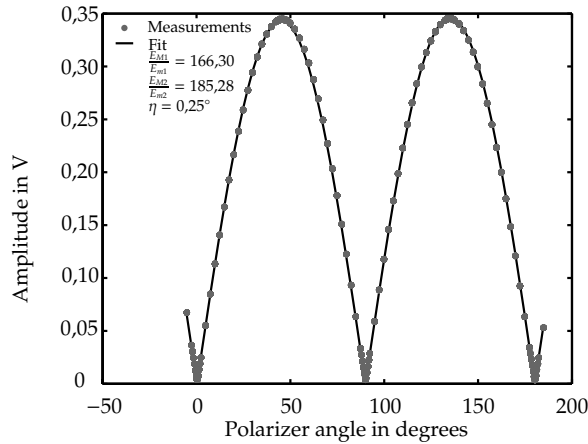


Figure 3.6: Output of the beat frequency measurement on a commercial laser head.

The advantage of this method is that it can be used everywhere in the optical system. After every optical component the polarization state can be measured in this way. The method is less time consuming compared to the carrier frequency method. Disadvantages of the method are that dedicated hardware is necessary to make the reference signal available. Further also for this method the linearity of the total detection system is not known a priori.

3.1.3 Measurement results of commercial laser systems

With both methods the ellipticity and nonorthogonality of three available heterodyne lasers were measured. Also the variation in time was measured. All lasers were measured just after turning on as well as after four hours or more. All lasers exhibited better polarization properties after a few hours. Even after a warm up period of 4 hours the laser polarization still changes. Depending on the initial quality of the polarization this may vary up to 1:200 (e.g. the ration of the 3403A00296 varied from 1:160 to 1:360). This also shows that the polarization state changes in time. The results of the measurements are presented in table 3.1. The values in the table are averages of 3 or more measurements with their standard deviations.

Laser	Ratio CF	η	Ratio BFM	η
3403A00296 $E_{m1} : E_{M1}$ $E_{m2} : E_{M2}$	1 : (241 \pm 50) 1 : (241 \pm 50)	0,30° \pm 0,05°	1 : (170 \pm 14) 1 : (172 \pm 23)	0,30° \pm 0,05°
US41111187 $E_{m1} : E_{M1}$ $E_{m2} : E_{M2}$	1 : (61 \pm 3) 1 : (62 \pm 3)	0,30° \pm 0,05°	1 : (69 \pm 6) 1 : (69 \pm 6)	0,35° \pm 0,05°
US40091151 $E_{m1} : E_{M1}$ $E_{m2} : E_{M2}$	1 : 500* 1 : 500*	0,15° \pm 0,05°	1 : 700* 1 : 700*	0,20° \pm 0,05°

Table 3.1: Measured laser polarization state and standard deviation of three commercial laser heads. η : non-orthogonality, CF: carrier frequency measurement, BFM: beat frequency measurement, * least ratio.

From the table it can be seen that the measured non-orthogonality (η), which can be measured with an uncertainty of 0,05°, shows consistency for both methods. The values for ellipticity sometimes differ significantly for both measurements. This may be a result of unknown effects in the amplification of the signals in both methods as mentioned in the previous sections. However it could also be a remaining effect of the plate beam splitter and beam reductor introduced in the carrier frequency method. As mentioned the effect on the circular polarized beam was calibrated out. However polarization effects on the linear polarized beams of the heterodyne laser cannot be calibrated out entirely. This is due to the fact that the alignment of the heterodyne laser is not necessarily equal to the alignment of the homodyne laser used to calibrate the effect. The latter was examined using the beat frequency method in the carrier frequency setup. The homodyne laser was blocked and the receiver and spectrum analyser of the carrier frequency measurement setup were replaced with the receiver and lock-in amplifier of the beat measurement setup. In the measurements with this system the ratios of polarization were less stable compared to measurements without the plate beam splitter. Additionally the ratios were higher and with these measurements both methods agreed within

noise. From this it may be concluded that the plate beam splitter and beam reductor influence the polarization and therefore the measurements on separate lasers do not overlap for both methods. Further it may be concluded from the comparison of both methods in one setup that the assumptions made in equations (3.9)-(3.11) are justified and that the beat frequency method produces correct results for the laser interferometer.

As described in section 2.6.1 the predicted periodic deviations are different for contra-rotating ellipticities (see figure 2.9) compared to equal rotating ellipticities (see figure 2.10). With the beat frequency measurement setup it is possible to test the direction of elliptical polarization. If initially the polarizer is aligned with the main amplitude of one frequency the relative phase difference is reset on the lock-in amplifier. Then the polarizer is rotated 90° and the relative phase is measured. If this measured phase is 180° the polarizations are contra rotating. If the phase remains equal the polarizations are equally rotating. The measurement was conducted on all three laser heads and a contra-rotating ellipticity was measured, as expected. The system was also used to test an AOM-laser head and here also the contra-rotating ellipticity was measured, also as expected.

In order to test whether the change in polarization affects the periodic deviations during measurement the periodic deviations resulting from the polarization properties of the measured laser heads were modeled. The results are presented in figure 3.7.

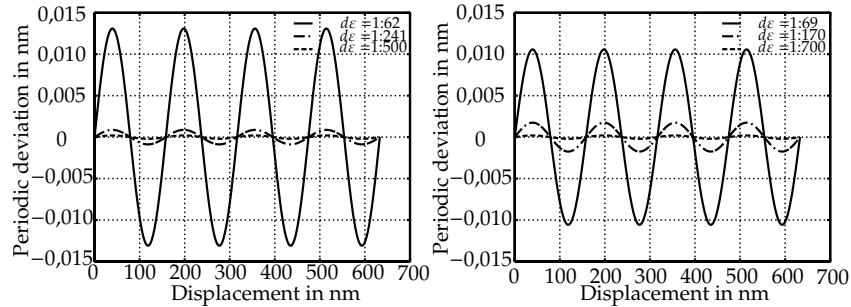


Figure 3.7: Model output of the periodic deviations resulting from laser head polarization deviations.

From this figure it may be concluded that the polarization as measured with both methods does not influence the periodic deviations within 0,015 nm. As already mentioned the changes during measurements depend on the initial quality of the laser. These changes affect the periodic deviations with a maximum of 0,02 nm. The effect of the measured non-orthogonality was already modeled in section 2.6.2. From figure 2.11 it can be seen that a non-orthogonality of $0,15^\circ$ produces a periodic deviation of 0,13 nm, and a non-orthogonality of $0,35^\circ$ produces a periodic deviation of 0,30 nm.

Concluding: both methods enable the measurement of the coarse category

of the laser head ellipticity, further the non-orthogonality can be measured with an uncertainty of $0,05^\circ$ with both methods. The beat frequency measurement setup provides a convenient measurement system, provided dedicated hardware is available to take the reference signal from the laser head. Further the assumptions of a small ellipticity and non-orthogonality, made to derive equations for the maximum and minimum signal, are justified. For the lasers measured, the effect of laser head ellipticity is negligible. Further it was concluded that the direction of ellipticity was contra-rotating for all lasers.

3.2 Optical components: Ellipsometry

After the light is emitted from the laser head it enters the interferometer optics. Polarization mixing can occur in all polarizing and non-polarizing components, and therefore it can result in extra periodic deviations. In chapter 2 it was already shown that every polarization error has to be considered to predict the total periodic deviation. Therefore it is essential to characterize the polarization mixing of each component. The effect of depolarized light depends on the electronics used. However these are not considered in the model and therefore the depolarization does not have to be included in the measurements. Further the assumption is made that the Jones representation of each component can be written as a diagonal matrix with linear basis of the form

$$M_{os} = A_0 * \begin{bmatrix} 1 & 0 \\ 0 & T_0 e^{i\delta_0} \end{bmatrix} \quad (3.13)$$

with A_0 the amplitude attenuation of the entire optical system, T_0 the amplitude difference between the ordinary and extraordinary polarization and δ_0 the phase retardation between the two polarization components.

3.2.1 Ellipsometry

The characterization of optical components present in laser interferometer systems is done by an ellipsometric setup as shown in figure 3.8.

From a homodyne laser source circular polarized light emerges through a polarizer with azimuth angle P , a compensator of the Babinet Soleil type enabling a phase difference of δ_C at an azimuth angle C , both in front of the optical system and a polarizer with azimuth angle A behind the optical system. By finding a set of azimuth angles for polarizer, compensator and analyzer (P, C and A) such that the light flux falling on the detector is extinguished, the Jones matrix of the optical system can be resolved. This results in the following equation [45]:

$$T_0 e^{i\delta_0} = \tan(\Psi) e^{i\Delta} = -\tan(A) \left[\frac{\tan(C) + T_C e^{i\delta_C} \tan(P - C)}{1 - T_C e^{i\delta_C} \tan(C) \tan(P - C)} \right] \quad (3.14)$$

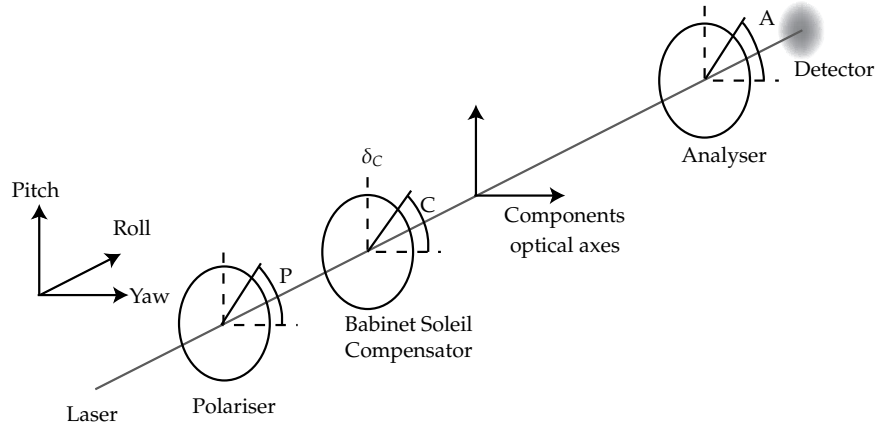


Figure 3.8: Schematical representation of the ellipsometer setup.

where T_C is the amplitude attenuation of the two polarization directions of the compensator. Ψ and Δ are the so-called ellipsometric angles. Ψ is the angle whose tangent gives the ratio of the amplitude attenuation upon transmission of the ordinary and extraordinary polarizations. Δ gives the difference between the phase shifts experienced upon transmission by the ordinary and extraordinary polarizations. The process of finding the azimuth angles where extinction occurs is called null-ellipsometry. It is also possible to adjust the relative phase retardation (δ_C) of the compensator. Since the resolution to which this parameter can be measured compared to the azimuth angles is magnitudes poorer this is not done. Instead we apply a method called four zone averaging. The compensator is fixed to an azimuth of $\pm \frac{\pi}{4}$ relative to the optical component and the relative phase retardation is given a fixed value of $\delta_C = \frac{\pi}{2}$. With $T_C = 1$, it follows from equation 3.14 that for each fixed azimuth of the compensator (C) two combinations of P and A result in extinction. The four solutions are tabulated in table 3.2. Averaging over these four solutions results in accurate estimates of

Polarizer	Compensator	Analyzer	Δ
P_1	-45°	Ψ	$2(P_1 + 45^\circ)$
P_2	45°	Ψ	$2(135^\circ - P_2)$
P_3	-45°	$-\Psi$	$2(P_3 + 135^\circ)$
P_4	45°	$-\Psi$	$2(45^\circ - P_4)$

Table 3.2: Four zone averaging angles.

the two ellipsometric angles Ψ and Δ . The advantage of this method is that any imperfection of the ellipsometer other than entrance and exit window birefringence are canceled out [45]. Since the optics to be tested don't have entrance and exit windows, in our setup all ellipsometer imperfections are canceled out.

3.2.2 Repeatability measurement

To test the feasibility, of the method the repeatability was tested using a polarizing beam splitter. Since the method assumes a compensator azimuth angle of $\pm 45^\circ$ with the axis of the optical component under testing the optical system was aligned before measurement. The extinction ratio of the Glan-Thompson type polarizer and analyzer combination was better than 1 : 100 000. The results of the repeatability measurements on the polarizing beam splitter are shown in figure 3.9. The standard deviation for Ψ was $0,02^\circ$, and the standard deviation for Δ was $0,25^\circ$. The same repeatability was obtained for a quarter wave plate.

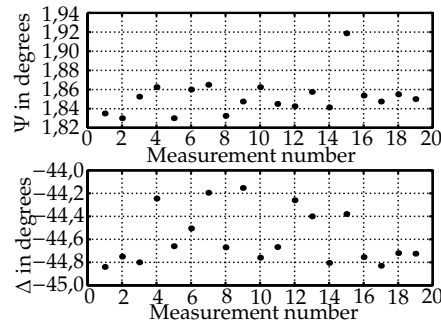


Figure 3.9: Repeatability of an ellipsometer measurement of a polarizing beam splitter.

The standard deviations of this repeatability measurement were used in the Jones model to calculate the resulting periodic deviation of a flat mirror interferometer. This resulted in a periodic deviation with an amplitude of 0,15 pm. From this it can be concluded that the repeatability of the ellipsometer measurements is sufficient to measure the polarization properties of optics which in turn are to be used in the Jones model.

3.2.3 Measurement results of optical components

With the knowledge mentioned above some measurements were done for a polarizing beam splitter and a quarter wave plate under different angles around the pitch axis (see figure 3.8). The different angles were chosen to investigate the influence of on axis rotational alignment, meaning that the main polarization axes of the optical components remain in the same orientation compared to the polarization of the light emitted from the laser head (rotation around the pitch axis in figure 3.8). The measurement results are shown in figure 3.10.

The figure of the polarizing beam splitter shows a minimal angle Ψ of $1,84^\circ$, representing an amplitude leakage of 3% in the beam splitter for the transmitted polarization component. The phase shift of the beam splitter depends on the pitch angle of the beam splitter. For the yaw angle the same result would hold

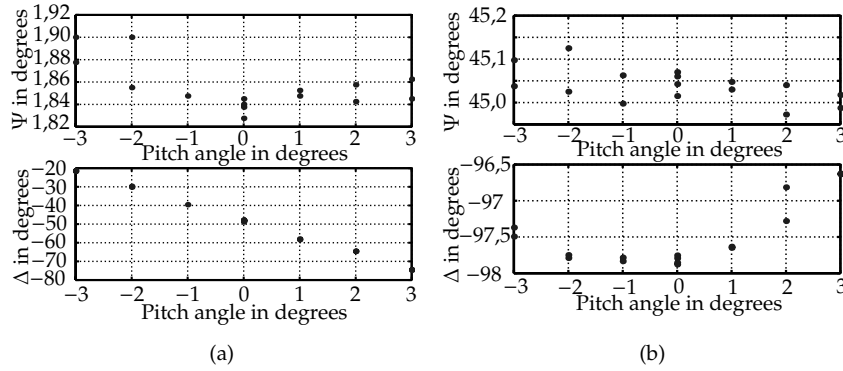


Figure 3.10: Pitch angle dependence of a polarizing beam splitter (a) and a quarter wave plate (b).

since this is also an on axis rotational alignment. Therefore also the resulting polarization state after the beam splitter depends on the alignment around pitch and yaw angle. The figure on the quarter waveplate shows an angle Ψ with a value of 45.05° , representing an amplitude leakage of less than 0,2% ($1 - 1/\tan(45.05^\circ)$), however the phase difference between the fast and slow axis is in a normal alignment -97.85° , in stead of the expected -90° . Further, from these figures it can be concluded that not only the rotational alignment around the optical axis is of importance, but also the alignment in both other directions (pitch and yaw, see figure 3.8). This should be taken into account when using the method of Stone and Howard [22] to measure periodic deviations in laser interferometers. They use a rotation around the pitch axis to introduce an optical path difference between the two arms of a linear interferometer. Since they only make a rotation of 0.5° to measure a periodic deviation of a beam splitter rotated 10.3° around the roll-axis this consideration is not yet necessary. However when dealing with systems with smaller non-linearities the effect of rotation around the pitch axis may well introduce an enlarged periodic deviation itself.

From different kind of interferometer optics the ellipsometric angles were measured. To reduce the influence of pitch and yaw angle the beam splitter optics were aligned so that the reference beam was perpendicular to the entering ellipsometer beam and remained at the same height. The quarter wave plates were placed perpendicular into the beam. The results are shown in table 3.3. The subscripts 'old' and 'new' represent optics made in an old manufacturing process and in a newly designed process of a manufacturer. With this it is clearly shown that in the new manufacturing process the polarization properties of the optics improved enormous. In the beam splitter the leakage is reduced from 3% to better than 0,1%. Depending on the manufacturing process used by optics suppliers the polarization state may vary widely.

As a result of the measurement principle where the compensator is aligned

Component	direction	$\tan(\Psi)_{exp}$	$\tan(\Psi)$	Δ_{exp}	Δ
NPBS	transmission	1	1,094	arb	$1,69^\circ$
NPBS	reflection	1	0,857	arb	$8,11^\circ$
PBS _{old}	transmission	0	-0,0318	arb	$-61,70^\circ$
PBS _{old}	reflection	0	0,0232	arb	$63,28^\circ$
QWP _{old}	transmission	1	0,9987	90°	$-97,85^\circ$
PBS _{new}	transmission	0	0,0003	arb	$-66,42^\circ$
PBS _{new}	reflection	0	0,0004	arb	$-20,67^\circ$
QWP _{new}	transmission	1	0,9977	90°	$90,91^\circ$

Table 3.3: Measured amplitude ratios and phase retardations for different kind of interferometer optics. The subscript *exp* stands for the expected value in the case ideal optics are used, arb means arbitrary: in this case no specific values were estimated from theory.

at 45° with the main axes of the optical component under investigation only single parts of interferometer optics can be measured. Combinations of optical components, like a polarizing beam splitter in combination with a wave plate with it's main axes rotated 45° compared to the beam splitter, can not be measured using this type of ellipsometry. A possible solution is to measure the polarization after the optics using the beat measurement setup from the previous section.

3.3 Resulting periodic deviations

In the previous sections the methods were described to measure the polarization properties of the laser head and the optics used. In order to know the effect

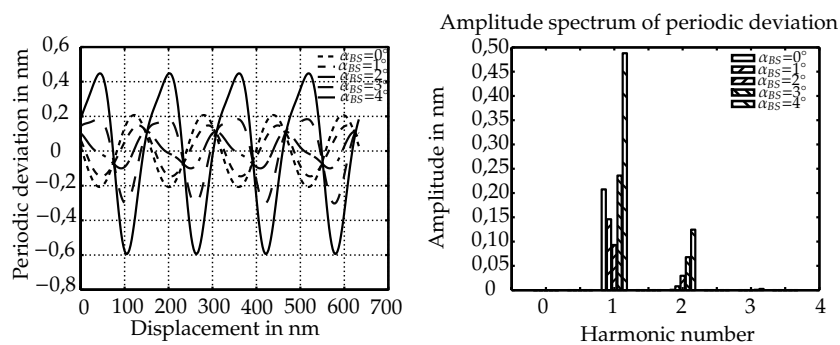


Figure 3.11: Calculated periodic deviation resulting from an ideal laser head with real optics rotated around the Roll axis at several angles.

of these polarization properties the periodic deviations of a complete system with flat mirror optics (components with subscription 'old') was modeled with

the Jones model. The results of this together with an additional increasing misalignment of the polarizing beam splitter are shown in figure 3.11. In this figure it can be clearly seen that in the case of these real optics an ideal alignment no longer produces the smallest periodic deviations. In this specific case a misalignment of the main polarization axes of the optics of $\alpha_{BS} = 2^\circ$ compared to the main polarization axes of the laser head will result in the smallest periodic deviation.

3.4 Conclusions

In this chapter two measurement methods were discussed to measure the polarization properties of commercial heterodyne laser heads. It appears that the ellipticity of the E-fields emerging from the laser head changes in time. Both methods discussed enable a categorization of the ellipticity of the lasers. The non-orthogonality can be determined with both methods with an uncertainty of $0,05^\circ$. Provided dedicated hardware is available to take the reference signal from the heterodyne laser head, the beat measurement setup provides a convenient and relatively easy method to measure the quality of a laser head. If the reference signal can not be taken from the laser head the carrier frequency method still provides a possibility for categorization of the quality of the laser head. However care must be taken to calibrate all influences of the optics used in the measurement system.

In this chapter also a measurement method was presented to measure the polarization properties of optics used in interferometers, based on ellipsometry. With this method only separate components with main optical axes can be measured. So a combination of interferometer optics, like a polarizing beam splitter in combination with a quarter wave plate can not be usefully measured with four zone ellipsometry.

With use of these measurement setups in combination with the Jones model derived in the previous chapter it is now possible to choose the optical components of an interferometer necessary to meet the periodic deviation specifications.

The measurement results of the polarization properties of commercial interferometer components were discussed in terms of predicted periodic deviations. It was concluded that a misalignment of interferometer optics can reduce the periodic deviations resulting from polarization errors in the hardware used in the interferometer.

Chapter 4

The integral calibration setup

In the previous chapter the measurement results of polarization effects of individual components were presented. Using these results and the model derived in chapter 2 the periodic deviations in an entire interferometer can be predicted. In order to investigate the behavior of the total interferometer system, being the laser, the phase measurement electronics and the optics, in a traceable way a setup is used based on a Fabry-Pérot cavity [26]. In this chapter the working principle of the system is explained and the results of some measurements are described and discussed. The model of chapter 2 is verified using the Fabry-Pérot system. Finally a new calibration setup was designed, built and some stability measurements were conducted.

4.1 Traceability

In order to determine the periodic deviations unambiguously a calibration setup must be used which is traceable to the standard of length. According to VIM (Vocabulaire international des termes fondamentaux et généraux de métrologie) the definition of traceability is given by [51]:

Definition 4.1 *Traceability is the property of the result of a measurement or the value of a standard whereby it can be related to stated references, usually national or international standards, through an unbroken chain of comparisons all having stated uncertainties.*

In this thesis laser interferometers are investigated which measure a displacement. So in order to calibrate a laser interferometer in a traceable way it has to be compared to the standard of length: the metre. The definition of the metre as accepted by CCGM (Comité consultatif pour la définition du mètre) is given by Quinn [52].

Definition 4.2 *The metre is the length of the path travelled by light in vacuum during a time interval of $1/299\,792\,458$ of a second.*

The practical realization of this definition [53] can be realized in three ways:

1. By means of the length l of the path that a plane electromagnetic wave travels in vacuum in a time t . The length is then obtained from the measured time t , using the relation $l = ct$ and the value of the speed of light in vacuum $c = 299\,792\,458\text{ m s}^{-1}$.
2. By means of the wavelength in vacuum λ of a plane electromagnetic wave of frequency f . The wavelength λ is obtained from the measured frequency f using the relation $\lambda = c/f$ and the value of the speed of light in vacuum $c = 299\,792\,458\text{ m s}^{-1}$.
3. By means of the wavelength in vacuum λ of radiations which are recommended by the CIPM.

For modern applications, the reference wavelengths are mostly provided by frequency-stabilized lasers (method 3), which is the method we are using also. The frequency stabilized laser used in our laboratory is an iodine stabilized HeNe-laser. Where the absolute frequency is based on the transition R(127)11-5 component i of iodine 127, with a value of 473 612 214,705 MHz ($\nu=12\text{ kHz}$) [54].

Instruments that are capable of traceable calibrations with nanometer uncertainties are rare. As mentioned in chapter 1 laser interferometers are used themselves, mostly with a remaining uncertainty due to the periodic deviations. Some new configurations are designed in principle free of periodic deviations as by Wu [31] who still measures a periodic deviation of 20 pm. For calibration of linear scales PTB developed a comparator [55] based on an interferometer with spatially separated frequencies based on Tanaka's setup [30]. A second principle is an X-ray interferometer as described by Basile [56] and Peggs [57]. It is based on the interference pattern originating from diffraction of an X-ray beam through three slices of silicon. When one of the slices is displaced the pattern changes periodically. The period is determined by the lattice spacing of silicon (220) planes: 0.192 nm. In order to provide sufficient range the system is coupled to a laser interferometer which is read out every half wavelength, and as a result eliminates the influence of periodic deviations. The measurement range of the system is 1 mm and the uncertainty depends on the range. For a range of 10 μm the uncertainty is stated as 15 pm, and rises to 85 pm over the total range. In this estimation uncertainties due to Abbe errors or cosine errors, occurring when calibrating a transducer, are omitted. Practical limitations are the slow detection system and the complex and unusual instruments necessary to operate the system. The third possibility is to use a Fabry-Pérot cavity (active or passive). This is the measurement system used in our laboratory and will be explained in more detail in the next section.

4.2 Fabry-Pérot interferometer

To verify the modeling of the entire interferometer (laser output + optics + detection system) a traceable measurement is carried out on a Fabry-Pérot

setup (figure 4.1). This system was originally developed to provide a traceable calibration for displacement measuring systems (capacitive, inductive, atomic force microscopes, laser interferometers, etc.) with nanometer uncertainty [58]. The measurement principle is based on a Fabry-Pérot interferometer cavity to which a tunable diode laser system is servo-locked via a locking technique based on frequency modulation. When one of the mirrors of the Fabry-Pérot interferometer is displaced, the slave laser tracks the change in resonance frequency of the cavity. At the same time the displacement of the upper cavity mirror is measured by a commercial displacement measuring system, e.g. a laser interferometer system with an optical configuration as modeled in chapter 2. A comparison of the probe (in this case a commercially available laser interferometer system [88]) readout with the displacement derived from the frequency change of the slave laser gives the calibration data. The frequency of the slave laser (order 473 THz) exceeds the possible frequency range which can be measured directly. Instead the beat frequency between the slave laser and a stabilized laser is measured. As a stabilized laser, an iodine stabilized HeNe-laser is used, of which the absolute frequency has been verified by inter-comparison and is known with an uncertainty of 12 kHz. The combination of a measurement against the standard of length and an uncertainty analysis of the calibration system results in a traceable calibration.

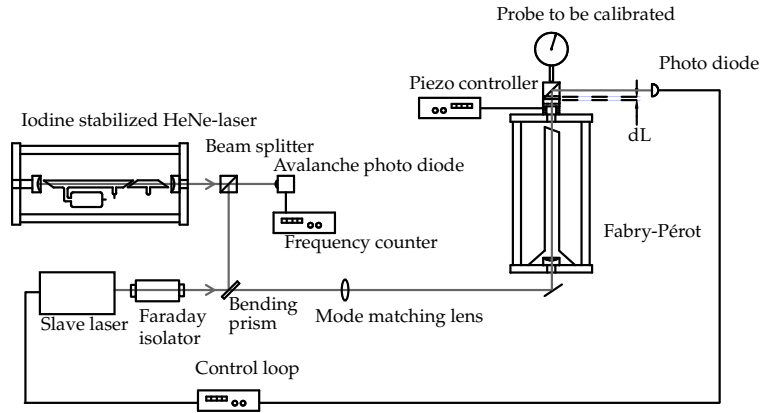


Figure 4.1: Schematic representation of the Fabry-Pérot calibration setup.

The Fabry-Pérot cavity consists of two mirrors spaced 140 mm from each other. The resonance frequency of the cavity is given by:

$$f = \frac{kc}{2nL_{mech}} \quad (4.1)$$

where k is the mode number, c the velocity of light, n the refractive index of the medium inside the cavity and L_{mech} the mechanical length of the cavity. In order to reduce the influence of the refractive index of air a vacuum tube with Brewster window is placed inside the cavity, leaving approximately 10 mm of

air in the entire cavity. During measurements the change in optical path length due to this 10 mm of air is compensated for and the uncertainty is taken into account in the uncertainty analysis. If one mirror is displaced over a distance ΔL_{mech} , the frequency will change by Δf according to:

$$\frac{\Delta f}{f} = -\frac{\Delta L_{mech}}{L_{mech}} \quad (4.2)$$

As the resonance frequency changes, the control loop will keep the slave-laser frequency locked to this resonance frequency. The feedback for the control loop comes from modulating the diode-laser over 15 MHz in combination with phase sensitive detection of the first harmonic of the transmitted signal from the Fabry-Pérot cavity. Calculation of the displacement is done using equation 4.2 in combination with the measurement of the Free Spectral Range (FSR), which is the distance between two successive longitudinal modes and equals $c/2nL_{mech}$. From this measurement the effective mechanical length can be derived, provided that the refractive index change during the FSR measurement is small. This was achieved by measuring the FSR within the shortest possible time (approximately 1 minute).

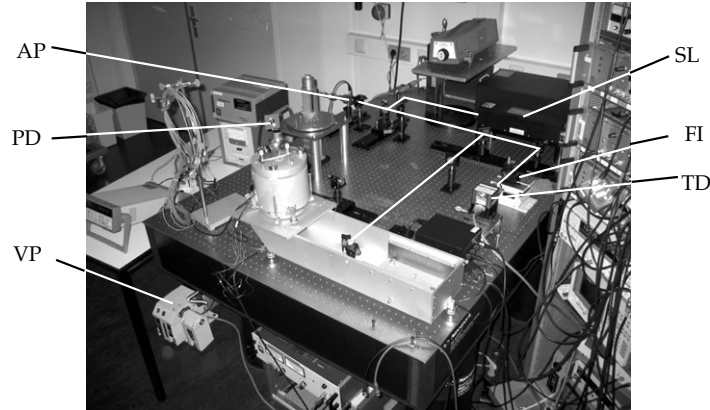


Figure 4.2: The used Fabry-Pérot calibration setup with SL: Stabilized HeNe-laser, TD: tunable diode laser, FI: Faraday Isolator, PD: Photo diode, VP: Vacuum pump, AP: Avalanche photo diode.

Compared to the setup developed by Wetzels [26] a commercial diode laser [89] replaced the HeNe-laser, and the lock-in amplifier used in the control loop was replaced by a commercial lock-in amplifier [90]. The relatively large modulation of the diode laser (15 MHz) compared to the gas laser could influence the uncertainty on the beat measurement. Experiments conducted by Wetzels [26] on different modulation widths with the gas laser showed no significant influence. Further a gate time of 1 second was used to measure the beat frequency. To prevent backscattering from disturbing the diode laser output a

Faraday isolator was added in the beam path. The system used for calibration is shown in figure 4.2.

4.2.1 Uncertainty of the traceable calibration setup

The calibrations can be affected by drift of the system. The mechanical construction of the Fabry-Pérot in combination with the interferometer optics is shown in figure 4.3.

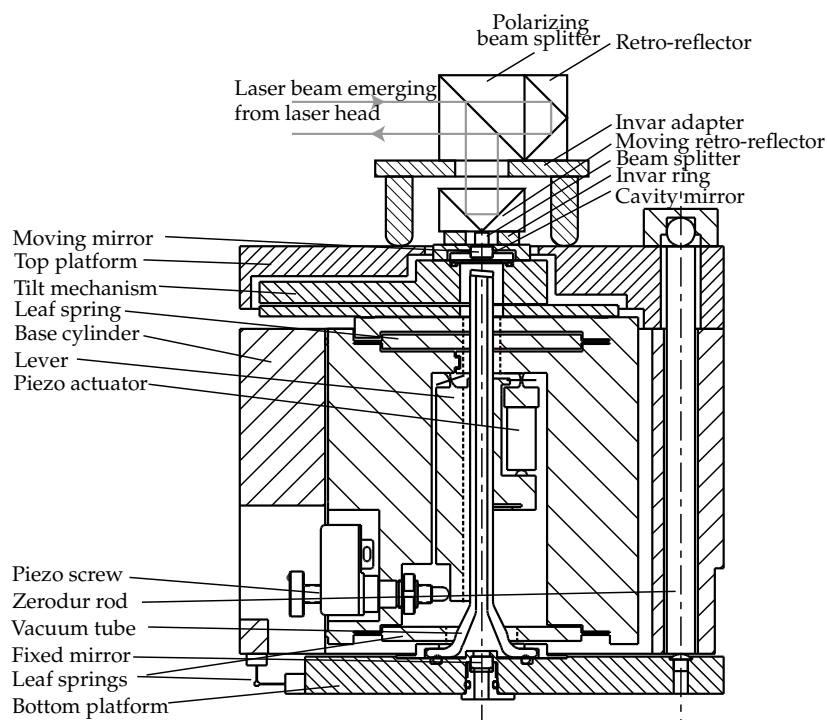


Figure 4.3: Cross-section of the Fabry-Pérot cavity.

As can be seen from this figure the top platform is the reference of the interferometer optics and the bottom mirror is the reference of the Fabry-Pérot system. The top platform is connected with the bottom mirror through the bottom platform and three zerodur rods. All other parts shown between top platform and bottom mirror are thermally compensated. A drift of the upper cavity mirror itself is measured by both the commercial interferometer and the Fabry-Pérot system, and is canceled out of the calibration results. Thermal expansion of the system between the moving retro reflector and the reflecting part of the upper cavity mirror however are measured as a displacement by the commercial interferometer, but not by the Fabry-Pérot and will affect the measurement

results. From the figure it can also be seen that the vacuum tube has a Brewster angle, leaving approximately 10 mm of air in the cavity. This is influenced by refractive index changes in the system. Uncorrected this could result in an optical path length change of 2 nm under normal laboratory conditions. Therefore it is corrected for during measurements and the uncertainty resulting from this is taken into account in the uncertainty analysis. In Appendix E all the influences on uncertainty are discussed in detail. The results of the uncertainty analysis are summarized in table 4.1.

Parameter	Uncertainty over 1 μm	Uncertainty over 300 μm
Axial mode effect	0,14 nm	0,14 nm
Transversal mode effect	0,00 nm	0,07 nm
Brewster window	16,5 nm K ⁻¹	16,5 nm K ⁻¹
Mirror tilt	0,4 nm	0,4 nm
Background slope	0	0
Thermal expansion	51,5 nm K ⁻¹	51,5 nm K ⁻¹
Gradient upper platform	0,4 nm	0,4 nm
Gradient lower platform	0,4 nm	0,4 nm
Gradient probe adapter	0,01 nm	0,01 nm
Cosine error (1,5 mrad)	0,001 nm	0,3 nm
Total ($\Delta T=0,01$ K)	0,89 nm	0,94 nm

Table 4.1: Results of the uncertainty analysis of the metrological Fabry-Pérot interferometer. The total uncertainty is based on a measurement with a maximum temperature change of 0,01 K.

From this table it can be concluded that the major influence of uncertainty lies in the thermal stability of the system and the mirror tilt. The latter depends on the radii of the mirrors used and the length of the cavity. Thermal effects can be divided into linear expansion and gradients. A possibility would be to measure the temperatures of all components and compensate for linear thermal expansion. However space is limited and no extra forces should be applied on the system. Further the measurement of temperature of the Zerodur rods is very difficult since the thermal conduction of Zerodur is very small. A third possibility is to measure the surrounding temperature close to the components and assume an equilibrium. Another problem are the thermal time constants of the components, complicating compensation. Therefore it was chosen to isolate the system from the surroundings using an insulator box and conducting a drift measurement before any real measurement. Further the temperature of different components during measurement is monitored. During measurements discussed the temperature changes remained limited to 0,01 K.

4.3 Short range calibration of an entire laser interferometer

In order to place the laser interferometer optics on the Fabry-Pérot cavity an adapter was made consisting of three legs of invar screwed on an invar platform (as shown in figure 4.3). Invar was used to prevent thermal expansion as much as possible and the design was kept simple to provide a possibility of thermal compensation. The optics are placed on top of the adapter and depending on the optical configuration the plane mirror or retro-reflector is placed on the top mirror of the Fabry-Pérot. Since a beam bender is glued on the top mirror to reflect the locking signal (see figure 4.3) the mirror/retro-reflector can not be placed directly on the mirror. Therefore an invar ring is placed over the top mirror on which the interferometer mirror or retro reflector is placed.

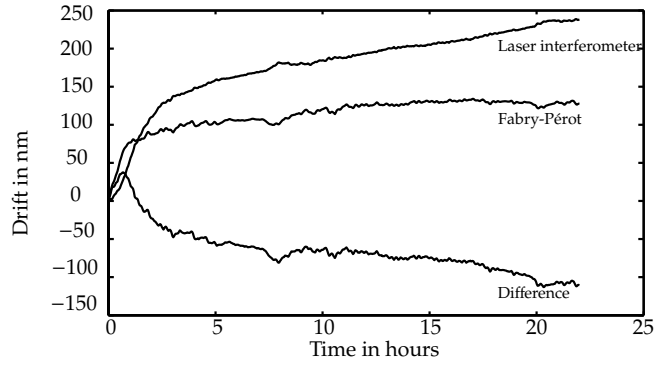
4.3.1 Linear optics

The single pass interferometer optics are investigated first. Linear optics consist of a polarizing beam splitter in combination with two retro reflectors as shown in figure 4.3.

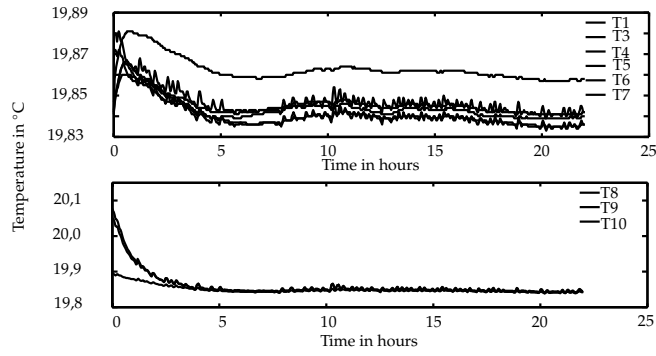
Drift measurement

Before measuring periodic deviations the stability of the setup was investigated. In order to do this a drift measurement was conducted. In the Fabry-Pérot thermistors are used to measure the temperature and gradients of the setup. Also the temperature of the invar holder, beam splitter holder and retro reflector are monitored during the entire measurement. Since there is still approximately 10 mm of air in the cavity also the pressure and temperature of the air inside the cavity are monitored and compensated. The drift measurement was conducted after assembly of the entire system and alignment of the optics. Both lasers and vacuum pump had been running for one hour. The results are shown in figure 4.4.

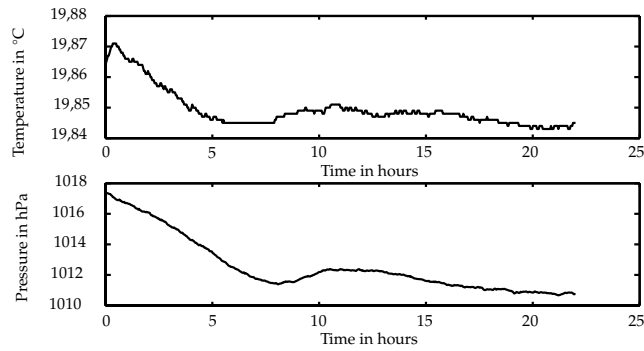
From this figure it can be seen that the Fabry-Pérot cavity stabilizes within 9 hours. In figure 4.4(b) the upper figure shows the temperature stabilization in 7 different places in the Fabry-Pérot cavity, the bottom figure shows the temperature stabilization of the optics holder and the optics, measured on the outside. It can be seen that the optics stabilize after 5 hours and the Fabry-Pérot after 9. From other measurements it appears this effect is mainly caused by the initiation of the vacuum pump. Further it can be seen that the drift of the laser interferometer does not stabilize. The initial drift resulting from temperature stabilization stabilizes after 5 hours. However after 5 hours a linear drift of 4.65 nm/hour remains. From measurements this effect seems to be caused by a drift of the optics in the holders. The optics are glued in steel holders, the construction does not inhibit a thermally stable point from which expansion can occur, therefore the expansion is not defined in any direction and hence can not be compensated for, it can only be measured as a drift. From figure 4.4(a)



(a) Drift of laser and Fabry-Pérot



(b) Temperature drift of the Fabry-Pérot (upper) and the optics holder (lower)



(c) Cavity temperature and pressure drift

Figure 4.4: Drift measurement with the Fabry-Pérot setup and laser interferometer with linear optics. T1= elastic guiding mechanism, T2= air in the cavity, T3=upper side bottom plate, T4= bottom side bottom plate, T5= top of elastic guiding mechanism, T6= bottom side upper plate, T7= upper side upper plate, T8= retro reflector, T9= polarizing beam splitter, T10= Invar holder

it can also be seen that after 8 hours something happens which is measured by the laser interferometer and the Fabry-Pérot cavity, however in opposite direction. This could be caused by a refractive index change which manifests itself opposite for both measurements since the direction of measurement of the laser interferometer is opposite to the direction of measurement of the Fabry-Pérot cavity. However temperature and pressure measurements indicate no changes at the same time. Also carbon dioxide and humidity measurements (not shown here) indicate no large changes at that time.

Rotation of linear optics

After the drift measurement a calibration was carried out of the commercial laser interferometer for different rotation angles of the interferometer optics. This was done to test the predictions of the model as described in section 2.6.4. Some earlier measurements were conducted by rotating the optics. However manipulation by hand for realignment introduces heat and since the optics are in steel holders the stabilization took a long time. Therefore these measurements were conducted by rotation of the laser head and aligning the optics on the invar holder once. The absolute angle of alignment (roll) of the optics was measured on the housing of the optics using an electronic level [91]. The angle of the laser head was measured on the housing also and the difference was used as rotation angle in the calculation. The pitch and yaw angle were guaranteed by optical alignment of the beam reflected by the end surface of the polarizing beam splitter on the emitted beam by the laser over a distance of 1 meter. This results in an alignment of ± 1 mrad. This was done for the first measurement. At each subsequent measurement all angles except the roll angle were kept constant using the electronic level. The results of the measurements are shown in figure 4.5. In this figure the lines are the periodic deviations predicted by the model and the dots are the measured values. From this measurement it can be seen that the amplitude of the periodic deviation predicted by the model resembles the amplitude of the periodic deviation measured on the calibration setup. The measurement was conducted in two directions to test for hysteresis. For reasons of clarity only one direction (movement of the mirror down) is shown. From the figure it can be seen that parts of the measurement region are missing (e.g. between 400 and 450 nm). This is due to the limited measuring range of the beat frequency measurement. For the measurement of the beat frequency a frequency counter [92] and a spectrum analyzer [93] were used. For beat frequencies above 1000 MHz the frequency counter deviated from the spectrum analyzer and measurements were not reliable. This was caused by the use of a beat frequency detector with a constant gain until 1000 MHz and a deteriorating gain above this frequency. The spectrum analyzer still enabled a beat frequency measurement which could be used in the control loop. However the resolution of the spectrum analyzer was limited to 5 MHz resembling a resolution of 1,48 nm, which is too large to enable a calibration. Therefore the spectrum analyzer's frequency was used in the control loop and the frequency counter was used for calibration data up to 1000 MHz.

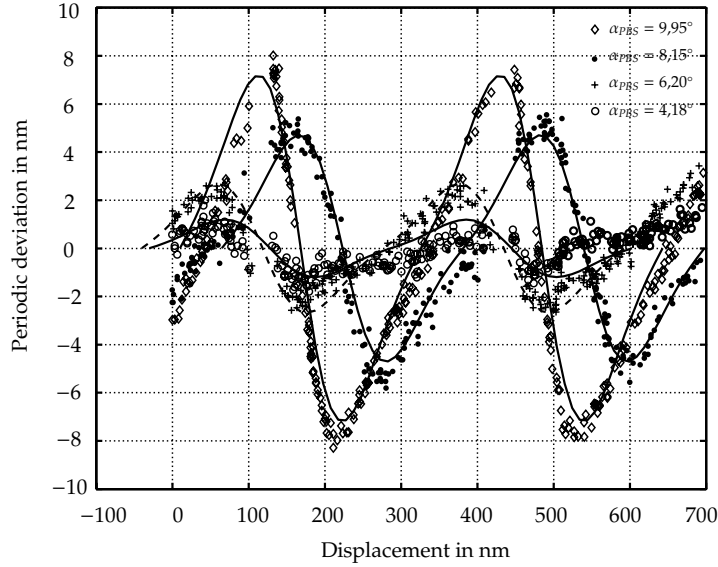


Figure 4.5: Periodic deviation measurement results of rotated linear optics on the Fabry-Pérot setup for different angles of rotation. The solid lines represent the predicted periodic deviations by the model of chapter 2.

4.3.2 Plane mirror optics

Next the plane mirror optics of which the polarization properties were measured earlier as described in chapter 3 were tested. First a drift measurement was conducted which showed a much more stable setup, with a maximum of 4 nm in the first hour. In this setup a plane mirror is placed on the invar ring on the Fabry-Pérot. In figure 4.6 two measurement results are shown. Here also the measurement was conducted in two directions as can be seen from figure 4.6(a). In figure 4.6(a) a measurement is shown with a rotated laser head compared to the optics. At this time no electronic level was available and the rotation of the optics was estimated with use of a least squares fitting algorithm of the model to the measurements. This resulted in a rotation of 3° . From this figure it can also be seen that there is a slight anti-symmetry in the periodic deviation above and below zero, this was predicted by the model and is a result of the optics used (combination of laser head and optics deviation). The standard deviation of the model compared to the measurements was 0,3 nm. To show the relevance of polarization errors in the optics the system was aligned as good as possible. Since only a very small periodic deviation was expected the influence of drift was minimized by measuring only over a distance slightly over $\lambda/4$: 180 nm. This measurement is shown in figure 4.6(b). From this figure it can be seen that the noise band is approximately 0,4 nm, which roughly equals the electronic noise of the interferometer stated by the

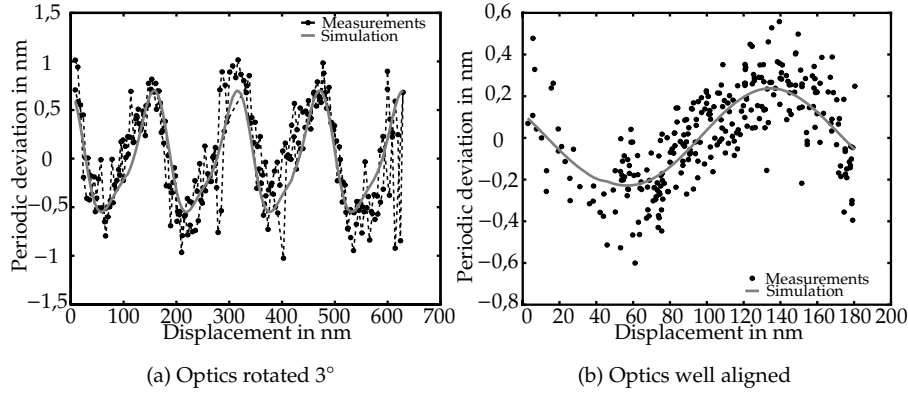
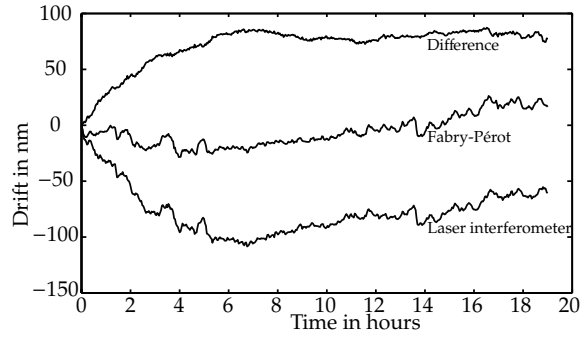


Figure 4.6: Measurements of a plane mirror interferometer with the Fabry-Pérot setup compared to the predicted periodic deviation by the model.

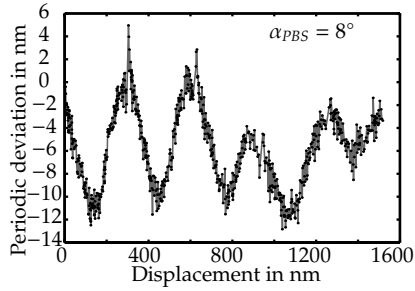
engineers of the system [59]. From this figure it can also be seen that a small periodic deviation still exists. This is mostly the result of the limited quality of the optics as described in section 3.3. Again fitting with a least squares method of the model to the measurement data revealed a small rotation error of $0,3^\circ$. The standard deviation of the model compared to the measurement data was $0,14$ nm.

4.4 Calibration of a homodyne interferometer

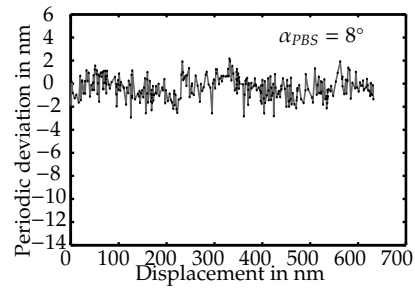
As already mentioned in section 1.1.1 homodyne interferometers also inhibit periodic deviations. However commercial homodyne interferometers exist with a compensation for periodic deviations. In order to investigate the effect of the Heydemann compensation of such a system a commercially available homodyne system was placed on the Fabry-Pérot cavity [94]. A drift measurement was conducted over 19 hours, of which the result is shown in figure 4.7(a). From this can be seen that after 8 hours the system stabilizes from temperature drift resulting of initiating the Fabry-Pérot system. From this it can also be seen that both Fabry-Pérot and laser interferometer register a relatively wild movement of the piezo. Most probably this was due to an electrical disturbance in the system. This will not affect calibration results since the difference of both measurements gives a more stable representation. Initially a measurement was conducted over a range of 600 nm, but no periodic deviations were measured. This is due to the effect of the Heydemann compensation (see chapter 5). The initial periodic deviations were compensated by the system. In this case the Heydemann constants are changed real time in the system [60] which tunes the constants each half wavelength of displacement. As a result after a displacement of 30 half wavelength the periodic deviations are minimized. In order to introduce periodic deviations the system was rotated approximately 8° and the system was scanned through several wavelengths. After this the optics were



(a) Drift measurement



(b) Periodic deviations



(c) Periodic deviations

Figure 4.7: Measurements of a commercially available homodyne interferometer on the Fabry-Pérot setup. In figure (a) the result of a drift measurement is presented, in (b) the periodic deviations with a deliberately initiated periodic deviation are shown without Heydemann compensation. In (c) the periodic deviation is shown with Heydemann compensation.

aligned the best way possible and the measurement was conducted. What happens is that the correction factors, tuned in the system while the optics were rotated, still compensate while the actual system is already aligned. As a result the compensation can be monitored during the scanning of several wavelengths. The measurement was conducted over a range of 1500 nm, and the result is shown in figure 4.7(b). The high frequency noise results from the mechanical setup of the homodyne interferometer on the Fabry-Pérot system. Since the mechanical lay out of the optics differs from regular optics the adapter was not ideal for the system, introducing vibrations. What can be seen from the figure is that the compensation reduces the amplitude of periodic deviation.

After the measurement the upper cavity mirror was displaced over several half wavelengths back and forth and a second measurement was conducted over a range of 600 nm. The result is shown in figure 4.7(c). In this figure it can be seen that the Heydemann compensation has successfully eliminated the periodic deviations.

4.5 New designed Fabry-Pérot interferometer

The uncertainty of the Fabry-Pérot interferometer was 0,89 nm, of which a main part is as a result of temperature drift and gradients. The influence of thermal expansion ($51,5 \text{ nm K}^{-1}$) and gradients of the upper and lower platform (0,8 nm) in the uncertainty analysis was relatively large. This was due to the relatively large length of the cavity and diameter of the sensor platform. Further the thermal expansion of the sensor holder was relatively large. In order to reduce the influence of thermal expansion and gradients a new Fabry-Pérot cavity was developed with smaller diameter and cavity length. Further the sensor platform was integrated in the design.

4.5.1 Cavity length

The choice of cavity length depends on three factors: free spectral range, range of the beat frequency measurement system and the total scanning range of the calibration measurement. All three factors will be discussed next.

The free spectral range of the slave laser needs to be larger than the free spectral range of the cavity in order to enable a measurement. In the original Fabry-Pérot cavity setup a HeNe-laser was used with a free spectral range of 1150 MHz. This limited the length of the original passive cavity to a minimum of 130 mm. During this research the original HeNe-laser was replaced by a diode laser with a tuning range of 70 GHz. As a result the free spectral range of the passive cavity can be increased, and the length decreased.

As mentioned also the beat frequency measurement range needs to be taken into account. PIN-diodes for frequency measurements up to 60 GHz are available, however the surface of the diodes decreases and intensity sensitivity deteriorates with increasing measurement range. With a larger detector surface the alignment of the beat frequency setup becomes less sensitive, reducing

the influence of pointing stability of the diode laser. The beat frequency is produced by mixing an Iodine stabilized HeNe-laser of $125 \mu\text{W}$ with the diode laser. Therefore a sensitive diode is necessary with preferably a larger surface for a practical setup.

The scan range of the calibration system depends on the actuator chosen. A piezo actuator is chosen to supply a smooth and continuous range. Since piezo ceramic materials expand a relatively small part of their volume mostly piezo stacks are built to provide sufficient range. The range depends on the number of piezo stacks, hence the size of the piezo depends on the range needed.

From the demands described above it can be concluded that the length of the cavity should be between 20 and 30 mm. To apply a displacement on the upper mirror and to reduce costs of the setup a commercially available piezo actuator was preferred. To reduce cost further the guiding mechanism is preferred in the actuator principle. In order to place two mirrors opposite to each other the piezo needs a clear aperture. There are commercially available piezo positioners consisting of three piezo linear actuators electrically connected in parallel providing parallel movement [95]. The range of this system is $6 \mu\text{m}$. To test the suitability of this system the tilt angle was measured using an auto-collimator. The measured tilt was $20 \mu\text{rad}$ resulting in a cavity length change of $0,05 \text{ nm}$ [61] which will be taken into account in the uncertainty analysis. The length of the system is 24 mm, resulting in a free spectral range of 6,25 GHz.

4.5.2 Refractive index change

As a result of a smaller cavity the influence of refractive index changes is reduced. Under normal conditions in the laboratory a change in refractive index of $2 \cdot 10^{-7}$ can be expected as will be shown in chapter 6, resulting in an optical path change of 4,8 nm in the cavity of 24 mm. One option would be placing the entire cavity in a vacuum. Since most sensors behave differently in vacuum than in air these would have to remain in air. In that case the upper mirror would form the barrier between air and vacuum. This in turn would result in mechanical forces acting on the cavity, introducing disturbances during measurement. Another option would be to place a vacuum tube within this cavity as in the original cavity. However the cavity would become very narrow and a small part would still have to be in air.

The uncertainty with which the refractive index change can be compensated using Edlén's modified equation is $1 \cdot 10^{-9}$, resulting in an uncertainty in optical path length change of 0,02 nm. Therefore the cavity will be in air and changes in refractive index will be compensated. The uncertainty in this compensation will be taken into account in the uncertainty analysis.

4.5.3 Mechanical construction

The mechanical construction was based on the setup of the existing cavity. Thermal compensation was applied where possible. As a result of a smaller setup, the thermal time constants decrease resulting in a faster temperature

change of all components. Invar was chosen as a construction material instead of aluminum to decrease the effect of gradients. Care was taken to prevent small diameters as occurring in elastic hinges, resulting in a small thermal capacity and high thermal resistance and as a result a fast response to temperature changes. In earlier research [62] an adapter was built to calibrate linear measurement systems on the Fabry-Pérot cavity with a parallel guiding mechanism. To align the adapter in the direction of calibration sprouts were used to support the parallel guiding mechanism and allow three degrees of freedom to be adjusted. During measurement a thermal compensation had to be applied to compensate for changing calibration forces as a result of thermal expansion of the sprouts in turn as a result of their small thermal capacity. To increase temperature stability a large thermal capacity is favorable, hence a base cylinder was used to increase this capacity.

To increase the stability of the sensor holder not the top platform was thermally compensated to the bottom mirror but the sensor holder. One demand was a stable calibration of laser interferometer systems and care was taken to enable the placement of retroreflectors and plane mirrors on the cavity. The result of the design is shown in figure 4.8.

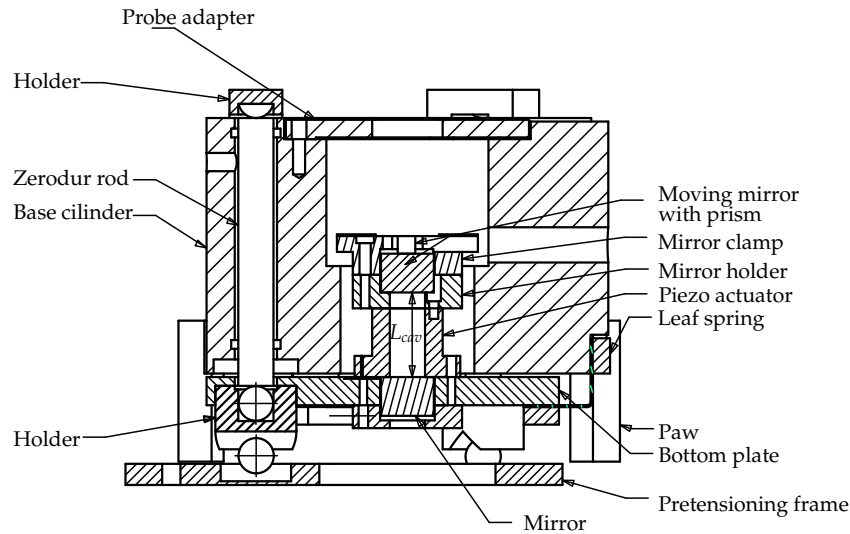


Figure 4.8: Small Fabry-Pérot cavity, with $L_{cav} = 24$ mm.

As the top mirror can not be placed directly onto the piezo actuator a mirror holder and a mirror clamp were designed to clamp the mirror on to the actuator and to provide a stable support to the retro reflector or plane mirror of the interferometer. In order to enable a calibration of different sensors a probe adapter can be made. The constraints for probe adapters are the maximum probe diameter of 46 mm (size of the space under the adapter), the height below the adapter (36 mm) and the thickness of the adapter (5 mm). The top

of the 5 mm thick adapter is thermally compensated to the bottom mirror. The thermal loop is explained in appendix E.

4.5.4 Uncertainty

The uncertainty of the small Fabry-Pérot cavity is derived in Appendix E and is summarized in table 4.2. From this table it can be seen that the major contribution on uncertainty still comes from the linear thermal expansion. This is mainly caused by the thermal expansion of the invar clamp of top mirror and prism. If further improvements in uncertainty should be made this could be done by decreasing the mirror height (now 11 mm). Mirrors are available to a height of 5 mm. Since these mirrors tend to be expensive in single production another possibility would be to omit the prism and switch to a different control system. There are two possibilities: The Pound-Drever-Hall technique based on phase modulation with an electro-optic phase modulator [63], or the Hansch-Couillaud technique based on polarization spectroscopy of a reflecting anisotropic cavity [64]. The latter can be used easily in the original Fabry-Pérot cavity since a Brewster window is in the cavity providing the anisotropy. The Pound-Drever-Hall technique can be used for both cavities. The advantage of this technique is that the prism on the top mirror can be omitted. The disadvantage is they work in reflection mode, so some extra optics should be placed in the entrance beam and as a result the intensity of the incident light in the cavity will reduce. If the prism would be omitted and a different mirror with a height of 5 mm is used the uncertainty as a result of thermal expansion would reduce to $7,5 \text{ nm K}^{-1}$.

Parameter	Uncertainty over $1\mu\text{m}$	Uncertainty over $6\mu\text{m}$
Axial mode effect	0,024 nm	0,024 nm
Transversal mode effect	0,001 nm	0,003 nm
Mirror tilt	0,05 nm	0,05 nm
Background slope	0	0
Thermal expansion	$24,8 \text{ nm K}^{-1}$	$24,8 \text{ nm K}^{-1}$
Gradient upper platform	0,03 nm	0,03 nm
Gradient lower platform	0,04 nm	0,04 nm
Cosine error (1,5 mrad)	0,05 nm	0,3 nm
Total ($\Delta T=0,01 \text{ K}$)	0,26 nm	0,40 nm

Table 4.2: Results of the uncertainty analysis of the small Fabry-Pérot interferometer.

4.5.5 Stability measurement

In order to test the stability of the small Fabry-Pérot cavity a drift measurement was conducted during 16 hours after setup. At this point the lasers of inter-

ferometer, slave laser and Iodine stabilized HeNe-laser had been running for more than 1 day. The interferometer optics were reinstalled on the Fabry-Pérot and the laserhead was aligned to the optics. The diode laser was aligned on the Fary-Pérot just before measurement. A photograph of part of the setup is shown in figure 4.9.

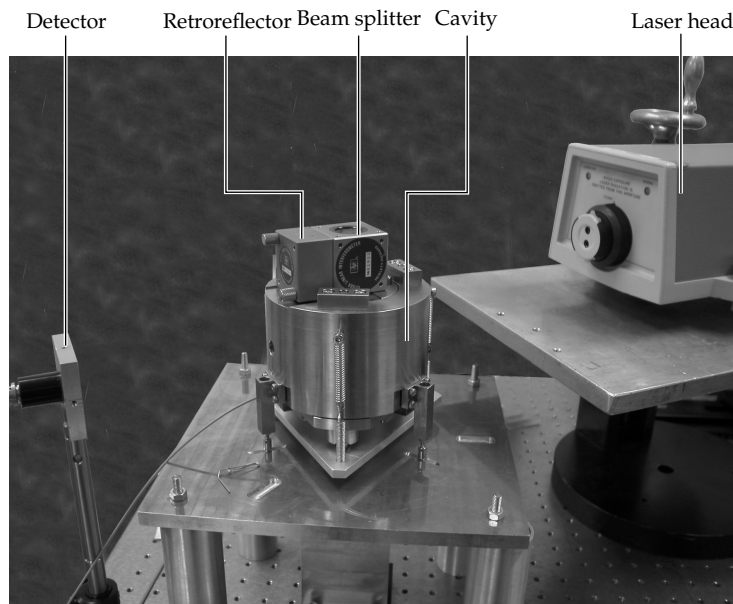


Figure 4.9: Setup of a commercial interferometer system on the small Fabry-Pérot cavity.

The results of the drift measurement are shown in figure 4.10. In this figure the air conditions in the laboratory and cavity are shown (a) as well as the drift without (b) and with (c) compensation of the change in refractive index of air according to Bönsch and Potulski (see chapter 6). At start both laser interferometer and Fabry-Pérot system show a rather large drift. This drift is a result of refractive index change as well as thermal expansion and changing temperature gradients but also from drift of the piezo, which was adjusted just before the measurement in order to lock the system. After 5 hours a drift of 1,5 nm/hour remained. Comparing the drift of the Fabry-Pérot in figures (b) and (c) it can be concluded that the drift of the system was opposite from the drift of the refractive index, resulting in a total zero drift of the Fabry-Pérot cavity in figure (b). The drift of both laser interferometer and Fabry-Pérot in figure (c) is therefore mainly due to drift of the commercial piezo.

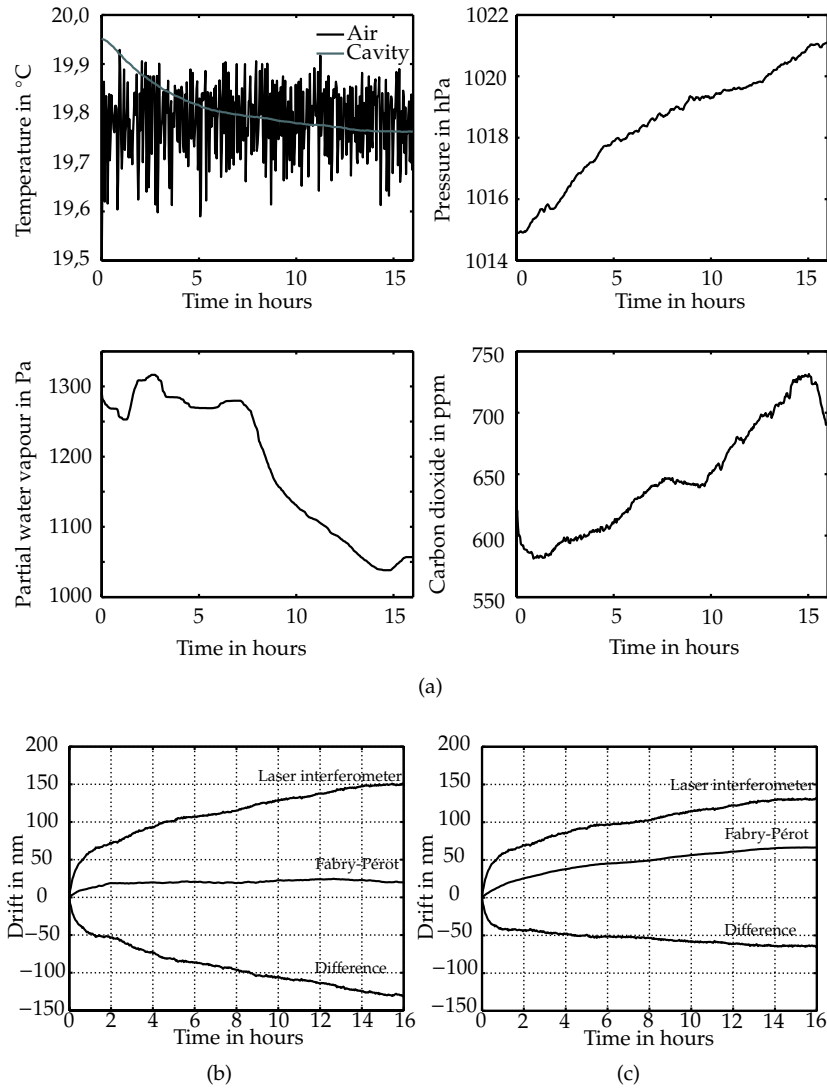


Figure 4.10: Drift measurement of the Small Fabry-Pérot cavity. In (a) the change in air conditions are shown which are used to compensate for refractive index changes, in (b) the uncorrected drifts are shown and in (c) the drift is shown, corrected for changes in refractive index.

4.6 Conclusion

In this chapter a traceable measurement setup was shown to calibrate displacement transducers with an uncertainty of 0,89 nm over a range of 1 μm and an uncertainty of 0,94 nm over a range of 300 μm . The drift of the system was analyzed and it was concluded that the drift of linear optics was more than twice the drift of plane mirror optics, most probably due to the optics holders and the construction of the optical components in their holder. Three calibrations of laser interferometers were presented. A calibration of a heterodyne interferometer with linear optics under different angles of rotation was performed. Of the plane mirror optics discussed in chapter 3 two calibrations were shown. One was over a range of a wavelength and one was over a range of a quarter wavelength. From these measurements the effect of the polarization properties from the optics could clearly be seen. The standard deviation of the predicted periodic deviation compared to the measured periodic deviation was 0,3 nm. This implies that the model described in chapter 2 is sufficient to predict periodic deviations with sub-nanometer uncertainty. Also a measurement was conducted with a commercial homodyne laser interferometer system inhibiting a real time Heydemann compensation. This measurement showed the effect of this compensation. Further a new calibration setup was developed with a reduced uncertainty of 0,26 nm over 1 μm . The stability was tested and showed a reduced drift of 1,5 nm per hour compared to 4 nm per hour of the original cavity. The major contribution of uncertainty is still the thermal expansion of the setup. This can be reduced further if another stabilization technique is used. Therefore it is recommended to investigate and imply the Pound-Drever-Hall technique.

Chapter 5

Compensation of periodic deviations

In the previous chapter it was shown that with the measurements discussed in chapter 3 combined with the Jones model of chapter 2 it is possible to predict the periodic deviations present in a heterodyne interferometer system. With this knowledge it should be possible to minimize periodic deviations in a new setup by choosing the correct laser head, optics and alignment. However it would be more convenient to compensate existing periodic deviations in commercially available systems. Hou and Wilkening suggested two measurement receivers with orthogonally aligned polarizers to compensate for periodic deviations resulting from laser head non-orthogonality and ellipticity. In this chapter this method is investigated using the model described in chapter 2, further it is tested in a measurement setup. In homodyne interferometry the Heydemann compensation [5] is a widely used compensation method for periodic deviations resulting from polarization mixing. As mentioned in section 1.1.1 it is based on compensating the phase quadrature measurement. In this chapter a new compensation method for heterodyne laser interferometers, based on Heydemann's compensation, will be described and the influence is investigated.

5.1 Compensation with two measurement receivers

Hou and Wilkening described a method for compensation of periodic deviations, resulting from laser head ellipticity and non-orthogonality, based on the use of two measurement receivers [17]. The laser beam is split before entering the measurement receiver and fed also to a second measurement receiver. The direction of the polarizer in one measurement receiver is oriented orthogonally compared to the polarizer in the second measurement receiver. The signals of both measurement receivers are compared to the reference measurement and the outputs are averaged. To test this compensation method a measurement setup was built, which is shown schematically in figure 5.1.

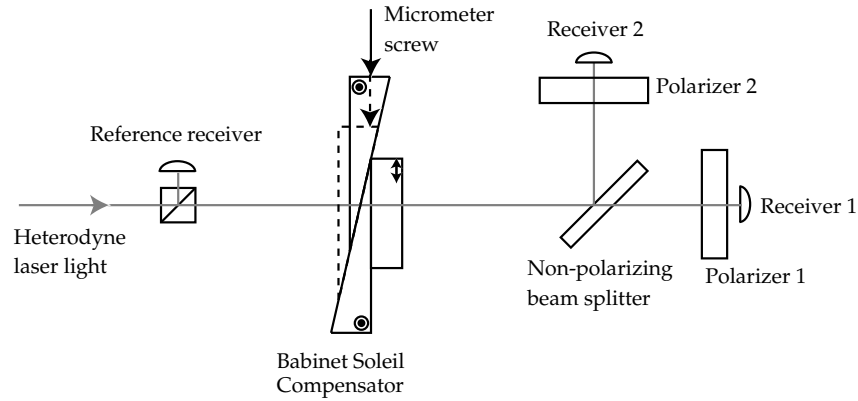


Figure 5.1: Schematic representation of the setup used to test the compensation method with two measurement receivers with orthogonally oriented polarizers.

Light emerging from a heterodyne laser head passes a non-polarizing beam splitter. Part is reflected, travels through a polarizer oriented under 45° with the lasers main polarization axes and forms a reference beat measurement. The part transmitted travels through a Babinet-Soleil compensator, where a relative optical phase shift is added to one of the polarization directions creating a virtual optical path difference. After passing the Babinet-Soleil compensator the light travels to a second non-polarizing beam splitter. There part of the light is transmitted by the second non-polarizing beam splitter, travels through a polarizer oriented under 45° with the lasers main polarization axes and enters the first measurement receiver. The other part is reflected by the second non-polarizing beam splitter, travels through a polarizer oriented under -45° with the lasers main polarization axes and enters the second measurement receiver.

From measurements with commercial heterodyne laser interferometers this compensation method appeared not to work. As mentioned in chapter 3 the periodic deviation is expected to be below 1 nm. Even with increased ellipticity, introduced by a rotated quarter wave plate between laser head and first non-polarizing beam splitter, both measurement receivers produced the same measurement results. Some simulations made with use of the Jones model described in chapter 2 revealed the cause: the direction of the elliptical polarization. As derived in chapter 3 in commercial heterodyne interferometer systems the polarization directions of both frequencies are contra-rotating and therefore produce an inherent compensation as could be seen in figure 2.9. In figure 5.2 the results of the Jones model for the compensation method are shown. In this figure the periodic deviations of the two measurement signals are shown as well as the averaged result. Here it can be clearly seen that only with equal rotating elliptical polarizations the periodic deviations are compensated by this method. With the measurement discussed in chapter 3 the

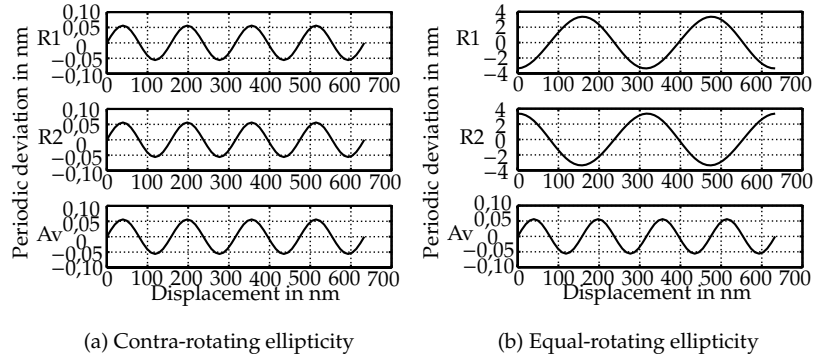


Figure 5.2: Simulated effect of averaging the result of two measurement receivers with orthogonally oriented polarizers. R1: Result of receiver 1, R2: Result of receiver 2, Av: averaged results.

polarization directions of two frequencies emerging from a fiber fed heterodyne interferometer were measured and were equally rotating. Therefore the compensation method was tested on such a system also. The fiber fed system was developed by Knarren [65] during his PhD-study and uses a commercial laser head [96]. The three measurement receivers were read out using a VME board [97] with a resolution of 1,23 nm (for linear optics). As a result of this limited resolution the effect of a well aligned fiber was negligible. Therefore the ellipticity of the fiber output was increased by rotation of the fibers main polarization axis in front of the heterodyne laser. The measurement result is shown in figure 5.3(a).

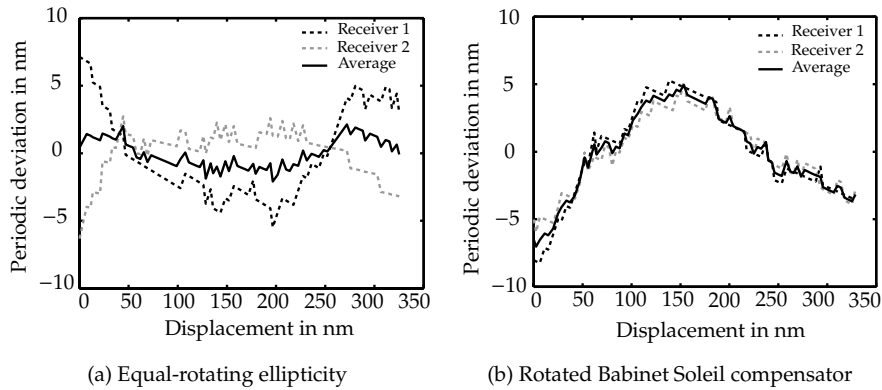


Figure 5.3: Measurement results of the effect of averaging the result of two measurement receivers with orthogonally oriented polarizers.

From this figure it can be seen that indeed the periodic deviation caused by the increased equal rotating elliptical polarized light is compensated. Due

to the limited resolution however the compensation is not ideal. Further the alignment of both measurement receiver polarizers is very difficult in practice.

In figure 5.3(b) the results are shown of the compensation method with an ideally aligned fiber, but with a rotated Babinet-Soleil compensator. Here both measurement receivers detect equal periodic deviations. From this it can be concluded that this compensation method will not work for periodic deviations resulting from rotated optics.

Strangely Hou and Thalmann report measurements with an interferometer where this compensation is used also [40]. They use a plane mirror interferometer of Agilent [98] with a measured periodic deviation before compensation of 8° , resembling a periodic deviation with an amplitude of 3,5 nm. Both the prediction of Hou and Wilkening [17] as well as the discussed measurements above indicate that only deviations originating from the laser head can be compensated. However to create a periodic deviation of 3,5 nm in a plane mirror interferometer only from laser head polarization errors is in practice impossible for a contra rotating elliptical polarized laser head. For example a non-orthogonality not smaller than 8° could explain such an amplitude, or equal rotating ellipticities with a ratio of 1 : 16. However in chapter 3 it was already derived that Zeeman lasers exhibit contra-rotating ellipticities. From measurements no non-orthogonalities larger than $0,35^\circ$ were measured. It is therefore not likely that the laser head produced these deviations. Most probably the influence of another source of periodic deviations is compensated.

From the measurement results, in combination with the knowledge that laser ellipticity and non-orthogonality is limited, it is concluded that this method would in practice not result in an improved interferometer. Therefore a different method has to be found.

5.2 Quadrature detection with a lock-in amplifier

Since the method with two measurement receivers is not suitable for the compensation of all periodic deviations another method was investigated. This method is based on a phase quadrature measurement using a lock-in amplifier. The method was proposed by Eom [33], only they use phase quadrature measurement in combination with a self developed heterodyne interferometer with low split frequency (160 kHz). A lock-in amplifier enables the phase detection between two signals with the same carrier frequency, due to a method called Phase Sensitive Detection. This method enables the filtering of a certain frequency. All noise signals with a different frequency are filtered out. For this method a reference frequency and phase is needed. In the ideal heterodyne laser interferometer 2 signals are generated (see equations (2.3) and (2.5)):

$$I_{ref} = A \cos(2\pi(f_1 - f_2)t + \phi_{ref}) \quad (5.1)$$

$$I_{meas} = B \cos(2\pi(f_1 - f_2)t + \phi_{ref} + \Delta\phi), \quad (5.2)$$

where I_{ref} is the reference signal, I_{meas} stands for the measurement signal and $\Delta\phi$ is the phase shift resulting from the mirror displacement in the interferometer. These signals can well be analysed using a lock-in amplifier. The reference signal of the laser interferometer provides the reference frequency and phase for the lock-in amplifier. With use of a mixer the reference and measurement signals are multiplied and passed through a band pass filter:

$$\begin{aligned} S_0 &= \int A \cos(2\pi(f_1 - f_2)t + \phi_{ref}) \times B \cos(2\pi(f_1 - f_2)t + \phi_{ref} + \Delta\phi) dt \\ &= \frac{1}{2} AB \cos(\Delta\phi), \end{aligned} \quad (5.3)$$

To enable a phase measurement a second reference signal, retarded $\frac{\pi}{2}$ in phase, is multiplied with the measurement signal and also integrated in the band pass filter, resulting in a sine function:

$$\begin{aligned} S_{90} &= \int A \sin(2\pi(f_1 - f_2)t + \phi_{ref}) \times B \cos(2\pi(f_1 - f_2)t + \phi_{ref} + \Delta\phi) dt \\ &= -\frac{1}{2} AB \sin(\Delta\phi), \end{aligned} \quad (5.4)$$

which indicates that both signals are in phase quadrature for an ideal interferometer. From these signals the phase to determine the displacement of the interferometer mirror can be calculated using the inverse equation:

$$\Delta\phi = \arctan\left(\frac{S_{90}}{S_0}\right) \quad (5.5)$$

From equations (2.14) and (2.16) it can be derived that, if the measurement signal contains periodic deviations, the equation for the measurement signal becomes of the form (see appendix F):

$$\begin{aligned} I_{meas} &= \left[t_1 + (t_3 + t_4) \cos(\Delta\phi) + (t_5 + t_6) \sin(\Delta\phi) \right] \cos(\Delta\omega t + \phi_{ref}) \\ &\quad + \left[-t_2 + (t_4 - t_3) \sin(\Delta\phi) + (t_6 - t_5) \cos(\Delta\phi) \right] \sin(\Delta\omega t + \phi_{ref}) \end{aligned} \quad (5.6)$$

If this signal is mixed with the reference signal and passed through a bandpass filter, the phase quadrature signals can be rewritten as (see appendix F):

$$S_0^{nl} = x_0 + R \cos(\Delta\phi) \quad (5.7)$$

$$S_{90}^{nl} = y_0 + R\left(\frac{1}{r}\right) \sin(\Delta\phi - \alpha_l), \quad (5.8)$$

Where the offset x_0 and y_0 represents a first order periodic deviation and the ellipticity characterized by r and α_l represents the second order periodic deviation, R represents the amplitude of the signals. Both signals now form the equation of an ellipse in stead of a circle, occurring for signals without periodic deviations. Using equation (5.5) would result in measurements containing

periodic deviations of the first and second order. Using a least square fitting algorithm to the inverse functions as derived by Heydemann [5](see appendix F) the parameters of the ellipse ($x_0, y_0, R, 1/r, \alpha_l$) can be determined and used to compensate the signals back to an ideal phase quadrature signal, resulting in the compensation of first and second order periodic deviations.

5.3 Practical application

The phase quadrature measurement is carried out with use of a commercial lock-in amplifier [87]. After an initiating measurement the ellipse parameters are calculated using a least square fit on the parameters of (5.7) and (5.8) using the method by Heydemann [5]. These parameters are used to compensate the interferometer system. The schematic setup is shown in figure 5.4. Note that Picotto [66] and Sacconi [67] used a similar setup, just there a phase detector is used instead of a lock-in amplifier.

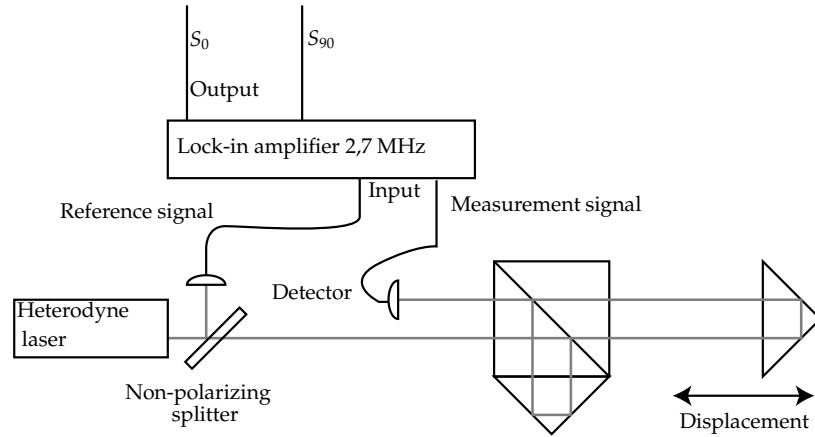


Figure 5.4: Schematic representation of the setup.

The reference signal is taken from the laser head [84] using dedicated hardware. The measurement signal is taken from an external fiber receiver (Agilent E10706B Remote dynamic receiver) using a probe providing the sinusoid shaped measurement signal. As a result of a mirror displacement the phase $\Delta\phi$ will change and the signals S_0^{nl} and S_{90}^{nl} will change accordingly. These signals are recorded on a pc using GPIB interface and averaged over 20 measurements for each mirror position. Recording the signals over a phase change of 2π is sufficient to derive the parameters of the ellipse, providing a possibility to compensate the measurements.

The lock-in amplifier is the same as described in chapter 3. The calibration described there about linearity (0,3%), drift (0,015 mV) and phase angle (0,6 μ rad) is used to determine the usability of the lock-in amplifier. Assuming

that noise in the recorded intensities can be phase noise as well as amplitude noise, the deviations in amplitude can be considered as a possible phase error [31]:

$$\Delta\phi = \frac{\Delta R}{R} \quad (5.9)$$

With this equation also an uncertainty estimation can be derived from the phase quadrature measurements:

$$u(\Delta\phi) = \frac{s(R)}{\bar{R}} \quad (5.10)$$

where s stands for the standard deviation and the bar in the denominator represents the mean value. Note that this is a worst-case estimation: if the laser intensity fluctuates this will also give an amplitude variation but not a phase variation. The noise emerging from the lock-in amplifier was 0,015 mV. The smallest amplitude measured using this system is 20 mV, resulting in a maximum error of 0,75 μ rad. For a linear interferometer this would result in an error of 0,04 nm. This indicates that the quality of the lock-in amplifier is sufficient to be used in a setup for compensation of periodic deviations to an amplitude below one nanometer.

5.4 Measurement results

The compensation method was tested on several setups. First a common path verification is carried out to test the compensation of periodic deviations resulting from rotational misalignments. Second the system is tested for two common interferometer setups, which will include periodic deviations of the optics. The system is also tested on a probe calibration setup used in the laboratory of Precision Engineering to calibrate high accuracy probes for coordinate measuring machines. Finally the setup was tested on the traceable verification setup which was already described in chapter 4. The measurement results of all these setups are shown and discussed in the next sections.

5.4.1 Common path verification

The compensation was tested first with use of the Babinet-Soleil compensator described in section 2.4. Measurements were carried out as follows: in the experimental setup the interferometer optics are replaced by the Babinet-Soleil compensator (as shown in figure 2.3). The Babinet-Soleil compensator is shifted in small steps over a bit more than two wavelength path-difference using a micrometer screw. Both signals S_0^{nl} and S_{90}^{nl} are recorded and a least-squares fit to equations 5.7 and 5.8 is made [68, 5] and the ellipse parameters are used to compensate the measurement results. Both the uncorrected phase $\phi = \arctan(\frac{S_{90}^{nl}}{S_0^{nl}})$ and corrected phase $\phi = \arctan(\frac{S_{90}}{S_0})$ are compared to the phase induced by the Babinet-Soleil compensator. This phase was induced linearly by the micrometer screw and a linear fit was made between the calibration points as determined in appendix B to form a linear reference.

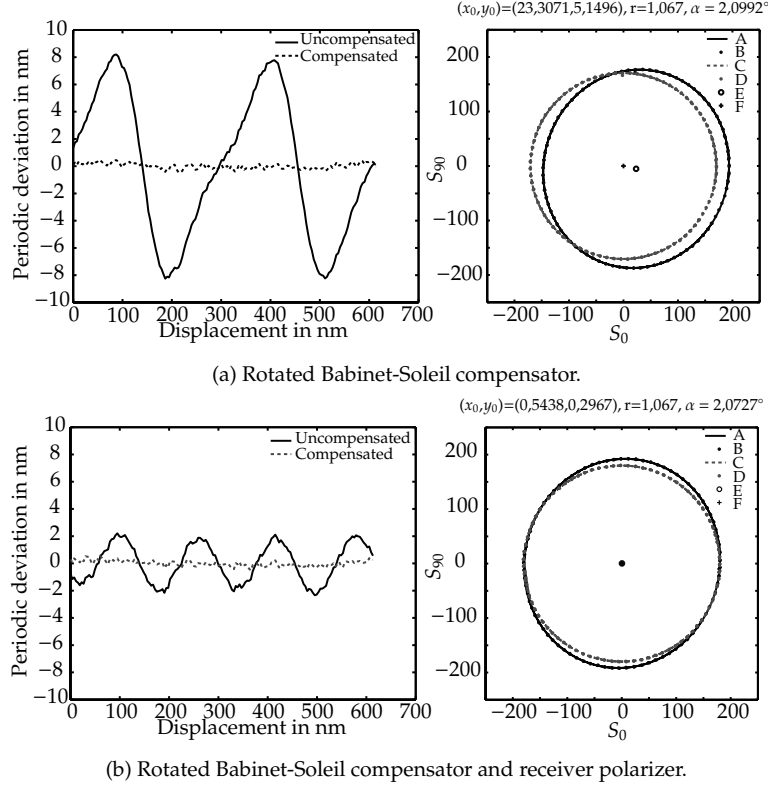


Figure 5.5: Results of a measurement with a rotated Babinet-Soleil compensator of 10° (a) and a combination of a rotated Babinet-Soleil compensator and receiver polarizer (b). On the left hand side the periodic deviation with and without compensation and on the right hand side the S_0 , S_{90} signal with Least square fit (A), Measurements (B), Corrected fit (C), Corrected measurements (D), Original offset (E) and the Corrected offset (F).

A measurement was taken with a rotation around the roll-axis of 10° of the Babinet-Soleil compensator. Figure 5.5 gives the corrected and uncorrected results where on the right the S_{90} signal is plotted against the S_0 signal and on the left the periodic deviation is shown compared to the linear displacement of the Babinet-Soleil compensator. The deviations in the corrected displacement indicate the remaining deviations of the system after correction. The periodic deviation, as it is measured in figure 5.5(a) without correction, can be characterized by an uncertainty of 5,3 nm; after correction this is reduced to an uncertainty of 0,2 nm. This is probably mainly caused by a nonlinear generated displacement by the micrometer screw and the operators hand. The uncertainty derived with equation (5.10) is 0,15 nm, almost covering the remaining uncertainty after correction as derived by the comparison with the

Babinet-Soleil compensator scale. From model calculations as presented in section 2.6.4 and by Cosijns [69] this type of deviation is known; the amplitude of the periodic deviation equals the amplitude predicted by the Jones model.

It is also known that the deviation turns into a second-order deviation once the receiver is given the same rotation as the optics (in this case the Babinet-Soleil compensator), as was shown in figure 2.17. The results of this experiment are given in figure 5.5(b). Comparing the right hand figures 5.5(a) and 5.5(b) one can observe that in figure 5.5(a) the measured circle is shifted right and down relative to the undisturbed corrected circle and becomes somewhat elliptical. In figure 5.5(b) the center point is shifted back and only the ellipticity remains. This is reflected in the fitted parameters: r and α are similar in both figures, but in figure 5.5(b) the bias in x-direction is almost vanished. This is shown in a vanished first order periodic deviation and a remaining smaller periodic deviation with double periodicity, for the uncorrected case at the left-hand of figure 5.5(b). In this case the uncertainty of the measurements is 1,4 nm for the uncompensated measurement which reduces to an uncertainty of 0,2 nm for the corrected measurement, referred to the Babinet-Soleil compensator scale. The uncertainty derived by equation (5.10) is 0,11 nm in this case.

5.4.2 Verification of basic interferometer setups

To verify the compensation of periodic deviations resulting from optics as predicted in chapter 3 also two setups were built with interferometer optics. One with linear optics and a second one with plane mirror optics. To generate a stable but slowly varying displacement an aluminum distance tube was placed between the polarizing beam splitter and the measurement optics, see figure 5.6(a) and 5.6(b). The displacement was generated by warming up the tube by hand and then letting it cool down slowly to room temperature. The result for the linear optics is given in figure 5.6(c). This figure shows that already without compensation the non-linearity is within 1 nm. In this method the actual displacement is unknown and the compensation method can only be tested against the ideal circle. As a result the remaining uncertainty of the compensated measurement contains the noise of calculation: 0,0012 nm. With the assumption that noise in the recorded amplitude can be amplitude noise as well as phase noise, equation (5.10) was used to derive an uncertainty of the compensation. The derived uncertainty was: 5,7 mrad which equals 0,29 nm.

The plane mirror optics give a more peculiar behavior, as depicted in figure 5.6(d). The same kind of behavior was noticed by Číp [70]. By modeling the optics and laser head polarization errors it was tried to explain the deviation. This can be done if the assumption is made that the optics were misaligned counter clockwise by $4,5^\circ$, further the quarter wave plate was misaligned $3,2^\circ$. The right hand side of figure 5.6(d) gives the result of the model calculation. For the measurement the optics were rotated on the table compared to the laser head, however the angle was unknown. The polarization errors of the optics were measured by ellipsometry (see section 3.2)[71] and the polarization error of the laser head was measured as explained in section 3.1 [72]. The

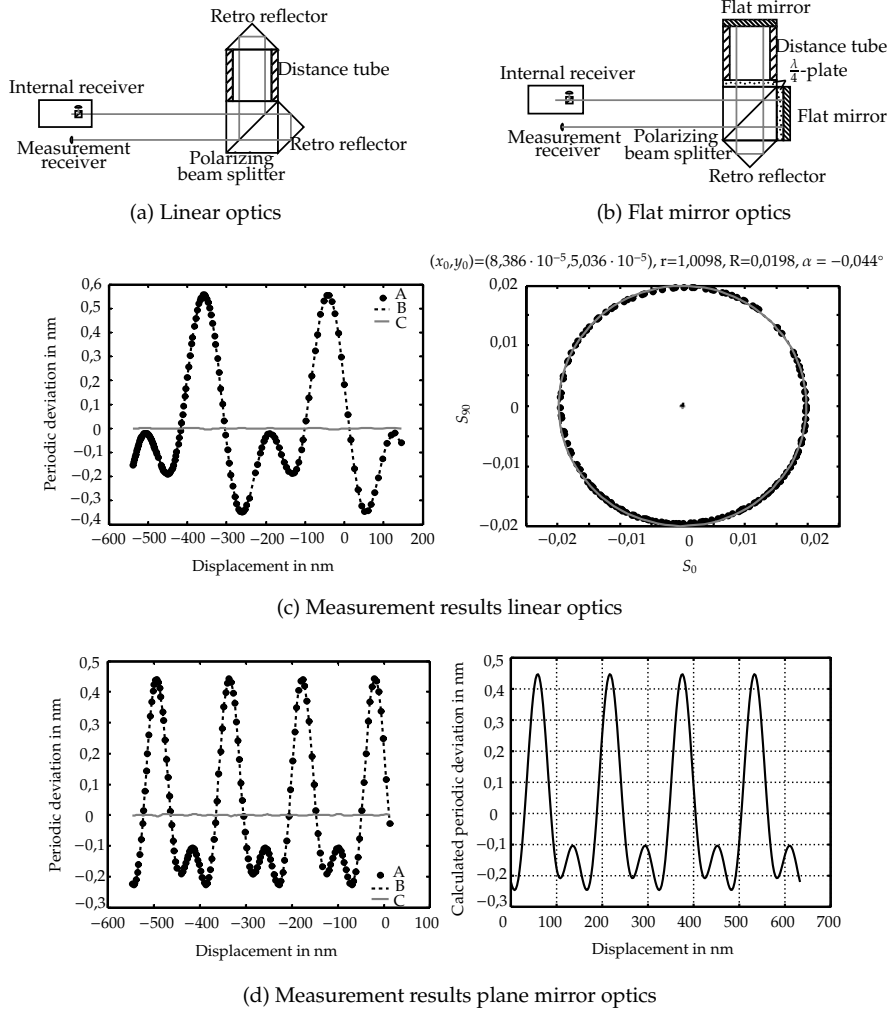


Figure 5.6: Results of a measurement with linear and plane mirror optics. Compared are Measurement (A), Fit(B) and compensated (C). In (a) the schematic setup is shown used to measure the effect of a linear interferometer, in (b) the schematic setup is shown used to measure the effect of a plane mirror interferometer. In (c) the measurement results are shown for the linear interferometer. On the left side the calculated original and compensated periodic deviation are shown, on the right the S_0^{nl}, S_{90}^{nl} signal is plotted along with the compensated circle (solid gray line). In (d) the results of the plane mirror interferometer are shown (left), along with the predicted periodic deviation (right).

ellipticity of the laser head was 1 : 170 for f_1 and 1 : 171 for f_2 in E-field one left hand elliptically polarized and one right hand elliptically polarized. The non-orthogonality between both laser polarizations was $0,3^\circ$. The compensation reduces the uncertainty of the non-linearity theoretically from 0,35 nm down to 0,23 nm derived from equation 5.10.

5.4.3 Comparison probe and plane mirror optics

In the laboratory of Precision Engineering a calibration system for probes of Coordinate Measuring Machines was developed based on a plane mirror interferometer [73], see figure 5.7. The system was developed to have an overall uncertainty of 5 nm. In earlier probe calibrations it appeared to show periodic deviations [73]. Therefore the compensation was tested on this system also. The system is based on a commercial interferometer system and with plane mirror optics.

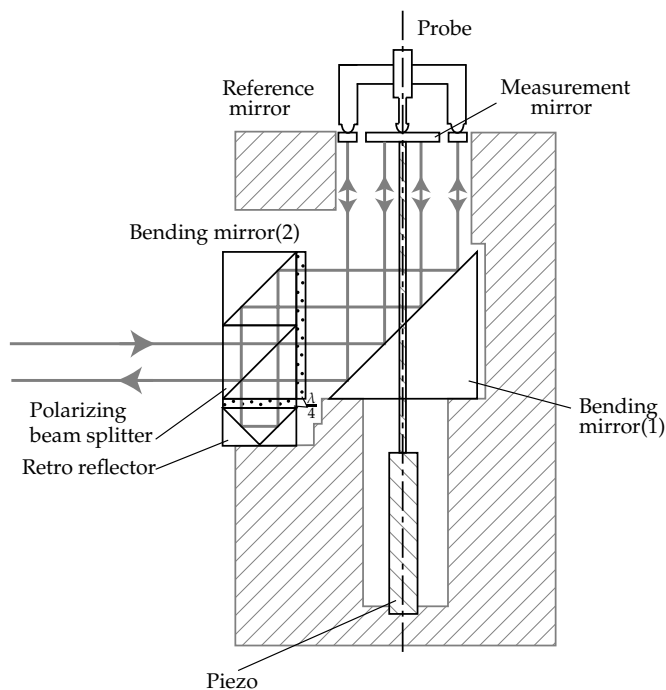


Figure 5.7: Principle of the calibration system based on a plane mirror interferometer.

The light emitted by a commercial laser head enters a polarizing beam splitter. There the light is split into a reference part and a measurement part. The measurement part is transmitted, passes a first quarter wave plate for the first time, is reflected by a bending mirror(1), reflected by the measurement

mirror, again reflected by the bending mirror(1), passes the first quarter wave plate for the second time and enters the polarizing beam splitter. As a result of the double passing of the quarter wave plate in combination with a reflection on the reference mirror the polarization is rotated 90° and the light is reflected by the polarizing beam splitter, passes a second quarter wave plate for the first time, is reflected by a retro reflector and passes the second quarter wave plate a second time. As a result of the double passing of the second quarter wave plate in combination with the reflection in the retro reflector the polarization is again rotated 90° and is transmitted by the polarizing beam splitter. Via a reflection by the bending mirror(2), transmission for the third time through the first quarter wave plate, reflection by the bending mirror(1), the measurement mirror for a second time, bending mirror(1), a fourth transmission through the first quarter wave plate, a reflection by the bending mirror(2), it enters the beam splitter. The polarization is again rotated 90° and the light is therefore reflected by the polarizing beam splitter out of the system back to the measurement receiver.

The reference part is reflected by the polarizing beam splitter, the bending mirror(2), passes the first quarter wave plate for the first time, is reflected by the bending mirror(1), the reference mirror, again the bending mirror(1), transmitted a second time through the first quarter wave plate, reflected by the bending mirror(2) and enters the polarizing beam splitter. Here it is now transmitted as a result of a rotated polarization as a result of double passing of the first quarter wave plate. After passing the polarizing beam splitter it passes the second quarter wave plate, is reflected by the retro reflector, passes the second quarter wave plate a second time (is therefore again rotated 90° in polarization) and reflected by the polarizing beam splitter. After reflection by the polarizing beam splitter the light passes the first quarter wave plate a third time, is reflected by the bending mirror(1), the reference mirror a second time, the bending mirror(1), passes the quarter wave plate a fourth time and is finally transmitted by the polarizing beam splitter and exits the system back to the measurement receiver.

The reference and measurement mirrors are placed concentric. By means of a piezo the center mirror is displaced in steps of approximately 8 nm. As a result of the reflection twice by the reference and measurement mirror the resolution of the interferometer is increased, and the periodic deviations double in frequency if measured against the actual displacement of the mirror. As a result the first order periodic deviation will have a period of $\lambda/4$ and the second order will have a period of $\lambda/8$ (expressed in mechanical displacement of the mirror).

To test the compensation method, the displacement of the measurement mirror is measured against a probe displacement of an inductive probe [99], see the photograph of figure 5.8. This probe was calibrated earlier on the traceable Fabry-Perot calibration system [26] and showed no periodic deviations with a periodicity of $\lambda/8$ or $\lambda/4$, enabling a comparison of periodic deviations of the laser interferometer with the inductive probe. The results of the measurement are shown in figure 5.9(a). From this figure it can be seen that the phase



Figure 5.8: Photograph of the setup used to test the compensation method on a probe calibration setup.

compensation does not reduce the periodic deviation although it is a first order periodic deviation. In fact the uncertainty of the measurement compared to the probe reference equals 0,89 nm, while the uncertainty of the compensated measurements compared to the probe reference equals 0,94 nm. Since this is a plane mirror interferometer with double pass properties, the first order periodic deviation exhibits four periods in a displacement of the mirror from one wavelength. In the right hand side of the picture it can be seen that the fit of the circle is rather good. The uncertainty derived from these measurements using equation 5.10 equals 0,15 nm. The system was tested several times, where the periodic deviation changed in amplitude, however the effect of compensation remained equal. After careful examination of the system it appeared to exhibit rather large ghost reflections. These are reflections of the measurement and reference beams on the end faces of the optics. These reflections can pass the measurement path also and end up in the detector as a higher order harmonic resulting in periodic deviations [10]. Wu [10] described the time varying property of these periodic deviations. Therefore it was decided to test whether this failure of compensation could be caused by ghost reflections. By introducing a glass plate (reflection of approximately 4% on end surfaces) into both the measurement and reference beams under an angle of 15 degrees the ghost reflections passing twice the measuring path were reduced in amplitude. The effect is shown in figure 5.9(b). The uncertainty of the uncompensated measurement compared to the probe is now 1,27 nm,

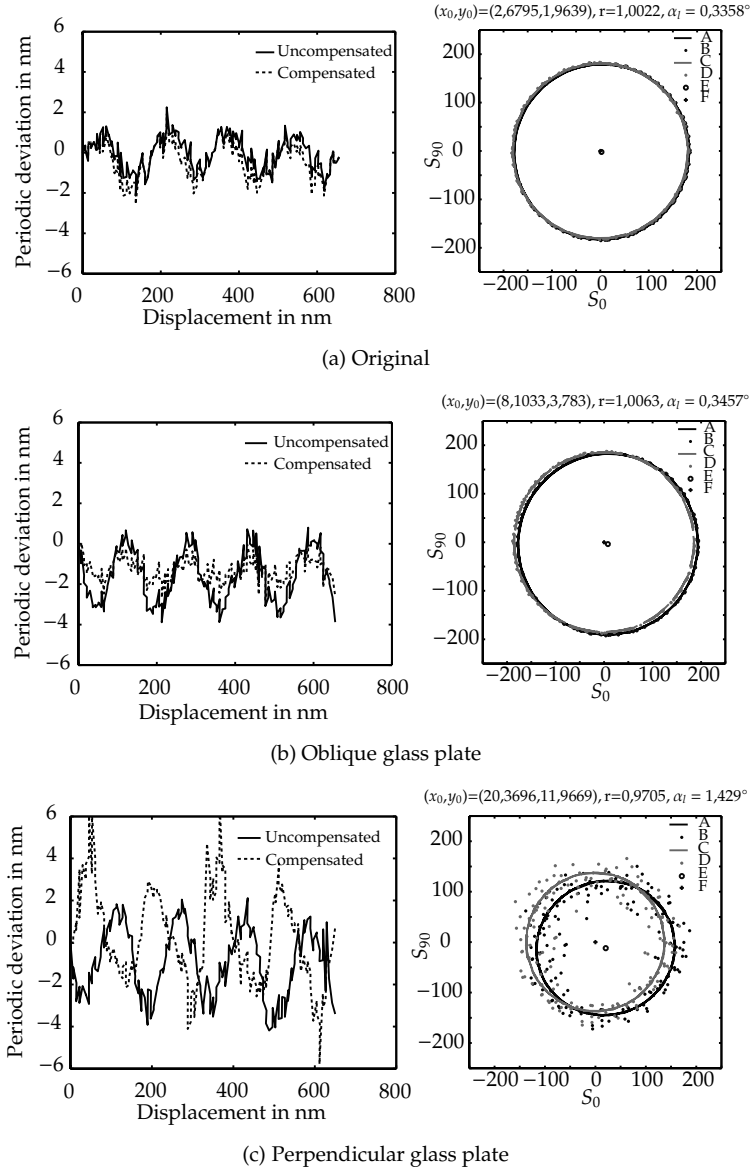


Figure 5.9: Results of the comparison of an inductive probe and a commercial heterodyne interferometer with and without phase compensation. On the left hand side the periodic deviation with and without compensation and on the right hand side the S_0, S_{90} signal with Least square fit (A), Measurements (B), Corrected fit(C), Corrected measurements (D), Original offset (E) and the Corrected offset (F).

while the uncertainty of the compensated measurement compared to the probe is 0,59 nm. The uncertainty to be expected from the amplitude variation, as derived by equation (5.10) is 0,10 nm. As a second test the plate was placed orthogonal in the measurement and reference path and aligned so that as many as possible ghost reflections entered the detector. The result of this is shown in figure 5.9(c). Here the uncertainty of the uncompensated measurement compared to the probe is 1,63 nm, where the uncertainty of the compensated measurement compared to the probe is 2,18 nm. The uncertainty derived by equation 5.10 is 3,56 nm. For sake of clarity the uncertainties for each measurement are summarized in table 5.1.

Setup	u_{meas}	u_{corr}	u_{eq}
Original	0,89 nm	0,94 nm	0,15 nm
Oblique glass plate	1,27 nm	0,59 nm	0,10 nm
Perpendicular glass plate	1,63 nm	2,18 nm	3,56 nm

Table 5.1: The uncertainties of the different measurements with the compensation method. u_{meas} and u_{corr} refer to the uncertainty of the uncompensated respectively the compensated measurement compared to the reference probe, u_{eq} refers to the uncertainty derived with equation (5.10).

When examining these results it can be seen that the oblique glass plate introduces an enlarged periodic deviation, which is partially compensated by the phase compensation. However a periodic deviation with an uncertainty of 0,59 nm remains. This remaining part is smaller than the original remaining part of figure 5.9(a) ($\sigma_{corr} = 0,94$ nm), but not convincing. The uncertainty derived by equation (5.10) still indicates a small periodic deviation. Looking at figure 5.9(c), the result of the increased ghost reflections, it is obvious that the periodic deviation is also increased. This increased periodic deviation is enlarged even by the phase compensation, implicating that the amount of ghost reflection in the setup influences the phase compensation. At the right hand side of figure 5.9(c) the S_0 S_{90} -signal exhibits large amplitude deviations, most probably also caused by ghost reflections. This is also reflected in the increased uncertainty derived by equation 5.10. From these examinations it is concluded that the uncompensated part in figure 5.9 is most probably introduced by ghost reflections and that phase quadrature compensation of Heydemann is unable to compensate for ghost reflections. One way to explain this would be that ghost reflections manifest themselves as a non-uniform distribution on the corrected circle when a uniform motion is applied on the interferometer mirror. This indeed is not corrected by the quadrature phase compensation.

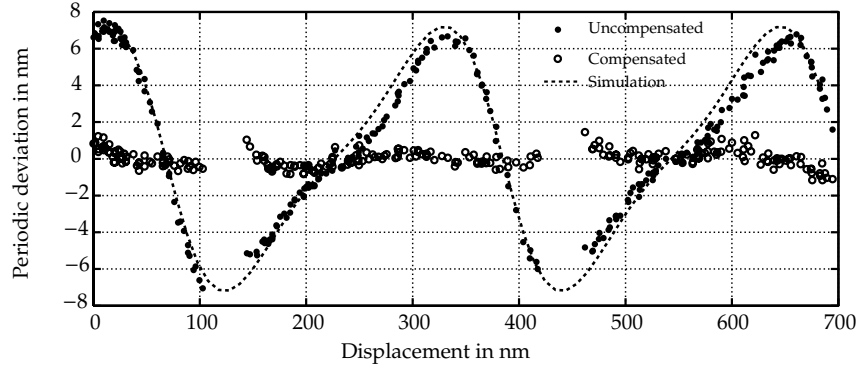
5.4.4 Traceable verification

The compensation method was tested also on the Fabry-Pérot setup described in chapter 4. The compensation was applied to measurements with a linear

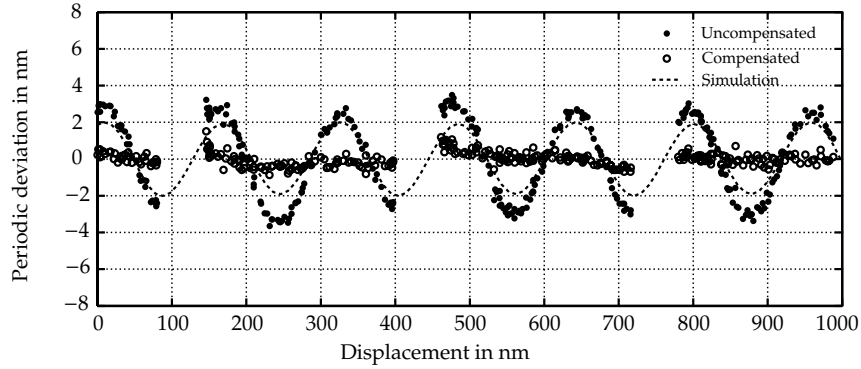
interferometer, as presented in figure 4.3. To test the stability of the setup a drift measurement was conducted. From this resulted that the Fabry-Pérot still drifts 4 nm/hour after 14 hours. At that time the measurements were made and the drift was subtracted from the measurement signal. Two measurements were done to test the compensation method. First a measurement was conducted where the laser head was rotated $9,96^\circ$ compared to the optics. The angle between optics and laser head was measured using an electronic level. Since the laser head includes the measurement receiver the result is the same as if only the optics were rotated. The result of this measurement is shown in figure 5.10(a). In this figure the uncompensated measurement is shown along with the compensated measurement and the periodic deviation predicted by the Jones model. In order to calculate the periodic deviation, the polarization properties of laser head and optics were measured and their Jones matrices used as input in the model. From this figure it can be seen that the model predicts the amplitude of the periodic deviations very well, however the slope of the predicted deviation differs from the slope of the measurements. This is probably caused by the linearization of the drift in the system, of which the cause could not. The uncertainty of the uncompensated measurement compared to the Fabry-Pérot reference is 3,99 nm, the uncertainty of the compensated measurement compared to the Fabry-Pérot reference is 0,45 nm. The predicted uncertainty by equation (5.10) is 0,42 nm.

A second measurement was conducted with a rotated laser head (again $9,96^\circ$) in combination with an external fiber optic receiver. In the alignment an attempt was made to align the receiver in 45° with the main axes of the optics. However the orientation of the polarizer in the fiber optic receiver is not known a priori. Therefore it was assumed that the polarizer of the external receiver was aligned in an angle of 45° with the base attached to it. This was aligned at the same absolute angle as the optics with aid of an electronic level. The measurement results of this measurement are shown in figure 5.10(b). In this figure the uncompensated periodic deviation is shown along with the compensated periodic deviation. Further here also the periodic deviation predicted by the Jones model is shown. From the figure it can be seen that the model prediction deviates from the measured periodic deviation. This may be caused by the alignment of the polarizer, however modeling revealed that such a deviation can not be the result of a misaligned polarizer. It could also be an effect of the lock-in amplifier, although the calibration showed no deviations large enough to explain these deviations it could however be the result of an unknown effect.

In both figures 5.10(a) and 5.10(b) it can be seen that the compensated measurements show a remaining first order deviation. Since this behavior has not been registered before it is unlikely to be an effect of the Fabry-Pérot cavity. A possible explanation would be the effect of ghost reflections. However the deviations appear to be stable in time, which differs from the effect measured in section 5.4.3. To be able to draw conclusions about ghost reflections modifications should be made to the setup in order to test the effect of reduced and extra induced ghost reflections. A second possibility is that it could be the result of



(a) Receiver polarizer aligned to laser axes



(b) Receiver polarizer aligned to optics

Figure 5.10: Measurement results of a linear interferometer system calibrated on the Fabry-Pérot calibration setup. In (a) the uncompensated results as well as the compensated results are shown of the measurements with a system with optics rotated $9,96^\circ$. The dashed line is the predicted periodic deviation by the Jones model. In (b) the uncompensated and compensated result are shown of the measurement with rotated optics (again $9,96^\circ$) and the receiver polarizer rotated approximately the same amount. Here also the predicted periodic deviation by the Jones model is shown as a dashed line.

an unknown effect in the lock-in amplifier. These deviations are within the measurement uncertainty of the Fabry-Pérot interferometer, which illustrates the need for a calibration system with reduced uncertainty, such as the small Fabry-Pérot cavity.

Comparing the uncertainties derived from equation (5.10) (0,42 nm and 0,30 nm) and the uncertainties of the compensated measurements (0,45 nm and 0,37 nm) it seems that the uncertainties derived by the measurement of amplitude variation predict the uncertainties of the compensated measurements

very well.

5.5 Conclusions

In this chapter methods were discussed to compensate periodic deviations in laser interferometers. The method described by Hou and Wilkening using two measurement receivers with orthogonal oriented polarizers was investigated and tested. It was concluded that this method only reduces periodic deviations originating from polarization errors in the laser head (ellipticity and non-orthogonality). Further periodic deviations caused by ellipticity of the laser head are only compensated if the laser head emits equal rotating elliptical polarizations, as is the case if using a heterodyne laser equipped with one fiber for both polarizations. A second method for compensation of periodic deviations based on quadrature detection was explained and tested on different setups. This method enables compensation of periodic deviations introduced by polarization mixing as raised by misalignment or polarization errors in the components. However periodic deviations introduced by ghost reflections seem impossible to correct. This could be explained if the ghost reflections manifest themselves as a virtual displacement by a non-uniform distribution on the quadrature circle. Since only the amplitude and origin of the ellipse is corrected, this method can not correct errors on the ellipse. Further research should be conducted to examine the effects of ghost reflections. It appears the effect of ghost reflections should be included in the Jones model also if standard optical setups are used to measure with nanometer uncertainty.

System	setup	u_{meas}	u_{corr}	u_{eq}
Common path	BS 10° P 0°	5,3 nm	0,2 nm	0,2 nm
	BS 10° P 10°	1,4 nm	0,2 nm	0,1 nm
Basic setups	Linear optics	-	-	0,3 nm
	Flat mirror optics	-	-	0,2 nm
Probe calibration	normal	0,9 nm	0,9 nm	0,2 nm
	reduced ghost	1,3 nm	0,6 nm	0,1 nm
	increased ghost	1,6 nm	2,2 nm	3,6 nm
Traceable setup	PBS 10° P 0°	4,0 nm	0,5 nm	0,4 nm
	PBS 10° P 10°	2,2 nm	0,4 nm	0,3 nm

Table 5.2: The uncertainties of the different measurements with the compensation method. u_{eq} refers to the uncertainty derived with equation 5.10, u_{meas} u_{corr} refer to the uncertainty of the uncorrected and corrected measurement compared to the reference used in the measurement setup (micrometer screw, probe, Fabry-Pérot) BS: Babinet-Soleil compensator, P: polarizer, PBS: polarizing beam splitter.

In table 5.2 the different setups used to test the compensation method with lock-in amplifier are summarized with the uncertainties of the uncompensated and compensated measurements compared to the reference used in the measurement setup (σ_{meas} and σ_{corr}). Further the uncertainties derived from the amplitude variations of the quadrature signal are presented (σ_{eq}). From the comparison of the uncompensated and compensated uncertainties it can be concluded that the compensation method reduces the uncertainty due to periodic deviations, except for measurements where ghost reflections are present. From the comparison of the uncertainties from the corrected measurements (σ_{corr}) and derived from the amplitude variations (σ_{eq}) it may be concluded that with absence of ghost reflections equation (5.10) gives a good estimation of the remaining uncertainty.

Chapter 6

The refractive index of air

While fundamental limitations for small displacement measurements are in the photonic noise and periodic deviations in the interferometer, for large displacement measurements the limitation lies within the refractive index of the medium used. Since vacuum applications are costly and require special skills, determination of the refractive index of air with improved accuracy is recommended. Most commonly the revised equation of Edlén is used. This is an empirically derived formula which expresses the refractive index as a function of the wavelength of the light and of the temperature, pressure, humidity and carbon dioxide content of the air surrounding the interferometer system. Another method is to measure the refractive index of air directly with a measurement instrument called a refractometer. A refractometer derives the change in refractive index by measuring an optical path difference while the mechanical distance remains constant. If this measurement is done compared to a vacuum chamber this is an absolute measurement while otherwise it is a relative measurement.

In this chapter first the three empirically derived equations are presented along with their uncertainties. Later an absolute refractometer is discussed which has been in use for several years. In order to improve the measurement of the refractive index of air a relative measurement system (tracker) was developed to test the feasibility of such a system for absolute measurements. This tracker enables a relative refractive index of air measurement with improved uncertainty and will be described later in this chapter along with the uncertainty calculation. Further this tracker will be compared to the earlier described absolute refractometer and the mostly used revised equations of Edlén. Since there are three versions, which are in use in laboratories over the world a comparison will be made with all three empirical equations.

6.1 Empirical equations

As already mentioned in chapter 1, the displacement measured with an interferometer depends on the wavelength of the light used. The wavelength depends on the refractivity of the medium through which it passes according to the next relationship:

$$\lambda = \frac{\lambda_{vac}}{n} \quad (6.1)$$

where λ_{vac} is the wavelength in vacuum and n is the refractive index of the medium. Generally the vacuum wavelength is known from a frequency measurement and the vacuum velocity of light ($299792458 \text{ ms}^{-1}$). As already mentioned air is most frequently used as medium. The refractivity ($n-1$) of a dry gas, without any pollution depends on the dispersion K_λ and density of the gas $D_{T,p}$:

$$(n - 1)_{T,p} = K_\lambda * D_{T,p} \quad (6.2)$$

Edlén published the dispersion equation based on the work of other authors' investigations [11]. He also presented a derivation for the density factor based on the Lorentz-Lorentz equation and the gaseous equation of state [74]. Further corrections were presented for humidity and carbon dioxide content. As starting point he defined standard air, meaning dry air with a temperature of 15°C , a total pressure of 760 Torr (101,325 kPa) and 300 ppm carbon dioxide content. Since then the ITS-90 temperature scale was accepted [35] and new data were available for the density of air and the refractivity of water vapour. Birch and Downs [36, 12] updated the equation with use of these data and increased the carbon dioxide content of normal laboratory air to a constant of 450 ppm. Schellekens [39] investigated the influence of different kinds of gases and concluded the influence of carbon dioxide in most cases cannot be neglected. Later Ciddor [37] derived a formula intended for a broader range of wavelengths and extreme environmental conditions (-40°C to 100°C , 80 to 120 kPa and 0 to 100% relative humidity). Bönsch and Potulski [38] revised Edlén's equation again, however no improvement of the accuracy was gained compared to Birch and Downs [12] and the results showed an agreement between the values calculated by both formula's within the stated uncertainties. However Bönsch and Potulski reintroduced a correction factor for the carbon dioxide content (standard 400 ppm), which Birch and Downs omitted. The exact equations of Birch and Downs, Bönsch and Potulski and the equation of Ciddor can be found in appendix G. These days all three equations are used in laboratories around the world. All three equations have slightly different sensitivities for the air parameters. In table 6.1 the sensitivities are summarized.

In order to calculate the refractive index of air using the equations of Birch, Bönsch or Ciddor the four parameters have to be measured as accurate as possible. The measurement of temperature, pressure, humidity and carbon dioxide content will be discussed next.

	Birch (1994)	Bönsch (1998)	Ciddor (1996)	unit
$\frac{\partial n}{\partial T}$	$-9,296 \cdot 10^{-7}$	$-9,296 \cdot 10^{-7}$	$-9,285 \cdot 10^{-7}$	K^{-1}
$\frac{\partial n}{\partial p}$	$2,684 \cdot 10^{-9}$	$2,683 \cdot 10^{-9}$	$2,683 \cdot 10^{-9}$	Pa^{-1}
$\frac{\partial n}{\partial f_w}$	$-3,63 \cdot 10^{-10}$	$-3,706 \cdot 10^{-10}$	$-3,642 \cdot 10^{-10}$	Pa^{-1}
$\frac{\partial n}{\partial CO_2}$	0	$1,447 \cdot 10^{-10}$	$1,438 \cdot 10^{-10}$	ppm^{-1}

Table 6.1: Sensitivity of refractive index of air depending on a certain parameter, for standard conditions: $T=20^\circ C$, $p=101325 Pa$, $f=926,8 Pa$ (40% relative humidity), and $CO_2=450 ppm$. All three equations result in a refractive index of 1,00027146 for these standard conditions.

6.1.1 Parameter measurement

Since all empirical equations are based on the measurement of air parameters the uncertainty of this method depends on the measurement systems used to measure these air parameters. The daily variation of those parameters and their influence on the refractive index of air are summarized in table 6.2. From this table it may be concluded that for daily use in metrology laboratories the pressure measurement is most important, followed by temperature, humidity and carbon dioxide content.

Parameter	Increment	Effect n	TDV	Effect n
Temperature	1 °C	$-9,30 \cdot 10^{-7}$	0,1 °C	$-9,30 \cdot 10^{-8}$
Pressure	1 hPa	$2,68 \cdot 10^{-7}$	20 hPa	$5,36 \cdot 10^{-6}$
Humidity	1 hPa	$-3,7 \cdot 10^{-8}$	1 hPa	$-3,7 \cdot 10^{-8}$
CO ₂ content	100 ppm	$1,45 \cdot 10^{-8}$	100 ppm	$1,45 \cdot 10^{-8}$

Table 6.2: Effect of air temperature, pressure, humidity and carbon dioxide content on refractive index of air (according to Bönsch). Here TDV stands for typical daily variation.

Temperature

The temperature is measured using thermistors and a four wire bridge measurement to exclude the resistance of lead wires. Thermistors are chosen for their high sensitivity compared to resistance temperature detectors. For the choice of thermistors a number of factors are important as stability (to prevent the need of quick recalibration) and self heating. The thermistors are used to measure the temperature of air, which is a good insulator. Further the air will be nearly still as it will be measured in an isolation box. Hence self heating may become an important aspect. For self heating the important factors are:

- Resistance of the thermistor
- Current of the measurement device

- Dissipation constant
- Thermal constant

A large resistance reduces the influence of wire resistance, and reduces the necessary measurement current. The heat dissipated by the thermistor is calculated using the following equation:

$$P_{supply} = P_{lost} + P_{selfheating} \quad (6.3a)$$

$$I^2 R = \delta(T - T_{surrounding}) + \tau \delta \frac{dT}{dt} \quad (6.3b)$$

where P_{supply} is the power supplied to the thermistor by an electrical circuit, P_{lost} is the energy lost to the surroundings and $P_{selfheating}$ is the thermal energy absorbed by the thermistor. Further I is the measurement current, R the resistance of the thermistor, δ the dissipation constant of the thermistor in $\text{mW } ^\circ\text{C}^{-1}$, T the temperature of the thermistor, $T_{surrounding}$ the temperature of ambient air (in our laboratory $20 \pm 0,5 ^\circ\text{C}$) and τ the thermal time constant of the thermistor.

An epoxy coated disc NTC-thermistor was chosen [100] with a resistance of $5 \text{ k}\Omega$ at $25 ^\circ\text{C}$, a dissipation constant of $1 \text{ mW } ^\circ\text{C}^{-1}$ (as given by the manufacturer) and a thermal time constant of 10 s , both in still air. A commercial data acquisition unit was chosen [101] with a measurement current of $100 \text{ }\mu\text{A}$, lasting 1 ms each second. From calibration the resistance of the thermistor at $20 ^\circ\text{C}$ was found to be $6250 \text{ }\Omega$. Further measurements are taken each 60 s . Using these constants and solving equation 6.3b results in a self heating of $1,55 \cdot 10^{-8} ^\circ\text{C}$ after 60 seconds. After 20 hours this would result in a self heating of $1,86 \cdot 10^{-5} ^\circ\text{C}$, smaller than the resolution of the measurement system which is $8,5 \cdot 10^{-5} ^\circ\text{C}$.

The thermistors were calibrated against two calibrated platinum RTD resistors which have a traceable uncertainty of $0,01 ^\circ\text{C}$. Both thermistors and platinum resistors were placed on an aluminum beam of which the temperature is controlled by circulation of water through the aluminum beam using a refrigerated circulator with a stability of $0,01 ^\circ\text{C}$. The beam and thermistors are placed in an isolation box. In order to reduce the effect of gradients in the aluminum beam all sensors are placed close to each other. Further the thermistors are placed between the RTD sensors and a linear gradient is assumed for which is compensated. After a stabilization period of several hours, to cancel out the effect of different time-constants of RTD's and thermistors, the resistance of the thermistors is measured simultaneously with the resistance of the RTD. The temperature of the sensors is calculated using equation 6.4a for the RTD sensor of which the constants were determined through calibration at the Dutch national metrology institute (NMI) and the Steinhart-Hart equation 6.4b [75] for the thermistor of which the constants are determined through calibration against the RTD sensors.

$$T_{RTD} = A_R + B_R \cdot R_{RTD} + C_R \cdot R_{RTD}^2 + D_R \cdot R_{RTD}^3 + E_R \cdot R_{RTD}^4 \quad (6.4a)$$

$$\frac{1}{T} = A_T + B_T \cdot \ln(R_{therm}) + C_T \cdot \ln(R_{therm})^2 + D_T \cdot \ln(R_{therm})^3 \quad (6.4b)$$

After calibration the expanded uncertainty of the thermistors is 0,01 °C [76]. The resistance of the thermistors is read out by computer using GPIB protocol.

Pressure

During a refractive index measurement the pressure is measured using a calibrated commercial digital barometer [102], consisting of a resonator with thin quartz crystal: a Piezoelectric Force Transducer. The resolution of the system is 1 Pa, provided that it is read out through RS232. The calibrated uncertainty of the calibrated instrument is 6 Pa.

Humidity

For high accuracy humidity measurements most commonly a chilled mirror hygrometer is used. This technique involves illuminating a cooled surface with a light source and measuring the intensity of the reflected light. Condensation on the surface scatters the light which manifests as a change in reflectance.

Recently a new type of dewpoint hygrometer was introduced which works on the principle of Surface Acoustic Waves (SAW). SAW in this case integrates the cooled surface and detection mechanism in one element. The element consists of a transmitting and a receiving antenna photo lithographically patterned on a single crystal quartz chip. A radio frequency (RF) signal fed to the transmitting antenna converts to a mechanical wave. The mechanical wave propagates along the sensor surface to the receiving antenna, where the mechanical wave converts back to a RF signal. The schematic principle of this measurement system is shown in figure 6.1 [103].

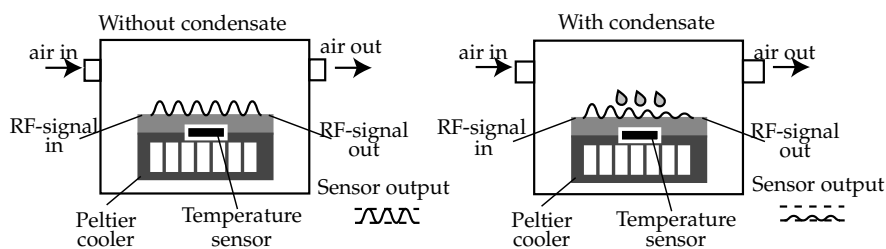


Figure 6.1: Schematic representation of the surface acoustic wave (SAW) Dew-point hygrometer setup.

The stated uncertainty by the manufacturer in the dewpoint measurement is 0,2 °C. The system was calibrated at the Dutch national metrology institute (NMI) where extensive tests were performed. Due to the construction of the calibration facility, the first calibration indicated some problems with the internal pump of the dewpoint hygrometer. The calibration facility inhibits also an internal pump to control the air flow. Neither of the pumps could be shut down and as a result at some dewpoints the measured values oscillated. In spite of

this problem the uncertainty of the calibration was 0,12 °C. Later the sensor had to be replaced as a result of a construction error in the system and also the pump was removed. The system was recalibrated and had an uncertainty of 0,1 °C. From this time an external pump was used to pump the air through the system.

The calculation of the dewpoint temperature into the partial water vapour pressure (f_w) is done using the density equation reported by Giacomo [77] (known as the BIPM 1981/91 density equation) and revised by Davis [78]:

$$f_w = 1\text{Pa} \times \exp\left(A_d * T_d^2 + B_d * T_d + C_d + \frac{D_d}{T_d}\right) \quad (6.5)$$

$$\text{where } A_d = 1,2378847 \cdot 10^{-5} \text{ K}^{-2} \quad (6.6)$$

$$B_d = -1,9121316 \cdot 10^{-2} \text{ K}^{-1} \quad (6.7)$$

$$C_d = 33,93711047 \quad (6.8)$$

$$D_d = -6,3431645 \cdot 10^3 \text{ K} \quad (6.9)$$

with T_d the dewpoint temperature in Kelvin. The uncertainty of the dewpoint measurement can be converted into the uncertainty of partial water vapour pressure which becomes 6 Pa. The dewpoint is read out by computer using RS232 protocol.

Carbon dioxide

The carbon dioxide level is monitored using a commercial infrared gas analyser [104]. The working principle is based on the absorption of infrared light with a wavelength of 4,26 μm by carbon dioxide molecules. The content of carbon dioxide in air is measured while pumping air through a sample cell. The intensity of light with this wavelength transmitted through a sample cell is measured and compared against the intensity of transmitted light through a reference cell. This reference cell is free of carbon dioxide by the use of soda-lime granules. The system is calibrated against a CO_2 analyser of the Dutch national metrology institute (NMI) and the expanded uncertainty is estimated to be 60 ppm. The system is read out using a Keithley multimeter which is connected to the computer through GPIB.

6.1.2 Uncertainty analysis of empirical equations

Previously the uncertainty of each measurement instrument used to measure the four parameters of air (temperature, pressure, humidity and Carbon dioxide content) was given. Together with the uncertainty of each equation itself, stated by the authors, these are used to determine the expanded uncertainty of each equation. This is done for the standard air conditions in our laboratory: $T=20^\circ\text{C}$, $P=101325 \text{ Pa}$, $f_w=926,8 \text{ Pa}$ (40% relative humidity) and 450 ppm carbon dioxide content. The combined uncertainty for the three empirical formulas is presented in tabel 6.3.

Parameter	SC	u	Birch (1994)	Bönsch (1998)	Ciddor (1996)
T	20°C	0,01	$9,296 \cdot 10^{-9}$	$9,296 \cdot 10^{-9}$	$9,285 \cdot 10^{-9}$
P	101325 Pa	6	$1,610 \cdot 10^{-8}$	$1,610 \cdot 10^{-8}$	$1,610 \cdot 10^{-8}$
f_w	926,8 Pa	6	$2,326 \cdot 10^{-9}$	$2,372 \cdot 10^{-9}$	$2,331 \cdot 10^{-9}$
CO ₂	450 ppm	60	0	$8,685 \cdot 10^{-9}$	$8,627 \cdot 10^{-9}$
Eq			$3 \cdot 10^{-8}$	$1 \cdot 10^{-8}$	$5 \cdot 10^{-8}$
Total (k=2)			$3,5 \cdot 10^{-8}$	$2,3 \cdot 10^{-8}$	$5,4 \cdot 10^{-8}$

Table 6.3: Uncertainty analysis of the three empirical equations used. Here u stands for expanded uncertainty, SC stands for standard conditions, T for Temperature, P for pressure, f_w for partial water vapour pressure and Eq represents the uncertainty of the revised equation stated by the authors.

6.2 The absolute refractometer

The absolute refractometer developed previously in the Precision Engineering group is an interference refractometer. Interference refractometers are based on the measurement of optical path length changes using Michelson type laser interferometers [39]. The optical path length depends on the mechanical path length along with the refractive index of the medium used through which is measured ($L_{op} = n \cdot L_{mech}$). Therefore the change in optical path length depends on changes in the refractive index and changes in the mechanical path length:

$$\Delta L_{op} = n \cdot \Delta L_{mech} + L_{mech} \cdot \Delta n \quad (6.10)$$

with ΔL_{op} the change in optical path length, n the refractive index of air, ΔL_{mech} the change in mechanical path length and Δn the change in refractive index. From this equation follows that if the mechanical length is kept constant the first term reduces to zero. Then the refractive index change can be calculated when the mechanical length is known. By measurement against a reference optical path in vacuum the absolute refractive index of air can be measured:

$$\Delta L_{op} = L_{mech} \cdot (n - 1) \quad (6.11)$$

The principle of the used refractometer is presented in figure 6.2. Light emitted from a commercial laser head is split by a polarizing beam splitter into a reference and measurement beam (see also chapter 1). The measurement beam passes through the measuring channel (solid lines in figure 6.2). The reference beam passes through the reference channel (dashed lines in figure 6.2). Finally both beams emerge from the polarizing beam splitter and are mixed by the polarizer inside the detector, which measures the phase of the interference signal.

At the start of a measurement both reference and measurement channels are evacuated down to 3 Pa using a vacuum pump. The interferometer is reset to zero and next air is flown slowly into the measuring channel. After the

measuring channel is at environmental pressure, air is pumped through the measurement chamber constantly with a smooth flow of $0,6 \text{ l min}^{-1}$ enabling the constant measurement of the environmental refractive index.

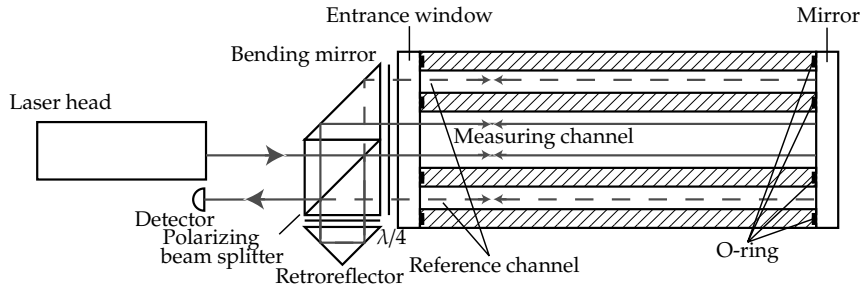


Figure 6.2: Schematic representation of the refractometer setup.

From equation 6.11 it can be seen that the mechanical length of the refractometer has to be known to calculate the refractive index of air. This length was measured using a Coordinate Measuring Machine with an uncertainty of $u = (2 \pm 2,86 \cdot 10^{-6} \cdot L) \text{ } \mu\text{m}$ (with L the length of the measured object in m). The uncertainty of the measurement of the block ($L \approx 400 \text{ mm}$) is therefore $3,1 \text{ } \mu\text{m}$. During calibration temperature corrections were applied which adds an uncertainty in length of $0,1 \text{ } \mu\text{m}$. To prevent gradients the refractometer block is built from aluminum. Further, from equation 6.10 it can be seen that the slightest change of mechanical length during measurement influences the measurement of the refractive index directly. Therefore the temperature of the block is monitored during measurement and the mechanical path length is corrected for linear expansion of the block at each measurement point.

To create a sufficient vacuum (3 Pa) the block is sealed with rubber O-rings between the block and the entrance window and between the block and the mirror surface. During the creation of the vacuum a difference in pressure between environment and block channels occurs, influencing the mechanical path length inside the refractometer. This effect was measured also using the coordinate measuring machine. This was done placing the block refractometer on the coordinate measuring machine and acclimatize it for 1 day. Then the length was measured in three different stages: Fully evacuated, partially evacuated (measurement channel filled with air and reference channel evacuated) and filled with air. This measurement was repeated 6 times and the averaged length change between vacuum and partially filled with air was $(0,58 \pm 0,07) \text{ } \mu\text{m}$. The resulting deviation in the determination of the refractive index in air that follows from this increase of effective length during filling was calculated to be $4,2 \cdot 10^{-10}$.

6.2.1 Uncertainty analysis of the absolute refractometer

As explained in chapter 1 the optical displacement measured by the laser interferometer is:

$$\Delta L = \Delta(nL_{mech}) = \frac{\Delta\phi\lambda_v}{4\pi} \quad (6.12)$$

In practice the electronics of the interferometer measure a number of digitized pulses and interpolate. As a result the formula can be written as:

$$\Delta L = \Delta(nL_{mech}) = \frac{k\lambda_v}{2R} \quad (6.13)$$

where k is the number of measured counts, R is the resolution (64) of the electronics board and the measurement is divided by a factor 2 since flat mirror optics are used. For a changing refractive index this results in:

$$\Delta n = n_{air} - n_{vac} = n - 1 = \frac{k\lambda_v}{2RL_{mech}} \quad (6.14)$$

From this equation it can be seen that the uncertainty of the refractive index of air measurement depends on the quality of the vacuum in the reference chamber, the uncertainty of the interferometer electronics, the vacuum wavelength of the interferometer and the mechanical path length of the block:

$$u(n - 1) = \sqrt{\sum_i \left(\frac{\partial(\Delta n)}{\partial i} \right)^2 u^2(i)}, \quad i = k, \lambda_v, L_{mech} \quad (6.15)$$

The resolution of the laser interferometer system used is 5 nm ($k/2R$), as a result the periodic deviations will be below the resolution. With a block length of 400 mm this results in a resolution of $1,23 \cdot 10^{-8}$ in refractive index. Cuijpers [79] estimated the uncertainty in counts due to drift, rest pressure in the reference channel and temperature changes in the glass window of the refractometer to be 2,4 counts. With a resolution R of 64 this results in an uncertainty of $2,97 \cdot 10^{-8}$ in refractive index.

The wavelength stability of the laser is $2 \cdot 10^{-8}$, on a wavelength of 632,991 nm this results in an uncertainty of $1,27 \cdot 10^{-14}$. This in turn results in an uncertainty of refractive index of $5,7 \cdot 10^{-12}$.

The mechanical path length of the block was measured using a coordinate measuring machine with an uncertainty of 3,1 μ m. The length during measurement is influenced by mechanical expansion due to the forces applied on the mirrors when applying a vacuum in the chambers and by thermal expansion of the system. As already mentioned the effect of the forces is limited to an effect of $4,2 \cdot 10^{-10}$ in refractive index. The thermal expansion is compensated for using a thermistor measuring the temperature of the aluminum block, assuming a homogeneous temperature. This thermistor was calibrated using the same procedure as for the thermistors used for measurement of the air temperature

for the empirical equations and had an uncertainty of 0,01 °C. The change in mechanical length due to thermal expansion is calculated as follows:

$$L_{mech} = L_{20}(1 + \alpha(T - 20)) \quad (6.16)$$

where L_{20} is the mechanical length at 20 °C, and α is the expansion coefficient of the material. The uncertainty in thermal expansion is calculated as follows:

$$u(L_{mech}) = \sqrt{\left(\frac{\partial L_{mech}}{\partial L_{20}}\right)^2 u^2(L_{20}) + \left(\frac{\partial L_{mech}}{\partial T}\right)^2 u^2(T)} \quad (6.17a)$$

From this it follows that the uncertainty in compensation of thermal expansion is 92 nm. So the uncertainty in expansion compensation and length change as a result of pressure variations is magnitudes smaller than the uncertainty with which the length is determined. The uncertainty of the effective block length is 3,1 μm , resulting in an uncertainty in refractive index of $2,17 \cdot 10^{-9}$. The total expanded uncertainty of the absolute refractometer can now be calculated. The result is shown in table 6.4.

Parameter	Nominal value	Uncertainty	Uncertainty in n-1
Counts	23000	2,4	$2,97 \cdot 10^{-8}$
Vacuum wavelength	632,991 nm	$1,27 \cdot 10^{-14}$	$5,7 \cdot 10^{-12}$
Block length	0,400197 m	$3,2 \cdot 10^{-6}$	$2,27 \cdot 10^{-9}$
Total (k=2)			$2,98 \cdot 10^{-8}$

Table 6.4: Uncertainty of the block refractometer.

6.3 Tracker with improved uncertainty

The empirical equations are all based on the measurement of the refractive index of air. Currently more applications of interferometers are running on different surroundings. In order to measure the refractive index of the medium in these systems a refractometer as described in the previous section can be used. In this section a different kind of interferometer will be discussed of which the theoretical uncertainty is smaller than the uncertainty of the refractometer mentioned.

In chapter 4 a calibration setup was described enabling the measurement of the optical path change in a cavity by means of frequency measurement:

$$\frac{\Delta f}{f} = \frac{\Delta L}{L} = \frac{\Delta L_{mech}}{L_{mech}} + \frac{\Delta n}{n} \quad (6.18)$$

As already mentioned the optical path is the product of mechanical path length and refractive index of the medium inside the cavity: $L = n \cdot L_{mech}$. In the setup described in chapter 4 a vacuum tube was placed to exclude the refractive index

of air and to measure a mechanical length change. If now the mechanical length is kept constant the refractive index change can be measured as a frequency change:

$$\frac{\Delta n}{n} = \frac{\Delta f}{f} \quad (L_{mech} = \text{constant}) \quad (6.19)$$

For this simplification the mechanical path length must be constant during measurement. The mechanical path length is influenced by forces on the cavity along with the thermal expansion of the cavity. In order to reduce the thermal expansion a spacer was designed made of a material with a low expansion coefficient. For this Zerodur was chosen, which is an amorphous material exhibiting length change in time. An aged block was used of 10 years old so that the slow length shrinking effect usually continuing over years is expected to play a minor role [80].

The distance holder is a monolith made out of zerodur. The end faces are parallel within 3,9 μrad , measured with the coordinate measuring machine. The orientation of the cavity is chosen vertical, so the symmetry axis of the thermal pattern and the mechanical construction will coincide, resulting in better thermal behavior. A length of 130 mm was chosen to enable the use with the current beat frequency measurement system. To attach the mirrors of the cavity on the zerodur a mirror holder was designed. Since the length of the cavity should remain stable during measurements of several hours it was chosen to clamp the mirrors directly onto the zerodur. The mirror is placed in the holder and pressed directly against the zerodur by pretensioning with a rubber O-ring in vertical direction. In horizontal direction the mirror is unconstrained. The zerodur rod is placed kinematically on a tilt adjustment plate which can be aligned around two horizontal axes to provide the correct alignment of the cavity around the beam. The design is shown in figure 6.3(a).

The mirrors are clamped to the zerodur and therefore can not be adjusted in angle. To enable a standing wave inside the cavity a flat-concave mirror configuration was chosen. Mirrors available from earlier experiments were used ($R=99,8\%$, radius 500 mm and $R=99,8\%$, radius ∞). To match the diode-laser to the cavity a mode matching lens was used. The stabilization scheme of the diode laser onto the cavity equals the scheme of the Fabry-Pérot as shown in figure 4.1. Frequency modulated light of the diode laser enters the cavity through the bottom. The light transmitted by the cavity falls onto a detector of which the signal is analysed by a digital lock-in amplifier that uses the first harmonic to create an error signal to stabilize the diode laser. The frequency of the diode laser is beated against an iodine stabilized HeNe-laser and measured using a frequency counter.

6.3.1 Uncertainty analysis of the tracker

The measured refractive index change (Δn) follows from the next equation:

$$\Delta n = n \left(\frac{\Delta L_{mech}}{L_{mech}} - \frac{\Delta f}{f} \right) \quad (6.20)$$

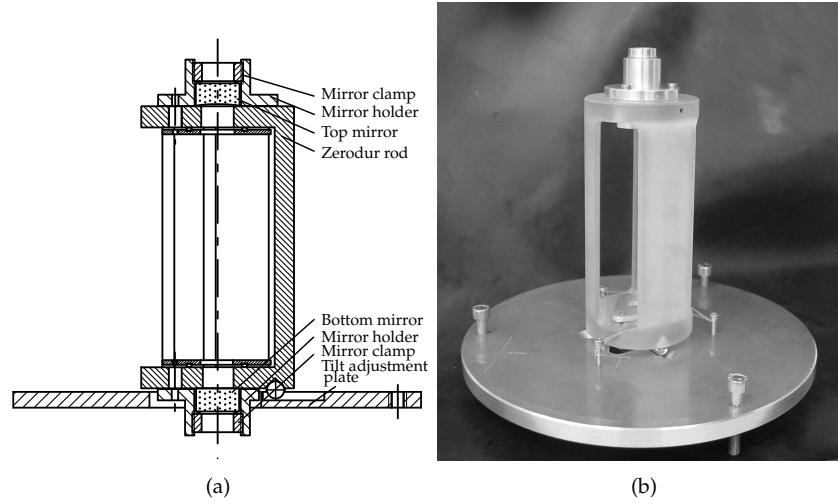


Figure 6.3: Design and photograph of the Fabry P rot tracker.

The uncertainty of the measured refractive index change can be calculated using:

$$u(\Delta n) = \sqrt{\sum_i \left(\frac{\partial(\Delta n)}{\partial i} \right)^2 u^2(i)}, \quad i = n, L, f, \Delta L, \Delta f \quad (6.21)$$

The uncertainty in the refractive index equals the uncertainty of the empirical equations ($\approx 5 \cdot 10^{-8}$). The absolute frequency uncertainty is the uncertainty in the frequency of the iodine stabilized HeNe-laser (12 kHz). The beat frequency can be measured with an uncertainty of 50 kHz. The cavity length is determined using a coordinate measuring machine with uncertainty $2,4 \mu\text{m}$ for a length of 131 mm. The length variations of the cavity during measurement depend on the thermal expansion of the Zerodur and confocal mirror and thermal gradients in the cavity. The uncertainty derived from this is $1 \cdot 10^{-10}$. For more information about the uncertainty analysis see Palmen [76]. The total uncertainty of a relative measurement with the Fabry-P rot tracker is summarized in the table 6.5.

6.3.2 Frequency measurement

During measurements it became clear that the beat frequency which can be measured continuously with the frequency counter is 1000 MHz. While the free spectral range of the tracker was 1150 MHz. With use of a spectrum analyzer a larger beat frequency could be measured enabling the tracking of the system over several modes. However the resolution of the spectrum analyzer was limited to 5 MHz resulting in a resolution of the tracker of $1 \cdot 10^{-8}$. This is

Parameter	Nominal value	Relative uncertainty	Uncertainty in Δn
n	1,000273	$5 \cdot 10^{-8}$	$1 \cdot 10^{-22}$
f	473,6 THz	$12 \cdot 10^3$ Hz	$1 \cdot 10^{-16}$
L	131,197 mm	$2,4 \cdot 10^{-6}$ m	$1 \cdot 10^{-10}$
Δf	240 MHz	$50 \cdot 10^3$ Hz	$8 \cdot 10^{-10}$
ΔL	$2 \cdot 10^{-10}$ m	$1 \cdot 10^{-10}$ m	$3 \cdot 10^{-14}$
Total			$8 \cdot 10^{-10}$

Table 6.5: Expanded uncertainty of a relative measurement with the Fabry-Pérot tracker. n : absolute refractive index, f : frequency of the diode laser, L : length of the cavity, Δf the frequency change, ΔL mechanical length change of the cavity.

unacceptable for comparison measurements. Therefore the control loop was based on measurements with the spectrum analyzer while the comparison was carried out using the measurements of the frequency counter.

6.4 Comparison of refractometers

In order to compare the measurements of the three systems (empirical equations, absolute refractometer and tracker) the three systems were placed as closely together as possible. The schematic diagram is shown in figure 6.4. All three systems have to measure the same air in order to enable a comparison. Therefore the tracker is placed in an isolating box. Two holes are in the box to allow air flow and to allow the laser light to enter the tracker and exit towards the detector necessary for stabilization.

The air is pumped through a tube towards the absolute refractometer after which it exits to the laboratory space. In order to compare all three measurement systems the air parameters, necessary for the empirical relations, are measured inside the system. The temperature is measured inside the isolation box, to be compared with measurements of the tracker (T). Also the temperature inside the absolute refractometer is measured at the inlet and outlet (T_{r1} and T_{r3}). A fourth thermistor is used to measure the temperature of the aluminum refractometer block to compensate for linear expansion (T_{r2}). The pressure can only be measured at a single place, so a trade off should be made. Since the tracker system is the new system to be tested, the pressure is measured at the isolation box (P). The humidity and carbon dioxide content are measured at the end of the system because the pump is inside the carbon dioxide measurement system and the flow meter is inside the humidity measurement system. If flow is constricted it is reasonably to believe that the carbon dioxide content and humidity of the total system are constant. Where possible large diameter tubes are used and during measurement the valves in the circulation area are totally opened.

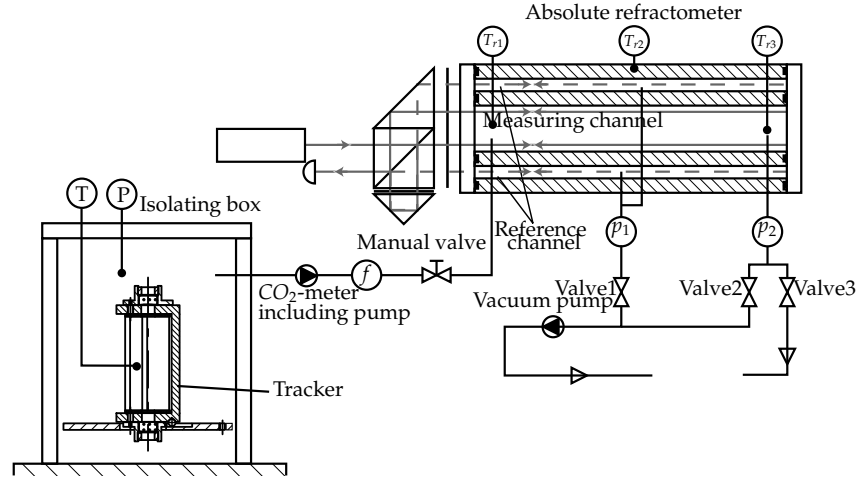


Figure 6.4: Schematic representation of the comparison setup. The measurement instruments for Edlén's comparison are schematically represented as T for temperature, p for pressure, f for humidity and CO_2 for carbon dioxide. The thermistors used to monitor temperature at the absolute refractometer are represented as T_{r1} and T_{r3} for air temperature and T_{r2} for the temperature of the aluminium block.

6.5 Measurement results

In this section some measurements conducted with the three measurement systems are presented and discussed. First the effect of pumping is investigated, followed by two comparison measurements over a time of 18 and 14 hours. Finally the measurement results are discussed in detail.

6.5.1 Absolute refractometer versus Empirical equations

Measuring the same air by three systems is not trivial. Pumping of air introduces pressure difference and therefore also refractive index differences. No pumping would imply that different samples of air are measured. Experiments conducted earlier by Schellekens [34, 39] showed the influence of pumping. Some new testing revealed that after initiating a measurement (filling the measurement path with air) an offset remained between the absolute refractometer and the three empirical formula (see K in figure 6.5). The offset was $2 \cdot 10^{-7}$ and had a repeatability of $1 \cdot 10^{-9}$ for five measurements. After applying a flow to the air the change of the airflow results in a changing offset (see L in figure 6.5). The pressure change in a cylindrical tube for a laminar flow ($\text{Re} < 2300$) can be

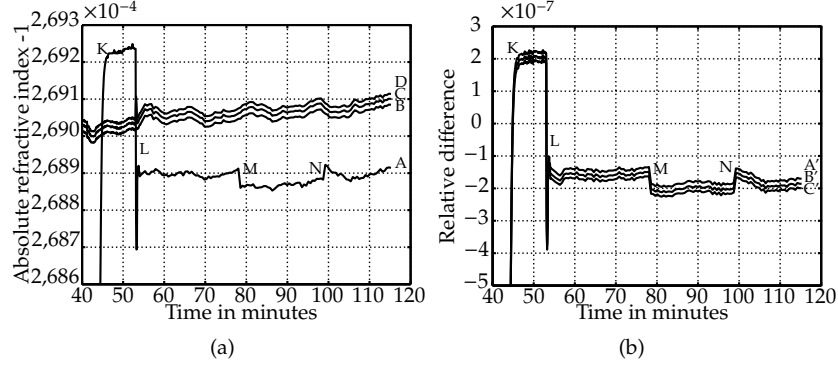


Figure 6.5: Absolute refractive index change as a result of changes in air flow. A: Absolute refractometer, B: Birch, C: Bönsch, D: Ciddor. A': Absolute refractometer-Birch, B': Absolute refractometer-Bönsch, C': Absolute refractometer-Ciddor. K: Initialization, L: Flow connected, M: Change of air flow, N: Change of air flow.

calculated using the Darcy-Weisbach equation [81]:

$$\Delta p = \lambda_d \frac{l}{d} \frac{1}{2} \rho \langle v \rangle^2 \quad (6.22)$$

$$\text{where } \lambda = \frac{64}{Re}$$

$$\text{and } Re = \frac{d \rho \langle v \rangle}{\eta_{air}} \quad (6.23)$$

here λ_d is the resistance factor, L is the length of the channel, d is the diameter of the channel, ρ is the air density ($1,29 \text{ kg m}^{-3}$), $\langle v \rangle$ is the average velocity, Re is the Reynoldsnumber and η_{air} is the dynamic viscosity of air ($17 \cdot 10^{-6} \text{ Pa s}$). The effect of introduced flow changes and offset changes in measurements was clearly visible (see M and N in figure 6.5). The air flow measured by the dewpoint meter was 0,68 slpm (standard liter per minute). Since the diameter of the measurement chamber of the dewpoint meter is unknown it was estimated that the diameter equals the inlet diameter (4 mm). The length of the tube between isolating box and absolute refractometer used also later in the comparison was 4 m with a diameter of 4 mm. The pressure drop resulting from this is 123 Pa resembling an offset in refractive index of $-3,3 \cdot 10^{-7}$. Combined with the offset of $2 \cdot 10^{-7}$ before the air flow was applied, this would result in an offset of $-1,3 \cdot 10^{-7}$, resembling the offset at point L in figure 6.5. The pressure changes at points M and N in figure 6.5 were calculated to be 14 Pa, resembling an offset in refractive index of $3 \cdot 10^{-8}$. This is smaller than the measured offset. However the offsets remaining are within the measurement uncertainties of both systems.

The same test was conducted using a tube of 1 m length. In this measurement the drop due to applying a flow of 0,69 slpm was $1,9 \cdot 10^{-7}$ resulting in an

eliminated offset. The calculated pressure drop is 31 Pa, resembling an offset in refractive index of $-8,3 \cdot 10^{-8}$. Together with the initiation offset of $2 \cdot 10^{-7}$ this results in a theoretical offset of $1,3 \cdot 10^{-7}$. From the measurements it can be concluded that the length and diameter of the tube are of influence on the offset. However the theoretically calculated pressure drop alone cannot explain the offset.

A second effect influencing the offset of the refractometer is correlation: if pressure changes occur, also temperature and humidity will change which also influence the refractive index. A better way to make a comparison would be to measure the pressure inside the measurement chamber of the absolute refractometer. For future comparisons of absolute refractive index this would be necessary. Further an external pump with more constant flow would improve the stability of measurements.

From the discussion above it may be concluded that the use of an absolute refractometer is always a trade off. If the refractive index should be measured with such a system a flow should be applied. However a flow introduces a changed refractive index. Therefore if a remote system should be used to measure absolute refractive index, for instance if no heat source can be applied to the system in which measurement should take place, the flow of air should be examined in more detail. To examine the uncertainty of the empirical functions relative measurements can be used to compare the system with a refractometer. If the uncertainty of the absolute determination of refractive index of air should be examined a refractometer without air flow is to be preferred. In this case we want to examine the feasibility of an absolute refractometer based on a Fabry-Pérot cavity, therefore first a relative measurement system based on the same principle; the tracker was examined. The results are shown and discussed in the next section. Since the tracker is a relative measurement system relative measurements of the empirical equations and absolute refractometer are compared also.

6.5.2 Refractive index measurements

The results presented here were derived from measurements with the spectrum analyzer. This results in larger noise figures, but enables continuous measurements. The standard deviations of the comparison were derived using the measurement results of the frequency counter with a limited range (225 MHz-1000 MHz).

Comparison measurement over 18 hours

First a comparison measurement over 18 hours is presented. The air parameter measurements are presented in figure 6.6. From this figure it can be seen that the change in temperature inside the isolation box is limited, while the pressure is changing. The resulting measurements of the absolute refractive index are shown in figure 6.7(a). In this figure the offset of the absolute refractometer becomes very clear. Further the trend of pressure change can be seen in the

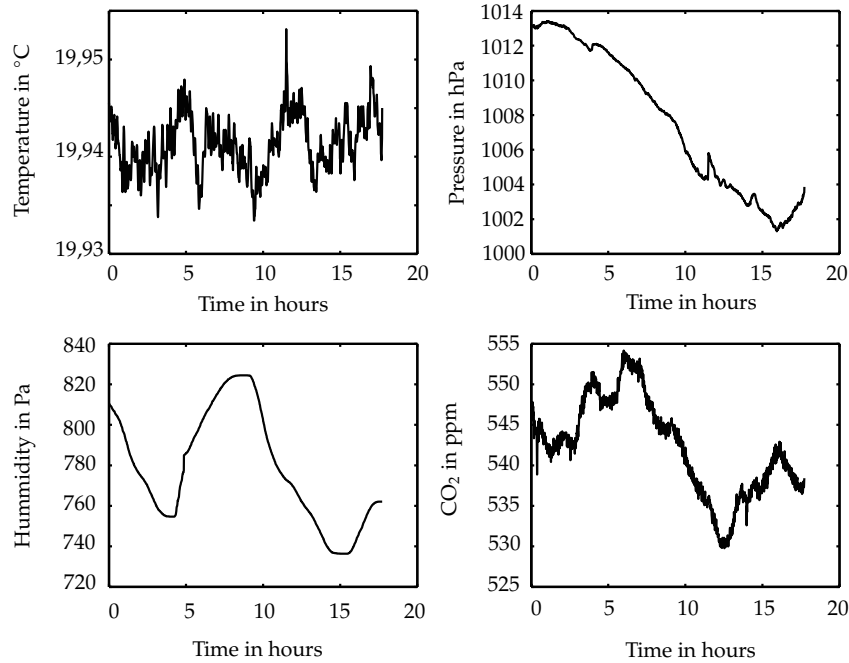


Figure 6.6: Air conditions during refractive index measurement (7-8 february).

refractive index variation. The tracker results are presented in this figure also, even though the tracker only measures relative changes. The mean value of the empirical equations of the first measurement was calculated and used to add as an offset to the tracker results. It can be seen in this figure that, apart from the offset of the absolute refractometer, the changes measured with all systems coincide very well. To enlarge the differences between all four measurement systems the relative measurements of the tracker were compared to the relative measurements with the empirical equations and the relative measurements of the absolute refractometer. In figure 6.7(b) the differences in measured relative refractive index change are depicted.

In this figure all three empirical equations and the tracker measurements coincide. The absolute refractometer differs slightly from these measurements. The mentioned comparison of tracker, absolute refractometer and empirical equations is carried out using the temperature measurement inside the isolation box. The mean values of the offsets and the standard deviations are presented in table 6.6.

In figure 6.8 the comparison of the absolute refractometer and empirical equations is made using temperatures measured inside the absolute refractometer (T_{r1} and T_{r3}). Here the relative measurements of the absolute refractometer and empirical equations do coincide (see figure 6.8(a)). From the comparison of figures 6.7(b) and 6.8(a) it can be seen that even the relative measurements of

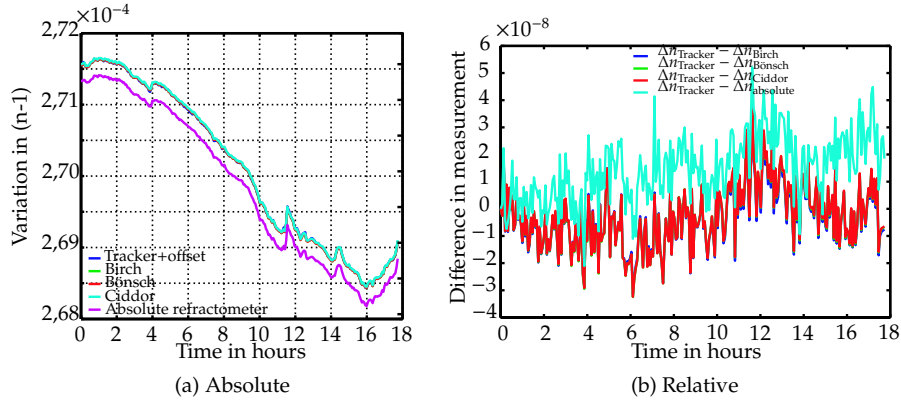


Figure 6.7: Refractive index variation (7-8 february 2004).

Comparison	Mean offset	standard deviation
Tracker-Birch	$-4,0 \cdot 10^{-9}$	$1,1 \cdot 10^{-8}$
Tracker-Bönsch	$-3,6 \cdot 10^{-9}$	$1,1 \cdot 10^{-8}$
Tracker-Ciddor	$-3,4 \cdot 10^{-9}$	$1,2 \cdot 10^{-8}$
Tracker-Absolute	$1,43 \cdot 10^{-8}$	$1,2 \cdot 10^{-8}$

Table 6.6: Mean offset and standard deviation of the relative measurements of all four systems (7-8 february).

the absolute refractometer differ from those measured by the empirical equations in the isolating box. In figure 6.8(b) the temperature measurements of the absolute refractometer are shown. In this figure it is clearly visible that the temperature change of the outlet is smooth compared to the temperature change in the inlet. This could be caused by some turbulence introduced when air enters the measurement chamber. Based on the comparison discussed before it is concluded that the air is also conditioned by the aluminum tubes used to connect the absolute refractometer with the manual valve. The offset in absolute refractive index expected from the temperature difference between air in the isolating box and in the refractometer ($-0,05^\circ$) is $5 \cdot 10^{-8}$. The calculated offset in refractive index, resulting from a pressure drop over a tube of 4 meters length and a diameter of 4 mm, is $3,3 \cdot 10^{-7}$ for an air flow of 0,68 slpm. From the measurements shown in figure 6.5 and discussed in section 6.5.1 it is known that without flow the refractive index offset is $2 \cdot 10^{-7}$, resulting in a refractive index offset of $-1,3 \cdot 10^{-7}$ with flow. With a refractive index offset of $5 \cdot 10^{-8}$ as a result of temperature difference between isolating box and absolute refractometer this would result in a refractive index offset of $-0,8 \cdot 10^{-7}$, while the measured refractive index offset is $-2,2 \cdot 10^{-7}$. This indicates that not only the pressure difference and temperature difference influence the offset. The noise in the difference of the relative measurements is partly caused by the resolution of the spectrum analyzer. Part of the noise also results from time differences in

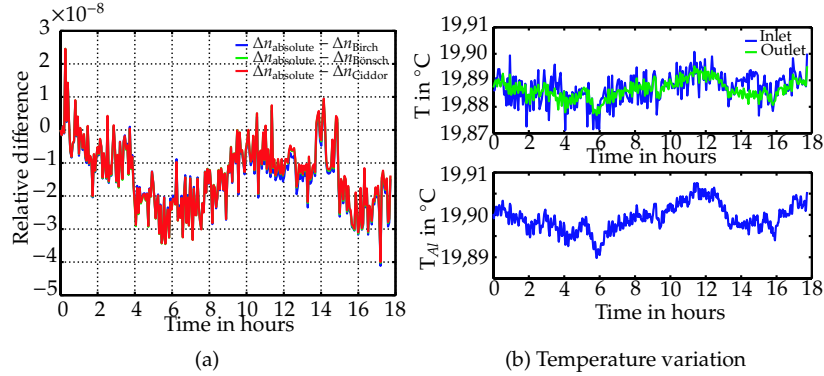


Figure 6.8: Difference in relative refractive index variation in absolute refractometer (7-8 february).

the measurements. Effort was made to read out all systems together as close as possible.

Comparison measurement over 14 hours

A second measurement was carried out over 14 hours of which the results will be discussed now. In figure 6.9 the air parameter measurements are shown. From these measurements it can be seen that pressure change is limited, and temperature change is larger compared to the measurement over 18 hours.

In figure 6.10(a) the measured absolute refractive index is presented. Due to the small changes in air parameters also the measured absolute refractive index change is limited during this measurement. Again the offset of the absolute refractometer compared to the other measurement systems is clearly visible. But also after 1 hour a difference between empirical equations and tracker becomes visible. Since the absolute refractive index can not be measured using the tracker the relative difference is presented in figure 6.10(b). Comparing this figure with the temperature measurement inside the isolation box (see figure 6.9) the trend is equal. However the cause of the difference in measurement between tracker and four other methods cannot be found from this figure. Comparing the measurement of the absolute refractometer with the tracker (to which the initial absolute refractive index is added) and empirical equations in figure 6.10(a) it can be seen that the temperature dip at 6,5 hours is clearly visible as a refractive index peak in the measurements of the absolute refractometer and empirical equations (region B in figure 6.10(a)). However the peak is absent in the tracker measurement. While in the first half hour the tracker registers a large variation compared to the absolute refractometer and empirical equations (region A in figure 6.10(a)).

In figure 6.11 the difference between the refractive index changes measured by the absolute refractometer and derived with the empirical equations are shown. In this figure the comparisons of the absolute refractometer with Börsch and Ciddor coincide, while the comparison of the absolute refractometer with

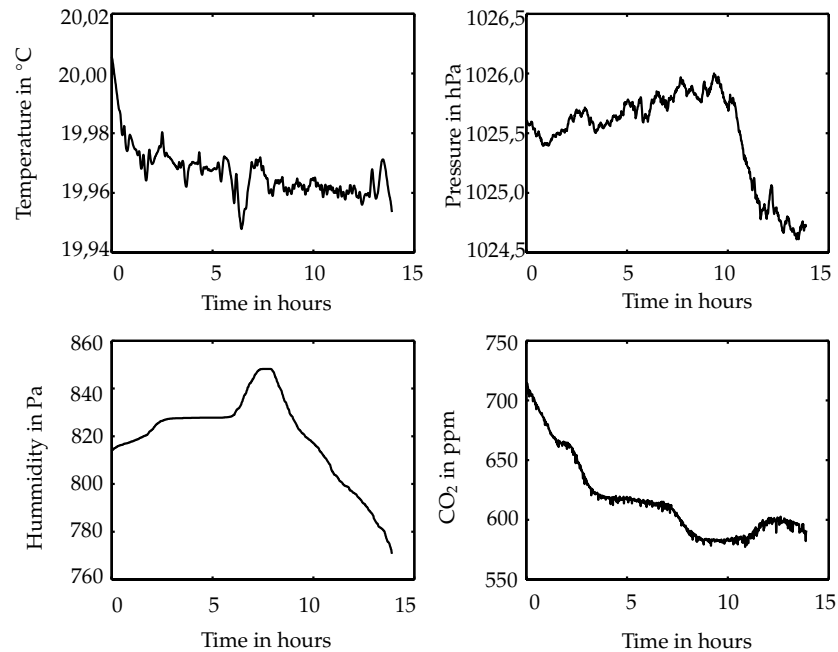


Figure 6.9: Air conditions during refractive index measurement (17-18 february).

the values of Birch are different, however closer to zero. From table 6.1 it follows that the major difference between these equations is the compensation for carbon dioxide which is not included by the equation of Birch. Further a small difference in the sensitivities for humidity exists. Examination of the difference between the comparison with Birch and the comparisons with Bönsch and Ciddor reveals exactly the shape of the carbon dioxide measurement. This indicates that the difference in humidity factor is negligible, and carbon dioxide compensation by Ciddor and Bönsch increases the difference.

In table 6.7 the mean offsets and standard deviations of this measurement are presented.

Comparison	Mean offset	standard deviation
Tracker-Birch	$-6,3 \cdot 10^{-8}$	$2,1 \cdot 10^{-8}$
Tracker-Bönsch	$-4,9 \cdot 10^{-8}$	$1,8 \cdot 10^{-8}$
Tracker-Ciddor	$-4,9 \cdot 10^{-8}$	$1,8 \cdot 10^{-8}$
Tracker-Absolute	$-4,2 \cdot 10^{-8}$	$2,1 \cdot 10^{-8}$

Table 6.7: Mean offset and standard deviation of the relative measurements of all four systems (17-18 february).

In figure 6.11(b) the temperature registration of the absolute refractometer

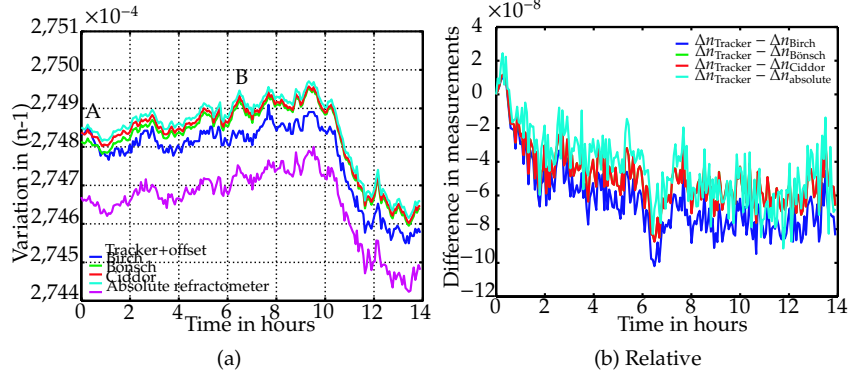


Figure 6.10: Refractive index variation (17-18 february). A and B are regions of special interest which are discussed in detail.

is presented. From this figure it can be seen that the temperature of the outlet is higher than the temperature of the inlet. Also here the outlet temperature is more smooth than the inlet temperature. Further the temperature of the aluminum block is higher than the temperature of the air. The averaged temperature difference of air inside the absolute refractometer compared with air in the isolation box is $0,01^\circ$, producing a refractive index offset of $1 \cdot 10^{-8}$. The refractive index offset resulting from the pressure drop due to the tube resistance as indicated before is $-1,3 \cdot 10^{-7}$, resulting in a total refractive index offset of $-1,2 \cdot 10^{-7}$ while the measured refractive index offset is $-1,6 \cdot 10^{-7}$.

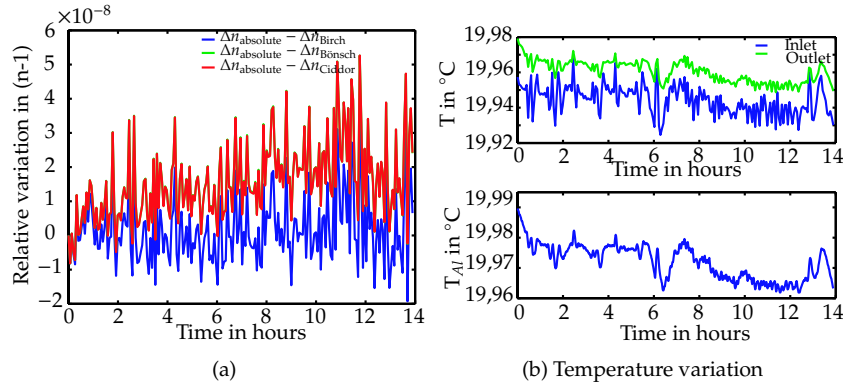


Figure 6.11: Relative refractive index variation in absolute refractometer (17-18 february).

6.5.3 Discussion

From the first comparison measurement it can be concluded that the tracker registers pressure changes accurately. In the second measurement the temper-

ature changes seem to have an extra effect on the tracker. This is also seen in the increased offset and standard deviation shown in tables 6.6 and 6.7. The same effect was found by Eickhoff and Hall [42]. They ascribe this to adsorption of water in the mirrors which were not dielectrically coated. However we use mirrors which are dielectrically coated, and the effect should therefore be minimized. Another possibility is that the effect is caused by relaxation of the Zerodur material after temperature changes of the surrounding. In order to investigate this, three temperature sensors were mounted on the Zerodur rod in different places, at the top, the middle and at the bottom. Even though the sensors were shielded from the air and effort was made to minimize influence of air temperature on the lead wires (as described by Ruijl [3]) the influence of the environment remained visible in the temperature measurements. Further the exact expansion coefficient was unknown. To improve measurements it would therefore be wise to conduct some measurements on the expansion coefficient and time constant of the Zerodur used. Further the temperature measurement of Zerodur should be improved. This could be done by drilling a hole in the Zerodur and inserting the temperature sensors in the hole, using thermally conductive paste.

It was tried to explain the offset of the absolute refractometer and the empirical equations by a temperature difference and a pressure difference due to the tubes used to connect the measurement chamber of the empirical equations and the absolute refractometer. The results are summarized in table 6.8. From

	7-8 Feb	17-18 Feb	4 m tube	1 m tube
Offset without flow	$2 \cdot 10^{-7}$	$2 \cdot 10^{-7}$	$2 \cdot 10^{-7}$	$2 \cdot 10^{-7}$
Calculated (T)	$5 \cdot 10^{-8}$	$1 \cdot 10^{-8}$	0	0
Calculated (P)	$-3,3 \cdot 10^{-7}$	$-3,3 \cdot 10^{-7}$	$-3,3 \cdot 10^{-7}$	$-8,3 \cdot 10^{-8}$
Total calculated	$-0,8 \cdot 10^{-7}$	$-1,2 \cdot 10^{-7}$	$-1,3 \cdot 10^{-7}$	$1,2 \cdot 10^{-7}$
Measurement	$-2,2 \cdot 10^{-7}$	$-1,6 \cdot 10^{-7}$	$-1,6 \cdot 10^{-7}$	$2 \cdot 10^{-8}$

Table 6.8: Calculated and measured offset of absolute refractometer and empirical equations due to tubes used. In the measurement with the 4 m tube and the 1 m tube the temperature was measured inside the absolute refractometer and no offset was present.

this table it can be seen that the measurements with different tube lengths (4 m tube and 1 m tube) indicate a dependency of the offset on pressure drop. From the Darcy-Weisbach equation 6.22 it is known that the calculated offset depends to the fourth order on the tube diameter. Unfortunately with this setup it was not possible to test the difference in tube diameter and a tube diameter of 4 mm was used. From the 4 m tube comparison together with the comparison of 17-18 February the calculation is in reasonable agreement with the measurements. Especially when taking into account that the measurement consists of the difference between the refractometer measurement with an uncertainty of $3 \cdot 10^{-8}$ and the empirical equation measurement with an uncertainty of $3,6 \cdot 10^{-8}$. However the comparisons of the calculated and measured offsets of the "1 m

tube" and of "7-8 February" measurements indicate a very large difference. Therefore it is concluded that the offset depends partially on a pressure drop due to friction in the tubes used, and the temperature offsets. If the use of an absolute refractometer is desired it is best used at the place of interest. If this is not possible and tubes have to be used, preferably large diameter tubes should be used and additional research is necessary to understand the influence of a flow in these kind of measurements exactly.

6.6 Conclusions

In this chapter three measurement setups were discussed and compared. One setup was based on empirical relations together with measurements of the four important parameters of air (temperature, pressure, humidity and CO₂ content). Another setup was based on the absolute refractive index of air measurement using a commercial heterodyne interferometer. Finally a new system was developed to measure the changes of refractive index with an improved uncertainty. A comparison, made between all three most used empirical equations with the absolute refractometer, revealed the influence of an air flow in the system. As a result the refractive index of air measured with such an absolute system will always have an offset compared to the air to be measured in a stable system. The offset can be tuned using the empirical equations, however no improved measurements of absolute refractive index will result from this. The advantage of such an absolute refractometer system is that it will measure changes of refractive index also if a medium different than air is used.

Theoretically a system based on a Fabry-Pérot cavity would result in a smaller measurement uncertainty and improved resolution. Such a system was developed for relative measurements where an uncertainty of $8 \cdot 10^{-10}$ was calculated. Since no other system is available with such a small uncertainty it could only be compared to the previously mentioned systems. This revealed some unexpected measurements resulting from temperature changes which cannot be explained yet. However the expectation is that such a system, when adapted for absolute measurements, would improve the absolute measurement of the refractive index.

Some extra research is recommended to improve understanding of refractometry. First the effect of a flow on the measured refractive index with the absolute refractometer should be examined in more detail. From measurements conducted on the absolute refractometer and the empirical equations with different tube length clearly the influence of the tube was found. A tube of 1 meter length reduced the offset between absolute refractometer and empirical equations, however from theory of temperature difference and pressure drop this could not be calculated. Since an absolute refractometer enables the measurement of influences of other gases than carbon dioxide it is unwanted to tune an absolute refractometer to the offset of the empirical equations. Therefore it is recommended to study the influence of flow on refractive index measurement separately. Further the effect of temperature changes on a zerodur cavity

should be examined in detail. Also the measurement of temperature of zero-dur material should be investigated in more detail to enable a compensation of thermal expansion.

Chapter 7

Conclusions and recommendations

Displacement laser interferometers are used widely as precision displacement measuring systems. Most interferometer systems use polarizing optics and as a result of alignment errors of the optics and polarization errors in the optics polarization mixing will occur. Polarization mixing will result in contrast errors when homodyne interferometers are used, or frequency mixing when heterodyne interferometers are used. Both result in periodic deviations in the measurement. In industrial environments this can lead to production errors in the case of new generation wafer scanners or to positioning errors in systems which use interferometers in their control loop. In this thesis the origin of periodic deviations was investigated in more detail in order to bring the accuracy of laser interferometer systems to the (sub-)nanometer level. Due to the high costs of vacuum technique mostly air is preferred as the medium through which the light is transported. In order to improve the accuracy of laser interferometer systems working in air the refractive index of air has to be measured with an uncertainty less than $2 \cdot 10^{-8}$. Therefore in this thesis also the measurement of the refractive index of air was investigated and systems for accuracy improvements were developed.

7.1 Periodic deviations

In order to investigate the effect of periodic deviations two models were developed. First an analytical model was made enabling the prediction of periodic deviations resulting from alignment errors and polarization errors of the light emitted by the laser head. This model was compared to literature where partial error sources were investigated and modeled. From this model it followed that interaction of periodic deviations exists and a simplification of the system by means of superposition is not allowed.

The number of different optical configurations used with interferometers is

enormous. Since the derivation of an analytical equation is time consuming a Jones model was presented also. The Jones model enables the prediction of periodic deviations resulting from a combination of sources in a heterodyne interferometer. The advantage is that this model is modular, therefore it enables a quick change of optical setup. Further it enables the input of Jones matrices representing the polarization properties of the optics used in the interferometer.

With use of the Jones model it was shown that interaction of periodic deviations exists and therefore the superposition principle does not hold: all possible causes of periodic deviations should be considered at once to enable an accurate prediction of the periodic deviations present in the interferometer.

Further the effect of contra-rotating ellipticity compared to equal rotating ellipticity of light emerging from the laser head was shown with use of the Jones model. From this it was concluded that a contra-rotating ellipticity exhibits an inherent compensation of periodic deviations.

In order to enable the incorporation of polarization properties of components used in interferometers, different measurement setups were discussed to measure such properties for heterodyne interferometers. In order to measure the polarization properties of the laser head two new methods were discussed to measure non-orthogonality and ellipticity of a heterodyne laser head. Both methods were compared to each other. From measurements it was appeared that the ellipticity varied over time and was different for different laser heads. However since the ellipticity proved to be contra-rotating the effect remained below 0,02 nm for all three laser heads measured. From the measurements it was also concluded that the non-orthogonality could be determined with an uncertainty of 0,05°. These measurements in combination with the Jones model revealed that the influence of the non-orthogonality on periodic deviations was significant within the nanometer region.

To measure the polarization properties of optical components null ellipsometry was used. A drawback of the method is that only optics with defined main optical axis can be measured. So a combination of interferometer optics, like a polarizing beam splitter in combination with a quarter wave plate can not be usefully measured with null ellipsometry. From measurements with this method the quality difference between old and new optics could clearly be distinguished.

From the measurements in combination with the Jones model it was concluded that a misalignment of non-ideal interferometer optics can reduce the periodic deviations present in the system.

With use of the measurements of polarization properties of optics and laser head in combination with the Jones model the periodic deviations resulting in a complete laser interferometer can now be predicted. To examine the correctness of the predicted periodic deviations, for two different systems they were compared to a measurement with a traceable measurement system based on a Fabry-Pérot cavity. The calculated uncertainty of this system was 0,89 nm over a range of 1 μm , and 0,94 nm over the maximum range of 300 μm , mainly due to temperature effects. The standard deviations of the measurements compared to the predictions of the model were below 0,14 nm for small periodic devia-

tions and 0,3 nm for large periodic deviations. From this it can be concluded that the model predicts the periodic deviations rather well. Therefore it is concluded that the Jones model in combination with the measurement results of the polarization property measurements is a practical tool for designers of interferometer systems and optical components. This tool enables the designer to choose right components and alignment tolerances for a practical setup with certain specifications about periodic deviations.

The uncertainty of the traceable calibration system is rather large compared to the amplitude of the periodic deviations measured with the system. In order to reduce the uncertainty of the calibration system a new system was designed and built. The calculated uncertainty of this system is 0,26 nm over a range of 1 μm , and 0,40 nm over the maximum range of 6 μm . Drift measurements showed an improvement of the system compared to the earlier developed system.

Sometimes in applications no new components can be used, or from cost perspective it is undesired to spend more effort on alignment. In these cases it is more efficient to compensate the periodic deviations of the system. In this thesis one compensation method based on two measurement receivers mentioned earlier in literature was tested. This compensation method appeared only to work with heterodyne interferometers which emit equal rotating elliptical polarized light.

In homodyne interferometry the Heydemann compensation is frequently used to compensate for periodic deviations. Therefore a new method was tested based on phase sensitive detection of a heterodyne interferometer in combination with the Heydemann algorithm. It was tested on several setups, of which one was the traceable calibration setup. In setups where only minor ghost reflections were present, or absent at all, the method could compensate periodic deviations with an uncertainty of 5,3 nm to a measurement signal with a standard deviation of 0,2 nm. This clearly indicates the potential of this compensation method. Due to the current electronics the compensation can be done only in a quasi-static environment.

7.2 Refractive index of air

For large displacements in air the periodic errors become overshadowed by the effect of refractive index. In this thesis three methods of measuring the refractive index of air were compared. One method was based on the measurement of air temperature, pressure, humidity and carbon dioxide content in combination with empirically derived equations as presented in literature. The second method was based on a refractometer in combination with a commercial laser interferometer. From comparison between these systems the influence of air flow became visible. It was concluded that in systems where refractometry was necessary, the refractive index should be determined at the same location as where interferometric measurements are taken. The third method to measure the refractive index of air was to measure with a Fabry-Pérot cavity the

change of optical path length while keeping the mechanical path length constant. Such a system was designed and built in the form of a relative refractive index measurement system. Changes of refractive index can be measured with a calculated uncertainty of $8 \cdot 10^{-10}$. From comparisons with this system it was concluded that the realization of an absolute refractometer based on this principle can improve measurement uncertainty.

7.3 Recommendations

Based on the measurements and analysis described in this thesis also some recommendations can be made. From the measurements conducted on the polarization of light emitted by commercial laser heads it appears that the ellipticity changes in time. Three systems were measured which indicated a large difference in ellipticity and non-orthogonality for these lasers. Further measurements are recommended to investigate the upper and lower limits of ellipticity and non-orthogonality in commercial lasers.

Further the newly developed Fabry-Pérot cavity should be tested more extensively. In order to do this a beat frequency detector with a range of 8 GHz should be bought. Further it would be interesting to investigate and imply the Pound-Drever-Hall technique to reduce measurement uncertainty even further.

Based on the analysis of the phase quadrature compensation method and the resulting potential of the method it is recommended that the method should be developed further to enable a real-time compensation in the system.

From measurements with the compensation method on a probe calibration setup, based on a flat mirror interferometer, it appeared that periodic deviations resulting from ghost reflections could not be compensated. This could be explained if ghost reflections manifest themselves as a non-uniform distribution on the $S_0 - S_{90}$ circle. It is recommended to investigate the influence of ghost reflections further. Of course ghost reflections should be avoided as much as possible in high-accuracy measurements, for example by the use of anti-reflection coatings. However some optical setups inhibit ghost reflections as a result of the use of plate optics resulting in small extra cavities in the optical configuration. Therefore it is recommended to include the existence of ghost reflections into the Jones model also.

Regarding the refractive index of air, the influence of air flow effects on the refractive index should be investigated in more detail. In the case a refractometer should be used to measure the effect of the environmental refractive index a gas flow is unavoidable. In order to compensate the effect correctly it must be known in great detail.

Also regarding the refractive index of air the influence of temperature changes on the Zerodur cavity should be investigated in more detail. Therefore the measurement uncertainty of the material temperature of Zerodur should be improved. From the measurements it appeared that there was some relaxation effect of the Zerodur. Since a diode laser is used nowadays, this could be investigated with a smaller cavity of the same design. For the large cavity

the expansion coefficient of the Zerodur cavity should be measured to improve measurement uncertainty. Finally to enable an absolute measurement of refractive index with improved uncertainty the cavity should be changed into an absolute refractive index measurement setup. This can be done by placing the tracker in a vacuum, or by moving in a vacuum tube during measurement.

Bibliography

- [1] I. Misumi, S. Gonda, T. Kurosawa, and K. Takamasu. Uncertainty in pitch measurements of one-dimensional grating standards using a nanometrological atomic force microscope. *Measurement Science and Technology*, (14):463–471, 2003.
- [2] K. Dirscherl and K.R. Koops. Developments on the NMi-VSL traceable scanning probe microscope. In *Proceedings of SPIE*, volume 5190 (Recent developments in traceable dimensional measurements II), pages 173–177, 2003. ISSN 0277-786X, ISBN 0-8194-5063-4.
- [3] T. Ruijl. *Ultra Precision Coordinate Measuring Machine; Design, Calibration and Error Compensation*. PhD thesis, TUD, May 2001.
- [4] The international roadmap for semiconductors 2003 edition metrology. <http://public.itrs.net>, December 2003.
- [5] P.L.M. Heydemann. Determination and correction of quadrature fringe measurement errors in interferometers. *Applied optics*, 20(19):3382–3384, October 1981.
- [6] E. Abbe. Meß apparate für physiker. *Zeitschrift für instrumentenkunde*, 10:446–448, 1890.
- [7] F.C. Demarest. High-resolution, high-speed, low data age uncertainty, heterodyne displacement measuring interferometer electronics. *Meas. Sci. Technol.*, 9:1024–1030, 1998.
- [8] N.M. Oldham, J.A. Kramar, P.S. Hetrick, and E.C. Teague. Electronic limitations in phase meter for heterodyne interferometry. *Precision Engineering*, 15(3):173–179, July 1993.
- [9] C. Wu and R. Deslattes. Analytical modeling of the periodic nonlinearity in heterodyne interferometry. *Applied optics*, 37(28):6696–6700, October 1998.
- [10] C. Wu. Periodic nonlinearities resulting from ghost reflections in heterodyne interferometry. *Optics communications*, 215:17–23, 2003.
- [11] B. Edlén. The refractive index of air. *Metrologia*, 2(2):71–80, 1966.

- [12] K.P. Birch and M.J. Downs. Correction to the updated edlén equation for the refractive index of air. *Metrologia*, 31:315–316, 1994.
- [13] N. Bobroff. Residual errors in laser interferometry from air turbulence and nonlinearity. *Applied optics*, 26(13):2676–2682, July 1987.
- [14] R.C. Quenelle. Nonlinearity in interferometer measurements. *Hewlett-Packard Journal*, page 10, April 1983.
- [15] C.M. Sutton. Non-linearity in length measurement using heterodyne laser Michelson interferometry. *J. Phys. E: Sci. Instrum.*, (20):1290–1292, 1987.
- [16] A.E. Rosenbluth and N. Bobroff. Optical sources of nonlinearity in heterodyne interferometers. *Precision Engineering*, 12(1):7–11, January 1990.
- [17] W. Hou and G. Wilkening. Investigation and compensation of the nonlinearity of heterodyne interferometers. *Precision Engineering*, (14), 1992.
- [18] J.M. De Freitas and M.A. Player. Importance of rotational beam alignment in the generation of second harmonic errors in laser heterodyne interferometry. *Measurement Science and Technology*, (4):1173–1176, 1993.
- [19] J.M. De Freitas and M.A. Player. Polarization effects in heterodyne interferometry. *Journal of modern optics*, 42(9):1875–1900, 1995.
- [20] W. Hou and X. Zhao. Drift of nonlinearity in the heterodyne interferometer. *Precision Engineering*, 16(1):25–35, January 1994.
- [21] J.M. De Freitas. Analysis of laser source birefringence and dichroism on nonlinearity in heterodyne interferometry. *Measurement Science and Technology*, (8):1356–1359, 1997.
- [22] J.A. Stone and L.P. Howard. A simple technique for observing periodic nonlinearities in Michelson interferometers. *Precision Engineering*, (22):220–232, 1998.
- [23] L.P. Howard and J.A. Stone. Computer modeling of heterodyne interferometer errors. In *Proceedings of the American Society for Precision Engineering*, volume 12, pages 143–146, 1995.
- [24] H. Haitjema, N. Rosielle, G. Kotte, and H. Steijaart. Design and calibration of a parallel-moving displacement generator for nano-metrology. *Measurement Science and Technolgy*, 9:1098–1104, 1998.
- [25] H. Haitjema. Dynamic probe calibration in the μm region with nanometric accuracy. *Precision Engineering*, 19:98–104, 1996.
- [26] S. Wetzels. *Laser based displacement calibration with nanometre accuracy*. PhD thesis, TUE, 1998.

- [27] L. Howard, J. Stone, and J. Foe. Real-time displacement measurements with a Fabry-Perot cavity and a diode laser. *Precision Engineering*, 25:321–335, 2001.
- [28] V.G. Badami and S.R. Patterson. A frequency domain method for the measurement of nonlinearity in heterodyne interferometry. *Precision Engineering*, 24:41–49, 2000.
- [29] S. Patterson and J. Beckwith. Reduction of systematic errors in heterodyne interferometric displacement measurement. In *Proceedings of the 8th IPES Conference, Compiègne, France*, pages 101–104, 1995.
- [30] M. Tanaka, T. Yamagami, and K. Nakayama. Linear interpolation of periodic error in a heterodyne laser interferometer at subnanometer levels. *IEEE transactions on instrumentation and measurement*, 38(2):552–554, April 1989.
- [31] C. Wu, J. Lawall, and R.D. Deslattes. Heterodyne interferometer with subatomic periodic nonlinearity. *Applied optics*, 38(19):4089–4094, July 1999.
- [32] S. Dubovitsky, O.P. Lay, and D.J. Seidel. Elimination of heterodyne interferometer nonlinearity by carrier phase modulation. *Optics letters*, 27(8):619–621, April 2002.
- [33] T. Eom, T. Choi, et al. A simple method for the compensation of the nonlinearity in the heterodyne interferometer. *Measurement Science and Technology*, 13:222–225, January 2002.
- [34] P.H.J. Schellekens. *Absolute meetnauwkeurigheid van technische laserinterferometers*. PhD thesis, TUE, 1986.
- [35] H. Preston-Thomas. The international temperature scale of 1990 (ITS-90). *Metrologia*, 27(1):3–10, 1990.
- [36] K.P. Birch and M.J. Downs. An updated edlén equation for the refractive index of air. *Metrologia*, 30:155–162, 1993.
- [37] P.E. Ciddor. Refractive index of air: new equations for the visible and near infrared. *Applied optics*, 35(9):1566–1573, March 1996.
- [38] G. Bönsch and E. Potulski. Measurement of the refractive index of air and comparison with modified edlén’s formulae. *Metrologia*, 35(2):133–139, 1998.
- [39] P. Schellekens, G. Wilkening, F. Reinboth, M.J. Downs, K.P. Birch, and J. Spronck. Measurements of the refractive index of air using interference refractometers. *Metrologia*, 22:279–287, 1986.
- [40] W. Hou and R. Thalmann. Accurate measurement of the refractive index of air. *Measurement*, 13:307–314, 1994.

- [41] M.J. Renkens and P.H. Schellekens. An accurate interference refractometer based on a permanent vacuum chamber-development and results. *Annals of the CIRP*, 42(1):581–583, 1993.
- [42] M.L. Eickhoff and J.L. Hall. Real-time precision refractometry: new approaches. *Applied optics*, 36(6):1223–1234, February 1997.
- [43] F.L. Pedrotti and L.S. Pedrotti. *Introduction to optics*. Prentice hall international editions, New Jersey, second edition, 1993.
- [44] J. Flügge. *Vergleichende untersuchungen zur messtechnischen leistungsfähigkeit von laserinterferometern und inkrementellen masstabmesssystemen*. PhD thesis, Physikalisch Technische Bundesanstalt, February 1996.
- [45] R.M.A. Azzam and N.M. Bashara. *Ellipsometry and polarized light*. Elsevier Science, Amsterdam, 1999.
- [46] J. Liu and R.M.A. Azzam. Polarization properties of corner-cube retroreflectors: theory and experiment. *Applied Optics*, 36(7):1553–1559, March 1997.
- [47] A.E. Siegman. *Lasers*. University science books, California, 1986.
- [48] Y. Xie and Y. Wu. Zeeman laser interferometer errors for high-precision measurements. *Applied optics*, 31(7):881–884, March 1992.
- [49] Y. Xie and Y. Wu. Elliptical polarization and nonorthogonality of stabilized zeeman laser output. *Applied optics*, 28(11):2043–2046, June 1989.
- [50] M.O. Scully M. Sargent and Jr. W.E. Lamb. *Laser physics*. Addison-Wesley Publishing Company, Reading, Massachusetts, 1974.
- [51] International vocabulary of basic and general terms in metrology, 2. edition (VIM). Published by ISO in names of BIPM - IEC - IFCC - ISO - IUPAC - IUPAP - OIML, 1993.
- [52] T.J. Quinn. Mise en pratique of the definition of the metre(1992). *Metrologia*, 30:523–541, 1993.
- [53] T.J. Quinn. Practical realization of the definition of the metre, including recommended radiations of other optical frequency standards(2001). *Metrologia*, 40:103–133, 2003.
- [54] Inc Winters Electro-optics. Model 100 iodine-stabilized HeNe laser operator's manual. 7160 Nimbus Road Longmont,CO,U.S.A., 2000.
- [55] J. Flügge and R. Köning. Nanometer comparator design and status. In *Requirements and recent developments in high precision length metrology*, volume 159, pages 7–22, 2001. ISSN 0179-0609, ISBN 3-89701-841-1.

- [56] G. Basile, P. Becker, et al. Combined optical and x-ray interferometry for high-precision dimensional metrology. In *Proceedings of the Royal Society of London series A*, volume 456, pages 701–729, 2000.
- [57] G.N. Peggs and A. Yacoot. A review of recent work in sub-nanometre displacement measurement using optical and x-ray interferometry. *Philosophical Transactions of The Royal Society of London Series A*, 360:953–968, 2002.
- [58] H. Haitjema, P.H.J. Schellekens, and S.F.C.L. Wetzels. Calibration of displacement sensors up to 300 μm with nanometre accuracy and direct traceability to a primary standard of length. *Metrologia*, 37(1):25–33, 2000.
- [59] Personal conversations with engineers from Agilent, November 2003.
- [60] E. Spanner and J. Thiel. Homodyne laser interferometer with new interferometer optics and fiber-coupled measuring head for ultra precision measurement below 1 nm. In *Proceedings of the 2nd Euspen International Conference*, pages 222–225, May 2001.
- [61] S.F.C.L. Wetzels. Ontwikkeling van een meetlaser voor kalibraties in het nanometergebied. Master's thesis, Sectie Precision Engineering TUE, Februari 1994.
- [62] S.C.L.M. de Bonth. Calibration of a linear measurement system. Master's thesis, Section Precision Engineering TU/e, May 2001.
- [63] R.W.P. Drever. Laser phase and frequency stabilization using an optical resonator. *Applied Physics B*, 31:97–105, 1983.
- [64] T.W. Hansch and B. Couillaud. Laser frequency stabilization by polarization spectroscopy of a reflecting reference cavity. *Optics Communications*, 35(3):441–444, December 2000.
- [65] B. Knarren. *Application of optical fibres in precision heterodyne laser interferometry*. PhD thesis, TUE, June 2003.
- [66] G.B. Picotto and M. Pisani. A sample scanning system with nanometric accuracy for quantitative SPM measurements. *Ultramicroscopy*, 86:247–254, 2001.
- [67] A. Sacconi, G.B. Picotto, and W. Pasin. Interferometric calibration of piezo-capacitive displacement actuators. In *Proceedings of 4th IMEKO symposium on Laser metrology*, 1996.
- [68] C. Wu, C. Su, and G. Peng. Correction of nonlinearity in one-frequency optical interferometry. *Measurement Science and Technology*, (7):520–524, 1996.
- [69] S.J.A.G. Cosijns, H. Haitjema, and P.H.J. Schellekens. Modeling and verifying non-linearities in heterodyne displacement interferometry. *Precision Engineering*, 26:448–455, 2002.

- [70] O. Číp and F. Petrů. A scale-linearization method for precise laser interferometry. *Meas. Sci. Technol.*, 11:133–141, 2000.
- [71] S.J.A.G. Cosijns, H. Haitjema, and P.H.J. Schellekens. The influence of polarization states on non-linearities in laser interferometry. In *Proceedings of the 3rd Euspen International Conference, Eindhoven, The Netherlands*, pages 593–596, May 2002.
- [72] D. Lorier, B. Knarren, S. Cosijns, H. Haitjema, and P. Schellekens. Polarisation state analysis of heterodyne laser beams. *CIRP Annals*, 25(1), August 2003.
- [73] W. Pril. *Development of high precision mechanical probes for coordinate measuring machines*. PhD thesis, TUE, December 2002.
- [74] A.J. Lewis. *Absolute length measurement using multiple-wavelength phase-stepping interferometry*. PhD thesis, Imperial College, London, 1993.
- [75] I.S. Steinhart and S.R. Hart. *Deep Sea Research*, 15:497, 1968.
- [76] I. Palmen. Realisation and uncertainty analysis of a refractometer tracker. Master's thesis, Section Precision Engineering TU/e, May 2004.
- [77] P. Giacomo. Equation for the determination of the density of moist air (1981). *Metrologia*, 18:33–40, 1982.
- [78] R.S. Davis. Equation for the determination of the density of moist air (1981/91). *Metrologia*, 29:67–70, 1992.
- [79] T. Cuijpers. Herontwerp van een refractometer. Onderzoeksraport WPA 310019, Februari 1995.
- [80] F. Bayer-Helms, H. Darnedde, and G. Exner. Längenstabilität bei raumtemperatur von proben der glaskeramik zerodur. *Metrologia*, 21:49–57, 1985.
- [81] H. Rouse. *Elementary mechanics of fluids*. John Wiley and Sons, New York, 1946.
- [82] S.F.C.L. Wetzels and P.H.J. Schellekens. Development of a traceable laser-based displacement calibration system with nanometer accuracy. *Annals of the CIRP*, 46(1):481–484, 1997.

Used equipment

- [83] Commercial equipment, and materials are identified in order to adequately specify certain procedures. In no case does such identification imply recommendation or endorsement by the author, nor does it imply that the materials or equipment identified are necessarily the best available for the purpose.
- [84] Agilent. *5519A laser head*.
- [85] Agilent. *Receiver type 10780B*.
- [86] Agilent. *PC calibrator board type 10887A*.
- [87] Stanford Research Systems. *Lock-in amplifier SRS844*.
- [88] Agilent. *5528 interferometer*.
- [89] New Focus. *Vortex model 6005*.
- [90] Stanford Research Systems. *Lock-in amplifier SRS830*.
- [91] Wyler. *Clinotronic plus*.
- [92] Agilent. *Frequency counter 53181A*.
- [93] Agilent. *Spectrum analyzer 8590E*.
- [94] Heidenhain. *Laser interferometer type ILM 1131*.
- [95] Physik Instrumente. *Open loop piezo positioner, PI S-310.10*.
- [96] Agilent. *5517C laser head*.
- [97] Agilent. *1897B-VME board*.
- [98] Agilent. *5527 laser head*.
- [99] Mahr. *Inductive probe, Militron Nr.1301*.
- [100] Thermometrics. *Thermistor type TK95F502V*.
- [101] Agilent. *Data acquisition switch unit 34970A*.

- [102] Paroscientific. *Digiquartz Intelligent transmitter model 710-1016/01*.
- [103] Vaisala. *SAW-type hygrometer DM500*.
- [104] ADC. *gas analyser*.

Appendix A

List of symbols

Terminology

Laser head System consisting of the laser source, conditioning optics and reference receiver.

Receiver AC-detector combined with a polarizer and electronics specially designed for measurements with a laser interferometer.

Abbreviations and Acronyms

AOM	Acousto optic modulator
BFM	Beat frequency measurement
BM	Bending mirror
BS	Babinet-Soleil compensator
CCGM	Comité consultatif pour la définition du mètre
CF	Carrier frequency method
CO ₂	Carbon dioxide
FSR	Free spectral range
GPIB	General purpose interface bus
LC	Liquid crystal
NMi	Dutch national metrology institute
NPBS	Non-polarizing beam splitter
PBS	Polarizing beam splitter
PTB	Physikalisch-Technischen Bundesanstalt
QWP	Quarter wave plate
RF	Radio frequency
RRF	Retro reflector
RTD	Resistance temperature detector

slpm	Standard liter per minute
SAW	Surface acoustic waves
VIM	Vocabulaire International des termes fondamentaux et généraux de métrologie

Symbols

Latin symbols:

symbol	description	unit
A	Azimuth angle of analyzer	rad
A_0	Amplitude attenuation of the entire optical system	-
A_d	Constant from the equation of Giacomo and Davis	K^{-2}
A_{PBS_x}	Leakage of the polarizing beam splitter in transmission direction	-
A_{PBS_y}	Leakage of the polarizing beam splitter in reference direction	-
A_R	Calibration constant of an RTD sensor	$^{\circ}C$
A_T	Calibration constant of a thermistor	K^{-1}
A_v	Averaged output	m
A_{WP_x}	Transmission coefficient of a wave plate in x-direction	-
A_{WP_y}	Transmission coefficient of a wave plate in y-direction	-
A_{x_M}	Reflection coefficient of the retro reflector in x-direction	-
A_{y_M}	Reflection coefficient of the retro reflector in y-direction	-
B_d	Constant from the equation of Giacomo and Davis	K^{-1}
B_R	Calibration constant of an RTD sensor	$^{\circ}C \Omega^{-1}$
B_T	Calibration constant of a thermistor	K^{-1}
c	Speed of light	$m s^{-1}$
C	Azimuth angle of compensator	rad
C_d	Constant from the equation of Giacomo and Davis	-
C_R	Calibration constant of an RTD sensor	$^{\circ}C \Omega^{-2}$
C_T	Calibration constant of a thermistor	K^{-1}
d	Diameter of the tube	m
D_d	Constant from the equation of Giacomo and Davis	K
$D_{T,p}$	Density of the gas	$kg m^{-3}$
D_R	Calibration constant of an RTD sensor	$^{\circ}C \Omega^{-3}$
D_T	Calibration constant of a thermistor	K^{-1}
\vec{e}_1	Unit vector	-
\vec{e}_2	Unit vector	-
\vec{E}_1	E-field vector emerging from laser head with frequency f_1	-
\vec{E}_2	E-field vector emerging from laser head with frequency f_2	-
E_{01}	Amplitude of E-field emerged from laser with frequency f_1	$kg m s^{-3} A^{-1}$
E_{02}	Amplitude of E-field emerged from laser with frequency f_2	$kg m s^{-3} A^{-1}$
E_{03}	Amplitude of E-field emerged from laser with frequency f_3	$kg m s^{-3} A^{-1}$
E_{M1}	Amplitude of major axis E-field emerged from laser with frequency f_1	$kg m s^{-3} A^{-1}$

symbol	description	unit
E_{M2}	Amplitude of major axis E-field emerged from laser with frequency f_2	$\text{kg m s}^{-3} \text{ A}^{-1}$
E_{m1}	Amplitude of minor axis E-field emerged from laser with frequency f_1	$\text{kg m s}^{-3} \text{ A}^{-1}$
E_{m2}	Amplitude of minor axis E-field emerged from laser with frequency f_2	$\text{kg m s}^{-3} \text{ A}^{-1}$
E_{p1}	Arbitrary amplitude E-field emerged from laser with frequency f_1	$\text{kg m s}^{-3} \text{ A}^{-1}$
E_{p2}	Arbitrary amplitude E-field emerged from laser with frequency f_2	$\text{kg m s}^{-3} \text{ A}^{-1}$
\vec{E}_{f1}	Resulting E-field of frequency 1 passing through the interferometer	-
E_r	Amplitude of E-field in reference arm	$\text{kg m s}^{-3} \text{ A}^{-1}$
E_R	Calibration constant of an RTD sensor	$^{\circ}\text{C } \Omega^{-4}$
\vec{E}_{ref}	Electric field vector in the reference arm	-
\vec{E}_{rf1}	Resulting E-field of frequency 1 after passing through reference arm	-
\vec{E}_{rf2}	Resulting E-field of frequency 2 after passing through reference arm	-
E_m	Amplitude of E-field in measurement arm	$\text{kg m s}^{-3} \text{ A}^{-1}$
\vec{E}_{meas}	Electric field vector in the measurement arm	-
E_x	E-field emerging from beam splitter in x-direction after passing of interferometer optics	$\text{kg m s}^{-3} \text{ A}^{-1}$
E_y	E-field emerging from beam splitter in y-direction after passing of interferometer optics	$\text{kg m s}^{-3} \text{ A}^{-1}$
f	Resonator frequency	Hz
f_{wv}	Partial water vapour pressure	Pa
f_1	Frequency emerging from the laser	Hz
f_2	Frequency emerging from the laser	Hz
f_3	Frequency emerging from the laser	Hz
I	Irradiance	W m^{-2}
I_0	Intensity	W m^{-2}
I_r	Reference signal	V
I_{ref}	Reference signal	V
I_m	Measurement signal	V
I_{meas}	Measurement signal	V
\vec{k}	Propagation vector	-
k	Propagation constant	m^{-1}
k	Mode number	-
K_λ	Dispersion of the gas	-
l	Length of the tube	m
L	Optical path length	m
L_{20}	Mechanical length at 20°	m
L_{cav}	Cavity length, small Fabry-Prot cavity	m
L_{mech}	Mechanical length	m
ΔL	Change in optical path length	m

symbol	description	unit
ΔL_{mech}	Change in mechanical length	m
M_{os}	Jones matrix of optical system	-
n	Refractive index	-
n_{air}	Refractive index of air	-
n_{\perp}	Refractive index Babinet-Soleil compensator	-
n_{\parallel}	Refractive index Babinet-Soleil compensator	-
n_{vac}	Refractive index of vacuum	-
P	Azimuth angle of polarizer	rad
P_{supply}	Power supplied to thermistor by an electrical circuit	W
P_{lost}	Energy lost to surroundings	W
$P_{selfheating}$	Thermal energy absorbed by the thermistor	W
$P1$	Amplitude ratio of amplitudes of major and minor axis of the ellipse of polarization of frequency f_1	-
$P2$	Amplitude ratio of amplitudes of major and minor axis of the ellipse of polarization of frequency f_2	-
P_1	Polarizer angle in first ellipsometric zone	rad
P_2	Polarizer angle in second ellipsometric zone	rad
P_3	Polarizer angle in third ellipsometric zone	rad
P_4	Polarizer angle in fourth ellipsometric zone	rad
PBS_r	Jones matrix for the reference arm of the polarizing beam splitter	-
PBS_t	Jones matrix for the transmission arm of the polarizing beam splitter	-
r	Ellipticity of phase quadrature signals	-
r_r	Coordinate along the propagation axis in reference arm	m
r_m	Coordinate along the propagation axis in measurement arm	m
$R(\alpha)$	Rotation matrix around angle α	-
R	Amplitude of phase quadrature signals	V
R	Resolution of the electronics board	-
Re	Reynoldsnumber	-
$R1$	Measurement output with receiver 1	m
$R2$	Measurement output with receiver 2	m
\bar{R}	Mean value of amplitudes	m
R_{RTD}	Measured resistance of a RTD sensor at a certain temperature	Ω
R_{therm}	Measured resistance of a thermistor at a certain temperature	Ω
$s(R)$	Standard deviation of the amplitude	V
S_0	Ideal phase quadrature signal	V
S_{90}	Ideal phase quadrature signal	V
S_0^{nl}	Phase quadrature signal of signal with periodic deviations	V
S_{90}^{nl}	Phase quadrature signal of signal with periodic deviations	V
t	Time	s
T	Temperature of the surrounding environment	$^{\circ}\text{C}$
T_0	Amplitude difference between the ordinary and extraordinary polarization	-
T_C	Amplitude attenuations of the two polarization directions of the compensator	-
T_d	Dewpoint temperature	K
T_{RTD}	Temperature of an RTD sensor	$^{\circ}\text{C}$

symbol	description	unit
ΔT	Temperature change during measurement	$^{\circ}\text{C}$
u	Uncertainty	
$u(\Delta\phi)$	Uncertainty of phase quadrature measurements derived from amplitude variation	m
u_{corr}	Uncertainty of the compensated measurements	m
u_{meas}	Uncertainty of the uncompensated measurements	m
u_{eq}	Uncertainty derived from amplitude variation	m
$\langle v \rangle$	Average velocity of air	m s^{-1}
v	Movement velocity of measurement mirror	m s^{-1}
v_l	Speed of light in air	m s^{-1}
x_0	Offset of phase quadrature signal	V
x_1	Abbreviation of $2\omega f_1 t + \phi_{01}$	-
x_2	Abbreviation of $2\omega f_2 t + \phi_{02}$	-
y_0	Offset of phase quadrature signal	V

Greek symbols:

symbol	description	unit
α	Rotation angle of E-field with frequency f_2 emitted by laser referred to beam splitter y-axis	rad
α_l	Phase deviation from phase quadrature	rad
α_{PBS}	Rotation angle of the beam splitter	rad
α_P	Rotation angle between fast axis polarizer and $\frac{\pi}{4}$	rad
α_p	Rotation angle fast axis polarizer compared to major axis E_1	rad
β	Rotation angle of E-field with frequency f_1 emitted by laser referred to beam splitter x-axis	rad
ϕ_{01}	Initial phase of E-field emerged by laser with frequency f_1	rad
ϕ_1	Phase retardance resulting from passing in reference arm	rad
ϕ_{02}	Initial phase of E-field emerged by laser with frequency f_2	rad
ϕ_2	Phase retardance resulting from passing measurement arm	rad
ϕ_{BS}	Phase shift introduced by Babinet Soleil Compensator	rad
ϕ_r	Phase in the reference arm	rad
ϕ_{ref}	Phase in the reference arm	rad
ϕ_m	Phase in the measurement arm	rad
ϕ_{meas}	Phase in the measurement arm	rad
$d\varepsilon_1$	Ellipticity of E-field with frequency f_1	rad
$d\varepsilon_2$	Ellipticity of E-field with frequency f_2	rad
η_{air}	Dynamic viscosity of air	Pa s
$d\eta_1$	Non-orthogonality angle of E-field with frequency 1	rad
$d\eta_2$	Non-orthogonality angle of E-field with frequency 2	rad
δ_0	Phase retardation between the ordinary and extraordinary polarization	rad
Δ	Ellipsometric angle	rad
$\Delta\phi$	Phase shift due to a movement of the measurement mirror	rad
$\Delta\phi_{pd}$	Portion of the measured phase representing the periodic deviation	rad

symbol	description	unit
Δ_C	Relative phase retardation between two polarization directions of the compensator	rad
Δd	Effective optical thickness of the Babinet-Soleil compensator	m
Δf	Frequency shift	Hz
Δz	Displacement of measurement mirror	m
λ	Wavelength of light	m
λ_d	Resistance factor	-
λ_{vac}	Vacuum wavelength of light	m
$\lambda_{\perp 0}$	Vacuum wavelength of light trough BS	m
$\lambda_{\parallel 0}$	Vacuum wavelength of light trough BS	m
Ψ	Ellipsometric angle	rad
θ	Rotation angle between fast axis polarizer and $\frac{\pi}{4}$ relative to beam splitter	rad
ω	Angular frequency	s ⁻¹
ρ	Air density	kg m ⁻³
ξ	Transmission coefficient of interferometer in y-direction	-
χ	Transmission coefficient of interferometer in x-direction	-

Appendix B

Babinet-Soleil compensator

In this appendix the principle of the Babinet-Soleil compensator is explained. The Babinet-Soleil compensator consists of two sections of quartz: a section with variable thickness and a section with fixed thickness as shown in figure B.1. One section consists of two wedges that slide with respect to each other with parallel optical axes. The second section consists of a single slab with its optic axis orthogonal to that of the wedges. For the Babinet-Soleil compensator the phase retardation becomes [45]:

$$\Delta\phi_{BS} = 2\pi \left| \frac{n_{\perp}}{\lambda_{\perp 0}} - \frac{n_{\parallel}}{\lambda_{\parallel 0}} \right| \Delta d \quad (\text{B.1})$$

where $\lambda_{\perp 0}$ and $\lambda_{\parallel 0}$ are the vacuum wavelengths of both polarization states, n_{\perp} and n_{\parallel} are the refractive indices for both polarization arms and $\Delta d = d_1 - d_2$ represents the thickness difference between both quartz sections.

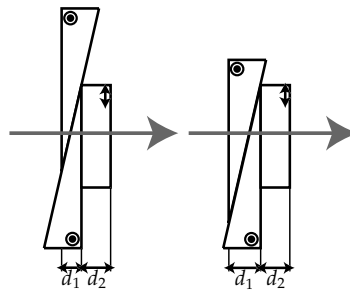


Figure B.1: Schematical representation of the principle of a Babinet-Soleil compensator.

This Babinet-Soleil compensator can be used as a variable retarder when placed in an angle of 45° with respect to the polarization axes of light. When placed at an angle of 0° in front of a laser interferometer it can be used to produce a

phase shift between two orthogonal polarized beams. This results in a virtual interferometer where measurement arm and reference arm coincide. As a result of this common path the changes in refractive index of air are canceled out and the noise is reduced also.

B.1 Calibration of the Babinet Soleil compensator

In order to align the Babinet Soleil Compensator to the heterodyne interferometer two polarizers are used as shown in figure B.2.

1. First the orientation of polarizer 1 has to be aligned to one of the laser frequencies. This is done omitting the Babinet-Soleil compensator and polarizer 2 and using an AC-detector. The polarizer is tuned by minimizing the beat frequency.
2. Next polarizer 2 is placed in the setup and the AC-detector replaced by a DC power detector. By rotating polarizer 2 the intensity signal on the power detector is minimized. At this time both polarizers are under 90° .
3. For the next step the Babinet-Soleil compensator is placed between the two polarizers. The retardance of the compensator is set to a certain value (not being 0). If the angle of the compensator differs from the angle of polarizer 1 the light behind the Babinet-Soleil compensator will be elliptically polarized and hence some light will be transmitted by polarizer 2. With this information the rotation angle of the Babinet-Soleil compensator can be calibrated.
4. The retardance of the Babinet-Soleil compensator can be calibrated at discrete steps of $\frac{\lambda}{2}$. For the steps of $k\lambda$ ($k = 0, 1, 2, \dots$) polarizer 2 is set orthogonal to polarizer 1, and the rotation angle of the Babinet Soleil compensator is set to 45° . Every minimum in DC intensity stands for a retardation of λ . For the steps of $(k + \frac{1}{2})\lambda$ ($k = 0, 1, 2, \dots$) polarizer 2 is set parallel to polarizer 1. Every minimum corresponds to a retardation of $\frac{\lambda}{2}$.

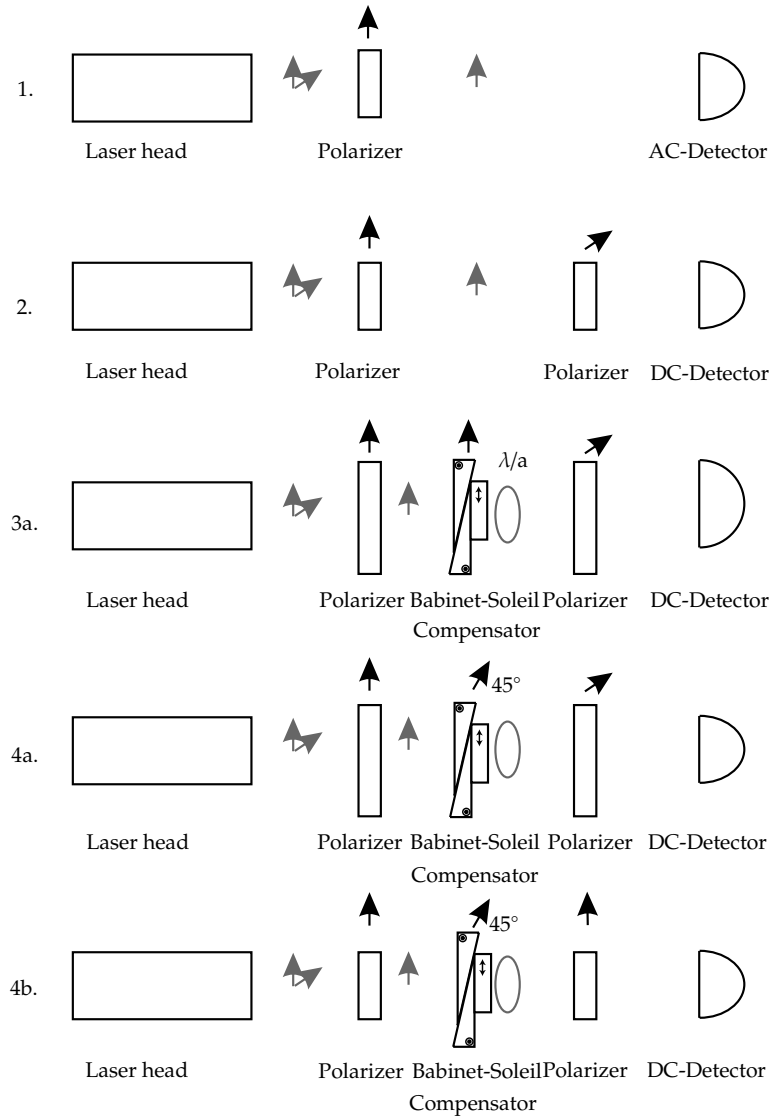


Figure B.2: Schematic representation of the setup for the alignment of the Babinet Soleil compensator with the laser interferometer. In gray the laser polarization directions are shown. The arrows in black on top of the components define the orientation of the components around the optical axis.

Appendix C

Verification of the Jones model

In this appendix two cases are described in the Jones model to verify it mathematically. First the non-linearity is calculated resulting of an elliptical polarized beam in combination with a further ideal interferometer. This is the case described by Hou and Wilkening [17], also used to verify the analytical model (equation 2.17). The second case is the non-linearity resulting from a rotated beam splitter in combination with a further ideal interferometer. This case was described by Player and De Freitas [18] and was also used to verify the analytical formula (equation 2.18).

C.1 Effect of an elliptical polarized beam

In this section the non-linearity as a result of an ideal interferometer with one elliptical polarized beam will be modeled using the modular model. It will be shown that with this model also formula 2.17 can be derived. The Jones vectors representing the elliptical polarized laser beam E_1 and ideal polarized beam E_2 are:

$$\vec{E}_1 = \begin{bmatrix} \cos(d\varepsilon_1) \\ -i * \sin(d\varepsilon_1) \end{bmatrix} e^{i(2\pi f_1 t + \phi_{01})} \quad (\text{C.1a})$$

$$\vec{E}_2 = \begin{bmatrix} 0 \\ 1 \end{bmatrix} e^{i(2\pi f_2 t + \phi_{02})} \quad (\text{C.1b})$$

The reference and measurement matrices for the ideal polarizing beam splitter are:

$$PBS_t = \begin{bmatrix} 0 & 0 \\ 0 & 1 \end{bmatrix} \quad (\text{C.2a})$$

$$PBS_r = \begin{bmatrix} 1 & 0 \\ 0 & 0 \end{bmatrix} \quad (C.2b)$$

The reference retroreflector (RRF) and measurement retroreflector (MRRF) are represented by:

$$RRF = \begin{bmatrix} -1 & 0 \\ 0 & -1 \end{bmatrix} \quad (C.3a)$$

$$MRRF = \begin{bmatrix} -e^{i\Delta\phi} & 0 \\ 0 & -e^{i\Delta\phi} \end{bmatrix} \quad (C.3b)$$

The electromagnetic field of the beam with frequency f_1 traveling through the reference arm is calculated as follows:

$$\begin{aligned} \vec{E}_{rf_1} &= PBS_r * RRF * PBS_r * \vec{E}_1 \\ &= \begin{bmatrix} 1 & 0 \\ 0 & 0 \end{bmatrix} * \begin{bmatrix} -1 & 0 \\ 0 & -1 \end{bmatrix} * \begin{bmatrix} 1 & 0 \\ 0 & 0 \end{bmatrix} * \begin{bmatrix} \cos(d\varepsilon_1) \\ -i * \sin(d\varepsilon_1) \end{bmatrix} e^{i(2\pi f_1 t + \phi_{01})} \\ &= \begin{bmatrix} -\cos(d\varepsilon_1) \\ 0 \end{bmatrix} e^{i(2\pi f_1 t + \phi_{01})} \end{aligned} \quad (C.4)$$

The electromagnetic field of the beam with frequency f_1 traveling through the measurement arm is calculated as follows:

$$\begin{aligned} \vec{E}_{mf_1} &= PBS_t * MRRF * PBS_t * \vec{E}_1 \\ &= \begin{bmatrix} 0 & 0 \\ 0 & 1 \end{bmatrix} * \begin{bmatrix} -e^{i\Delta\phi} & 0 \\ 0 & -e^{i\Delta\phi} \end{bmatrix} * \begin{bmatrix} 0 & 0 \\ 0 & 1 \end{bmatrix} * \begin{bmatrix} \cos(d\varepsilon_1) \\ -i * \sin(d\varepsilon_1) * e^{i\Delta\phi} \end{bmatrix} e^{i(2\pi f_1 t + \phi_{01})} \\ &= \begin{bmatrix} 0 \\ i * \sin(d\varepsilon_1) * e^{i\Delta\phi} \end{bmatrix} e^{i(2\pi f_1 t + \phi_{01})} \end{aligned} \quad (C.5)$$

So the total electromagnetic field with frequency f_1 coming out of the beam splitter is represented as:

$$\begin{aligned} \vec{E}_{BS_1} &= \vec{E}_{rf_1} + \vec{E}_{mf_1} \\ &= \begin{bmatrix} -\cos(d\varepsilon_1) \\ i * \sin(d\varepsilon_1) * e^{i\Delta\phi} \end{bmatrix} e^{i(2\pi f_1 t + \phi_{01})} \end{aligned} \quad (C.6)$$

The electromagnetic field of the beam with frequency f_2 traveling through the reference arm is calculated as follows:

$$\begin{aligned} \vec{E}_{rf_2} &= PBS_r * RRF * PBS_r * \vec{E}_2 \\ &= \begin{bmatrix} 1 & 0 \\ 0 & 0 \end{bmatrix} * \begin{bmatrix} -1 & 0 \\ 0 & -1 \end{bmatrix} * \begin{bmatrix} 1 & 0 \\ 0 & 0 \end{bmatrix} * \begin{bmatrix} 0 \\ 1 \end{bmatrix} e^{i(2\pi f_2 t + \phi_{02})} \\ &= \begin{bmatrix} 0 \\ 0 \end{bmatrix} e^{i(2\pi f_2 t + \phi_{02})} \end{aligned} \quad (C.7)$$

The electromagnetic field of the beam with frequency f_2 traveling through the measurement arm is calculated as follows:

$$\begin{aligned}
 \vec{E}_{mf_2} &= PBS_t * MRRF * PBS_t * \vec{E}_2 \\
 &= \begin{bmatrix} 0 & 0 \\ 0 & 1 \end{bmatrix} * \begin{bmatrix} -e^{i\Delta\phi} & 0 \\ 0 & -e^{i\Delta\phi} \end{bmatrix} * \begin{bmatrix} 0 & 0 \\ 0 & 1 \end{bmatrix} * \begin{bmatrix} 0 \\ 1 \end{bmatrix} e^{i(2\pi f_2 t + \phi_{02})} \\
 &= \begin{bmatrix} 0 \\ -e^{i\Delta\phi} \end{bmatrix} e^{i(2\pi f_2 t + \phi_{02})}
 \end{aligned} \tag{C.8}$$

So the total electromagnetic field with frequency f_2 emerging from the beam splitter is represented as:

$$\begin{aligned}
 \vec{E}_{BS_2} &= \vec{E}_{rf_2} + \vec{E}_{mf_2} \\
 &= \begin{bmatrix} 0 \\ -e^{i\Delta\phi} \end{bmatrix} e^{i(2\pi f_2 t + \phi_{02})}
 \end{aligned} \tag{C.9}$$

The total electromagnetic field emerging from the beam splitter is now:

$$\begin{aligned}
 \vec{E}_{BS} &= \vec{E}_{BS_1} + \vec{E}_{BS_2} \\
 &= \begin{bmatrix} -\cos(d\varepsilon_1)e^{ix_1} \\ i * \sin(d\varepsilon_1)e^{i(x_1+\Delta\phi)} - e^{i(x_2+\Delta\phi)} \end{bmatrix}
 \end{aligned} \tag{C.10}$$

with

$$x_j = 2\pi f_j t + \phi_{0j}, \quad j = 1, 2 \tag{C.11}$$

The electromagnetic field transmitted by the receiver polarizer under 45° is:

$$\begin{aligned}
 \vec{E}_P &= P * \vec{E}_{BS} \\
 &= \frac{1}{2} \begin{bmatrix} 1 & 1 \\ 1 & 1 \end{bmatrix} * \begin{bmatrix} -\cos(d\varepsilon_1)e^{ix_1} \\ i * \sin(d\varepsilon_1)e^{i(x_1+\Delta\phi)} - e^{i(x_2+\Delta\phi)} \end{bmatrix} \\
 &= \frac{1}{2} \begin{bmatrix} -\cos(d\varepsilon_1)e^{ix_1} + i * \sin(d\varepsilon_1)e^{i(x_1+\Delta\phi)} - e^{i(x_2+\Delta\phi)} \\ -\cos(d\varepsilon_1)e^{ix_1} + i * \sin(d\varepsilon_1)e^{i(x_1+\Delta\phi)} - e^{i(x_2+\Delta\phi)} \end{bmatrix}
 \end{aligned} \tag{C.12}$$

Since the x- and y-component of this vector are equal, the intensity on the detector is:

$$\begin{aligned}
I_m &= E_P^\dagger E_P = E_{P_x}^* E_{P_x} + E_{P_y}^* E_{P_y} = 2 * E_{P_x}^* E_{P_x} \quad (C.13) \\
&= \frac{1}{2} \left[-\cos(d\varepsilon_1) e^{ix_1} + i * \sin(d\varepsilon_1) e^{i(x_1 + \Delta\phi)} - e^{i(x_2 + \Delta\phi)} \right] \\
&\quad * \left[-\cos(d\varepsilon_1) e^{-ix_1} - i * \sin(d\varepsilon_1) e^{-i(x_1 + \Delta\phi)} - e^{-i(x_2 + \Delta\phi)} \right] \\
&= \frac{1}{2} \left[\begin{aligned} &1 + \cos(d\varepsilon_1)^2 + \sin(d\varepsilon_1)^2 \\ &+ \cos(d\varepsilon_1) * (e^{i(x_2 - x_1 + \Delta\phi)} + e^{-i(x_2 - x_1 + \Delta\phi)}) \\ &+ i \sin(d\varepsilon_1) * (e^{i(x_2 - x_1)} - e^{-i(x_2 - x_1)}) \end{aligned} \right] \\
&= \frac{1}{2} \left[2 + 2 \cos(d\varepsilon_1) \cos(x_2 - x_1 + \Delta\phi) - 2 \sin(d\varepsilon_1) \sin(x_2 - x_1) \right] \quad (C.14)
\end{aligned}$$

Knowing:

$$\sin(\alpha - \beta) = \sin(\alpha) \cos(\beta) - \cos(\alpha) \sin(\beta) \quad (C.15)$$

Equation C.14 can be rewritten as:

$$\begin{aligned}
I_m &= (\cos(d\varepsilon_1) + \sin(d\varepsilon_1) \sin(\Delta\phi)) \cos(x_2 - x_1 + \Delta\phi) \\
&\quad - \sin(d\varepsilon_1) \cos(\Delta\phi) \sin(x_2 - x_1 + \Delta\phi) \quad (C.16)
\end{aligned}$$

Further:

$$A \cos(\alpha) + B \sin(\alpha) = \sqrt{A^2 + B^2} \cos\left(\alpha - \arctan\left(\frac{B}{A}\right)\right) \quad (C.17)$$

Rewriting formula C.16

$$I_m = Z \cos\left(x_2 - x_1 + \Delta\phi - \arctan\left(\frac{-\sin(d\varepsilon_1) \cos(\Delta\phi)}{\cos(d\varepsilon_1) + \sin(d\varepsilon_1) \sin(\Delta\phi)}\right)\right) \quad (C.18)$$

with amplitude Z:

$$Z = \sqrt{1 + 2 \sin(d\varepsilon_1) \cos(d\varepsilon_1) \sin(\Delta\phi)} \quad (C.19)$$

The electromagnetic field on the reference detector can be calculated as:

$$\begin{aligned}
\vec{E}_{P_r} &= P * \vec{E} = P * (\vec{E}_1 + \vec{E}_2) \\
&= \frac{1}{2} \begin{bmatrix} 1 & 1 \\ 1 & 1 \end{bmatrix} * \begin{bmatrix} \cos(d\varepsilon_1) e^{ix_1} \\ -i \sin(d\varepsilon_1) e^{ix_1} + e^{ix_2} \end{bmatrix} \\
&= \frac{1}{2} \begin{bmatrix} (\cos(d\varepsilon_1) - i \sin(d\varepsilon_1)) e^{ix_1} + e^{ix_2} \\ (\cos(d\varepsilon_1) - i \sin(d\varepsilon_1)) e^{ix_1} + e^{ix_2} \end{bmatrix} \quad (C.20)
\end{aligned}$$

The intensity of the reference signal therefore becomes:

$$\begin{aligned}
 I_r &= \vec{E}_{P_r}^\dagger \vec{E}_{P_r} = \vec{E}_{P_r x}^* \vec{E}_{P_r x} + \vec{E}_{P_r y}^* \vec{E}_{P_r y} = 2 * \vec{E}_{P_r x}^* \vec{E}_{P_r x} \\
 &= \frac{1}{2} \left(2 + \cos(d\varepsilon_1) \left(e^{i(x_2-x_1)} + e^{-i(x_2-x_1)} \right) - i \sin(d\varepsilon_2) \left(e^{i(x_2-x_1)} - e^{-i(x_2-x_1)} \right) \right) \\
 &= 1 + \cos(d\varepsilon_1) \cos(x_2 - x_1) + \sin(d\varepsilon_1) \sin(x_2 - x_1) \\
 &= 1 + \cos(x_2 - x_1 - d\varepsilon_1)
 \end{aligned} \tag{C.21}$$

The phase difference between reference and measurement signal is now:

$$\Delta\phi_m - \phi_r = d\varepsilon_1 + \Delta\phi - \arctan \left(\frac{-\sin(d\varepsilon_1) \cos(d\phi)}{\cos(d\varepsilon_1) + \sin(d\varepsilon_1) \sin(\Delta\phi)} \right) \tag{C.22}$$

The first term is a constant phase term. Since the interferometer measures displacement this term is not in the measurement itself. From this it can be concluded that the non-linearity resulting from an ideal interferometer with an elliptical polarized beam derived by the modular model equals equation 2.17.

C.2 Effect of a rotated beam splitter

In this section the non-linearity as a result of an ideal interferometer with a rotated beam splitter will be modeled using the modular model. It will be shown that with this model also formula 2.18 can be derived. The Jones vectors representing the linear polarized laser beams E_1 and E_2 are:

$$\vec{E}_1 = \begin{bmatrix} 1 \\ 0 \end{bmatrix} e^{i(2\pi f_1 t + \phi_{01})} \tag{C.23a}$$

$$\vec{E}_2 = \begin{bmatrix} 0 \\ 1 \end{bmatrix} e^{i(2\pi f_2 t + \phi_{02})} \tag{C.23b}$$

The reference and measurement matrices for the rotated polarizing beam splitter over angle α are:

$$\begin{aligned}
 PBS_t &= \begin{bmatrix} \cos(\alpha) & -\sin(\alpha) \\ \sin(\alpha) & \cos(\alpha) \end{bmatrix} * \begin{bmatrix} 0 & 0 \\ 0 & 1 \end{bmatrix} * \begin{bmatrix} \cos(\alpha) & \sin(\alpha) \\ -\sin(\alpha) & \cos(\alpha) \end{bmatrix} \\
 &= \begin{bmatrix} \sin^2(\alpha) & -\sin(\alpha) \cos(\alpha) \\ -\sin(\alpha) \cos(\alpha) & \cos^2(\alpha) \end{bmatrix}
 \end{aligned} \tag{C.24}$$

$$\begin{aligned}
 PBS_r &= \begin{bmatrix} \cos(\alpha) & -\sin(\alpha) \\ \sin(\alpha) & \cos(\alpha) \end{bmatrix} * \begin{bmatrix} 1 & 0 \\ 0 & 0 \end{bmatrix} * \begin{bmatrix} \cos(\alpha) & \sin(\alpha) \\ -\sin(\alpha) & \cos(\alpha) \end{bmatrix} \\
 &= \begin{bmatrix} \cos^2(\alpha) & \sin(\alpha) \cos(\alpha) \\ \sin(\alpha) \cos(\alpha) & \sin^2(\alpha) \end{bmatrix}
 \end{aligned} \tag{C.25}$$

Player and De Freitas assumed an orientation of the receiver polarizer under 45° with the beam splitter axes. Therefore in the modular model, the Jones matrix representing the polarizer is represented by:

$$\begin{aligned} P &= \begin{bmatrix} \cos^2(\frac{\pi}{4} + \alpha) & \sin(\frac{\pi}{4} + \alpha) \cos(\frac{\pi}{4} + \alpha) \\ \sin(\frac{\pi}{4} + \alpha) \cos(\frac{\pi}{4} + \alpha) & \sin^2(\frac{\pi}{4} + \alpha) \end{bmatrix} \\ &= \frac{1}{2} \begin{bmatrix} 1 - 2 \sin \alpha \cos \alpha & \cos^2 \alpha - \sin^2 \alpha \\ \cos^2 \alpha - \sin^2 \alpha & 1 + 2 \sin \alpha \cos \alpha \end{bmatrix} \end{aligned} \quad (C.26)$$

The electromagnetic field of the beam with frequency f_1 traveling through the reference arm is calculated as follows:

$$\vec{E}_{rf_1} = PBS_r * RRF * PBS_r * \vec{E}_1 \quad (C.27)$$

$$\begin{aligned} &= \begin{bmatrix} \cos^2(\alpha) & \sin(\alpha) \cos(\alpha) \\ \sin(\alpha) \cos(\alpha) & \sin^2(\alpha) \end{bmatrix} * \begin{bmatrix} -1 & 0 \\ 0 & -1 \end{bmatrix} \\ &\quad * \begin{bmatrix} \cos^2(\alpha) & \sin(\alpha) \cos(\alpha) \\ \sin(\alpha) \cos(\alpha) & \sin^2(\alpha) \end{bmatrix} * \begin{bmatrix} 1 \\ 0 \end{bmatrix} e^{i(2\pi f_1 t + \phi_{01})} \\ &= \begin{bmatrix} -\cos^2 \alpha \\ -\sin \alpha \cos \alpha \end{bmatrix} e^{i(2\pi f_1 t + \phi_{01})} \end{aligned} \quad (C.28)$$

The electromagnetic field of the beam with frequency f_1 traveling through the measurement arm is calculated as follows:

$$\vec{E}_{mf_1} = PBS_t * MRRF * PBS_t * \vec{E}_1 \quad (C.29)$$

$$\begin{aligned} &= \begin{bmatrix} \sin^2(\alpha) & -\sin(\alpha) \cos(\alpha) \\ -\sin(\alpha) \cos(\alpha) & \cos^2(\alpha) \end{bmatrix} * \begin{bmatrix} -e^{i\Delta\phi} & 0 \\ 0 & -e^{i\Delta\phi} \end{bmatrix} \\ &\quad * \begin{bmatrix} \sin^2(\alpha) & -\sin(\alpha) \cos(\alpha) \\ -\sin(\alpha) \cos(\alpha) & \cos^2(\alpha) \end{bmatrix} * \begin{bmatrix} 1 \\ 0 \end{bmatrix} e^{i(2\pi f_1 t + \phi_{01})} \\ &= \begin{bmatrix} -\sin^2 \alpha e^{i\Delta\phi} \\ \sin \alpha \cos \alpha e^{i\Delta\phi} \end{bmatrix} e^{i(2\pi f_1 t + \phi_{01})} \end{aligned} \quad (C.30)$$

So the total electromagnetic field with frequency f_1 coming out of the beam splitter is represented as:

$$\vec{E}_{BS_1} = \vec{E}_{rf_1} + \vec{E}_{mf_1} \quad (C.31)$$

$$= \begin{bmatrix} -\cos^2 \alpha - \sin^2 \alpha e^{i\Delta\phi} \\ \sin \alpha \cos \alpha (e^{i\Delta\phi} - 1) \end{bmatrix} e^{i(2\pi f_1 t + \phi_{01})} \quad (C.32)$$

The electromagnetic field of the beam with frequency f_2 traveling through the reference arm is calculated as follows:

$$\vec{E}_{rf_2} = PBS_r * RRF * PBS_r * \vec{E}_2 \quad (C.33)$$

$$\begin{aligned} &= \begin{bmatrix} \cos^2(\alpha) & \sin(\alpha) \cos(\alpha) \\ \sin(\alpha) \cos(\alpha) & \sin^2(\alpha) \end{bmatrix} * \begin{bmatrix} -1 & 0 \\ 0 & -1 \end{bmatrix} \\ &\quad * \begin{bmatrix} \cos^2(\alpha) & \sin(\alpha) \cos(\alpha) \\ \sin(\alpha) \cos(\alpha) & \sin^2(\alpha) \end{bmatrix} * \begin{bmatrix} 0 \\ 1 \end{bmatrix} e^{i(2\pi f_2 t + \phi_{02})} \\ &= \begin{bmatrix} -\sin \alpha \cos \alpha \\ -\sin^2 \alpha \end{bmatrix} e^{i(2\pi f_2 t + \phi_{02})} \end{aligned} \quad (C.34)$$

The electromagnetic field of the beam with frequency f_2 traveling through the measurement arm is calculated as follows:

$$\vec{E}_{mf_2} = PBS_t * MRRF * PBS_t * \vec{E}_2 \quad (C.35)$$

$$\begin{aligned} &= \begin{bmatrix} \sin^2(\alpha) & -\sin(\alpha) \cos(\alpha) \\ -\sin(\alpha) \cos(\alpha) & \cos^2(\alpha) \end{bmatrix} * \begin{bmatrix} -e^{i\Delta\phi} & 0 \\ 0 & -e^{i\Delta\phi} \end{bmatrix} \\ &\quad * \begin{bmatrix} \sin^2(\alpha) & -\sin(\alpha) \cos(\alpha) \\ -\sin(\alpha) \cos(\alpha) & \cos^2(\alpha) \end{bmatrix} * \begin{bmatrix} 0 \\ 1 \end{bmatrix} e^{i(2\pi f_2 t + \phi_{02})} \\ &= \begin{bmatrix} \sin \alpha \cos \alpha e^{i\Delta\phi} \\ -\cos^2 \alpha e^{i\Delta\phi} \end{bmatrix} e^{i(2\pi f_2 t + \phi_{02})} \end{aligned} \quad (C.36)$$

So the total electromagnetic field with frequency f_2 emerging from the beam splitter is represented as:

$$\vec{E}_{BS_2} = \vec{E}_{rf_2} + \vec{E}_{mf_2} \quad (C.37)$$

$$= \begin{bmatrix} \sin \alpha \cos \alpha (-1 + e^{i\Delta\phi}) \\ \sin^2 \alpha - \cos^2 \alpha e^{i\Delta\phi} \end{bmatrix} e^{i(2\pi f_2 t + \phi_{02})} \quad (C.38)$$

The total electromagnetic field emerging from the beam splitter is now:

$$\vec{E}_{BS} = \vec{E}_{BS_1} + \vec{E}_{BS_2} \quad (C.39)$$

$$= \begin{bmatrix} -\cos^2 \alpha e^{ix_1} - \sin \alpha \cos \alpha e^{ix_2} - \sin^2 \alpha e^{i(x_1 + \Delta\phi)} + \sin \alpha \cos \alpha e^{i(x_2 + \Delta\phi)} \\ -\sin \alpha \cos \alpha e^{ix_1} - \sin^2 \alpha e^{ix_2} + \sin \alpha \cos \alpha e^{i(x_1 + \Delta\phi)} - \cos^2 \alpha e^{i(x_2 + \Delta\phi)} \end{bmatrix}$$

with

$$x_j = 2\pi f_j t + \phi_{0j}, \quad j = 1, 2 \quad (C.40)$$

The electromagnetic field transmitted by the receiver polarizer under 45° with the beam splitter is:

$$\begin{aligned}
\vec{E}_P &= P * \vec{E}_{BS} = P * \begin{bmatrix} A' \\ B' \end{bmatrix} \\
&= \frac{1}{2} \begin{bmatrix} 1 - 2 \sin \alpha \cos \alpha & \cos^2 \alpha - \sin^2 \alpha \\ \cos^2 \alpha - \sin^2 \alpha & 1 + 2 \sin \alpha \cos \alpha \end{bmatrix} * \begin{bmatrix} A' \\ B' \end{bmatrix} \\
&= \frac{1}{2} \begin{bmatrix} (1 - 2 \sin \alpha \cos \alpha) A' + (\cos^2 \alpha - \sin^2 \alpha) B' \\ (\cos^2 \alpha - \sin^2 \alpha) A' + (1 + 2 \sin \alpha \cos \alpha) B' \end{bmatrix} \quad (C.41)
\end{aligned}$$

After some calculation it follows:

$$\begin{aligned}
E_{P_x} &= \frac{1}{2} \left(-\cos^2 \alpha + \sin \alpha \cos^3 \alpha + \sin^3 \alpha \cos \alpha \right) e^{ix_1} \\
&+ \frac{1}{2} \left(-\sin \alpha \cos \alpha + \sin^2 \alpha \cos^2 \alpha + \sin^4 \alpha \right) e^{ix_2} \\
&+ \frac{1}{2} \left(-\sin^2 \alpha + \sin^3 \alpha \cos \alpha + \sin \alpha \cos^3 \alpha \right) e^{i(x_1 + \Delta\phi)} \\
&+ \frac{1}{2} \left(\sin \alpha \cos \alpha - \sin^2 \alpha \cos^2 \alpha - \cos^4 \alpha \right) e^{i(x_2 + \Delta\phi)} \\
&= \frac{1}{2} \left(A e^{ix_1} + B e^{ix_2} + C e^{i(x_1 + \Delta\phi)} + D e^{i(x_2 + \Delta\phi)} \right) \quad (C.42)
\end{aligned}$$

$$\begin{aligned}
E_{P_y} &= \frac{1}{2} \left(-\cos^4 \alpha - \sin^2 \alpha \cos^2 \alpha - \sin \alpha \cos \alpha \right) e^{ix_1} \\
&+ \frac{1}{2} \left(-\sin \alpha \cos^3 \alpha - \sin^3 \alpha \cos \alpha - \sin^2 \alpha \right) e^{ix_2} \\
&+ \frac{1}{2} \left(\sin^2 \alpha \cos^2 \alpha + \sin^4 \alpha + \sin \alpha \cos \alpha \right) e^{i(x_1 + \Delta\phi)} \\
&+ \frac{1}{2} \left(-\sin \alpha \cos^3 \alpha - \sin^3 \alpha \cos \alpha - \cos^2 \alpha \right) e^{i(x_2 + \Delta\phi)} \\
&= \frac{1}{2} \left(E e^{ix_1} + F e^{ix_2} + G e^{i(x_1 + \Delta\phi)} + H e^{i(x_2 + \Delta\phi)} \right) \quad (C.43)
\end{aligned}$$

The intensity on the detector is:

$$I_m = \vec{E}_P^\dagger \vec{E}_P = E_{P_x}^* E_{P_x} + E_{P_y}^* E_{P_y} \quad (C.44)$$

$$\begin{aligned}
E_{P_x}^* E_{P_x} &= \frac{1}{2} \left(A e^{ix_1} + B e^{ix_2} + C e^{i(x_1+\Delta\phi)} + D e^{i(x_2+\Delta\phi)} \right) \\
&\quad * \frac{1}{2} \left(A e^{-ix_1} + B e^{-ix_2} + C e^{-i(x_1+\Delta\phi)} + D e^{-i(x_2+\Delta\phi)} \right) \\
&= \frac{1}{4} \left(\begin{aligned} &A^2 + B^2 + C^2 + D^2 + (AC + BD) \cos(\Delta\phi) \\ &+ (AB + CD) \cos(x_2 - x_1) + AD \cos(x_2 - x_1 + \Delta\phi) \\ &+ BC \cos(x_2 - x_1 - \Delta\phi) \end{aligned} \right) \quad (C.45) \\
E_{P_y}^* E_{P_y} &= \frac{1}{2} \left(E e^{ix_1} + F e^{ix_2} + G e^{i(x_1+\Delta\phi)} + H e^{i(x_2+\Delta\phi)} \right) \\
&\quad * \frac{1}{2} \left(E e^{-ix_1} + F e^{-ix_2} + G e^{-i(x_1+\Delta\phi)} + H e^{-i(x_2+\Delta\phi)} \right) \\
&= \frac{1}{4} \left(\begin{aligned} &E^2 + F^2 + G^2 + H^2 + (EG + FH) \cos(\Delta\phi) \\ &+ (EF + GH) \cos(x_2 - x_1) + EH \cos(x_2 - x_1 + \Delta\phi) \\ &+ FG \cos(x_2 - x_1 - \Delta\phi) \end{aligned} \right)
\end{aligned}$$

Due to the use of a band-pass filter in the detector the DC components are not in the measurement, eliminating the first five components of equations C.45 and C.46. The measurement signal on the detector becomes:

$$\begin{aligned}
I_m &= E_{P_x}^* E_{P_x} + E_{P_y}^* E_{P_y} \\
&= \frac{1}{2} (AD + EH) \cos(x_2 - x_1 + \Delta\phi) + \frac{1}{2} (BC + FG) \cos(x_2 - x_1 - \Delta\phi) \\
&\quad + \frac{1}{2} (AB + CD + EF + GH) \cos(x_2 - x_1) \\
&= \frac{1}{2} (AD + EH) \cos(x_2 - x_1 + \Delta\phi) + \frac{1}{2} (BC + FG) \cos(x_2 - x_1 + \Delta\phi - 2\Delta\phi) \\
&\quad + \frac{1}{2} (AB + CD + EF + GH) \cos(x_2 - x_1 + \Delta\phi - \Delta\phi) \quad (C.46)
\end{aligned}$$

Knowing:

$$\cos(\alpha - \beta) = \cos(\alpha) \cos(\beta) + \sin(\alpha) \sin(\beta) \quad (C.47)$$

Equation C.46 can be rewritten as:

$$\begin{aligned}
I_m &= \frac{1}{2} \left(\begin{aligned} &(AD + EH) + (BC + FG) \cos(2\Delta\phi) \\ &+ (AB + CD + EF + GH) \sin(\Delta\phi) \end{aligned} \right) \cos(x_2 - x_1 + \Delta\phi) \\
&\quad + \frac{1}{2} \left(\begin{aligned} &(BC + FG) \sin(2\Delta\phi) \\ &+ (AB + CD + EF + GH) \cos(\Delta\phi) \end{aligned} \right) \sin(x_2 - x_1 + \Delta\phi) \quad (C.48)
\end{aligned}$$

$$\begin{aligned}
AD &= (-\cos^2 \alpha + \sin \alpha \cos^3 \alpha + \sin^3 \alpha \cos \alpha) \\
&\quad * (\sin \alpha \cos \alpha - \sin^2 \alpha \cos^2 \alpha - \cos^4 \alpha) \\
&= -\sin \alpha \cos^3 \alpha + 2 \sin^2 \alpha \cos^4 \alpha + \cos^6 \alpha - 2 \sin^3 \alpha \cos^5 \alpha \\
&\quad - \sin \alpha \cos^7 \alpha + \sin^4 \alpha \cos^2 \alpha - \sin^5 \alpha \cos^3 \alpha \quad (C.49)
\end{aligned}$$

$$\begin{aligned}
EH &= (-\cos^4 \alpha - \sin^2 \alpha \cos^2 \alpha - \sin \alpha \cos \alpha) \\
&\quad * (-\sin \alpha \cos^3 \alpha - \sin^3 \alpha \cos \alpha - \cos^2 \alpha) \\
&= \sin \alpha \cos^7 \alpha + 2 \sin^3 \alpha \cos^5 \alpha + \cos^6 \alpha + \sin^5 \alpha \cos^3 \alpha \\
&\quad + 2 \sin^2 \alpha \cos^4 \alpha + \sin^4 \alpha \cos^2 \alpha + \sin \alpha \cos^3 \alpha \quad (C.50)
\end{aligned}$$

$$\begin{aligned}
AD + EH &= 2 \cos^6 \alpha + 4 \sin^2 \alpha \cos^4 \alpha + 2 \sin^4 \alpha \cos^2 \alpha \\
&= 2 \cos^2 \alpha \quad (C.51)
\end{aligned}$$

$$\begin{aligned}
BC &= (-\sin \alpha \cos \alpha + \sin^2 \alpha \cos^2 \alpha + \sin^4 \alpha) \\
&\quad * (-\sin^2 \alpha + \sin^3 \alpha \cos \alpha + \sin \alpha \cos^3 \alpha) \\
&= \sin^3 \alpha \cos \alpha - 2 \sin^4 \alpha \cos^2 \alpha - \sin^2 \alpha \cos^4 \alpha + 2 \sin^5 \alpha \cos^3 \alpha \\
&\quad + \sin^3 \alpha \cos^5 \alpha - \sin^6 \alpha + \sin^7 \alpha \cos \alpha \quad (C.52)
\end{aligned}$$

$$\begin{aligned}
FG &= (-\sin \alpha \cos^3 \alpha - \sin^3 \alpha \cos \alpha - \sin^2 \alpha) \\
&\quad * (\sin^2 \alpha \cos^2 \alpha + \sin^4 \alpha + \sin \alpha \cos \alpha) \\
&= -\sin^3 \alpha \cos^5 \alpha - 2 \sin^5 \alpha \cos^3 \alpha - \sin^2 \alpha \cos^4 \alpha - \sin^7 \alpha \cos \alpha \\
&\quad - 2 \sin^4 \alpha \cos^2 \alpha - \sin^6 \alpha - \sin^3 \alpha \cos \alpha \quad (C.53)
\end{aligned}$$

$$\begin{aligned}
BC + FG &= -4 \sin^4 \alpha \cos^2 \alpha - 2 \sin^2 \alpha \cos^4 \alpha - 2 \sin^6 \alpha \\
&= -2 \sin^2 \alpha \quad (C.54)
\end{aligned}$$

$$\begin{aligned}
AB &= (-\cos^2 \alpha + \sin \alpha \cos^3 \alpha + \sin^3 \alpha \cos \alpha) \\
&\quad * (-\sin \alpha \cos \alpha + \sin^2 \alpha \cos^2 \alpha + \sin^4 \alpha) \\
&= \sin^7 \alpha \cos \alpha + 2 \sin^5 \alpha \cos^3 \alpha + \sin^3 \alpha \cos^5 \alpha \\
&\quad - 2 \sin^2 \alpha \cos^2 \alpha + \sin \alpha \cos^3 \alpha \quad (C.55)
\end{aligned}$$

$$\begin{aligned}
CD &= (-\sin^2 \alpha + \sin^3 \alpha \cos \alpha + \sin \alpha \cos^3 \alpha) \\
&\quad * (\sin \alpha \cos \alpha - \sin^2 \alpha \cos^2 \alpha - \cos^4 \alpha) \\
&= -\sin^5 \alpha \cos^3 \alpha - 2 \sin^3 \alpha \cos^5 \alpha - \sin^3 \alpha \cos \alpha \\
&\quad + 2 \sin^2 \alpha \cos^2 \alpha - \sin \alpha \cos^7 \alpha \quad (C.56)
\end{aligned}$$

$$\begin{aligned}
EF &= (-\cos^4 \alpha - \sin^2 \alpha \cos^2 \alpha - \sin \alpha \cos \alpha) \\
&\quad * (-\sin \alpha \cos^3 \alpha - \sin^3 \alpha \cos \alpha - \sin^2 \alpha) \\
&= \sin^5 \alpha \cos^3 \alpha + 2 \sin^3 \alpha \cos^5 \alpha + \sin^3 \alpha \cos \alpha \\
&\quad + 2 \sin^2 \alpha \cos^2 \alpha + \sin \alpha \cos^7 \alpha \quad (C.57)
\end{aligned}$$

$$\begin{aligned}
GH &= (\sin^2 \alpha \cos^2 \alpha + \sin^4 \alpha + \sin \alpha \cos \alpha) \\
&\quad * (-\sin \alpha \cos^3 \alpha - \sin^3 \alpha \cos \alpha - \cos^2 \alpha) \\
&= -\sin^7 \alpha \cos \alpha - 2 \sin^5 \alpha \cos^3 \alpha - \sin^3 \alpha \cos^5 \alpha \\
&\quad - 2 \sin^2 \alpha \cos^2 \alpha - \sin \alpha \cos^3 \alpha \quad (C.58)
\end{aligned}$$

$$AB + CD + EF + GH = 0 \quad (C.59)$$

Substitution of equations C.51, C.54 and C.59 in equation C.48 gives:

$$\begin{aligned}
I_m &= (\cos^2 \alpha - \sin^2 \alpha \cos(2\Delta\phi)) \cos(x_2 - x_1 + \Delta\phi) \\
&\quad + (-\sin^2 \alpha \sin(2\Delta\phi)) \sin(x_2 - x_1 + \Delta\phi) \quad (C.60)
\end{aligned}$$

Further:

$$A \cos(\alpha) + B \sin(\alpha) = \sqrt{A^2 + B^2} \cos\left(\alpha - \arctan\left(\frac{B}{A}\right)\right) \quad (C.61)$$

Rewriting formula C.60 with use of this equation:

$$I_m = Z' \cos\left(x_2 - x_1 + \Delta\phi - \arctan\left(\frac{-\sin^2 \alpha \sin(2\Delta\phi)}{\cos^2 \alpha - \cos^2 \alpha \cos(2\Delta\phi)}\right)\right) \quad (C.62)$$

Since the amplitude Z' does not influence the phase measurement it is not calculated further.

In this case the reference intensity signal equals an ideal interferometer:

$$I_r = 1 + \cos(x_2 - x_1) \quad (C.63)$$

The phase difference between reference and measurement signal is now:

$$\Delta\phi_m - \phi_r = \Delta\phi - \arctan\left(\frac{-\sin^2 \alpha \sin(2\Delta\phi)}{\cos^2 \alpha - \cos^2 \alpha \cos(2\Delta\phi)}\right) \quad (\text{C.64})$$

From this it can be concluded that the non-linearity resulting from a rotated beam splitter derived with the modular model equals equation 2.18.

Appendix D

Calculation of laser head polarization state measurements

In chapter 3 two methods are presented to measure the polarization state of a heterodyne laser head. In this appendix the theoretical intensity signals for both methods are derived.

D.1 Carrier frequency measurement

In the carrier frequency measurement the beam of the heterodyne laser (containing two frequencies) is mixed with the beam emerging from a homodyne interferometer.

With the laser properties defined as in figure D.1, the Jones vectors of all frequencies can be described as:

$$\vec{E}_1 = R(0)E_{01} \begin{bmatrix} \cos(d\varepsilon_1) \\ -i \sin(d\varepsilon_1) \end{bmatrix} e^{i(2\pi f_1 t + \phi_{01})} = \begin{bmatrix} E_{M1} \\ E_{m1} \end{bmatrix} e^{i(2\pi f_1 t + \phi_{01})} \quad (D.1a)$$

$$\vec{E}_2 = R(\eta)E_{02} \begin{bmatrix} i \sin(d\varepsilon_2) \\ \cos(d\varepsilon_2) \end{bmatrix} e^{i(2\pi f_2 t + \phi_{02})} = \begin{bmatrix} E_{m2} \cos(\eta) - E_{M2} \sin(\eta) \\ E_{m2} \sin(\eta) + E_{M2} \cos(\eta) \end{bmatrix} e^{i(2\pi f_2 t + \phi_{02})} \quad (D.1b)$$

$$\vec{E}_3 = E_{03} \begin{bmatrix} 1 \\ i \end{bmatrix} e^{i(2\pi f_1 t + \phi_{01})} = \begin{bmatrix} E_{M3} \\ E_{m3} \end{bmatrix} e^{i(2\pi f_1 t + \phi_{01})} \quad (D.1c)$$

Here E_{mk} , $k=1,2,3$ stands for the minor component of the E-field and E_{Mk} , $k=1,2,3$ stands for the major component in the E-field. The total electromagnetic field entering the polarizer is now described as:

$$\vec{E}_{in} = \begin{bmatrix} E_{M1}e^{i\omega_1 t} + (\cos(\eta)E_{m2} - \sin(\eta)E_{M2})e^{i\omega_2 t} + E_{M3}e^{i\omega_3 t} \\ E_{m1}e^{i\omega_1 t} + (\sin(\eta)E_{m2} + \cos(\eta)E_{M2})e^{i\omega_2 t} + E_{m3}e^{i\omega_3 t} \end{bmatrix} \quad (D.2)$$

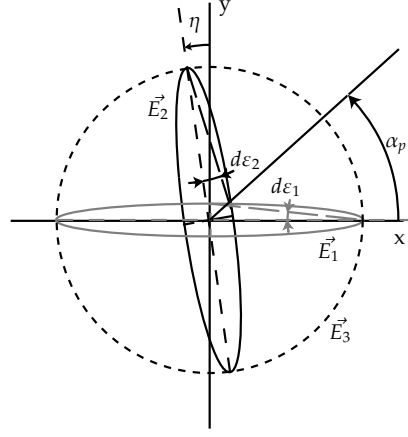


Figure D.1: Schematic representation of the E-fields present in the carrier frequency method as well as the schematic representation of the output of this measurement setup. \vec{E}_1, \vec{E}_2 are the E-fields emerging from the heterodyne laser of which the ellipticity is $d\epsilon_1$ and $d\epsilon_2$ respectively, \vec{E}_3 emerges from the circular reference source and α_p represents the angle of the polarizer.

where $\omega_f = 2\pi f_f t + \phi_{0f}$ and $f = 1, 2, 3$. A polarizer under angle α_p can be presented with the following Jones matrix:

$$P_{\alpha_p} = \begin{bmatrix} \cos^2 \alpha_p & \sin \alpha_p \cos \alpha_p \\ \sin \alpha_p \cos \alpha_p & \sin^2 \alpha_p \end{bmatrix} \quad (D.3)$$

The electromagnetic field entering the detector is calculated by multiplying the Jones matrix, representing the polarizer, and the Jones vector, representing the E-field entering the polarizer:

$$E_p = P(\alpha_p)E_{in} = \begin{bmatrix} E_{px} \\ E_{py} \end{bmatrix} \quad (D.4)$$

From calculation it follows:

$$E_{px} = \cos(\alpha_p) \left[\begin{aligned} & (\cos(\alpha_p)E_{M1} + \sin(\alpha_p)E_{m1})e^{i\omega_1 t} \\ & + \begin{pmatrix} (\cos(\alpha_p)\cos(\eta) + \sin(\alpha_p)\sin(\eta))E_{m2} \\ -(\cos(\alpha_p)\sin(\eta) - \sin(\alpha_p)\cos(\eta))E_{M2} \end{pmatrix} e^{i\omega_2 t} \\ & + (\cos(\alpha_p)E_{M3} + \sin(\alpha_p)E_{m3})e^{i\omega_3 t} \end{aligned} \right] \quad (D.5)$$

$$= \cos(\alpha_p) \left[\begin{aligned} & (\cos(\alpha_p)E_{M1} + \sin(\alpha_p)E_{m1})e^{i\omega_1 t} \\ & + (\cos(\alpha_p - \eta)E_{m2} + \sin(\alpha_p - \eta)E_{M2})e^{i\omega_2 t} \\ & + (\cos(\alpha_p)E_{M3} + \sin(\alpha_p)E_{m3})e^{i\omega_3 t} \end{aligned} \right] \quad (D.6)$$

and

$$E_{py} = \sin(\alpha_p) \left[\begin{aligned} & \left(\cos(\alpha_p)E_{M1} + \sin(\alpha_p)E_{m1} \right) e^{i\omega_1 t} \\ & + \left(\begin{aligned} & (\cos(\alpha_p) \cos(\eta) + \sin(\alpha_p) \sin(\eta))E_{m2} \\ & - (\cos(\alpha_p) \sin(\eta) - \sin(\alpha_p) \cos(\eta))E_{M2} \end{aligned} \right) e^{i\omega_2 t} \\ & + \left(\cos(\alpha_p)E_{M3} + \sin(\alpha_p)E_{m3} \right) e^{i\omega_3 t} \end{aligned} \right] \quad (D.7)$$

$$= \cos(\alpha_p) \left[\begin{aligned} & \left(\cos(\alpha_p)E_{M1} + \sin(\alpha_p)E_{m1} \right) e^{i\omega_1 t} \\ & + \left(\cos(\alpha_p - \eta)E_{m2} + \sin(\alpha_p - \eta)E_{M2} \right) e^{i\omega_2 t} \\ & + \left(\cos(\alpha_p)E_{M3} + \sin(\alpha_p)E_{m3} \right) e^{i\omega_3 t} \end{aligned} \right] \quad (D.8)$$

The intensity signal resulting from this E-field is calculated using:

$$I_p^{\alpha_p} = E_{px}^* E_{px} + E_{py}^* E_{py} \quad (D.9)$$

Since $E_{px} = \cos(\alpha_p) * E_{sub}$ and $E_{py} = \sin(\alpha_p) * E_{sub}$ it follows that $I_p = E_{sub}^* E_{sub}$.
Where

$$\begin{aligned} E_{sub} = & \left(\cos(\alpha_p)E_{M1} + \sin(\alpha_p)E_{m1} \right) e^{i\omega_1 t} \\ & + \left(\cos(\alpha_p - \eta)E_{m2} + \sin(\alpha_p - \eta)E_{M2} \right) e^{i\omega_2 t} \\ & + \left(\cos(\alpha_p)E_{M3} + \sin(\alpha_p)E_{m3} \right) e^{i\omega_3 t} \end{aligned} \quad (D.10)$$

Knowing E_{m1} , E_{m2} and E_{m3} are complex numbers this can be written as:

$$\begin{aligned} E_{sub} &= (A + iB)e^{i\omega_1 t} + (C + iD)e^{i\omega_2 t} + (E + iF)e^{i\omega_3 t} \quad (D.11) \\ \text{where } A &= \cos(\alpha_p)E_{01}\cos(d\varepsilon_1) \\ B &= -\sin(\alpha_p)E_{01}\sin(d\varepsilon_1) \\ C &= \cos(\alpha_p - \eta)E_{02}\sin(d\varepsilon_2) \\ D &= \sin(\alpha_p - \eta)E_{02}\cos(d\varepsilon_2) \\ E &= \cos(\alpha_p)E_{03} \\ F &= \sin(\alpha_p)E_{03} \end{aligned} \quad (D.12)$$

From this the intensity I_p can be calculated:

$$\begin{aligned} I_p &= (A + iB)e^{i\omega_1 t} + (C + iD)e^{i\omega_2 t} + (E + iF)e^{i\omega_3 t} \\ &\quad * \left[(A - iB)e^{-i\omega_1 t} + (C - iD)e^{-i\omega_2 t} + (E - iF)e^{-i\omega_3 t} \right] \end{aligned} \quad (D.13)$$

$$\begin{aligned} &= A^2 + B^2 + C^2 + D^2 + E^2 + F^2 \\ &+ 2(AC + BD)\cos((\omega_2 - \omega_1)t) + 2(AD - BC)\sin((\omega_2 - \omega_1)t) \\ &+ 2(AE + BF)\cos((\omega_3 - \omega_1)t) + 2(AF - BE)\sin((\omega_3 - \omega_1)t) \\ &+ 2(CE + DF)\cos((\omega_3 - \omega_2)t) + 2(CF - DE)\sin((\omega_3 - \omega_2)t) \end{aligned} \quad (D.14)$$

With use of a spectrum analyser only the beat frequencies f_3 with f_1 and f_3 with f_1 are measured:

$$\begin{aligned} I(f_1, f_3)^{\alpha_p} &= 2(AE + BF) \cos((\omega_3 - \omega_1)t) + 2(AF - BE) \sin((\omega_3 - \omega_1)t) \\ &= 2\sqrt{(AE + BF)^2 + (AF - BE)^2} \cos((\omega_3 - \omega_1)t - \arctan\left(\frac{AF - BE}{AE + BF}\right)) \end{aligned} \quad (D.15)$$

$$\begin{aligned} I(f_2, f_3)^{\alpha_p} &= 2(CE + DF) \cos((\omega_3 - \omega_2)t) + 2(CF - DE) \sin((\omega_3 - \omega_2)t) \\ &= 2\sqrt{(CE + DF)^2 + (CF - DE)^2} \cos((\omega_3 - \omega_2)t - \arctan\left(\frac{CF - DE}{CE + DF}\right)) \end{aligned} \quad (D.16)$$

Of this intensity signal only the amplitude is measured, not the phase. Therefore only the amplitude will be calculated here.

$$\begin{aligned} I_a(f_1, f_3)^{\alpha_p} &= 2\sqrt{(AE + BF)^2 + (AF - BE)^2} \\ &= 2\sqrt{(AE)^2 + (BF)^2 + (AF)^2 + (BE)^2} \end{aligned} \quad (D.17)$$

$$\begin{aligned} I_a(f_2, f_3)^{\alpha_p} &= 2\sqrt{(CE + DF)^2 + (CF - DE)^2} \\ &= 2\sqrt{(CE)^2 + (DF)^2 + (CF)^2 + (DE)^2} \end{aligned} \quad (D.18)$$

Filling in $A - F$ from equation D.12 results in:

$$I_a(f_1, f_3)^{\alpha_p} = 2E_{01}E_{03} \sqrt{\cos^2(\alpha_p) \cos^2(d\varepsilon_1) + \sin^2(\alpha_p) \sin^2(d\varepsilon_1)} \quad (D.19)$$

$$I_a(f_2, f_3)^{\alpha_p} = 2E_{02}E_{03} \sqrt{\cos^2(\alpha_p - \eta) \sin^2(d\varepsilon_2) + \sin^2(\alpha_p - \eta) \cos^2(d\varepsilon_2)} \quad (D.20)$$

Representing the intensities measured by the carrier frequency measurement as a function of the polarizer angle (α_p).

D.2 Beat frequency measurement

For the beat frequency measurement a polarizer is rotated directly in front of the heterodyne laser head. In this case the intensity of the beat frequency signal consists of frequencies f_1 and f_2 . From equation D.14 this beat frequency is:

$$\begin{aligned} I(f_1, f_2)^{\alpha_p} &= 2(AC + BD) \cos((\omega_2 - \omega_1)t) + 2(AD - BC) \sin((\omega_2 - \omega_1)t) \\ &= 2\sqrt{(AC + BD)^2 + (AD - BC)^2} \cos((\omega_2 - \omega_1)t - \arctan\left(\frac{AD - BC}{AC + BD}\right)) \end{aligned} \quad (D.21)$$

Of this intensity signal also only the amplitude is measured, not the phase. Therefore only the amplitude will be calculated here.

$$\begin{aligned} I_a(f_1, f_2)^{\alpha_p} &= 2\sqrt{(AC + BD)^2 + (AD - BC)^2} \\ &= 2\sqrt{(AC)^2 + (BD)^2 + (AD)^2 + (BC)^2} \end{aligned} \quad (D.22)$$

Filling in $A - D$ from equation D.12 results in:

$$\begin{aligned} I_a(f_1, f_2)^{\alpha_p} &= 2E_{01}E_{02} \sqrt{\begin{pmatrix} \cos^2(\alpha_p) \sin^2(\alpha_p - \eta) \cos^2(d\varepsilon_1) \cos^2(d\varepsilon_2) \\ + \sin^2(\alpha_p) \cos^2(\alpha_p - \eta) \sin^2(d\varepsilon_1) \sin^2(d\varepsilon_2) \\ + \cos^2(\alpha_p) \cos^2(\alpha_p - \eta) \cos^2(d\varepsilon_1) \sin^2(d\varepsilon_2) \\ + \sin^2(\alpha_p) \sin^2(\alpha_p - \eta) \sin^2(d\varepsilon_1) \cos^2(d\varepsilon_2) \end{pmatrix}} \\ &= 2E_{01}E_{02} \sqrt{\begin{pmatrix} (\cos^2(\alpha_p) \cos^2(d\varepsilon_1) + \sin^2(\alpha_p) \sin^2(d\varepsilon_1)) \\ * (\cos^2(\alpha_p - \eta) \sin^2(d\varepsilon_2) + \sin^2(\alpha_p - \eta) \cos^2(d\varepsilon_2)) \end{pmatrix}} \end{aligned}$$

Representing the intensity measured by the beat frequency measurement as a function of the polarizer angle (α_p).

Appendix E

Uncertainty analysis of the Fabry-Pérot cavities

In this appendix the uncertainty analysis of the existing and the new Fabry-Pérot cavity are derived. Part of the analysis is based on the work of Wetzels [82].

E.1 Existing Fabry-Pérot cavity

The uncertainty of the Fabry-Pérot cavity depends on the uncertainty with which the measurement system works and on all subsystems such as the frequency counter. Further some fundamental principles influence the uncertainty of the system. Finally the uncertainty resulting from the calibration procedure should be mentioned. All these are discussed in detail next.

E.1.1 Axial mode effect

In order to derive a calibration displacement equation 4.1 is used to derive:

$$\Delta L = -L \left(\frac{\Delta f}{f} + \frac{\Delta n}{n} \right) \quad (\text{E.1})$$

Here L is the mechanical length of the cavity, f is the frequency (473 THz), Δf is the measured frequency change, n is the refractive index in the system and Δn is the refractive index change during measurement inside the system.

The length of the cavity is determined by measuring the Free Spectral Range (\mathcal{FSR} : frequency difference between two longitudinal modes) of the system:

$$L = \frac{c}{2n \mathcal{FSR}} \quad (\text{E.2})$$

The uncertainty of this length can be calculated as follows:

$$u(L) = \sqrt{\sum_{i=1}^z \left(\frac{\partial L}{\partial x_i} u(x_i) \right)^2} \quad (\text{E.3})$$

Parameter	Nominal value	Uncertainty	Uncertainty in L
c	299792458 m s ⁻¹	0 m s ⁻¹	0
n	1,000273	2,3 · 10 ⁻⁸	-3,3 · 10 ⁻⁹ m
\mathcal{FSR}	1050 · 10 ⁶ Hz	51,4 · 10 ³ Hz	-7,0 · 10 ⁻⁶ m
Total			7 · 10 ⁻⁶ m

Table E.1: Uncertainty of the length derived by the Free Spectral range measurement. c: speed of light, n: absolute refractive index, \mathcal{FSR} : Free spectral range.

The uncertainty of the measured length change with the Fabry-Pérot cavity can now be derived from equation E.1 combined with the uncertainties of the measurement systems and the nominal values of the parameters:

Parameter	Nominal value	Uncertainty	Uncertainty in ΔL
L	140 · 10 ⁻³ m	7 · 10 ⁻⁶ m	0,01 nm
Δf	700 · 10 ⁶ Hz	50 · 10 ³ Hz	0,02 nm
f	473 · 10 ¹² Hz	12 · 10 ³ Hz	0,00 nm
Δn	2 · 10 ⁻⁷	1 · 10 ⁻⁹	0,14 nm
n	1,000273	2,3 · 10 ⁻⁸	0,00 nm
Total			0,14 nm

Table E.2: Uncertainty of the displacement derived by the frequency measurement. L: Length of the cavity, Δf : measured frequency difference, f: absolute frequency, Δn : refractive index change, n: absolute refractive index.

E.1.2 Transversal mode effect

The working principle of the Fabry-Pérot cavity is based on the measurement of the resonance frequency of the cavity as described in equation 4.1:

$$f = \frac{kc}{2nL} \quad (\text{E.4})$$

This equation is based on the assumption that no transversal modes exist in the cavity. The resonance frequency of the axial-plus-transverse modes in the cavity is given by [47]:

$$f = \frac{c}{2nL} \left[k + \frac{\psi_{nm}}{2\pi} - \frac{\Delta\beta_m p_m}{2\pi} \right] \quad (\text{E.5})$$

The first term equals equation E.4 and represents the plane wave resonance frequency, the second term represents the influence of transversal modes on the frequency and the third term represents an additional atomic frequency pulling effect resulting from an active medium inside the cavity. Since there is no active medium inside the cavity this term reduces to zero. The effect of the transversal modes can be calculated using equation:

$$\psi_{nm} = 2(n + m + 1) \arccos \left(\pm \sqrt{\left(1 - \frac{L}{R_1}\right) \left(1 - \frac{L}{R_2}\right)} \right) \quad (\text{E.6})$$

In the existing cavity the length of the cavity (L) is 140 mm, the radius of both mirrors (R_1 and R_2) is 600 mm. The normal working mode of the laser is TEM₀₀ resulting in a frequency effect of 238 MHz. For a displacement of 1 μm the effect on frequency is 813 Hz and for a displacement of 300 μm the extra effect is 245 kHz. With a sensitivity of 3,3802 MHz nm⁻¹ of the system, this results in an error of 0,00 nm for a displacement of 1 μm and 0,07 nm for a displacement of 300 μm .

E.1.3 Linear thermal expansion

In order to calibrate sensors, a sensor platform is constructed on the Fabry-Pérot cavity. This platform is called the top platform. Effort was made to place this platform thermally on the bottom mirror, using thermal compensation in the construction loop in combination with low expansion materials. The thermal structure is shown in figure E.1.

From this figure it can be seen that there are some uncompensated parts in the construction which are: Zerodur rods ($L_{\text{Zerodur}}=140 \text{ mm}$, $\alpha = 5 \cdot 10^{-8} \text{ K}^{-1}$), aluminum clamp ($L_{\text{alu}}=4,5 \text{ mm}$, $\alpha = 23 \cdot 10^{-6} \text{ K}^{-1}$) of the upper mirror, the invar ring ($L_{\text{Invar}}=5 \text{ mm}$, $\alpha = 1,5 \cdot 10^{-6} \text{ K}^{-1}$) to support the moving retroreflector and the invar adapter ($L_{\text{Invar}}=35 \text{ mm}$, $\alpha = 1,5 \cdot 10^{-6} \text{ K}^{-1}$). These result in a calibration error of:

$$\Delta L_{\Delta T} = \left(\alpha_{\text{alu}} \cdot L_{\text{alu}} + \alpha_{\text{Invar}} \cdot L_{\text{Invarring}} - \alpha_{\text{Zerodur}} \cdot L_{\text{Zerodur}} - \alpha_{\text{Invar}} \cdot L_{\text{Invaradapter}} \right) \Delta T \quad (\text{E.7})$$

This results in a linear expansion of 51,5 nm K⁻¹.

E.1.4 Thermal gradients

Upper and lower mirror are in the middle of the Fabry-Pérot setup. The zerodur rods to connect upper and lower platform are placed on a radius of 70 mm from the center to provide a large platform. As a result thermal gradients will influence the position of the probe and mirror resulting in uncertainties. Gradients are calculated using the next equation:

$$\Delta z = \alpha \frac{T_1 - T_2}{h} \frac{R^2}{2} \quad (\text{E.8})$$

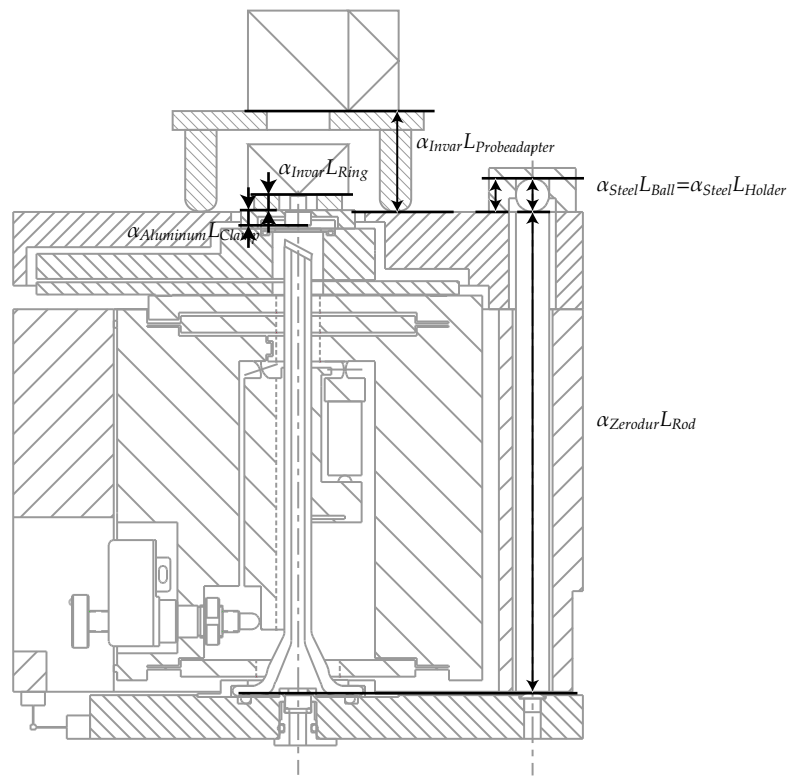


Figure E.1: Fabry-Pérot cavity with a schematical representation of the thermal loop in the construction. Here α represents the linear expansion coefficient of the material named by the subscription, L represents the length of the component named by the subscription.

where Δz represents the displacement in measurement direction of the center compared to the connection points of the zerodur rods, α represents the linear expansion coefficient, $T_1 - T_2$ represents the temperature difference of upper and lower part of the platform, h represents the height of the platform, R represents the distance between connection points and center of the platform. For top and bottom platform ($\alpha = 24 \cdot 10^{-6}$, $h=15$ mm, $R=70$ mm, and $T_1 - T_2 = 0,1$ mK) this results in a displacement of 0,4 nm. For the invar adapter ($\alpha = 1,5 \cdot 10^{-6}$, $h=9$ mm, $R=37$ mm, $T_1 - T_2 = 0,1$ mK) this results in a displacement of 0,01 nm.

E.1.5 Mirror tilt

The parallel guiding mechanism was tested for tilt by Wetzels. The maximum tilt was $2,5 \mu\text{rad}$. As a result the orientation of the optical axis may change while the probe still measures the same mirror position. Wetzels [61] also derived an equation to determine the effect of this, resulting in an error of 0,4 nm over the range of $300 \mu\text{m}$ and 0,00 nm over a range of $1 \mu\text{m}$.

E.1.6 Background slope

In the original Fabry-Pérot a HeNe-laser was used with a non-constant background slope. As a result the locking point of the slave laser is shifted from the left of the resonance curve toward the right of the resonance curve while scanning through the active area of the laser. This effect was already negligible with the gas laser. The diode laser used now has a gain curve with a constant slope in the used working area, resulting in a constant shift of the frequency. Since the measurement consists of a frequency change this will not affect measurement uncertainty.

E.1.7 Cosine error

Due to alignment errors the translation axis of the moving mirror and the probe under calibration will not be exactly in line. It is estimated that in practice the alignment error can be reduced to $1,5 \text{ mrad}$. Based on the equation derived by Wetzels [61] this results in an error of 0,3 nm for the entire range of $300 \mu\text{m}$ and an error of 0,001 nm for the range of $1 \mu\text{m}$.

E.1.8 Total uncertainty of the Fabry-Pérot cavity

In the previous sections different parts of the Fabry-Pérot cavity were discussed along with the resulting uncertainties. In table E.3 the total uncertainty of a measurement with the Fabry-Pérot cavity is calculated. From the table it can be seen that the major part of uncertainty originates from thermal effects. Further the mirror tilt is an important aspect. The effect of mirror tilt depends on the radii of the mirrors used and the length of the cavity. The gradients depend on the homogeneity of the system, the size and the expansion coefficient.

Parameter	Uncertainty over 1 μm	Uncertainty over 300 μm
Axial mode effect	0,14 nm	0,14 nm
Transversal mode effect	0,00 nm	0,07 nm
Brewster window	16,5 nm K ⁻¹	16,5 nm K ⁻¹
Mirror tilt	0,4 nm	0,4 nm
Background slope	0	0
Thermal expansion	51,5 nm K ⁻¹	51,5 nm K ⁻¹
Gradient upper platform	0,4 nm	0,4 nm
Gradient lower platform	0,4 nm	0,4 nm
Gradient probe adapter	0,01 nm	0,01 nm
Cosine error (1,5 mrad)	0,001 nm	0,3 nm
Total ($\Delta T=0,01$ K)	0,89 nm	0,94 nm

Table E.3: Results of the uncertainty analysis of the metrological Fabry-Pérot interferometer. The total uncertainty is based on a measurement with a maximum temperature change of 0,01 K.

E.2 New designed cavity

The uncertainty analysis of the newly designed cavity is based on the analysis of the existing cavity .

E.2.1 Axial mode effect

The uncertainty at the displacement measurement is calculated based on the same arguments as in section E.1.1. As a result of different cavity length and free spectral range the uncertainties are also different. Further a different detector has to be used in combination with a different frequency counter. The uncertainty of this frequency counting system is estimated to equal the former system. The uncertainty in the cavity length for the small cavity is shown in table E.4.

Parameter	Nominal value	Uncertainty	Uncertainty in L
c	299792458 m s ⁻¹	0 m s ⁻¹	0
n	1,000273	$2,3 \cdot 10^{-8}$	$-0,55 \cdot 10^{-9}$ m
\mathcal{FSR}	$6,25 \cdot 10^9$ Hz	$51,4 \cdot 10^3$ Hz	$-1,97 \cdot 10^{-7}$ m
Total			$1,97 \cdot 10^{-7}$ m

Table E.4: Uncertainty of the length derived by the Free Spectral range measurement. c: speed of light, n: absolute refractive index, \mathcal{FSR} : Free spectral range.

The uncertainty of the measured length change with the Fabry-Pérot cavity can now be derived from equation E.1 combined with the uncertainties of the measurement systems and the nominal values of the parameters:

Parameter	Nominal value	Uncertainty	Uncertainty in ΔL
L	$24 \cdot 10^{-3}$ m	$1,97 \cdot 10^{-7}$ m	0,001 nm
Δf	$3,15 \cdot 10^9$ Hz	$50 \cdot 10^3$ Hz	0,002 nm
f	$473 \cdot 10^{12}$ Hz	$12 \cdot 10^3$ Hz	0,000 nm
Δn	$2 \cdot 10^{-7}$	$1 \cdot 10^{-9}$	0,024 nm
n	1,000273	$2,3 \cdot 10^{-8}$	0,000 nm
Total			0,024 nm

Table E.5: Uncertainty of the displacement derived by the frequency measurement for the small Fabry-Pérot. L : Length of the cavity, Δf : measured frequency difference, f : absolute frequency, Δn : refractive index change, n : absolute refractive index.

E.2.2 Transversal mode effect

The frequency effect according to equations E.5 and E.6 now becomes 619 MHz. The total stroke of the actuator is 6 μm which results in a frequency change of 55,2 kHz which in turn results in an error of 0,003 nm. For a stroke of 1 μm the frequency change equals 12,8 kHz resulting in an error of 0,001 nm.

E.2.3 Mirror tilt

The tilt of the actuator was measured using an autocollimator. The maximum tilt was 20 μrad . Based on the equation derived by Wetzels [61] this will result in a cavity length change of 0,05 nm. A second effect of mirror tilt will manifest itself in this setup also. As a result of the tilt a cosine effect will result. The distance between the probe and the point where top mirror and optical axis cross is 16,5 mm. This is a result of a relatively thick mirror (11 mm) and a bending prism on top of it (5 mm), in order not to put load on the mirror 0,5 mm is left between prism and calibration object. As a result an extra cosine error of 3 pm exists.

E.2.4 background slope

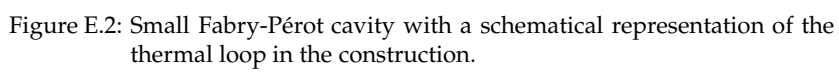
The background slope of the diode laser is in one direction and is relatively constant over the used range. Hence the effect is negligible.

E.2.5 cosine error

It was estimated that the alignment can be done within 10 mrad, resulting in an error of 0,3 nm over the range of 6 μm , and 0,05 nm over the range of 1 μm .

E.2.6 Linear thermal expansion

In figure E.2 the schematical representation of the thermal loop of the small Fabry-Pérot cavity is given.



From this figure it can be seen that the thermal expansion of the balls is compensated by a thermal expansion of their holders. Further the thermal expansion of the adapter equals the thermal expansion of the part on the base cylinder. The thermal expansion of the bottom plate ($\alpha = 1,5 \cdot 10^{-6}$, $L=2,5$ mm) and zerodur rod ($\alpha = 5 \cdot 10^{-8}$, $L=76$ mm) compensate to $0,05 \text{ nm K}^{-1}$. Finally the remaining uncompensated part is formed by the upper mirror holder and clamp. Since the mirror is relatively thick (11 mm) and a prism (height 5 mm) is necessary for the control loop the length is relatively large ($\alpha = 1,5 \cdot 10^{-6}$, $L=16,5$ mm). The thermal expansion remaining (including the difference of zerodur rod and invar bottom plate) is $24,8 \text{ nm K}^{-1}$.

E.2.7 Thermal gradients

As a result of vertical thermal gradients the structural components will bend. The effect of vertical gradients will come from the probe adapter and the bottom plate. The vertical displacement of the center of the plates is calculated using equation E.9:

$$\Delta z = \alpha \frac{T_1 - T_2}{h} \frac{R^2}{2} \quad (\text{E.9})$$

where T_1 is the temperature on top of the plate, T_2 the temperature at the bottom of the plate, h is the thickness of the plate, R the radius of the plate to the zerodur connection points. The radius (R) on which the plates are supported by the zerodur rods is 43 mm. The thickness of the probe adapter is 5 mm, and the thickness of the bottom plate is 8 mm. Assuming a temperature difference of 10^{-4} K over the plate, equal as in the original Fabry-Pérot this results in a gradient of $0,029 \text{ nm}$ for the probe adapter and $0,035 \text{ nm}$ of the bottom plate.

E.2.8 Total uncertainty

Based on the subjects discussed above the total uncertainty of the small Fabry-Pérot cavit can be calculated. The results are shown in table E.6. From this table it can be seen that the major part of uncertainty again emerges from linear expansion of the mirror and prism clamp.

Parameter	Uncertainty over 1 μm	Uncertainty over 6 μm
Axial mode effect	0,024 nm	0,024 nm
Transversal mode effect	0,001 nm	0,003 nm
Mirror tilt	0,05 nm	0,05 nm
Background slope	0	0
Thermal expansion	24,8 nm K ⁻¹	24,8 nm K ⁻¹
Gradient upper platform	0,03 nm	0,03 nm
Gradient lower platform	0,04 nm	0,04 nm
Cosine error (1,5 mrad)	0,05 nm	0,3 nm
Total ($\Delta T=0,01$ K)	0,26 nm	0,40 nm

Table E.6: Results of the uncertainty analysis of the small Fabry-Pérot interferometer. The total uncertainty is based on a measurement with a maximum temperature change of 0,01 K.

Appendix F

Lock-in amplifier signals

In chapter 2 an equation was derived for the periodic deviations resulting from a linear interferometer. The entire measurement signal was given by equation 2.14:

$$\begin{aligned} I_{meas} = & M \cos(2\pi(f_2 - f_1)t + \phi_{ref} + \Delta\phi) \\ & + N \sin(2\pi(f_2 - f_1)t + \phi_{ref} + \Delta\phi) \end{aligned} \quad (F.1)$$

In combination with equation 2.16, it can be derived that:

$$M = (A + C) + (A - C) \sin(2\theta) + E \cos(2\theta) \quad (F.2)$$

$$N = (B + D) + (B - D) \sin(2\theta) + F \cos(2\theta) \quad (F.3)$$

where A, B, C, D, E and F are equal as in equation 2.16. These can also be rewritten into a form representing first and second order periodic-deviations:

$$A = \chi^2 [a_1 \cos \Delta\phi + a_2 \sin \Delta\phi] \quad (F.4)$$

$$B = \chi^2 [-a_2 \cos \Delta\phi + a_1 \sin \Delta\phi] \quad (F.5)$$

$$C = \xi^2 [c_1 \cos \Delta\phi + c_2 \sin \Delta\phi] \quad (F.6)$$

$$D = \xi^2 [-c_2 \cos \Delta\phi + c_1 \sin \Delta\phi] \quad (F.7)$$

$$E = \chi\xi [e_1 + e_2 \cos 2\Delta\phi + e_3 \sin 2\Delta\phi] \quad (F.8)$$

$$F = \chi\xi [e_4 - e_3 \cos 2\Delta\phi + e_2 \sin 2\Delta\phi] \quad (F.9)$$

where

$$a_1 = \cos \beta \sin \alpha \cos(d\varepsilon_1) \cos(d\varepsilon_2) + \sin \beta \cos \alpha \sin(d\varepsilon_1) \sin(d\varepsilon_2) \quad (\text{F.10})$$

$$a_2 = -\cos \beta \cos \alpha \cos(d\varepsilon_1) \sin(d\varepsilon_2) + \sin \beta \sin \alpha \sin(d\varepsilon_1) \cos(d\varepsilon_2) \quad (\text{F.11})$$

$$c_1 = \sin \beta \cos \alpha \cos(d\varepsilon_1) \cos(d\varepsilon_2) + \cos \beta \sin \alpha \sin(d\varepsilon_1) \sin(d\varepsilon_2) \quad (\text{F.12})$$

$$c_2 = -\cos \beta \cos \alpha \sin(d\varepsilon_1) \cos(d\varepsilon_2) + \sin \beta \sin \alpha \cos(d\varepsilon_1) \sin(d\varepsilon_2) \quad (\text{F.13})$$

$$e_1 = \cos \beta \cos \alpha \cos(d\varepsilon_1) \cos(d\varepsilon_2) - \sin \beta \sin \alpha \sin(d\varepsilon_1) \sin(d\varepsilon_2) \quad (\text{F.14})$$

$$e_2 = \sin \beta \sin \alpha \cos(d\varepsilon_1) \cos(d\varepsilon_2) - \cos \beta \cos \alpha \sin(d\varepsilon_1) \sin(d\varepsilon_2) \quad (\text{F.15})$$

$$e_3 = -\cos \beta \sin \alpha \sin(d\varepsilon_1) \cos(d\varepsilon_2) - \sin \beta \cos \alpha \cos(d\varepsilon_1) \sin(d\varepsilon_2) \quad (\text{F.16})$$

$$e_4 = -\cos \beta \sin \alpha \cos(d\varepsilon_1) \sin(d\varepsilon_2) - \sin \beta \cos \alpha \sin(d\varepsilon_1) \cos(d\varepsilon_2) \quad (\text{F.17})$$

The measurement signal can be rewritten as follows:

$$I_{meas} = \begin{aligned} & \left(M \cos(\Delta\phi) + N \sin(\Delta\phi) \right) \cos \left(2\pi(f_2 - f_1)t + \phi_{ref} \right) \\ & + \left(-M \sin(\Delta\phi) + N \cos(\Delta\phi) \right) \sin \left(2\pi(f_2 - f_1)t + \phi_{ref} \right) \end{aligned} \quad (\text{F.18})$$

where

$$\begin{aligned} M &= (A + C) + (A - C) \sin(2\theta) + E \cos(2\theta) \\ &= (a_1 + c_1) \cos(\Delta\phi) + (a_2 + c_2) \sin(\Delta\phi) \\ &\quad + (a_1 - c_1) \sin(2\theta) \cos(\Delta\phi) + (a_2 - c_2) \sin(2\theta) \sin(\Delta\phi) \\ &\quad + e_1 \cos(2\theta) + e_2 \cos(2\theta) \cos(2\Delta\phi) + e_3 \cos(2\theta) \sin(2\Delta\phi) \\ &= (a_1 + c_1 + (a_1 - c_1) \sin(2\theta)) \cos(\Delta\phi) \\ &\quad + (a_2 + c_2 + (a_2 - c_2) \sin(2\theta)) \sin(\Delta\phi) \\ &\quad + e_1 \cos(2\theta) + e_2 \cos(2\theta) \cos(2\Delta\phi) + e_3 \cos(2\theta) \sin(2\Delta\phi) \\ &= t_1 \cos(\Delta\phi) + t_2 \sin(\Delta\phi) + t_3 + t_4 \cos(2\Delta\phi) + t_5 \sin(2\Delta\phi) \end{aligned} \quad (\text{F.19})$$

and

$$\begin{aligned} N &= (B + D) + (B - D) \sin(2\theta) + F \cos(2\theta) \\ &= (-a_2 - c_2) \cos(\Delta\phi) + (a_1 + c_1) \sin(\Delta\phi) \\ &\quad + (c_2 - a_2) \sin(2\theta) \cos(\Delta\phi) + (a_1 - c_1) \sin(2\theta) \sin(\Delta\phi) \\ &\quad + e_4 \cos(2\theta) - e_3 \cos(2\theta) \cos(2\Delta\phi) + e_2 \cos(2\theta) \sin(2\Delta\phi) \\ &= -(a_2 + c_2 + (a_2 - c_2) \sin(2\theta)) \cos(\Delta\phi) \\ &\quad + (a_1 + c_1 + (a_1 - c_1) \sin(2\theta)) \sin(\Delta\phi) \\ &\quad + e_4 \cos(2\theta) - e_3 \cos(2\theta) \cos(2\Delta\phi) + e_2 \cos(2\theta) \sin(2\Delta\phi) \\ &= t_1 \sin(\Delta\phi) - t_2 \cos(\Delta\phi) + t_6 + t_4 \sin(2\Delta\phi) - t_5 \cos(2\Delta\phi) \end{aligned} \quad (\text{F.20})$$

Filling in equations F.19 and F.20 in F.18 results in:

$$\begin{aligned} I_{meas} &= \left[t_1 + (t_3 + t_4) \cos(\Delta\phi) + (t_5 + t_6) \sin(\Delta\phi) \right] \cos \left(\Delta\omega t + \phi_{ref} \right) \\ &\quad + \left[-t_2 + (t_4 - t_3) \sin(\Delta\phi) + (t_6 - t_5) \cos(\Delta\phi) \right] \sin \left(\Delta\omega t + \phi_{ref} \right) \end{aligned} \quad (\text{F.21})$$

where $t_i (i=1,2,3,4,5,6)$ are a function of $a_1, a_2, c_1, c_2, e_1, e_2, e_3, e_4, \sin(2\theta), \cos(2\theta)$ as can be seen from equations F.19 and F.20. The signals resulting from the lock-in amplifier are:

$$\begin{aligned} S_0^{nl} &= \int I_{ref}(\Delta\omega t + \phi_{ref}) \times I_{meas}(\Delta\omega t + \phi_{ref}) dt \\ &= \frac{1}{2} [t_1 + (t_3 + t_4) \cos(\Delta\phi) + (t_5 + t_6) \sin(\Delta\phi)] \\ &= t_1' + t_3' \cos(\Delta\phi - t_4'), \end{aligned} \quad (F.22)$$

$$\begin{aligned} S_{90}^{nl} &= \int I_{ref}(\Delta\omega t + \phi_{ref} + \frac{\pi}{2}) \times I_{meas}(\Delta\omega t + \phi_{ref}) dt \\ &= \frac{1}{2} [-t_2 + (t_4 - t_3) \sin(\Delta\phi) + (t_6 - t_5) \cos(\Delta\phi)] \\ &= t_2' + t_5' \sin(\Delta\phi - t_6'), \end{aligned} \quad (F.23)$$

Since in the phase quadrature measurement only the relative phase is measured and in the compensation method only the relative amplitude is important these signals may be rewritten into:

$$S_0^{nl} = x_0 + R \cos(\Delta\phi) \quad (F.24)$$

$$S_{90}^{nl} = y_0 + R \frac{1}{r} \sin(\Delta\phi - \alpha_l), \quad (F.25)$$

where x_0 and y_0 are offsets in the signal representing a first order periodic deviation, R is the amplitude of both signals and $\frac{1}{r}$ and α_l represent the amplitude ratio of both signals and the deviation from phase quadrature. The ellipse parameters expressed in the parameters of equations F.10-F.17:

$$x_0 = \frac{1}{2} (a_1 + c_1 + (a_1 - c_1) \sin(2\theta)) \quad (F.26)$$

$$y_0 = -\frac{1}{2} (a_2 + c_2 + (a_2 - c_2) \sin(2\theta)) \quad (F.27)$$

$$R = \frac{1}{2} \cos(2\theta) \sqrt{(e_1 + e_2)^2 + (e_3 + e_4)^2} \quad (F.28)$$

$$r = \frac{\sqrt{(e_1 + e_2)^2 + (e_3 + e_4)^2}}{\sqrt{(e_2 - e_1)^2 + (e_4 - e_3)^2}} \quad (F.29)$$

$$\alpha_l = \arctan\left(\frac{e_2 - e_1}{e_4 - e_3}\right) - \arctan\left(\frac{e_3 + e_4}{e_1 + e_2}\right) \quad (F.30)$$

According to Heydemann [5] the equation of the distorted ellips:

$$[S_0^{nl} - x_0]^2 + \left[\frac{(S_{90}^{nl} - y_0)r + (S_0^{nl} - x_0) \sin \alpha_l}{\cos(\alpha_l)} \right]^2 = R^2 \quad (F.31)$$

can be fitted in the following form:

$$A_f (S_0^{nl})^2 + B_f (S_{90}^{nl})^2 + C_f S_0^{nl} S_{90}^{nl} + D_f S_0^{nl} + E_f S_{90}^{nl} = 1 \quad (\text{F.32})$$

$$\text{where } A_f = (R^2 \cos^2(\alpha_l) - x_0^2 - r^2 y_0^2 - 2r x_0 y_0 \sin(\alpha_l))^{-1} \quad (\text{F.33})$$

$$B_f = A_f r^2 \quad (\text{F.34})$$

$$C_f = 2A_f r \sin(\alpha_l) \quad (\text{F.35})$$

$$D_f = -2A_f (x_0 + r y_0 \sin(\alpha_l)) \quad (\text{F.36})$$

$$E_f = -2A_f (r y_0 + x_0 \sin(\alpha_l)) \quad (\text{F.37})$$

From this the parameters of the ellipse can be derived:

$$\alpha_l = \arcsin\left(\frac{C_f}{\sqrt{4A_f B_f}}\right) \quad (\text{F.38})$$

$$r = \sqrt{\frac{B_f}{A_f}} \quad (\text{F.39})$$

$$x_0 = \frac{2B_f D_f - E_f C_f}{C_f^2 - 4A_f B_f} \quad (\text{F.40})$$

$$y_0 = \frac{2A_f E_f - D_f C_f}{C_f^2 - 4A_f B_f} \quad (\text{F.41})$$

And the corrected signals are:

$$S_0 = S_0^{nl} - x_0 \quad (\text{F.42})$$

$$S_{90} = \frac{1}{\cos(\alpha_l)} \left[(S_0^{nl} - x_0) \sin(\alpha_l) + r (S_{90}^{nl} - y_0) \right] \quad (\text{F.43})$$

Appendix G

Refractive index equations

In this appendix the used equations to determine the refractive index of air are presented. All derived for a wavelength of $\lambda = 632,991$ nm. The temperature (T) should be filled in in K, the pressure (P) in Pa, the humidity (f) in Pa and the CO₂content (x_{CO_2}) in ppm.

G.1 Birch and Down's equation

$$\begin{aligned} n_{TPf} - 1 &= \frac{D \cdot P}{96095,43} \cdot \frac{1 + 10^{-8} (0,601 - 0,00972(T - 273,15)) P}{1 + 0,0036610(T - 273,15)} \\ &\quad - f \cdot 3,63442 \cdot 10^{-10} \\ \text{with } D &= 2,7653 \cdot 10^{-4} \end{aligned} \quad (G.1)$$

G.2 Bönsch and Potulski

$$\begin{aligned} n_{TPfx} - 1 &= \frac{D \cdot P}{93214,60} \cdot \frac{1 + 10^{-8} (0,5953 - 0,009876(T - 273,15)) P}{1 + 0,0036610(T - 273,15)} \\ &\quad - f \cdot 3,70616 \cdot 10^{-10} \\ \text{with } D &= 2,68227 \cdot 10^{-4} \cdot (1 + 0,5327 \cdot (x_{CO_2} - 400)) \end{aligned} \quad (G.2)$$

G.3 Ciddor

$$\begin{aligned}
 n_{TPfx} - 1 &= \frac{\rho_a}{\rho_{as}} \cdot n_{as-1} \frac{\rho_w}{\rho_{ws}} \cdot n_{ws-1} & (G.3) \\
 \text{with } \frac{\rho_a}{\rho_{as}} &= \frac{P}{P_{as}} \frac{Z(P_{as}, T_{as})}{Z(P, T)} \frac{T_{as}}{T} (1 - x_w) \\
 \frac{\rho_w}{\rho_{ws}} &= \frac{P}{P_{ws}} \frac{Z(P_{ws}, T_{ws})}{Z(P, T)} \frac{T_{ws}}{T} x_w \\
 n_{as-1} &= 2,765303241 \cdot 10^{-4} \cdot (1 + 0,534 \cdot 10^{-6} (x_{CO_2} - 450)) \\
 n_{ws-1} &= 3,083274424 \cdot 10^{-6} \\
 x_w &= \left(1,00062 + 3,14 \cdot 10^{-8} P + 5,6 \cdot 10^{-7} (T - 273,15)^2 \right) \cdot \frac{f}{P} \\
 Z(P, T) &= 1 - \frac{P}{T} \cdot \left(\begin{aligned} &a_0 + a_1(T - 273,15) + a_2(T - 273,15)^2 \\ &+ (b_0 + b_1(T - 273,15)) \cdot x_w + (c_0 + c_1(T - 273,15)x_w^2) \end{aligned} \right) \\
 &\quad + \left(\frac{P}{T} \right)^2 \cdot (d + e \cdot x_w^2)
 \end{aligned}$$

where the standard conditions for dry air (subscript a) and wet air (subscript w) are $P_{as} = 101325$ Pa, $P_{ws} = 1333$ Pa, $T_{as} = 288,15$ K and $T_{ws} = 293,15$ K.

The constants used are:

$$R = 8,314510 \text{ J mol}^{-1} \text{ K}^{-1} \quad (G.4)$$

$$M_w = 0,018015 \text{ kg mol}^{-1} \quad (G.5)$$

$$a_0 = 1,58123 \cdot 10^{-6} \text{ K Pa}^{-1} \quad (G.6)$$

$$a_1 = -2,9331 \cdot 10^{-8} \text{ Pa}^{-1} \quad (G.7)$$

$$a_2 = 1,1043 \cdot 10^{-10} \text{ K}^{-1} \text{ Pa}^{-1} \quad (G.8)$$

$$b_0 = 5,707 \cdot 10^{-6} \text{ K Pa}^{-1} \quad (G.9)$$

$$b_1 = -2,051 \cdot 10^{-8} \text{ Pa}^{-1} \quad (G.10)$$

$$c_0 = 1,9898 \cdot 10^{-4} \text{ K Pa}^{-1} \quad (G.11)$$

$$c_1 = -2,376 \cdot 10^{-6} \text{ Pa}^{-1} \quad (G.12)$$

$$d = 1,83 \cdot 10^{-11} \text{ K}^2 \text{ Pa}^{-2} \quad (G.13)$$

$$e = -0,765 \cdot 10^{-8} \text{ K}^2 \text{ Pa}^{-2} \quad (G.14)$$

Acknowledgments

It is a pleasure to thank the people who have contributed each in their own way in the work that has led to this thesis.

First of all I would like to thank my parents for supporting me to do whatever I wanted as long as it was with dedication. Ever since my father was working in metrology his enthusiasm about the field of work infected me.

It was my first promotor Piet Schellekens who gave me the opportunity to finish my Master's thesis Technical Physics at the section Precision Engineering of the department of Mechanical Engineering. Thereby he introduced me into the world of Precision Engineering and his enthusiasm convinced me to conduct my own PhD research in this field. His inspiration and dedication to the field of Precision Engineering, especially metrology, stimulated me throughout the whole research. For all this I am much obliged to him.

Further I would like to thank all the members of my core committee for their support and for reviewing this thesis: prof.dr.ir. G.M.W. Kroesen, dr. H. Haitjema, prof.dr.ir. A.A. van Steenhoven and prof.dr. K.A.H. van Leeuwen. Special thanks go to Han Haitjema for his dedicated support and valuable discussions during the research. Further I would like to express my thanks to Chris Velzel for his reviewing as a keen observer.

The work was financially supported by the Dutch Ministry of Economic Affairs in the framework of the program "IOP Precisie Technologie", for which I would like to express my gratitude. Further I should mention the guidance committee, consisting of Marcel Beems (ASML), Rob Bergmans (NMI), Kees Bos (Agilent), Jarl Buskop (NIKHEF), Rene Klaver (Philips) and Jan Sturre (Heidenhain). I thank them all for their contributions and support during the project.

During the research I was assisted by the following students: Bas de Bonth, Carmen Gus, Dennis Lorier, Gerben van Eijck, Iris Palmen, Jeroen Heijmans, Martijn te Voert, Niek Roset, Robert Schijvenaars, Ronald Hegers en Willem-Jan de Pinth. Thanks a lot for the work carried out and the fun during our cooperation.

I would like to thank the GTD for the realization of parts of the setup. Special thanks go to Frans Kuijpers and Leen Kik for realizing the HeNe-lasers and the zerodur distance holder. A special word of thanks goes to Willie ter Elst for introducing me to real mechanical engineering, his enthusiasm and support. The small cavity would not have been realized without him.

The next (ex-)colleagues have supported to the unique atmosphere in our group:

Maarten Jansen, for his patience with all my (Matlab) problems.

Bastiaan Knarren, ally in the laboratory and always friendly and enthusiastic. From here I would like to congratulate you with your survival as my roommate.

Guido Gubbels, always a great support, always with good advice and with an eye for important things in life. I will really miss that cup of coffee in the morning.

Alper Tiftikçi, from whom I learned that everything has it's own meaning.

Greet Aarts, our friendly, hardworking secretary, always willing to lend an ear.

Frank Delbressine, who told me many times my promotion was most important, and as a result learned me to put things into perspective.

Erik Homburg, from whom I will never forget the phrase: "Gij zult niet meten".

Bas van Dorp, an inexhaustible source of stories.

Edwin Bos, keep on smiling, rules can be twisted.

Guido Florussen, a calm and pleasant colleague.

Michel Morel, a French cheese buff with an unmatched passion for roughness measurements.

John Compter, as a result of your sharp analytical view on all sorts of subjects there was never a dull moment during coffee breaks on friday.

Charlotte Groothuis, thanks for all the help during the research, I will never forget your introduction of a different way of living.

Piet de Waal I thank for the opportunity to participate in the "bedrijfshulpverlening". All members of this organization I want to thank for the sometimes strenuous but also relaxing hours.

Further I thank everyone, I have not mentioned earlier, and contributed in any positive way. Finally I thank Maarten for his patience, tranquility and unconditional support during my PhD-study.

Curriculum Vitae

Suzanne Cosijns was born on September 16th, 1975 in Eindhoven, The Netherlands. She attended the Bisschop Bekkers College, where she obtained her Atheneum degree in 1993. The same year she started her Applied Physics study at the Eindhoven University of Technology. Where she conducted a work placement in the group of "Atomic and Optical interaction" named: study of a high-finesse optical cavity. She conducted her thesis subject at the department of Mechanical Engineering in the group of Precision Engineering on the new optical design of a three dimensional measuring probe for a coordinate measuring machine. At February 11th, 1999 she received her Master's degree in Applied Physics.

Immediately after her graduation she started her PhD study at the section Precision Engineering at the Eindhoven University of Technology which resulted in this thesis.